



## AN ABSTRACT OF THE DISSERTATION OF

Erika Lorna Kraft for the degree of Doctor of Philosophy in Water Resources Engineering presented on April 21, 2011.

Title: Quantitative, Multi-Spectral, Light-Transmission Imaging of Colloid Transport in Porous Media at the Meso Scale.

Abstract approved:

---

Jonathan (Jack) D. Istok

Colloids, particles smaller than ten microns in diameter, are ubiquitous in the subsurface. Colloids have an effect on the transport of contaminants that bind to their surfaces, and can reduce the permeability of aquifer materials through deposition. Some microorganisms, including pathogens, are also transported in the subsurface as colloids. The study of colloid transport behavior is important to the improvement of contaminant transport predictions, and thus to the protection of water quality. Imaging technologies provide detailed spatial-temporal concentration data not obtainable by traditional methods, which rely on the collection and analysis of water samples at discrete locations.

A quantitative, light-transmission imaging system was developed for the observation of solute and colloid transport in a chamber containing porous media. Multi-spectral LEDs and high-quality optical filters were used with a sensitive charge-coupled device camera to obtain images of a 47x57cm sand pack containing two fluorescent tracers—disodium fluorescein and red-fluorescent latex colloids. The properties of the optical components, and the selection of tracers, were optimized to allow for collection of data on three distinct properties of the system in time and space—water content, fluorescein concentration, and colloid concentration. An image processing technique was developed to normalize collected images and to remove noise. The system was calibrated through comparison of

processed intensities with known fluorescein and colloid concentrations. Quantification was possible over the concentration range  $10^{-2}$  to  $10^2$  ppm for fluorescein, and  $10^{-1}$  to  $10^3$  ppm for colloids. This wide range of detection and the very low detection limits were made possible by the improvement in the signal-to-noise ratio that resulted from system development.

Experiments were conducted to demonstrate the utility of this method to observe and quantify fluorescein and colloid transport. Model predictions compared favorably with collected data over multiple data sets, each containing approximately 300 data points. Colloid transport was reasonably fit by the advection-dispersion equation using a retardation factor and a first-order deposition coefficient to represent colloid interactions with the sand surface. In some cases, accurate description of colloid transport will require a more detailed parameterization of colloid dynamics that was beyond the scope of this work. Data presented in this thesis however demonstrate the power of this system to provide insight into the fate and transport of fluorescein and colloids in porous media. These insights facilitate prevention of groundwater pollution by colloidal contaminants, and contribute to effective design of remediation strategies for colloid-contaminated environments.

© Copyright by Erika Lorna Kraft

April 21, 2011

All Rights Reserved

Quantitative, Multi-Spectral, Light-Transmission Imaging of Colloid  
Transport in Porous Media at the Meso Scale

by  
Erika Lorna Kraft

A DISSERTATION

submitted to  
Oregon State University

in partial fulfillment of  
the requirement for the  
degree of

Doctor of Philosophy

Presented April 21, 2011  
Commencement June 2011

Doctor of Philosophy dissertation of Erika Lorna Kraft presented on April 21, 2011

APPROVED:

---

Major Professor, representing Water Resources Engineering

---

Director of the Water Resources Graduate Program

---

Dean of the Graduate School

I understand that my dissertation will become part of the permanent collection of Oregon State University Libraries. My signature below authorizes release of my dissertation to any reader upon request.

---

Erika Lorna Kraft, Author

## ACKNOWLEDGEMENTS

I thank Dr. John Selker for years of participation in this project, and for the training that he has provided on many levels. I thank Dr. Jack Istok for his extensive help in putting together this dissertation—I am forever indebted. I thank Dr. Dorthe Wildenschild and Dr. Anne Nolin for suggestions along the way and for serving on my committee. I thank Dr. Sharyn Clough and Dr. Mary Santelmann for their advice, and for being advocates for my degree completion. I thank Dr. Frank Chaplen for his advice, consultation, and editing. I thank Dr. Rockie Yarwood, Dr. Noam Weisbrod, Dr. Nick Tufillaro, Dr. Yangzhen Fan, Dr. Roger Ely, Dr. Brian Wood, Dr. John Bolte, Dr. Richard Cuenca, Dr. John Baham, Dr. John Westall, Dr. Markus Kleber, Dr. Maria Dragila, Dr. Hatem Mohamed, Dr. Martin Schroth, Dr. Roy Haggerty, Dr. Bob Mitchell, Dr. M Consuelo Carbonell Moore, Ed Lindsley, and Mike Niemet for their consultation. I thank Jim Wagner, Dr. Jed Eberly, Dr. Dave Dickson, Dr. David Rupp, Dr. Elizabeth Burrows, Dr. SunHwa Park, Dr. Chris Graham, Laila Parker, Laura Jensen, Mark Luterra, Tara O'Donnell, Aristides Petrides, Travis Roth, Chadi Sayde, Jennifer Vomocil, and Ryan Stewart for technical assistance.

I thank Bob Schnekenburger for help in the machine shop, for keeping my computers running, and for being my friend. I thank Elena Maus, Susan Atkinson, and Julie Cope for their assistance, their expertise, and their friendship. I thank the National Science Foundation (NSF) IGERT Subsurface Biosphere Program for funding my early years at OSU—giving me the opportunity to begin this journey. I thank NSF Hydrologic Sciences for funding my proposal to develop this work. I thank the Department of Biological and Ecological Engineering for being my home and my family at OSU. I also thank the Institute of Water and Watersheds, the OSU Water Resources Graduate Program, and the Hydrophiles community for providing a context for this experience.

My community, family, and dear friends have provided consistent support and encouragement.

Bikram Yoga teachers and students here in Oregon and around the world have inspired me and given me a sense of belonging. My parents, Don and Midge Kraft, have been tireless in their championing my cause in higher education; they are my great friends and teachers, and my gratitude to them has no bounds. Steve Swenson has provided unwavering love, kindness, gentleness, confidence, and support. Rick Phelps provided tremendous help in system design and manufacturing, has helped keep my life running, and has been a wonderful friend. Sarah Lopath was enthusiastic about this mission from its start. Michael Roberts kindly worked on several revisions of early versions of the thesis. Lynn Walker, Kathryne Parker, Arva Gray, and the MacGamwells have been my guardian angels. John Bain provided significant editing, and has wisely, calmly, and lovingly held my hand in the crucible. Delilah loved me every moment along the way; she sacrificed for my success, and I dedicate this work to her memory.

Lastly, I thank my teacher Bikram Choudhury and my guru Paramahansa Yoganada for their guidance in the path of yoga. The strength and calm that I have received through practicing their teachings has made this dissertation possible. ~~Gratitude for all the Blessings~~

# TABLE OF CONTENTS

	<u>Page</u>
Chapter One: Introduction .....	2
Chapter Two: Literature Review .....	4
Visualization .....	4
Sub-Disciplines .....	5
Components .....	7
Configurations .....	8
Aim .....	10
Control Variables.....	12
Methods .....	12
2-D Meso-Scale Optical Systems .....	14
Non-Quantitative .....	15
Semi-Quantitative .....	18
Quantitative, Non-Fluorescent .....	24
Quantitative Fluorescence Imaging .....	35
Quantitative Fluorescence Imaging via Light-Transmission.....	38
Chapter Three: System Design, Construction, and Operation.....	42
Objectives.....	42
Light-Transmission Fundamentals .....	43
Light-Transmission System Components .....	46
Selection of Optical Components.....	48
System Construction .....	59
System Operation.....	66
Data Collection .....	71
Image Processing.....	75
Evaluation of System Modifications.....	77
Occlusion .....	80
Fluorescein Degradation .....	80
Optical Noise .....	82
Autofluorescence .....	84
Chapter Four: System Calibration.....	86
Calibration Objectives .....	86
Calibration Data Collection .....	87
Calibration Experiments.....	88
Statistics of Processed Intensities .....	115
Calibration Experiment Summary .....	116
Calibration Functions .....	121
Conclusion .....	127

## TABLE OF CONTENTS (Continued)

	<u>Page</u>
Chapter Five: Fluorescein and Colloid Transport.....	128
Objective .....	128
No Flow, Two-Dimensional Transport.....	129
One-Dimensional Flow, One Dimensional Transport.....	137
One-Dimensional Flow, Two-dimensional Transport.....	148
Discussion of Derived Parameters .....	156
Two-Dimensional Flow, Two-dimensional Transport.....	159
Chapter Six: Conclusions.....	163
BIBLIOGRAPHY.....	166
APPENDICES.....	189
Appendix A: Spectral Curves of Optical Components .....	190
Appendix B: Experimental Protocol .....	192
Chamber assembly, packing, and calculations.....	192
Sealing the imaging volume .....	193
Dry images .....	194
Saturating the sand pack and saturated images.....	194
Solution preparation.....	195
Dye plume application and imaging.....	196
Appendix C: Fluorometer Calibration .....	197
Appendix D: Imaging Protocol.....	199
Exposure Time Series .....	199
Power Considerations .....	199
Imaging .....	199
Appendix E: Image Processing.....	201
Protocol.....	201
MatLAB Script .....	203

## List of Figures

<u>Figure</u>	<u>Page</u>
3.1	Light-transmission imaging system attenuation diagram. Three hypothetical fluorescent dye molecules are shown emplaced in a porous medium held between two glass sheets. Excitation light from the light source is shown on the left side of the fluorescent dye molecules. Emission light is shown on the right side of the fluorescent dye molecules. Detection and collection of emitted light (data) occurs at the plane represented by the vertical broken line. The detected intensity of molecules (a) and (b) are the same despite their position in the sand pack. ....44
3.2	Reflexive imaging system attenuation diagram. Excitation light is shown as left-pointing arrows originating at the light source. Emitted light is shown as right-pointing arrows terminating at the plane of light detection and data collection. The detected intensity (thinner arrow) of a dye molecule deeper in the pack (a) is less bright than the detected intensity (thicker arrow) of a dye molecule closer to the active surface (b).....45
3.3	Intensity of emitted light reaching imaging detector in two system configurations. Light intensity collected from molecules as a function of depth is calculated for the two configurations according to Beer's Law. Calculated light intensity using light-transmission (open diamonds) is constant with depth. Calculated light intensity using light reflection (closed diamonds) declines logarithmically with depth. ....46
3.4	Optical properties of components used to determine water content. The dotted curve is the spectrum of light emitted by the 630nm LED. Spectra are shown in terms of percent light intensity as a function of wavelength. The vertical black line represents the wavelength cut-off imposed on the 630nm LEDs by the long-pass filters. The right-pointing triangle indicates that wavelengths longer than 630nm are allowed to pass through the filter and penetrate the porous medium. ....50
3.5	Excitation (closed stars) and emission (open stars) curves for red fluorescent colloids from manufacturer's data plotted as percent maximum intensity. The heavy arrow between plots designates the width of the Stoke's shift between maximum excitation and emission. ....51
3.6	Spectrofluorometer scan of 10 <sup>0</sup> ppm red fluorescent colloids in RO water excited at 580nm. The primary peak is the excitation spectrum reflecting off the colloidal particles. The secondary peak, with maximum at 601nm, is the emission spectrum of the red fluorescent dye. ....52
3.7	Excitation (closed stars) and emission (open stars) spectra for fluorescein dye (two on left) and colloids (two on right). The distance between all peaks was maximized in dye selection to allow for separation of fluorescein and colloid signals. Vertical black lines represent the excitation (488 and 581nm) and emission (512 and 602nm) settings of the spectrofluorometer used to further characterize the dye, and for in-line fluorescence breakthrough data collection. ....53

## List of Figures (Continued)

<u>Figure</u>		<u>Page</u>
3.8	Excitation spectra for the light-transmission system (closed stars). Spectral curves for three sets of LEDs are shown in dashed lines. Black vertical lines show the cut-off wavelength for filters used on LEDs. The colored triangles on these lines point to the side of the line on which wavelengths are allowed to pass. Light is prevented from passing at wavelengths on the other side of the black line.....	55
3.9	Spectral plots of bandpass emission filters #D535-40m (a) and #D620/30m (b) from Chroma Technology Corporation. These filters are used in front of the CCD camera for collection of fluorescein and colloid signals respectively. ....	56
3.10	Emission spectra (closed stars) for fluorescein (left) and colloids (right). Solid lines show bandpass of emission filters used during collection of the fluorescein (left) and colloid (right) emission signals.....	57
3.11	Reduction in noise in a 10mL, 2000ppm colloid plume by use of emission filter. Images were taken with 1s exposure time and were median-filtered to remove noise and colored for ease of viewing. A line has been superimposed on images to show transect location. (a) Image of plume without emission filter in place show background noise and high intensities overall. (b) Transect of plume image without filter shows sloping transition between plume peak and zero values. (c) Image of plume with filter shows background reduced to a flat field and overall lower intensities. (d) Transect from plume image with filter shows improved sharpness of cut-off between plume and background values. ....	58
3.12	Percent average image intensity (-) variation from the maximum value (open triangles) of 530nm light travelling through a dry sand pack, with 76sec exposure, and no emission filter. Power (watts) data (diamonds) from the two power supplies running the 530nm LEDs at the time of image collection.....	60
3.13	Schematic of light box and light array geometry. Exploded view of three optical “collectives” is shown in the upper right corner of the anodized aluminum plate; each collective includes an LED, an optic, an optical filter, and a holographic diffuser. ....	61
3.14	Light-transmission system images showing attrition from the sand pack as a result of poor function of the lower manifold (a) and an uneven margin as a result of poor upper mask (b). Image (a) was taken of 10 <sup>1</sup> ppm fluorescein with a 0.5 second exposure time. Image (b) was taken of 10 <sup>-3</sup> ppm fluorescein with a 191 second exposure time. ....	63
3.15	Full light-transmission system configuration. ....	65

## List of Figures (Continued)

<u>Figure</u>		<u>Page</u>
3.16	Examples of fluorescein bleeding. Images are from the same experiment with (a) having been taken four days prior to (b). Fluorescein bleeding upwards from the influent manifold during upward water flow is apparent in (a) and (b). Also shown in (b) is fluorescein bleeding from the sand surface—likely generated by retention in the foam blocks used around the upper mask for light containment, and caused by downward water flow and radial dispersion. ....	71
3.17	Mean image intensity (left axis) vs. exposure time is shown in closed symbols. Mean image intensity normalized to exposure time (right axis) is shown as open symbols. Images were collected on 2/26/07 of a static sand pack containing fluorescein and colloids at the end of a calibration experiment. Solid black lines are linear regression to the average of the 470 and 530 nm values for exposure time 0.1s (dashed line) and greater where image intensity is shown to be linear ( $R^2=0.99$ , $R^2=0.96$ ) with exposure time. ....	74
3.18	Example of horizontal striping from coolant failure. Image (left) is of water-saturated sand pack collected with a 5-hour exposure time using optical settings for colloid imaging (530nm). Zoom (right) of boxed area shows strips of bright pixels caused by coolant failure. ....	75
3.19	Image processing protocol. Images (two dimensional arrays) are shown as boxes. Scalar values are shown in bold. Operations are shown in italics or with symbols. The subscript $\lambda$ refers to the image having been taken at a specific wavelength. The subscript $d *$ refers to the dark image having been collected with an emission filter matching the image that it is being used to correct. The subscript $f,c$ refers to the actual concentration image being specific to fluorescein or colloids. ....	76
3.20	Signal-to-noise ratio for each of seven concentrations of fluorescein and colloids (a) plotted with “limit of detection” cutoff defined as $SNR=3$ . Images of each concentration were collected three times during a calibration experiment (2/25/09). The maximum value was calculated for each image, and the mean and standard deviation were taken of the replicate maximum values. $SNR$ was calculated as the mean divided by the standard deviation. Bottom plots show the mean of the three maximum processed intensity values for fluorescein (b) and colloids(c) plotted with the standard deviation around that mean. ....	79
3.21	Occlusion by fluorescein at $10^3$ ppm. Images are processed intensity of a $10^3$ ppm plume during a calibration experiment (12/03/07) in a saturated sand pack. Images are collected at 630nm (a), 470nm (b) and 530nm (c) to view water content, fluorescein, and colloids respectively. Matching transects show that emission from fluorescein (b) is blocked, as is transmission of light at 630nm (a). High concentration colloids (b) show little effect of occlusion on fluorescein emission. ....	80

## List of Figures (Continued)

<u>Figure</u>	<u>Page</u>
3.22 Photodegradation of fluorescein over time. Plotted data are the normalized average of the processed intensity maxima of three $10^0$ ppm fluorescein plumes from 2/25/09. Images were taken at 30.52s exposure time with a 10s delay. ....	82
3.23 Fluorescein and colloid concentration images over time (a-e) at 10 mL/min downward flow. Images were taken with 5sec exposure for fluorescein and 3.2min exposure for colloids with flow stopped. Colloid images (bottom row) show evidence of the transport pattern expressed by fluorescein (top row). For the colloid image at time 1 (a), the maximum of the colloid plume is 7.1ppm, while the maximum concentration value generated by fluorescein intensity is 1.2ppm. ....	83
3.24 Flow chart of image processing step aimed at removing fluorescein signal from colloid images. Fluorescein relative concentration and colloid relative concentration arrays are those shown in the next to last processing step in Figure 3.19. The decimal value used to generate the ratio fluorescein relative concentration array was varied to find the value that would lead to the most accurate prediction of colloid mass. ....	84
3.25 Processed intensity images of autofluorescence from quartz sand and craft paper. Images (a) and (b) were illuminated at 470nm and collected with emission filters centered at 535nm. Images (c) and (d) were illuminated at 530nm and collected with emission filters centered at 620nm. Autofluorescence at 470/535nm (a) and (b) is two orders of magnitude brighter than at 530/620nm (c) and (d). Autofluorescence of paper (b and d) is two orders of magnitude brighter than that of sand (a and c). ....	85
4.1 Images of processed intensity from calibration experiment 1. Concentrations are $10^{-3}$ ppm (a, d) $10^{-1}$ ppm (b, e), and $10^1$ ppm (c, f). Images represent a physical area of 33.5 x 40.3cm. ....	89
4.2 Images of processed intensity from calibration experiment 2. Concentrations are $10^{-4}$ ppm (a, d), $10^{-2}$ ppm (b, e), and $10^0$ ppm (c, f). Images represent a physical area of 45.3 x 40.3cm. ....	90
4.3 Images of processed intensity from calibration experiment 3. Concentrations are $10^{-3}$ ppm (a, d), $10^{-1}$ ppm (b, e), and $10^1$ ppm (c, f). Images represent a physical area of 45.3 x 40.3cm. ....	91
4.4 Images of processed intensity from calibration experiment 4. Concentrations are $10^{-3}$ ppm (a), $10^{-1}$ ppm (b), and $10^1$ ppm (c). Images represent a physical area of 45.3 x 40.3cm. ....	91
4.5 Images of processed intensity from calibration experiment 5. Concentrations are $10^{-3}$ ppm (a, d), $10^{-1}$ ppm (b, e), and $10^1$ ppm (c, f). Images represent a physical area of 45.3 x 40.3cm. ....	92

## List of Figures (Continued)

<u>Figure</u>	<u>Page</u>
4.6 Images of processed intensity from calibration experiment 6. Concentrations are $10^{-3}$ ppm (a, d), $10^{-1}$ ppm (b, e), and $10^1$ ppm (c, f). Images represent a physical area of 45.5 x 40.7cm. ....	93
4.7 Images of processed intensity from calibration experiment 7. Concentrations are $10^{-3}$ ppm (a, f), $10^{-2}$ ppm (b, g), $10^{-1}$ ppm (c, h), $10^0$ ppm (d, i), and $10^1$ ppm (e, j). Images represent a physical area of 45.3 x 40.3cm. ....	94
4.8 Images of processed intensity of plumes from calibration experiment 7. Static images taken during downward flushing were collected of fluorescein after seven minutes (a) and colloids after 13 minutes (b). Images represent a physical area of 45.3 x 40.3cm. ....	95
4.9 Images of processed intensity from calibration experiment 8. Concentrations are (a, f) $10^{-3}$ ppm (a, f), $10^{-2}$ ppm (b, g), $10^{-1}$ ppm (c, h), $10^0$ ppm (d, i), and $10^1$ ppm (e, j). Images represent a physical area of 45.3 x 40.3cm. ....	96
4.10 Images of processed intensity of plumes from calibration experiment 8 processed to relative concentration. Static images are of fluorescein (a) and colloids (b) taken after 600mL of flushing. Images represent a physical area of 45.3 x 40.3cm. ....	97
4.11 Images of processed intensity from calibration experiment 9. Concentrations are $10^{-3}$ ppm (a, f), $10^{-2}$ ppm (b, g), $10^{-1}$ ppm (c, h), $10^0$ ppm (d, i), and $10^1$ ppm (e, j). Images represent a physical area of 45.3 x 40.3cm. ....	98
4.12 Images of processed intensity of plumes from calibration experiment 9. Static images are of fluorescein (a) and colloids (b) taken after 500mL had been pumped upwards after the plume. Images represent a physical area of 45.3 x 40.3cm. ....	99
4.13 Images of processed intensity from calibration experiment 10. Concentrations are $10^{-3}$ ppm (a, f), $10^{-2}$ ppm (b, g), $10^{-1}$ ppm (c, h), $10^0$ ppm (d, i), and $10^1$ ppm (e, j). Images represent a physical area of 45.3 x 40.3cm. ....	100
4.14 Images of processed intensity of plumes from calibration experiment 10. Static images are of fluorescein (a) and colloids (b) taken after 300mL flushing. Images represent a physical area of 45.3 x 40.3cm. ....	101
4.15 Images of processed intensity from calibration experiment 11. Concentrations are $10^3$ ppm (a, d), $10^2$ ppm (b, e), and $10^1$ ppm (c, f). Images represent a physical area of 45.9 x 40.3cm. ....	102
4.16 Images of processed intensity from calibration experiment 12. Concentrations are $10^3$ ppm (a, d), $10^2$ ppm (b, e), and $10^1$ ppm (c, f). Images represent a physical area of 46.3 x 40.3cm. ....	103

## List of Figures (Continued)

<u>Figure</u>	<u>Page</u>
4.17 Images of processed intensity from calibration experiment 13. Concentrations are $10^{-3}$ ppm (a, e), $10^{-4}$ ppm (b, f), $10^{-5}$ ppm (c, g), and $10^{-6}$ ppm (d, h). Images represent a physical area of 43.5 x 40.3cm. ....	104
4.18 Images of processed intensity from calibration experiment 14. Concentrations are $10^{-6}$ ppm (a, e), $10^{-5}$ ppm (b, f), $10^{-4}$ ppm (c, g), and $10^{-3}$ ppm (d, h). Images represent a physical area of 43.5 x 40.3cm. ....	106
4.19 Images of fluorescein processed intensity from calibration experiment 15. Concentrations are $10^2$ ppm (a), $10^1$ ppm (b), $10^0$ ppm (c), $10^{-1}$ ppm (d), $10^{-2}$ ppm (e), $10^{-3}$ ppm (f), $10^{-4}$ ppm (g), $10^{-5}$ ppm (h), and $10^{-6}$ ppm (i). Images represent a physical area of 53.8 x 42.6cm. ....	108
4.20 Images of colloid processed intensity from calibration experiment 15. Concentrations are $10^2$ ppm (a), $10^1$ ppm (b), $10^0$ ppm (c), $10^{-1}$ ppm (d), $10^{-2}$ ppm (e), $10^{-3}$ ppm (f), $10^{-4}$ ppm (g), $10^{-5}$ ppm (h), and $10^{-6}$ ppm (i). Images represent a physical area of 53.8 x 42.6cm. ....	109
4.21 Images of processed intensity Processed plume images from calibration experiment 15. 20mL of 10ppm fluorescein and colloids were imaged to view (a) fluorescein and (b) colloids. Images represent a physical area of 16.8 x 42.4cm. ....	110
4.22 Images of fluorescein processed intensity from calibration experiment 16. Concentrations are $10^2$ ppm (a), $10^1$ ppm (b), $10^0$ ppm (c), $10^{-1}$ ppm (d), $10^{-2}$ ppm (e), $10^{-3}$ ppm (f), and $10^{-4}$ ppm (g). Images represent a physical area of 54.1 x 42.4cm. ....	111
4.23 Images of colloid processed intensity from calibration experiment 16. Concentrations are $10^2$ ppm (a), $10^1$ ppm (b), $10^0$ ppm (c), $10^{-1}$ ppm (d), $10^{-2}$ ppm (e), $10^{-3}$ ppm (f), and $10^{-4}$ ppm (g). Images represent a physical area of 54.1 x 42.4cm. ....	112
4.24 Images of processed intensity fluorescein from calibration experiment 17. Concentrations are $10^2$ ppm (a), $10^1$ ppm (b), $10^0$ ppm (c), $10^{-1}$ ppm (d), $10^{-2}$ ppm (e), $10^{-3}$ ppm (f), and $10^{-4}$ ppm (g). Images represent a physical area of 54.1 x 42.4cm. ....	114
4.25 Images of colloid processed intensity from calibration experiment 17. Concentrations are $10^3$ ppm (a), $10^2$ ppm (b), $10^1$ ppm (c), $10^0$ ppm (d), $10^{-1}$ ppm (e), $10^{-2}$ ppm (f), $10^{-3}$ ppm (g), and $10^{-4}$ ppm (h). Images represent a physical area of 54.1 x 42.4cm. ....	115
4.26 Fluorescein statistics of processed intensities from all 17 calibration experiments plotted against known concentration. ....	119
4.27 Colloid statistics of processed intensities from all 17 calibration experiments plotted against known concentration. ....	120

## List of Figures (Continued)

<u>Figure</u>	<u>Page</u>
4.28 Model fitting to statistics of measured intensities from calibration experiment 15 (a) and calibration experiment 17 (b).....	123
4.29 Model fitting to statistics of measured intensities for fluorescein (a) and colloids (b).....	124
4.30 Fluorescein (a) and colloid (b) concentration values for $1 \times 10^1$ ppm calibration solutions from calibration experiment 15 computed using derived calibration functions and fitted parameters. Images represent a physical area of 16.7 x 42.4cm. ....	126
4.31 Fluorescein (a) and colloid (b) concentration values for $1 \times 10^1$ ppm calibration solutions from calibration experiment 17 computed using derived calibration functions and fitted parameters. Images represent a physical area of 16.8 x 42.4cm. ....	127
5.1 Water content images from the 2/25/09 sand pack for early time (a) and late time (b), where vertical lines in the images indicate transect locations. Transects are shown for early time left (c) and right (d) and late time left (e) and right (f). Dashed lines indicate the reference value for porosity. ....	131
5.2 Horizontal transects of water content across the region shown in Figure 5.1 at early time (black lines) and late time (grey lines). Legend shows vertical elevation (cm) of transects from the sand surface. Stars indicate transect elevation used in diffusion calculations.....	132
5.3 Fluorescein concentrations at early time (a) and late time (b) with corresponding transect plots (c-f). Dashed lines indicate location of late time transects. ....	132
5.4 Vertical fluorescein transects through plume at early and late time from the center of mass outwards. ....	133
5.5 Horizontal transects of fluorescein concentration at early time (black) and late time (green). Legend shows vertical elevation of transects (cm). Stars indicate data used for analysis. ....	134
5.6 Horizontal fluorescein transects from Figure 5.5 (stars, right plume) at early and late times used to calculate diffusion coefficient in Table 5.2. ....	134
5.7 Colloid concentrations at early time (a) and late time (b), and vertical transects (c-f).....	135
5.8 Vertical transects through colloid plume in Figure 5.7b and d. Analyses were conducted on data where $0 < x < 7.4$ cm (a) and where $0 < x < 22$ (b). Colloid concentration values in the range $12 < x < 22$ cm that are not included in (b) decline from a maximum of 0.23 ppm to a minimum of 0.010 ppm. ....	136

## List of Figures (Continued)

<u>Figure</u>		<u>Page</u>
5.9	Horizontal transects of colloids at early time (black) and late time (red). Legend shows vertical elevation of transects (cm). Stars indicate data used for modeling. ....	136
5.10	Horizontal colloid transects from Figure 5.9 at early and late times used to calculate diffusion coefficient in Table 5.3. ....	137
5.11	Photodegradation of fluorescein fit with a first order exponential decay model. ....	139
5.12	Water content full image (a), cropped area (b), and transect (c) of 10/9/07 sand pack after emplacement of $10^{-3}$ ppm calibration solution in calibration experiment 10. ....	140
5.13	Water content full image (a), cropped area (b), and transect (c) of 10/9/07 sand pack prior to emplacement of $10^{-2}$ ppm calibration solution in calibration experiment 10. ....	141
5.14	Fluorescein concentration full image (a), cropped area (b), and transect (c) of 10/9/07 sand pack after 60s upward pumping with $10^{-1}$ ppm calibration solution. ....	141
5.15	Equation 28 fit to fluorescein data transect in Figure 5.14c. ....	142
5.16	Water content full image (a), cropped area (b), and transect (c) of 6/29/08 sand pack while saturated with $10^{-1}$ ppm calibration solution. Dashed line represents the value for porosity. ...	142
5.17	Fluorescein concentration full image (a), cropped area (b), and transect (c) of 6/29/08 sand pack after 269s upward pumping with $10^{-1}$ ppm calibration solution. ....	143
5.18	Equation 28 fit to 6/29/08 $10^{-1}$ ppm fluorescein transect from Figure 5.17c. ....	143
5.19	Colloid concentration full image (a), cropped area (b), and transect (c) of 10/9/07 sand pack after 93s upward pumping of $10^0$ ppm calibration solution. ....	145
5.20	Equation 31 fit to colloid transect in Figure 5.19c. ....	145
5.21	Water content full image (a), cropped area (b), and transect (c) of 6/29/08 sand pack while saturated with $10^0$ ppm calibration solution. Dashed line is the gravimetrically calculated value for porosity. ....	146
5.22	Colloid concentration full image (a), cropped area (b), and transect (c) of 6/29/08 sand pack after 388s upward pumping with $10^0$ ppm calibration solution during calibration experiment 15. ....	146
5.23	Equation 28 fit to colloid concentration transect in Figure 5.22c. ....	147

## List of Figures (Continued)

<u>Figure</u>	<u>Page</u>
5.24 In-line fluorometer readings of fluorescein at $10^{-3}$ ppm and colloids at $10^0$ ppm from 6/29/08 experiment. Equation 28 is fit to the fluorescein data.....	148
5.25 Water content full image (a), cropped area (b), and transect (c) of 12/3/07 sand pack while emplaced with $10^1$ ppm calibration plume. The cropped area measures 22.3cm wide by 27.3cm long.....	150
5.26 Longitudinal transects through 10ppm fluorescein plume at three time steps (a-c) under downward flow. Shaded rectangle is area of data where concentration measurements were affected by the plume application tubing. ....	150
5.27 Longitudinal transect of fluorescein concentrations fit using Equation 36.....	151
5.28 Transverse fluorescein concentration transects through the longitudinal center of mass of the 12/3/07 10ppm calibration plume at three time steps (a-c) under downward flow. Shaded rectangle is area of data where concentration measurements were affected by the plume application tubing.....	152
5.29 Transverse transect of fluorescein concentration fit using Equation 36.....	152
5.30 Longitudinal transects through 10ppm colloid plume at three time steps (a-c) under downward flow. Shaded rectangle is area of data where concentration measurements were affected by the plume application tubing. Deposition for colloids is seen in the bluish grey shading above the plume in b and c.....	153
5.31 Longitudinal colloid concentration transect fit by Equation 36. ....	154
5.32 Transverse colloid concentration transects through the longitudinal center of mass of the 12/3/07 10ppm calibration plume at three time steps (a-c) under downward flow. Shaded rectangle is area of data where concentration measurements were affected by the plume application tubing.....	155
5.33 Transverse transect of colloid concentration fit by Equation 36. ....	155
5.34 Colloid concentration images (a-c) matched morphologically with simulated tracer concentrations (d-f) at three early times. Panel d shows boundary conditions-- vertical edges (red bars) are no flux, and horizontal edges (grey bars) are 0.182 and -0.182 constant flux boundaries on top and bottom respectively.....	161

## List of Figures (Continued)

<u>Figure</u>	<u>Page</u>
5.35 Colloid concentration images (a-c) matched with simulated tracer concentrations (d-f) at three late times.....	162

## List of Tables

<u>Table</u>	<u>Page</u>
2.1 Summary of statistics pertinent to imaging system performance. Works cited are those that include quantification across the spatial domain.....	41
3.1 Unit conversion reference for 1 $\mu$ m polystyrene colloids. ....	69
3.2 Summary of SNR statistics for all constant concentration experiments. ....	78
4.1 Summary of experimental details pertinent to data comparison. Color coding distinguishes similarities and differences among experiments. ....	117
4.2 Estimated parameters for three calibration experiments with coefficients of determination. .	125
5.1 Summary of transport experiments. ....	129
5.2 Computed spatial moments, spatial variance, and effective diffusion coefficients for fluorescein. ....	135
5.3 Computed spatial moments, variance, and effective diffusion coefficients for colloids. ....	137
5.4 Fluorescein fitted parameters. ....	144
5.5 Colloid fitted parameters ....	147
5.6 Fitted parameters from 12/3/07 fluorescein transects modeled using Equation 36. ....	151
5.7 Fitted parameters from 12/3/07 colloid transects modeled using Equation 37. ....	154
5.8 Error associated with fit of the two-dimensional models (Equation 36 for fluorescein, Equation 37 for colloids) to 12/3/07 transport data. ....	156
5.9 Summary of fitted parameters obtained from transport experiments. ....	158
5.10 Flow rate comparison for transport experiments. ....	159
5.11 Input parameters relevant to saturated flow for materials Hydrus2D simulation. ....	160
A.1 Exposure times used in calibration experiments. ....	200

## List of Appendix Figures

<u>Figure</u>	<u>Page</u>
A.1	Excitation and emission curves for fluorescein at pH9 from data provided by Molecular Probes plotted with led spectrum, excitation filter cutoff and emission filter bandpass. ....190
A.2	Fluorescent spectra for red fluorescent microspheres overlain by chosen optical components for microsphere excitation and detection. ....190
A.3	Excitation and emission curves of FluoSpheres® red fluorescent microspheres/H <sub>2</sub> O and Fluorescein/pH 9.0 generated from data provided by Molecular Probes, Inc. Overlain are the properties of optical components used in the system. Black dotted lines denote the wavelengths used for fluorometer excitation and emission. ....191
A.4	Fluorometer calibration curves for fluorescein excited at 488nm and emitting at 512nm. Legend notes sensitivity settings, condition of the standards, and linear fits. ....197
A.5	Fluorometer calibration curves for colloids excited at 577nm and emitting at 601nm. Legend notes sensitivity settings, condition of the standards, and linear fits. ....198

Quantitative, Multi-Spectral, Light-Transmission Imaging of Colloid  
Transport in Porous Media at the Meso Scale

## Chapter One: Introduction

Colloids, particles smaller than ten microns in diameter, are important in groundwater hydrology and contaminant transport due to their ubiquitous occurrence in the subsurface [McCarthy and Shevenell, 1998], their effect on transport of contaminants that bind to their surfaces [Corapcioglu and Jiang, 1993], and their ability to reduce permeability of aquifer materials through deposition to sediment surfaces [Blume *et al.*, 2002]. Many microorganisms including some pathogens are also transported in the subsurface as colloids [eg. Pang *et al.*, 2008]. Study of colloid behavior in porous media in a laboratory setting facilitates understanding of fundamental principles controlling colloid transport. Methodologies used to study solute and colloid transport through porous media are reviewed in Chapter Two of this thesis.

Research on colloid transport has historically focused on column experiments that record concentration as a function of time at the column outlet or at a few points along the column length [eg. Grolimund *et al.*, 1998]. In recent years, visualization has become an increasingly popular method for identifying and quantifying the mechanisms controlling colloid transport [eg. Yoon *et al.*, 2006]. Some methods allow microscopic observation of colloid interactions with surfaces over micron length scales (i.e. the pore scale) [eg. Auset and Keller, 2006; Li *et al.*, 2006; Wan and Wilson, 1994a]. Other methods allow observation of colloid concentrations over centimeter length scales (i.e. the meso scale) using x-ray tomography [eg. DiCarlo *et al.*, 2006], MRI [eg. Baumann and Werth, 2005; Sherwood *et al.*, 2003], epi-fluorescence [eg. Bridge *et al.*, 2006; Zhang and Wang, 2006], or light-transmission [eg. Weisbrod *et al.*, 2003b]. These meso-scale systems allow for evaluation of transport behaviors that occur as a result of heterogeneities in the media and fluid distribution, which are critical for accurately predicting transport at the field scale.

In the work presented here, the technical precision of a meso-scale light-transmission visualization system [Weisbrod *et al.*, 2003b] was improved (Chapter Three) and calibrated (Chapter Four) for use in

quantitative solute and colloid transport visualization experiments in saturated porous media (Chapter Five). The goal of this work was to improve the light-transmission visualization system to allow for quantification of water content, fluorescein concentrations, and colloid concentrations, and detection over a broad range of concentrations for more precise analysis of colloid transport behavior. The capacity of this system to achieve these goals was demonstrated in a series of experiments, where one-dimensional and two-dimensional fluorescein and colloid transport were visualized and quantified.

## Chapter Two: Literature Review

### ***Visualization***

Observation is critical to our understanding of the world. As a sense fundamental to human experience, sight can aid researchers in exploration of natural phenomena [Ewing and Horton, 1999b]. Observation allows us to relate intuitively to our subject. Scientific visualization is a powerful tool for attaining and assimilating information [Ewing and Horton, 1999a; Kuester et al., 2005]. Visualizing events occurring in a system of interest allows a more full understanding of collected data [eg. Gao et al., 2006]. According to Friendly [2008], “Data and information visualization is concerned with showing quantitative and qualitative information, so that a viewer can see patterns, trends or anomalies, constancy or variation, in ways that other forms—text and tables—do not allow.” Supplementing point measurements with images creates a result that is more exact, complete, and compatible with the full range of human comprehension styles. Data images also offer increased spatial-temporal resolution, where expanded dimensions facilitate the breadth of understanding [eg. Culligan et al., 2004]. Many disciplines employ the use of a wide number of visualization techniques to address a vast array of scientific questions [eg. White et al., 1996].

Researchers are challenged to report what is happening below the surface, which they can not see directly [Werth et al., 2010]. Subsurface hydrology has benefited greatly from the use of advanced imaging technologies [Conrad et al., 2002]. Many hydrologic experiments have been conducted where high-resolution, quantitative visualization could have significantly aided understanding of targeted questions [eg. Bradford and Bettahar, 2006; Cumbie and McKay, 1999; Liu et al., 2002; Silliman et al., 2001]. Since the late 1970s, the science of subsurface visualization has developed more powerful, reliable, creative, and sensitive technologies for monitoring and recording activity otherwise masked beneath the surface of the earth [Keller and Auset, 2007]. Prior to the development of sophisticated technological capabilities, researchers devised simplified techniques to address questions about the

natural world [eg. *Bouma et al.*, 1977]. Medical science has led the way in developing imaging technologies [*Reinecke et al.*, 1998] dating back to the 19<sup>th</sup> century [*Deinert et al.*, 2004]. Several of these techniques have been adapted to hydrologic applications [*Hall et al.*, 1997], thereby opening up potential avenues for data collection [*Thieme et al.*, 2003]. This chapter surveys the ways in which visualization has been used in subsurface hydrology, and leads to a discussion of the particular technique that is used in this work.

### ***Sub-Disciplines***

Visualization in subsurface hydrology can offer insight into a range of sub-disciplines. These may be grouped as: those that address the soil matrix or solid phase, those that address the mobile phase, those related to contamination, those related to other applied fields, and those that address mathematical applications. The solid matrix has been addressed by visualization techniques in several disciplinary areas. The ways in which solids may be examined using x-ray microtomography have been reviewed from the perspective of materials science [*Stock*, 1999]. In geophysics, tomography [eg. *Vinegar and Wellington*, 1987] and photography [eg. *Schincariol*, 1989] have been used to evaluate multi-phase flow, sandstones have been probed for their transport capacity [eg. *Auzerais et al.*, 1996; *Spanne et al.*, 1994], and fractured rock has been analyzed for its flow variation in response to heating [*Kneafsey and Pruess*, 1998]. In soil science, the solid matrix has been imaged for soil properties such as bulk density [eg. *Petrovic et al.*, 1982], porosity [*Gotz et al.*, 2002], the surface fractal dimension [*Dathe et al.*, 2001], hydraulic conductivity [*Anderson and Bouma*, 1973], and the penetration [*Tester and Morris*, 1987] and transmission of light through various materials have been evaluated [*Mandoli et al.*, 1990]. Soil physics has utilized visualization to observe many phenomena, including lateral flow [*Sinai and Dirksen*, 2006], tracer transport through structured soils [*Nobles et al.*, 2004], and the relationship between hydraulic properties and transport [*Kasteel et al.*, 2000].

The mobile phase of the subsurface may be approached from many perspectives. The physics of fluids have been studied [eg. *Khalili et al.*, 1998; *Khalili et al.*, 1999; *Oates and Harvey*, 2006]. Vadose zone phenomena such as wetting front instability [eg. *Mortensen et al.*, 2001; *Selker et al.*, 1992c] and air flow [*Geistlinger et al.*, 2009; *Wong and Wibowo*, 2000] have been directly observed. Petroleum science has used direct observation techniques [eg. *Coles et al.*, 1998; *Kantzas et al.*, 1992; *Wellington and Vinegar*, 1987]. Soil microbiology has found applications for various observation techniques including fluorescence microscopy [eg. *Chen and Koopman*, 1997; *Li et al.*, 2004; *Wan et al.*, 1994], and magnetic resonance imaging (MRI) [eg. *Manz et al.*, 2003; *Olson et al.*, 2004; *Potter et al.*, 1996]. Colloid science has used visualization techniques extensively to observe transport behavior [eg. *Sirivithayapakorn and Keller*, 2003a; *Smith et al.*, 2008; *Steenhuis et al.*, 2005; *Wan and Wilson*, 1994a]. A review of visualization techniques used in experiments specific to colloid transport has previously been prepared [*Ochiai et al.*, 2005].

Disciplines concerned with contamination in the subsurface have utilized direct observation to study mass transfer processes [eg. *Zinn et al.*, 2004], contaminant transport [eg. *Rimmer et al.*, 1998; *Werth et al.*, 2010], and colloid-facilitated contaminant transport [eg. *de Jonge et al.*, 2004a; *de Jonge et al.*, 2004b]. Processes related to remediation have been analyzed [eg. *Chevalier and Petersen*, 1999; *Conrad et al.*, 2002; *Jeong et al.*, 2000], including those specific to bioremediation [eg. *Huang et al.*, 2003; *Shonnard et al.*, 1994; *Thullner et al.*, 2002a]. Other disciplines potentially related to subsurface hydrology that have utilized visualization include agriculture [eg. *Petersen et al.*, 1997], industry [eg. *Sederman and Gladden*, 2001; *Seymour et al.*, 2004], and chemical engineering [eg. *Reinecke et al.*, 1998; *Sederman et al.*, 1997]. Studies in mathematics make use of imaging data for modeling [eg. *Sun et al.*, 2001], and upscaling [eg. *Wan et al.*, 1996].

## **Components**

Many groundwater components are targeted by researchers using visualization techniques.

Characteristics of components may facilitate or impede detection by imaging. A survey of these groundwater components is presented here, and organized as matrix, water, gas, other fluid, fractional, organism, and process components. These are the targets of the visualization experiment, and define the way in which researchers design and conduct experiments.

Matrix components targeted by visualization include porosity [eg. *Prado et al.*, 2009], pore structure [eg. *Iassonov and Tuller*, 2010; *Neethirajan and Jayas*, 2008; *Schena and Favretto*, 2007], macropores [eg. *Booltink and Bouma*, 1991; *Bouma et al.*, 1977], fractures [eg. *Detwiler et al.*, 1999], volume [Macari et al., 1997], and interfacial area [eg. *Culligan et al.*, 2004; *Niemet et al.*, 2002]. Components of the groundwater phase that have been targeted for direct observation include water-conservative dye [eg. *Aeby et al.*, 1997; *Forrer et al.*, 2000], and other solutes [eg. *Glass et al.*, 1989a; *Zhu et al.*, 2007; *Zinn et al.*, 2004]. The gas phase is a subsurface component that has been visualized [eg. *Kaiser et al.*, 2000; *Mumford et al.*, 2009b]. Non-aqueous-phase liquids (NAPLs) [eg. *Rangel-German and Kavscek*, 2006; *Schincariol*, 1989], including Trichloroethylene (TCE) [eg. *Ferrand et al.*, 1986], are other fluid components, sometimes present in the subsurface, that have been imaged.

The colloidal fraction has been targeted in many imaging experiments [eg. *Auset et al.*, 2005; *Sirivithayapakorn and Keller*, 2003a; *Smith et al.*, 2008], some utilizing natural colloidal materials [eg. *Lenhart and Sayers*, 2004]. Microbial organisms have been observed both as colloidal components [eg. *Sherwood et al.*, 2003] and as biofilms [eg. *Seymour et al.*, 2004]. Processes such as colorimetric reaction [Oates and Harvey, 2006; *Vanommen et al.*, 1988] may also be the target of a visualization experiment. This reaction serves as a proxy for observing fluid behavior.

## **Configurations**

The target components enumerated above lend themselves to different techniques, and each technique requires a certain physical configuration. Experiments aimed at observing groundwater components have been conducted in various configurations and locations, either *in situ* or *ex situ*, in natural or artificial media, at scales ranging from microscopic to the field scale, and in two or three dimensions. Multiple dimensions were implied earlier by Friendly [2008] as a qualification of visualization. Techniques such as gamma radiation, which fundamentally generate a 1-D data stream [eg. *Oostrom et al.*, 1995], may be extended to multiple dimensions [eg. *Dirksen and Huber*, 1978; *Oostrom et al.*, 1997]. Several methods generate two-dimensional (2D) images [eg. *Kechavarzi et al.*, 2000; *Montemagno and Gray*, 1995; *Wan et al.*, 1996]. Also a few methods generate three-dimensional (3D) data [eg. *Kaiser et al.*, 2000]. These 3D images are often digitally sectioned to reveal 2D output, which is more amenable to visual interpretation.

In addition to the configuration of the data, the dimensionality of the subject is important to consider. There is discussion [eg. *Catania et al.*, 2008; *Reylea*, 1982; *Simantiraki et al.*, 2009] regarding the reduction of 3D model systems to nominally two dimensions; in this review, systems will be presented based on the dimensionality asserted by the authors. There are many types of these nominally 2D systems [eg. *Chevalier and Petersen*, 1999]. Some researchers have created single-grain-thickness models [eg. *Ochiai et al.*, 2010] in an attempt to reduce the third dimension more completely. In regards to data dimensionality, some systems are able to represent 3-D processes with 3D data matrices [eg. *Huang et al.*, 2008; *Khalili et al.*, 1998; *Sederman et al.*, 1997]. Others have developed tools to take a 2-D image from within a 3-D matrix [*Chen and Wada*, 1986].

Important in visualization is the scale at which the process takes place. A great deal of work has been done at the pore- or micro-scale [eg. *Wan et al.*, 1996]. Imaging these small systems is facilitated by microscopy. Meso- or Darcy-scale systems are on the order of decimeters, and have the capability to

visualize processes that involve more complexity and heterogeneities above that found at the pore scale. There are fewer of these meso-scale systems [eg. *Zhang and Wang, 2006*], due in part to challenges involved with imaging and managing larger structures. There are also visualization experiments that have been conducted at the field scale [eg. *Petersen et al., 1997*], however, imaging a natural, large-scale system requires simplification or reduction in resolution. Constructing an artificial “field scale” model requires very intensive preparation, long set-up time, and logistical challenges [*Schwille, 1988; Selker, 2010*].

The setting of an experiment is an important piece of the system configuration. Many imaging experiments involving natural media have been conducted on cores [eg. *Majdalani et al., 2007; Soltani et al., 2010*]. Both thin sections [eg. *Hangen et al., 2004; Hatano and Booltink, 1992 1698*] and cross sections [eg. *Seyfried and Rao, 1987; Vanderborght et al., 2002b*] of cores have also been imaged. Some visualization experiments have been conducted on fractures, both natural [eg. *Polak et al., 2003*] and artificial [eg. *Wan et al., 1996*]. Artificial pore networks or micromodels are commonly used [eg. *Auset and Keller, 2006; Jia et al., 1999*] due to their well-defined characteristics, including pore structure and chemical surface properties. Transparent Hele-shaw cells have also been used extensively for almost 50 years as a simplified proxy for porous media in visualization experiments [eg. *Oltean et al., 2004; Wooding, 1963*]. Many experiments too, especially early soil science investigations, have used soil profiles in the field [eg. *Ghodrati and Jury, 1990; Petersen et al., 1997*].

Porous media, both natural and artificial, have been packed into a variety of containers for visualization. These include thin-slab chambers [eg. *Glass et al., 1989c; Schroth et al., 1998b*], tanks [eg. *Konz et al., 2008*], flumes [eg. *Kecharvarzi et al., 2000*], columns [eg. *Baumann and Werth, 2005*] and capillary tubes [*Ochiai et al., 2005*]. Natural media reported in the visualization literature include chalk [eg. *Polak et al., 2003; Zhu et al., 2007*], sandstone [eg. *Vinegar and Wellington, 1987*], sediment [eg. *Khalili et al., 1999*], shale [eg. *Cumbie and McKay, 1999*] and soil [eg. *Klauth et al., 2007*]. Artificial

media that have been used include gel [eg. *Baumann and Werth*, 2005], glass beads [eg. *Burns and Zhang*, 1999; *McNeil et al.*, 2006], idealized sand [*Glass et al.*, 1989c; *Schroth et al.*, 1996], engineered transparent soil [eg. *Welker et al.*, 1999], and zeolite [eg. *Kaiser et al.*, 2000]. Some researchers have used experimental set ups with a configuration appropriate for visualization, without collecting the 2D data [eg. *Shonnard et al.*, 1994].

### **Aim**

Each experiment addresses a hypothesis--and the information being pursued to address the hypothesis is referred to here as the experimental aim. This survey of experimental aims is grouped by physical quantities, spatial distributions, processes, motion, parameters, and mathematical relationships. Examples of physical quantities evaluated through imaging include bulk density [eg. *Garnier et al.*, 1998; *Petrovic et al.*, 1982], concentration [eg. *Zhang and Wang*, 2006], mass [eg. *Wang et al.*, 2008], and porosity [eg. *Wong and Wibowo*, 2000 1814]. Spatial distributions of media features observed with visualization techniques include interfacial area [eg. *Culligan et al.*, 2004; *Niemet et al.*, 2002] and pore structure [eg. *Vogel and Roth*, 2001]. Fluid phase distributions that have been the aim of visualization studies include saturation [eg. *DiCarlo et al.*, 2010], water film configuration [eg. *Zevi et al.*, 2005], and dye tracer distribution [eg. *Aeby et al.*, 2001]. Colloid related distributions that have been imaged include particle flow paths [eg. *Baumann and Werth*, 2004], and particle retention [eg. *Morales et al.*, 2009]. Microbe-related distributions that have been imaged include bacterial distributions [eg. *Yarwood et al.*, 2002], and microhabitats [eg. *Thieme et al.*, 2003].

Hydrologic processes that have been the aim of imaging experiments include those related to fluid, chemicals, colloids, and microbes. Fluid processes that have been evaluated include mixing [eg. *Gramling et al.*, 2002], drainage [*von Wandruska and Wineforder*, 1986], and displacement [eg. *Jawitz et al.*, 1998]. Chemical processes that have been evaluated include solubilization [eg. *Jia et al.*, 1999], dissolution [eg. *Brusseau et al.*, 2002], remediation [eg. *Conrad et al.*, 2002], diffusion [eg. *Polak et al.*,

2003], and hydrodynamic dispersion [eg. *Theodoropoulou et al.*, 2003]. Colloidal processes that have been evaluated include deposition [eg. *Amitay-Rosen et al.*, 2005], release [eg. *Sirivithayapakorn and Keller*, 2003b], and size exclusion [eg. *Sirivithayapakorn and Keller*, 2003a]. Microbial processes that have been evaluated include growth [eg. *Seymour et al.*, 2007], diffusion [*Olson et al.*, 2005], denitrification [*Istok et al.*, 2007], methanogenesis [eg. *Ye et al.*, 2009], and biodegradation [eg. *Huang et al.*, 2003].

Fluid flow in porous media has been evaluated using imaging in experiments specific to lateral flow [eg. *Sinai and Dirksen*, 2006] bypass flow [eg. *Nobles et al.*, 2004], fingered flow [eg. *Glass et al.*, 1989b], fracture flow [eg. *Loggia et al.*, 2009], funneled flow along a capillary fringe [eg. *Walter et al.*, 2000], gas flow [eg. *Mumford et al.*, 2009a], multi-phase flow [eg. *Kechavarzi et al.*, 2005], preferential flow [*DiCarlo et al.*], infiltration [eg. *Rangel-German and Kovscek*, 2006], and imbibition [*Weisbrod et al.*, 2003a]. Researchers have observed various types of particle motion, including transport [eg. *Oates et al.*, 2005], mobilization [eg. *Gao et al.*, 2006], trajectory [eg. *Auset and Keller*, 2004], velocity [eg. *Baumann and Werth*, 2005], microbial motility [eg. *Sherwood et al.*, 2003], and migration [eg. *Olson et al.*, 2004].

Colloid transport parameters that have been determined via imaging methods include attachment rates [eg. *Baumann and Niessner*, 2006], collision efficiency [eg. *Baumann and Werth*, 2005], detachment rates [eg. *Smith et al.*, 2008], Derjaguin-Landau-Verwey-Overbeek (DLVO) parameters [eg. *Bridge et al.*, 2007], filtration theory parameters [eg. *Baumann and Werth*, 2004], removal efficiency [eg. *Crist et al.*], and residence time [eg. *Auset and Keller*, 2004]. Solute flow parameters that have been determined via imaging methods include diffusivity [eg. *de Jonge et al.*, 2004b], dispersion coefficient [eg. *Gaganis et al.*, 2005], and the solute mixing regime [eg. *Aeby et al.*, 1997].

Mathematical relationships may be developed via visualization. Many results from imaging studies have been modeled [eg. *Kechavarzi et al.*, 2005; *Rockhold et al.*, 2007] and precision of image data has

been addressed [eg. *Detwiler et al.*, 1999]. Hysteretic relationships have been defined using imaging [eg. *Hoà et al.*, 1977], as have particle-surface interactions [eg. *Wan and Wilson*, 1994a] and velocity profiles [eg. *Gotz et al.*, 2002].

### **Control Variables**

As in any scientific experiment, visualization of subsurface processes utilizes control variables to address hypotheses. These control variables may be chemical in nature, such as pH [eg. *Lenhart and Saiers*, 2004] or ionic strength [eg. *Zevi et al.*, 2009 1739]. Parameters may be physical, such as boundary conditions [eg. *Nicholl et al.*, 1994], heat [eg. *Kneafsey and Pruess*, 1998; *O'Carroll and Sleep*, 2007], or pressure [eg. *Sirivithayapakorn and Keller*, 2003a]. Controls may be placed on the colloidal fraction e.g. colloid type [eg. *Wan and Wilson*, 1994a], input concentration [eg. *Klauth et al.*, 2007], particle size [eg. *Sirivithayapakorn and Keller*, 2003a], and particle surface characteristics [eg. *Chen and Flury*, 2005; *Crist et al.*, 2005]. The fluid phase may be varied to affect a response as a function of flow rate [eg. *Wan and Tokunaga*, 1997], density or viscosity [eg. *Jawitz et al.*, 1998], saturation level [eg. *Chen and Flury*, 2005], or the transiency of infiltration [eg. *Auset et al.*, 2005; *Gao et al.*, 2006]. The media may also be controlled by grain size or texture [eg. *Crestana et al.*, 1985], heterogeneity [eg. *Brusseau et al.*, 2000], surface chemistry [eg. *Johnson et al.*, 1996], surface roughness [eg. *Morales et al.*, 2009], or pore structure [eg. *Lanning and Ford*, 2002]. This sampling of control variables shows the breadth of experimental possibilities even in systems simplified for direct observation.

### **Methods**

Methods developed for acquisition of 2D or 3D data include non-imaging techniques, photography, gamma ray techniques, X-ray techniques, positron emission techniques, magnetic resonance imaging, and optical imaging. There are advantages and challenges with each of these methods, as well as resolution and detection limits. Non-imaging visualization techniques include tracings [eg. *Jawitz et al.*, 1998; *Nobles et al.*, 2004; *Schroth et al.*, 1995], tensiometer arrays [eg. *DiCarlo et al.*, 1999; *Hoà et al.*,

1977], fiber optics [eg. *Ghodrati, 1999; Ptak and Schmid, 1996*], and core stains [eg. *Hatano et al., 1992*]. While these techniques may have the potential to generate spatial distributions of data regarding subsurface properties, the data they produce is qualitative in nature or lacks resolution. Still photographs [eg. *Walter et al., 2000*] and analog video [eg. *Glass et al., 1989d*] have been used for direct imaging, yet data lacks quantitative power or requires a digitization step for quantification.

Gamma ray probes have been used extensively to collect soil property point measurements [eg. *Barataud et al., 1999; Hopmans and Dane, 1986; Oostrom and Lenhard, 1998*]. Gamma probes have also been used in transects [eg. *Istok et al., 2007*] or arrays [eg. *Brusseau et al., 2000; Walker et al., 1998*] to yield improved resolution, or in combination with scanning technology that generates data with high spatial resolution [eg. *Dirksen, 1978; Hsieh et al., 1998*]. Computer-assisted tomography (CT) is a scanning method that has been used with gamma rays, as well as positron emission [*Khalili et al., 1998*] and X-rays, to generate 3D representations of hydrologic properties such as soil water content [*Hainsworth and Aylmore, 1983*]. X-rays have been used with tomography both at the micro/pore scale [eg. *Clausnitzer and Hopmans, 2000; Li et al., 2006*] and the meso/Darcy scale [eg. *Chen et al., 1996; Crestana et al., 1985*]. Higher intensity sources such as synchrotrons have improved the capability of X-ray techniques [eg. *Altman et al., 2005; DiCarlo et al., 2006; Garnier et al., 1998; Liu et al., 1993; Wildenschild et al., 2002; 2005*]. MRI has also been used to generate 3D representations of static [eg. *Hall et al., 1997*] and dynamic [eg. *Chen et al., 2002*] hydrologic phenomena at the meso scale [*Baumann and Werth, 2005*] and the pore scale [eg. *Ciobanu et al., 2002*].

When three dimensions and opaque media are not central to the aim of the study, visible light (optical) techniques in two dimensions offer an affordable and accessible means of addressing scientific questions. For small systems, microscopy has been extensively utilized to address such phenomena as distribution of colloids [eg. *Wan and Tokunaga, 2005; Zevi et al., 2005*] and dispersion of bacteria [eg. *Lanning and Ford, 2002*]. Charge-coupled device (CCD) cameras have been used

without the aid of microscopy to capture processes such as solute dispersion [Theodoropoulou et al., 2003], oil migration [eg. Loggia et al., 2009], and biodegradation [eg. Huang et al., 2003].

Experimental configurations may even allow for a combination of micro and meso scale imaging [eg. Yoon et al., 2006]. Some optical imaging systems target fluorescent probes to capitalize on the light-transmission capacity of translucent media [eg. Yoon et al., 2006]. Fluorescence imaging may be conducted using various spectra of light including visible [eg. Crist et al., 2004] and ultra violet (UV) [eg. Dunn et al., 2005].

The experimental system presented in this thesis is designed primarily to address questions pertaining to fluid physics and colloid science, yet the experimental system has potential for application in several of the aforementioned areas of subsurface hydrology. The work here targets model colloids and conservative dye tracer components of the groundwater system, and has the ability for *in situ* observation in idealized media at the meso scale. Transport behavior of colloids over Darcy scale heterogeneities was the aim of this work, and the system developed could be used to collect data to demonstrate physical and chemical processes shown to be important at the pore scale and at the field scale. Sand texture, pH, ionic strength, and colloid size are control variables that were used in this system to address solute and colloid transport response. Fluorescence imaging is used here to detect broad concentration ranges of model tracers in porous media, with visible light being used to excite tracer dye molecules. This work presents the largest quantitative, multi-spectral, fluorescence imaging system with the largest range of detection as compared with all previous studies to date. Evidence of this claim is presented in the following section.

## **2-D Meso-Scale Optical Systems**

Many 2-dimensional meso-scale systems have been designed that utilize optical methods to collect high-resolution data appropriate for image processing and analysis. These systems may be described in the context of their technological evolution, the research questions they were used to address, and

the parameters that have been used to assert their usefulness. Those systems that are most similar to the one developed in this work are presented here with analysis of their features. Specifically addressed will be the dimensions of the experimental system, imaging hardware and resolution, image processing protocol, and error analysis. As work within a research group evolves and technical capabilities improve, the data tend to demonstrate improved resolution, sensitivity, and precision. The primary measures of visualization capability are detection limits, signal-to-noise ratio, and resolution. When available, these measures will be presented as a means of comparing the capability of our system to the work that has come before. This section will be presented with increasing relevance to our system, and will conclude with a comparison of the quantitative power of those systems most similar to ours.

## Non-Quantitative

Quantitative imaging is defined here as the use of digital images to quantify component properties (e.g., concentration) across the spatial range of the collected data. Targeted component properties vary according to the aim of the experiment. Image processing and calibration to known physical values (eg. input concentration) are required to convert image intensities to targeted component properties. There are a number of systems that have been developed that lack this quantitative power yet offer much of the basic functionality of, and are thus relevant to, the system described in this thesis.

Optical systems that generated qualitative 2D data include a very early one in Minnesota, where dyed blobs of colored non-wetting liquid were imaged in 2 x 2 x 15cm glass tubes packed with plastic beads [Ng *et al.*, 1978]. At UC Berkeley, a 2D model was constructed to observe the emplacement of nonaqueous liquids in the vadose zone [Pantazidou and Sitar, 1993]. Observations were recorded by hand tracing. In Vermont, channel structure was imaged in a transparent replica of a natural fracture [Brown *et al.*, 1998]. In the Netherlands, a 40 x 40 x 2.5cm tank was packed with silica sand and dyed

LNAPL distributions were imaged with a digital camera [Wipfler *et al.*, 2004]. Qualitative image contours were compared with those from model simulations. In Germany, a 79 x 14 x 1cm flow tank was built and packed with glass beads or sand to visualize the degradation of contaminant plumes by microorganisms [Bauer *et al.*, 2008]. The use of resazurin in this system as an indicator of redox processes was qualitative [Bauer *et al.*, 2009a; Bauer *et al.*, 2009b].

In Connecticut, an 86 x 72 x 2.5cm tank was packed with glass beads and illuminated from behind to reveal a shadow graph of air flow [Ji *et al.*, 1993]. Camera and video recordings were used to qualitatively address air flow as a function of air injection pressure and grain size. A similar tank measuring 90 x 90 x 2cm was used in Michigan to image air flow in sand [Peterson *et al.*, 1999]. This experiment used a colorimetric reaction to observe the locations and geometry of airflow pathways, and results were recorded by photography and acetate tracings. The same system was used to study the air-flow geometry during air sparging into fine grained sand [Peterson *et al.*, 2001], and the effect of air sparging on toluene reduction [Peterson *et al.*, 2000].

In Germany, extensive work was conducted on the qualitative imaging of chlorinated hydrocarbon (CHC) transport under a variety of model conditions [Schwille, 1988]. Glass columns (20-40cm i.d., 100-200cm height) and a large trough (560 x 160 x 28cm) were packed with various grades of sand and dyed CHCs were imaged. A lysimeter was made of glass and packed with gravel. It was imaged for fluorescein and then CHC transport to compare both infiltration with transport, and results from model sand with those from heterogeneous material. CHC infiltration into 70cm-high model fractures was imaged, and microscopic visualization in glass beads was also conducted.

A group at Auburn University visualized the transport of dense leachate plumes in sand [Oostrom *et al.*, 1992]. This experiment used three containers ranging in size from 80 x 40 x 5cm to 205 x 100 x 8cm packed with glass beads or sand. Photographs of plumes marked by various types of dye were interpreted qualitatively in conjunction with gamma radiation measurements of NaI concentrations.

Much of Oostrom's subsequent work has utilized gamma radiation measurements and scanning techniques [eg. *Oostrom et al.*, 1998], but, a review was later prepared on intermediate-scale experiments, that also included optical saturation imaging [*Oostrom et al.*, 2007].

Collaboration between groups in New York and Montana resulted in digital imaging of a 12 x 8 x 1cm reactor packed with glass beads for detection of biofilm growth and concomitant change in hydrodynamics [*Sharp et al.*, 1999]. Image cross sections were analyzed. Digital time lapse images were collected of the same sized system, and used fixed diamond elements as a proxy for porous media [*Sharp et al.*, 2005]. Natural bioluminescence and dye tracer distributions were qualitatively interpreted.

At Imperial College in London, immiscible displacement of dyed oil phase as a function of media heterogeneity was photographed in a 56 x 10 x 0.6cm glass bead model, and diagrams drawn from the photographs were presented [*Dawe et al.*, 1992]. Flow variability in glass beads was examined via light transmission imaging in 20 x 10 x 0.6cm pack as a function of bead surface wettability [*Caruana and Dawe*, 1996]. Results were again shown diagrammatically. This group also studied these multi-fluid processes at the microscale [*Dawe et al.*, 2010].

Collaboration between researchers in Colorado and Denmark resulted in an observation of dye through a 53cm long x 42cm soil monolith [*Wildenschild et al.*, 1994]. Stained soil slices were cut from the monolith and digitized for visualization of macropore structure. The Colorado research group then used dual gamma spectroscopy to image NAPLs in a large flume [*Illangasekare et al.*, 1995a; *Illangasekare et al.*, 1995b], and a very large 2D tank was used for non-visualization experiments [*Barth et al.*, 2001a; *Barth et al.*, 2001b]. The Danish contingent used a 100 x 100 x 8cm heterogeneously-packed tank with both video and photographic equipment to qualitatively observe dye transport through heterogeneous sand [*Wildenschild and Jensen*, 1999]. X-ray tomography was later used [*Wildenschild et al.*, 2002; *Wildenschild et al.*, 2005].

## Semi-Quantitative

This section presents those studies that generated 2D digital data that were processed to quantify parameters in one dimension. These studies did not result in arrays that were quantitative across the spatial extent of the data.

In Switzerland, a quantitative imaging system was designed to count microspheres in fluid samples [Nehren *et al.*, 1995]. This system was small-scale and did not include porous media, but demonstrates the technical imaging capabilities of this group. They reviewed the use of MRI for visualization of flow and transport in porous media [Chen *et al.*, 2002], and MRI was used for investigation of density-dependent flow [Oswald *et al.*, 2002]. A CCD camera was used to collect images of solute transport in 40 x 40cm fracture models [Su and Kinzelbach, 2001]. Solute transport over the same fractures were imaged via light-transmission with a CCD camera and images were processed to concentration [Lunati *et al.*, 2003]. Related work had been conducted on a 22 x 33cm transparent replica of a natural rock fracture, where qualitative images were collected of dyed water via light transmission [Su *et al.*, 1999]. And subsequently a study on a natural fracture utilized dyed water and a video camera to observe preferential flow [Su *et al.*, 2003].

In this large Swiss research group, digital images were collected of microbial growth in 56 x 44 x 1cm pack of glass beads using light transmission [Thullner *et al.*, 2002a]. Brilliant Blue FCF dye was used as a reference for glucose distribution and qualitative images were collected of water flow and biomass distribution. Clogging was also visualized at the pore scale [Thullner *et al.*, 2002b]. A review of flow systems used for addressing bioclogging was compiled [Thullner, 2010b], which generated some dialogue [Baveye, 2010; Thullner, 2010a]. A 38 x 60 x 0.6cm transparent cell packed with crushed, fused silica glass was illuminated from behind, and images were taken of air channels [Kong *et al.*, 2009] and media response to air injection [Kong *et al.*, 2010b] with a fast camera. The same cell was

also packed with spherical glass beads and imaged to see the effect of air injection on grain packing [Kong *et al.*, 2010a]. Distributions across the spatial domain were not quantified.

In Alberta Canada, researchers used halogen light transmission through a 0.3mm-thick glass bead pack and a time lapse imaging and image processing technique to study and model diffusion mass transfer of miscible oil [Hatiboglu and Babadagli, 2008]. Pixel resolution was not reported. In this study, oil saturation and displacement geometry were interpreted qualitatively, while the fractal dimension of the displacement front was quantitatively determined by image analysis. These quantitative results were compared with model predictions, but error in estimation was not reported. Light transmission through a 5 x 5 x 0.3cm media-packed chamber resulted in images used qualitatively to explain results from experiments on core samples [Hatiboglu and Babadagli, 2010a; b]. The same quality camera as in previous experiments was used, and details on image processing were not provided. Pore scale visualization of gas injection into a fracture was also performed by this group [Er and Babadagli, 2010].

At Texas A&M, video photography at two scales was used to image air bubble migration in 4cm i.d. columns packed with glass beads to a height of 90cm [Roosevelt and Corapcioglu, 1998]. Columns were illuminated from behind with a fluorescent light source, and blue dye was used to accentuate the contrast between water and air. Image analysis was conducted to quantify bubble migration velocity in one dimension; however quantitative mapping of the gas phase was not accomplished for the full spatial extent of image data.

In France, two rough-walled glass plates measuring 30 x 16cm were used to create a 1cm fracture aperture through which dyed oil was imaged using a light-transmission technique [Loggia *et al.*, 2009]. A 12-bit camera with 0.34mm/pixel resolution was used to measure aperture width and oil saturation, but quantitative results were limited to representative dimensionless numbers. Light transmission had also been used at UC Berkeley in an 8 x 7 x 2cm fracture model replicating natural rock to qualitatively measure two phase flow [Persoff and Pruess, 1995].

In New York, a 17.8 x 12 x 2.9cm cell was packed with quartz sand of different grades and tracer transport was observed [Nambi and Powers, 2000; Powers et al., 1998]. These experiments were aimed at quantifying NAPL dissolution using effluent analysis, and visual observations aided in their interpretation [Nambi and Powers, 2003]. A larger stainless steel tank (112 x 68 x 3cm) with a glass front was packed with sand and imaged to reveal the spatial distribution of 0.1mg/L Oil Red-O-dyed gasoline and 0.05mg/L fluorescein -dyed ethanol in a simulated spill [McDowell et al., 2003; McDowell and Powers, 2003]. Bit depth and pixel resolution of the imaging hardware were not reported. Images of the dyed gasoline phase were analyzed to quantify the size and the perimeter of the gasoline pool. From these values, LNAPL saturation values were determined, but no 2D mapping of oil saturation was produced.

Dye tracers and digital imaging techniques have been used extensively by a group in the United Kingdom (UK) [Mooney et al., 1999; Mooney and Nipattasuk, 2003; Mooney and Morris, 2008; Morris and Mooney, 2004]. Images in these experiments were taken of exposed soil profiles illuminated by a tungsten lamp; images had a 0.2mm/pixel resolution, but their bit depth was not reported. Concentration prediction from image processing was calibrated by destructive sampling [Forrer et al., 2000]. Images were processed for standardization and thresholding, but homogeneous illumination was assumed. Results were used to quantify the average percentage dye cover for each soil type, but did not generate quantitative maps of dye across the image domain. A related paper reviewed the ways in which researchers had quantified the penetration of light through soil [Tester and Morris, 1987].

A US group tested the use of artificial transparent "soil" in visualization of flow from a prefabricated vertical drain into media packed cylinders [Welker et al., 1999]. The dyed front was mapped by hand. In related work, a group in New York state explored the range of transparent media for use in imaging experiments [Iskander et al., 2002; Sadek et al., 2002]. The consolidation and permeability of these

media were studied using digital image correlation (DIC). The goal was to determine if the geotechnical properties of the idealized media were similar to those of natural soils [Liu *et al.*, 2003]. The DIC technique was tested for its accuracy in quantifying media deformation [Sadek *et al.*, 2003], and an adaptive cross correlation technique was devised to reduce errors associated with DIC [Liu and Iskander, 2004]. The same technique was used to evaluate the modeling capacity of the transparent media [Liu and Iskander, 2010]. A spatial deformation experiment was run on these transparent media using a packed 5 x 15 x 30cm tank [Iskander and Liu, 2010]. The DIC technique was used in an experiment where a novel transparent porous medium (Aquabeads--a water absorbing polymer) was packed into a 40 x 14.7 x 2.8cm tank; the calibrated system was used to observe multiphase flow [Lo *et al.*, 2010]. A fluorometer was used to develop a linear calibration relationship between concentration and fluorescence over the red dye and Oil Red-O concentration range 0-0.5g/L and 0-0.06g/L respectively; fluorescence was then shown to be proportional to image intensity. An 8-bit CCD camera was used and the model was illuminated by a fluorescent light source from above at an angle normal to the axis of imaging. Pixel resolution was not reported. A black curtain was used to reduce light scattering, but optical filters were not used to control light spectra. 2D contour maps were presented representing five percentage levels of intensity in processed images, but maps of actual predicted dye concentration were not developed. DIC was also used by a group in Illinois to quantify localized displacements in a 14 x 8 x 4cm sand packed cell [Finno *et al.*, 1996; Harris *et al.*, 1995; Rechenmacher and Finno, 2004].

In Sweden, after an imaging experiment on dye transport in vertical field sections [Persson *et al.*, 2001], a comparison was made of the accuracy of dye concentration estimation from various image processing techniques [Persson, 2005a]. These techniques were tested on multiple soils in a 10 x 5 x 2.5cm chamber illuminated at a 45° angle with halogen lamps, and imaged by a 12-bit CCD camera; pixel resolution was not reported. A calibration routine was used to generate red-green-blue (RGB) values to Vitasyn-Blau AE 85 dye concentration relationship for several soil types over the

concentration range 0-1.5g/L. Exposure time was varied, several methods of image processing were compared, and optimized root mean square errors (RMSE) of dye concentration estimates ranged from 0.075 – 0.094g/L across soil types, but no 2D maps of dye concentration were shown. A 100 x 100 x 0.03cm sand packed Hele-Shaw cell was also used to demonstrate accurate dye tracer prediction by image processing and calibration [Persson *et al.*, 2005]. The same illumination and imaging set up were used, and here the reported pixel resolution was 0.6 x 0.6mm/pixel. Brilliant Blue dye concentrations were calibrated to processed intensity over the dye concentration range 0 – 1.4g/dm<sup>3</sup>, with an overall RMSE of 0.057 g/dm<sup>3</sup>. Concentration maps across the cell were not presented. Surface soil moisture of static samples was also determined in this laboratory as a function of soil or sand color via image analysis [Persson, 2005b].

A group in Greece used a 100 x 120 x 2cm tank to observe dyed NAPL distributions in variably saturated sand [Simantiraki *et al.*, 2009]. Quantitative mapping of LNAPL saturations using 0.003% Sudan III dye was achieved through image processing and calibration. A calibration relationship was developed for each combination of two sand types and two LNAPL types using six levels of LNAPL saturation. No camera specifications were reported, but images were processed to hue-saturation-intensity (HSI) format and intensity values allowed for generation of LNAPL movement profiles, where color intensity is a linear function of LNAPL saturation. Profiles are mapped directly to LNAPL saturation for the final image in each experiment, yet no estimation of error in prediction was made.

An artificial model aquifer measuring 1400 x 50 x 13cm was built of steel and glass by a group in Germany and used to visualize longitudinal mixing [Jose *et al.*, 2004], and vertical transverse mixing in quartz sand [Rahman *et al.*, 2005]. Dye tracers illuminated with neon lights through the front glass pane were imaged by a digital camera having a 0.6mm/pixel resolution. Camera bit depth was not reported. Efforts were made to limit error from ambient light. Images were geometrically corrected and color calibrated to Cochineal Red A dye concentration. A concentration of 0.3g/L dye was used for

tracer experiments, and concentration profiles are presented with associated model fit. Concentration was not mapped quantitatively, but rather as the ratio of concentration to starting concentration; and estimation of error comes only from the theoretical model rather from physical validation. Dispersion coefficients were determined from the experiments.

A group in Canada utilized halogen light transmitted through a 50 x 60 x 1cm chamber packed with glass beads to observe DNAPL fingering processes either by a 35-mm camera and then digitized, or by a video camera connected directly to a PC [Smith and Zhang, 2001; Zhang and Smith, 2001; Zhang and Smith, 2002]. Finger velocities were quantified, but 2D DNAPL saturations were not mapped. Other systems were subsequently built in this laboratory to observe gas expansion due to NAPL partitioning. One such system having dimensions 10 x 8 x 0.8cm, was packed with silica sand, illuminated with a halogen bulb, and imaged with a CCD camera at a resolution of  $0.05\text{mm}^2/\text{pixel}$  [Mumford *et al.*, 2009a]. Critical gas cluster length was quantified, but 2D quantitative maps were not presented. Two other flow cells were built with dimensions 68 x 59 x 1cm [Mumford *et al.*, 2009b] and 62 x 44 x 1cm [Mumford *et al.*, 2010]. These cells both were packed with layers of glass beads and silica sand, illuminated from behind by a fluorescent light bank, and imaged with two CCD cameras--one at the pore scale and one at the macro scale, with resolutions of  $0.023$  and  $0.2\text{mm}^2/\text{pixel}$  respectively. Bit depth of these cameras was not reported. Images were collected of the depth-averaged gas saturation. Image processing converted RGB values to grayscale, removed the background image, and corrected for image alignment, but no attempt was made to generate quantitative 2D maps of saturation [Mumford *et al.*, 2009b].

A multi-national team used a fluorescent black light imaging system to quantify leaching of pyranine dye in a 19.6 x 7.1 x 1cm soil monolith [Duwig *et al.*, 2008]. This 12-bit camera had a resolution of  $0.25\text{mm}^2/\text{pixel}$  and dye concentration was calibrated from 5 to 40g/L. The imaged surfaces were soil profiles or cores section faces, and thus dynamic flow behavior was not able to be observed. Several

members of this group used some of these image processing techniques to evaluate the relationship between soil structure and water tracer transport parameters [Prado *et al.*, 2009].

In Quebec , Canada, an image processing technique was developed to determine chemical concentration in a 15cm i.d. x 61cm length glass bead packed cylinder [Dong and Selvadurai, 2006]. Concentration of sodium chloride acid red dye at the surface of the column was determined from images of reflected light. The starting concentration was 1g/L, and image processing utilized a calibration curve over the range 0 – 1g/L. Error analysis was not conducted.

## Quantitative, Non-Fluorescent

The use of fluorescent tracers in scientific visualization creates a particular set of challenges and advantages [Persson, 2005a]. Non-fluorescence imaging experiments resulting in quantitative data arrays will be presented in this section. The range of targets is broad, as are the range of imaging geometries. Those systems using light-transmission will be grouped together due to their closer relevance to the system described in this thesis. Studies will be drawn from this section as deemed appropriate for the comparison of quantitative power presented in Table 2.1. Qualitative studies will be included in this section where they have played a role in a research group's development of quantitative systems.

A large group in Switzerland developed a technique used for many experiments over a seven year period. Photographs were collected of dye mixing in sections of an 80cm length x 12cm i.d. column [Aeby *et al.*, 1997]. These color and near-infrared images were of a static condition post-mixing and were processed and calibrated to dye concentration. Dissertations were written in this group describing imaging of fluorescent tracers in field soils [Aeby, 1998; Forrer, 1997]. Several quantitative imaging experiments on tracer transport through soil profiles [Aeby *et al.*, 2001; Forrer *et al.*, 1999; Forrer *et al.*, 2000] soil monoliths [Albrecht *et al.*, 2003; Stadler *et al.*, 2000] and soil sections [Vanderborght *et al.*, 2002a; Vanderborght *et al.*, 2002b; Weiler and Fluhler, 2004] were conducted.

Some of these studies utilized optical filters for control of light spectra, and profiles of relative dye concentration with depth were presented [Aeby *et al.*, 2001]. A related group in Germany developed an image processing protocol for the determination of colloid concentrations in column sections [Klauth *et al.*, 2007].

A sand tank was constructed by the Swiss group to compare laboratory results to field observations [Ursino *et al.*, 2001a]. The tank was 75 x 40 x 5cm, packed with a random layering of three textures of sand, and illuminated by a xenon lamp. CCD images with a resolution of 225pixels/cm<sup>2</sup> and collected using an emission filter were processed to concentration, and spatial moments of tracer plume were calculated. Tracer dispersion was also addressed in this system [Ursino *et al.*, 2001b]. Image analysis was improved for this system to correct for non-homogeneous illumination from the 45° incident light, and high-resolution maps of material distribution were generated [Gimmi and Ursino, 2004]. The 16-bit images were processed using segmentation to account for different sand textures, corrected for inhomogeneity of illumination and reflection, and filtered to extract color features and reduce noise. Calibration was conducted on 25 areas of the sand tank, and fractional comparisons were made between estimated and designed material distributions.

This Swiss system was also used to classify soil attributes [Ursino and Gimmi, 2004] and to observe solute mixing [Rossi *et al.*, 2007]. In the solute mixing experiment, 0.5g/L Acid Yellow fluorescent dye was applied as a point source, the dye was excited by optically filtered light from a xenon lamp, and filtered light images were collected of dye emission by the 16-bit CCD camera. Images had a pixel resolution of 0.004cm<sup>2</sup>/pixel, and were processed to dye concentration from intensity using a power law relationship, and by correcting for nonuniform illumination and optical spatial variations. The method of moments was used to track plume evolution. Concentration maps were not presented and mass balance was not conducted as a means of estimation validation. These solute dilution results were also modeled [Rossi *et al.*, 2008]. The PI from the above efforts was also involved in imaging

experiments addressing the effect of water saturation on radiative transfer [Banninger *et al.*, 2005] and tracer fluorescence [Banninger *et al.*, 2006] in a 6 x 6cm flow cell of varying thickness using a beam tracing model [Banninger, 2004].

Before joining a group in Ontario Canada, O'Carroll [2004] imaged perchloroethylene (PCE) infiltration into silica sand using a digital camera. The study was not quantitative and images captured oil present only on the imaging surface of the 31 x 38 x 1.7cm sand pack. Later a quantitative light-transmission imaging system was developed using a 55 x 45 x 1.3cm chamber packed with silica sand, a CCD camera, an emission filter on the camera lens, and an image processing protocol. Bit depth and pixel resolution of the camera were not provided. This system was used to study NAPL displacement [O'Carroll and Sleep, 2007] and flow alteration resulting from biofilm growth [Ye *et al.*, 2009]. In the NAPL study, the NAPL was dyed with Sudan III, and images were processed to NAPL saturation using a normalized light intensity correlation [Niemet and Selker, 2001] adapted to a multiphase system. A calibration curve relating NAPL concentration to image intensity was generated for the system, but details of the concentration range utilized were not presented. The accuracy of NAPL saturations at each pixel could not be quantified. In the biofilm study, gas formation, migration and distribution were observed. Water saturation was estimated through correlation to normalized light intensity [Niemet and Selker, 2001], and 2D quantitative maps of liquid saturation across the spatial domain were presented at multiple time steps, yet validation of the image based estimates was not addressed. Tracer tests using Rhodamine WT (RWT) and fluoride were also conducted in this study, but dye concentrations were not quantified.

A group at Auburn University packed chambers (each slightly different dimensions, but roughly 50 x 30 x 2cm) with glass beads and used a digital camera to image salt water intrusion [Goswami and Clement, 2007], nanoparticle transport [Kanel *et al.*, 2008], and fluid mixing [Abarca and Clement, 2009]. This group also developed an error estimation technique for measurements obtained from

image analysis [Goswami *et al.*, 2009]. This effort included a simulation component as well as an experimental component conducted in a 23 x 20 x 1.2cm glass bead packed chamber, and imaged by an 8-bit CCD camera with a 0.027mm<sup>2</sup>/pixel resolution. Red dye solutions with concentration ranging from 0.1 - 5mg/L were illuminated from behind with a fluorescent light source and imaged to generate a calibration relationship between concentration and image intensity. Images were processed by cropping and using a median filter. Calibration was possible only at concentrations less than 4mg/L due to limits of the imaging system sensitivity. A power-law function was determined to best fit the calibration curve, and quantitative maps of dye distribution were presented. Error in concentration was estimated through an image analysis approach. This analysis was broken into error caused by the calibration relationship and error caused by noise, and a relationship to concentration was presented for each. The total fractional error with respect to concentration determined by this method ranged between 15 – 30%. Error estimation determined by mass balance ranged between 1.2 – 10.2%. It is therefore asserted that use of mass balance for error estimation may under-represent actual error, and image analysis estimates should be used.

A group based at Massachusetts Institute of Technology used a light-transmission technique with image processing and calibration to quantify a number of processes in three different chambers. A 36 x 5.5 x 1.8cm chamber packed with cryolite sand was used to generate reactive transport data for comparison with model predictions [Gramling *et al.*, 2002]. Reactive microbial transport in a 30 x 6 x 1.9cm chamber packed with the same type of media was compared to a conceptual model [Oates *et al.*, 2005]. A 40 x 20 x 0.6cm chamber was packed with glass beads and imaged with a 14-bit camera to visualize and quantify solute transport and mass transfer [Zinn *et al.*, 2004], and fluid mixing as detected by a colorimetric reaction [Oates and Harvey, 2006]. Pore scale visualization was also conducted by this group [eg. Yoon *et al.*, 2006]. The solute transport and mass transfer study [Zinn *et al.*, 2004] utilized a fluorescent light source behind the chamber, and an optical filter on the camera which had a resolution of ~0.16mm<sup>2</sup>/pixel to image a starting concentration of 30mg/L FD&C Blue 1

dye as it was flushed from the chamber down to a lower detection limit of  $\sim 0.3$  mg/L. Images were processed to relative concentration maps, but calibration and error estimates were not conducted.

The colorimetric reaction study [Oates and Harvey, 2006] imaged color change as a result of fluid mixing with a resolution of  $\sim 0.1$  mm<sup>2</sup>/pixel. Tiron and molybdate were the mixing species, and diffuse white light was transmitted through the medium. Images were processed to normalized absorbance, and those values were then converted to concentration via a calibration curve generated for the range 0.05 – 0.0375M (Tiron + Molybdate). Mass balance comparing image-predicted to known injected mass showed less than 3% error in prediction. Presented maps of fluid mixing across the spatial domain were quantified as a fraction of the maximum value, but not to actual concentration. Product absorbances were recorded with a dynamic range over more than 1.5 orders of magnitude.

In Alberta, Canada, Schincariol [1989] pioneered much of the meso-scale visualization techniques in use today. This thesis project developed a photographic imaging system to observe DNAPL migration in a 117 x 71 x 5cm tank packed with glass beads. The same system was used to address variable density flow and mixing [Schincariol and Schwartz, 1990]. Some images from this experiment were used to develop an image processing technique [Schincariol et al., 1993]. The technique was tested on an additional data set collected in Ohio using the original flow tank. Optical density of reflected light versus dye concentration curves were generated over the range 0-500mg/L for five different grain sizes of porous media. The image processing technique was later improved in Ontario to systematically address varying porous media properties or lighting conditions [McNeil et al., 2006].

A similar flow tank was built in Ontario Canada measuring 150 x 120 x 6cm and imaged on color slide film [Vangeel and Sykes, 1994]. The slides were digitized and processed to obtain LNAPL saturations. A tank similar to that of Schincariol et al. [1990] was also built in Ohio [Swartz, 1993], packed with glass beads, and imaged with time lapse photography. Images of the 183 x 61 x 10cm tank were digitized and processed to evaluate mixing and instability development in variable-density systems [Swartz and

*Schwartz, 1998*). The results of these experiments were later modeled [*Ibaraki et al., 2000*]. This tank and method were also used to image tracer plumes in layered glass beads of varying permeability [*Yu and Schwartz, 1999*]. Processed images and calibration allowed for mapping of tracer concentration distributions. The same digital monitoring approach was used to observe potassium permanganate concentration in test tubes [*Seol et al., 2001*] and tracer transport through a transparent fracture network [*Kim et al., 2006*].

The tracer plume study [*Yu and Schwartz, 1999*] imaged Rhodamine dye through the glass wall of the tank and processed images using a calibration curve generated over the range 2 – 97mg/L. Though Rhodamine does fluoresce, it was used in these experiments at high concentrations without the use of optical filter, and thus it will be categorized with the non-fluorescence experiments. The photographic negatives were digitized to 8-bits with a resolution of 200dpi. The relationship between optical density and pixel value was fitted with a second-order polynomial function, and optical density was related to dye concentration by a third-order polynomial function. Maps of dye plumes were presented as normalized concentration between 0 – 1, and no error analysis was reported.

In the UK, photographs were collected of dye flow patterns through ballotini glass beads in a 15 x 19 x 1cm flow cell in response to temperature differentials [*Menand et al., 2003*]. These images were interpreted qualitatively. A 34 x 15 x 1cm pack of glass beads was illuminated from behind with a projector and imaged and images were used to quantify the location of the fluid interface between two mixing fluids [*Menand and Woods, 2005*]. Images in this study had a resolution of 7pixels/mm (bit depth was not reported), and were processed to red dye concentration, which was calibrated by a linear relationship over the range 0.1 to 0.5g/L with a maximum error of 5%. Another experiment used a 10 x 60 x 1cm cell packed with ballotini and saturated with saline solution [*Verdon and Woods, 2007*]. Images were collected of this cell as dyed fresh water was injected and flow proceeded

horizontally. Images were not processed, but image data on reaction front depth as a function of time were used to validate the proposed gravity-driven flow model.

A group in Germany designed an imaging system for a 40 x 45 x 1.2cm tank packed with glass beads and illuminated by an array of light-emitting diodes (LEDs), where two CCD cameras were utilized to capture gas flow phenomena at two spatial scales [Geistlinger *et al.*, 2006]. Gas flow was further observed by oblique light reflection in this system [Geistlinger *et al.*, 2009; Lazik *et al.*, 2008] with 12-bit CCD resolution of 0.48mm/pixel and 12.7 $\mu$ m/pixel for the overview and detail cameras respectively. Optical gas saturation was calibrated to the gravimetric value by creating a linear relationship between the two. The fit of this line to the data on a plot of optical estimation vs. gravimetric estimation had an  $R^2 = 0.991$ .

A group in France followed 2D experiments that used tensiometer and gamma radiation array measurements [Hoa *et al.*, 1977] by designing a 2D system based on visible light transmission [Hoa, 1981]. This system used a 15 x 5.5 x 1cm sand pack illuminated by an incandescent light, and a photosensitive element. Calibration of light intensity to water content was based on light transmission theory, and was accurate with a confidence level of greater than 95%. Water content estimates from this method were also compared favorably to estimates from the gamma ray absorption method.

A Danish group explored bioclogging in a 30 x 44 x 3.8cm sandbox [Kildsgaard and Engesgaard, 2001]. Digital images were processed to dye concentration using a calibration routine, and showed an effect of microbial growth on flow [Kildsgaard and Engesgaard, 2002]. Brilliant Blue dye concentrations were calibrated to processed image intensity over the range 0 – 180mg/L and concentration was mapped over the spatial domain. Neither camera specifications nor error analysis were reported. These experimental results were used to validate a model developed by a Swiss group simulating the effect of biomass growth on hydraulic properties [Brovelli *et al.*, 2009].

In Georgia, a light-transmission imaging system was built to quantify PCE saturation distributions in 150 x 48 x 1.4cm silica sand pack [Suchomel and Pennell, 2006]. A fluorescent light source, Oil Red-O dye, and a digital camera were used. Camera specifications were not provided. Images were processed using hue-NAPL calibration curve whose range was not stated, and obtained PCE volumes were within 5% of the known applied. Maps of PCE distributions were presented. A similar study had been conducted on a 64 x 40 x 1.2cm sand packed flow tank to investigate the effect of surfactants on the distribution of PCE [Rathfelder et al., 2003].

At the EPA, a group used light-transmission visualization to study DNAPL saturation in 15 x 15 x 1.4cm and 48 x 48 x 1.4cm sand packed chambers [Bob et al., 2008]. Fluorescent tubes were used for illumination, 16-bit CCD camera was used for image capture with a resolution of 0.5mm<sup>2</sup>/pixel, and images were processed without the use of a calibration curve to quantify un-dyed PCE to a lower limit of 0.025 saturation. PCE saturation estimates were compared to known values with a relationship having  $R^2 = 0.993$ . PCE dyed with Oil Red-O was also quantified in these chambers, this time with the use of a calibration curve. The  $R^2$  for this approach compared with known values was 0.999. Maps of PCE saturation across the spatial domain were presented.

A group in Arizona used a 40 x 20 x 2.6cm flow chamber packed with sand and a light reflection visualization technique [DiFilippo, 2008] to image TCE distribution [DiFilippo et al., 2010]. TCE was dyed with 100mg/L Sudan IV. Mass balance analysis yielded volumes of immiscible liquid with error between 0 and 82%.

In Germany, an image processing protocol was developed to map solute concentrations in a 78 x 15 x 1.1cm glass bead packed chamber [Jaeger et al., 2009]. In this experiment, light transmission was used and data was captured in RGB by the CCD camera. The camera had a resolution of 5 megapixels, and the bit-depth was not reported. Acid Red 18 dye concentration was determined using a calibration

relationship ranging from 0.5 – 100mg/L dye. Error in concentration prediction was within 5% of the known applied value.

A group in the UK developed a multispectral image analysis method to quantify non-aqueous phase liquid (LNAPL) flow in a 180 x 120 x 8cm flume packed with silica sand [Kechavarzi *et al.*, 2000]. Images were taken of reflected light from the illuminated sand surface with a 12-bit digital infrared camera. An image processing protocol corrected for noise and imaging error and mass balance was conducted to determine the overall error associated with the method. The same flume and image processing technique were used to quantify and model LNAPL flow [Kechavarzi *et al.*, 2005]. In this experiment, water saturation and fluid pressure were also measured using resistivity probes and tensiometers, respectively. The technique was also used to evaluate the effect of macro-heterogeneity on LNAPL distribution in unsaturated sand [Kechavarzi *et al.*, 2008]. The LNAPL was dyed with Oil Red O and a linear calibration relationship was used to convert images from optical density to saturation. Error in these image estimates was determined by mass balance, which averaged 8.7% over all experiments.

Research originated at Cornell University in New York State has led to considerable development of non-invasive imaging techniques. Theoretical discussions of wetting front instability were presented [Glass *et al.*, 1989b; Hill and Parlange, 1972] accompanied by images from a method to observe finger persistence over sand layers in an 80 x 30 x 1cm chamber [Glass, 1985]. A slab chamber was built with dimensions 100 x 30 x 1cm, packed with two layers of silica sand, and dyed infiltration events were recorded with time lapse photography [Glass *et al.*, 1988]. The collected images were then projected to a screen and traced to acetate sheets, where qualitative inferences were made about wetting front instability. Solute transport across layered sand was then observed via the same method in a 140 x 51 x 1cm chamber [Glass *et al.*, 1989a]. The experimental system was improved through a sand washing and preparation step and by achieving homogeneous and dense sand packing. Finger flow was observed using the same imaging method [Glass *et al.*, 1989c]. The method was adapted to three

dimensions to obtain wetting front instability results that were asserted to be applicable to the field scale [Glass *et al.*, 1990]. Columns were sectioned and dye staining patterns observed. A grid lysimeter was also used to increase spatial resolution of data on solute transport [Andreini and Steenhuis, 1990].

Qualitative observations that had been made with the 2-D method were explained by a physically based theory, and that theory was tested by an improved method using light-transmission [Glass *et al.*, 1989d]. Based on the work of Hoa [1977; 1981] relative moisture content was determined via digitized images of fluorescent light travelling through the 80 x 50 x 1cm sand packed chamber. Theoretical considerations of light transmission, and calibration to moisture content and matric potential were discussed [Bell *et al.*, 1990]. This improved technique was used to study the effect of hysteresis on finger flow [Liu *et al.*, 1991]. The method was further improved by addition of miniature, high-speed, planar tensiometers for simultaneous measurement of matric potential during infiltration into a 97 x 51 x 1cm sand packed chamber [Selker *et al.*, 1992a]. These results were used in conjunction with further studies to model and predict finger moisture profiles [Selker *et al.*, 1992b]. 2D (40 x 51 x 1cm) and 3D (40 x 30cm i.d.) sand packed columns were used with the developed methods to evaluate the boundary conditions required for unstable wetting [Selker *et al.*, 1992c].

A related study was conducted by researchers at , where a 30 x 5 x 0.2cm dry glass bead packed chamber was illuminated from behind by a fluorescent light source and infiltration was imaged with a video cassette recorder [Lu *et al.*, 1994b]. Inferences were made about infiltration and finger flow, and meso-scale observations were supported by microscopic images of finger tips. The same chamber and method were used to compare capillary rise in porous media to that in simple cylinders [Lu *et al.*, 1994a].

Researchers at Cornell continued work with the light transmission system by measuring oil and water content using hue variation of blue dye in a 57 x 51 x 1cm sand packed chamber [Darnault *et al.*, 1998]. The accuracy of this technique was checked by mass balance and by comparison with

synchrotron X-ray measurements. The Cornell High Energy Synchrotron Source was also being used as the sole visualization technique for other experiments within this group [eg. *Rimmer et al.*, 1998].

Tensiometers were used with light transmission to acquire pressure and water content measurements in a 55 x 30 x 1.2cm chamber, and address the development of preferential flow paths in sand [*DiCarlo et al.*, 1999]. Wetting and non-wetting fluids have been non-quantitatively imaged in a 120 cm long x 2.5cm i.d. column [*Chao et al.*, 2000]. Funneled flow mechanisms were evaluated in a 110 x 180 x 1cm chamber using the same method [*Walter et al.*, 2000]. Here, a tensiometer array was installed along the upper surface of a coarse inclusion in a fine matrix to determine hydrodynamic phenomena occurring along the capillary diversion. Oil, water, and air distributions were quantified by light transmission and a color CCD video camera in 55 x 45 x 1cm [*Darnault et al.*, 2001] and 62 x 52 x 1cm [*Darnault et al.*, 2002] sand packed chambers. Results were validated by X-ray measurements. A fluorescent light source was used and RGB images were converted to HIS format before calibration relationships were applied. Water content was related to hue, total liquid content (water + oil) was related to intensity, as water was dyed blue with 28% CuSO<sub>4</sub>. Agreement between image predictions agreed with X-ray validation to a standard deviation of 0.023 for water and 0.037 for oil. Microscopic visualizations were also conducted by this group [*Crist et al.*, 2004; *Crist et al.*, 2005; *Gao et al.*, 2009].

Robert Glass, who did his graduate work at Cornell, continued his work on meso-scale visualization in his position at Sandia National Laboratory in New Mexico. He observed gravity-driven instability in non-horizontal fractures using a 61 x 31cm fracture plate, food coloring dye and an 8-bit CCD camera [*Nicholl et al.*, 1994]. This laboratory also uses X-ray absorption for imaging, and the precision of the two techniques was compared [*Tidwell and Glass*, 1994]. X-ray absorption was used by this laboratory to observe dye tracer distributions in a quarter-scale replica of a Yucca Mountain emplacement drift [*Tidwell et al.*, 2003]. Light transmission and a 12-bit digital imaging system were used to quantify entrapped phase dissolution within a 15 x 30cm fracture plate [*Glass and Nicholl*, 1995]. Mounting of this system on a rotating stand allowed for evaluation of gravity driven fingering within the fracture

[*Glass and Nicholl, 1996*]. This system had a spatial resolution of 0.15mm/pixel. These fracture flow experiments used a fluorescent light source, and the precision of the technique improved over time [*Detwiler et al., 1999*]. Gravity-destabilized fingering was also observed in a 26 x 60 x 1cm sand packed chamber [*Glass et al., 2000*]. The 12 bit camera had a resolution of 0.25mm<sup>2</sup>/pixel, and images were processed to saturation fields with a maximum nonwetting volume error of 12%. These results were modeled [*Glass et al., 2001*] as were those from the fracture plate experiments [*Glass and Yarrington, 2003*]. Dyed DNAPL migration was imaged in a 61 x 60 x 1cm sand filled chamber using light transmission [*Conrad et al., 2002*]. This study used a 12-bit camera with a resolution of 0.36mm<sup>2</sup>/pixel, the DNAPL was dyed with Oil Red O, and confounding factors made quantification of DNAPL saturation untenable.

Collaborators of this group used X-ray transmission to collect data on solute transport through a 31 x 31 x 2.1cm slab of sandstone [*Klise et al., 2008*]. Visualization experiments were also conducted by this group at the micro scale [*Mortensen et al., 2001; Zhong et al., 2001*].

## Quantitative Fluorescence Imaging

In Australia, a 120 x 118 x 5.3cm flow tank was packed with sand, enclosed in a dark curtain, illuminated from above with fluorescent light, and imaged with a digital camera [*Simmons et al., 2002*]. The images were corrected for lighting nonuniformity as described by Schincariol et al. [1993], but were not calibrated to concentration due to complex patterns in dye distribution. A 110 x 60 x 5cm tank was later used by this group to image fingering of saline solution marked by fluorescein dye in a heterogeneous packing of low-permeability glass bead lenses in high-permeability sand [*Post and Simmons, 2010*]. Again no attempt was made to quantify dye concentration, but comparisons were made to numerical simulations. This experiment is included here to illustrate the challenge associated with quantification of fluorescent tracers.

A group in the UK developed a fluorescent UV imaging technique for viewing solute transport in an 18 x 28 x 1cm glass bead packed flow cell [Huang *et al.*, 2002]. A linear calibration function was developed over the range 0 – 400mg/L fluorescein to relate fluorescent intensity to fluorescein concentration. Light transmission images were processed to relative concentration using this relationship, but no maps of actual concentration were presented. The same system was used to quantify non-equilibrium partitioning tracer transport [Jones and Smith, 2005]. Here the NAPL phase was dyed with acidified fluorescein dye and imaged by the CCD camera. Images were processed to NAPL saturation using non-linear calibration relationships over the tracer concentration range 0 – 0.08g/L. No estimate of prediction error was presented. Similar chambers and the same method were used to image dissolved oxygen generation [Huang *et al.*, 2003] as well as biodegradation processes [Rees *et al.*, 2007] via an oxygen-sensitive fluorescent indicator. Fluorescein and oxygen distributions were mapped spatially in the 16 x 12 x 3cm sand packed chamber imaged by Huang [2003] using linear calibration functions over the range 0 – 8mg/L fluorescein and 0 – 7mg/L oxygen. Image estimations were compared with model simulations. In the biodegradation study [Rees *et al.*, 2007] oxygen concentrations in the range 0 – 10mg/L were mapped spatially from images of the fluorescent  $\text{Ru}(\text{phen})_3\text{Cl}_2\text{O}_2$  tracer. Quantitative arrays were not presented.

A researcher at Notre Dame did extensive work using a large flow tank without the aid of visualization [Dunn and Silliman, 2003; Silliman *et al.*, 1987; Silliman and Simpson, 1987; Silliman, 1995; Silliman *et al.*, 1998; Silliman, 2001 #26]. Non-imaging visualization via application of a curing resin to porous media was accomplished [Silliman *et al.*, 1994]. Collaboration with a researcher in Israel later resulted in direct observation of many intermediate scale experiments. Fluid flow at the capillary fringe was photographed qualitatively in two large flow tanks (27 x 17 x 21cm and 100 x 13 x 89cm) [Silliman *et al.*, 2002]. That study plus others used to study the capillary fringe were reviewed [Berkowitz *et al.*, 2004]. A 27 x 19 x 15cm chamber was later built and illuminated with UV light to image green fluorescent protein (GFP) bacteria transport into the capillary fringe from below the water table [Dunn

*et al.*, 2005]. Two additional large scale chambers (86 x 45 x 10cm and 213 x 65 x 10cm) were built to observe dispersion in heterogeneous media [*Levy and Berkowitz*, 2003] and the effect of air injection on lateral flow [*Dror et al.*, 2004].

An associated group based in the UK developed a system for quantitative imaging of fluorescent colloid and fluorescein transport in a 20 x 10 x 0.7cm chamber packed with quartz sand [*Bridge et al.*, 2006]. UV light was used for fluorescence excitation in a reflexive geometry, and image processing and calibration yielded concentration detection of less than  $1 \times 10^{-3}$  M fluorescein and in the range 2-200mg/L colloids. This system used an 8-bit camera with a  $0.5 \text{mm}^2/\text{pixel}$  resolution. The mass prediction at initial time for fluorescein was 74% of the known mass, and 87% for colloids. The same chamber and technique were used to quantify pore saturation and colloid removal efficiency [*Bridge et al.*, 2007], colloid mobilization and redeposition during drainage [*Bridge et al.*, 2009], and microbial transport [*Bridge and Banwart*, 2009].

A group in New York State designed an epi-fluorescence imaging system with a 10 x 18 x 1cm flow cell packed with quartz sand. Fluorescent colloids were excited with a halogen lamp and imaged with a 14-bit CCD camera with a  $4 \times 10^{-4}$  mm pixel resolution to a detection limit of  $2.5 \times 10^5$  spheres/mL [*Zhang and Wang*, 2006]. Mass recovery in transport experiments was 93-103%. The same system was used in collaboration with researchers in Connecticut and Pennsylvania to observe solute mixing and plume containment [*Zhang et al.*, 2009].

A group in Switzerland used a 158 x 60 x 4cm flow tank packed with two textures of glass beads and illuminated from above to quantify solute concentration with a 12-bit digital camera [*Konz et al.*, 2008]. Reflection images were processed, and the image intensity to concentration relationship was quantified. An error analysis was conducted for this technique, and the measurements were compared to those attained via resistivity. A slightly larger tank (158 x 98 x 4cm) was built and used to image variable density flow in heterogeneous media using the same quantitative imaging technique

[Konz *et al.*, 2009c]. These results were also compared with model simulations. Both flow tanks were also used with the same imaging technique in a set of parallel experiments comparing variable density flow in two distinct layered media geometries [Konz *et al.*, 2009b]. This reflection technique was compared to a light transmission method using the 4cm thick flow tank and non-fluorescent dye, and found to perform better with regard to light scattering effects [Konz *et al.*, 2009a].

### Quantitative Fluorescence Imaging via Light-Transmission

A group in Florida constructed a 61 x 39 x 1.5 cm chamber packed with silica sand to observe tracer dye displacement [Jawitz *et al.*, 1998]. Observations in this early experiment were recorded as digitized tracings. The same chamber was used to study NAPL distribution using breakthrough curves; direct observations were not made [Jawitz *et al.*, 2003]. NAPL distributions in silica sand were again studied, but now digital images of the dye distribution in the chamber were collected and processed to allow for semi-quantitative interpretation of the NAPL architecture [Fure *et al.*, 2006; Kaye *et al.*, 2008]. A light transmission visualization method using a fluorescent light source was then developed to quantify dye concentration in a 30 x 20 x 1.7cm chamber packed with silica sand [Wang *et al.*, 2008]. Imaging was conducted in a darkened room to minimize light noise. Images from a 16-bit CCD camera fitted with one of two bandpass filters were processed to remove noise, and image intensity was calibrated to Acid Blue 9 dye concentration over the range 3 to 30mg/L. Water phase dye was correlated to PCE saturation, and PCE saturation distributions were mapped across the spatial extent of the images. Mass recovery from this imaging technique was greater than 95% for higher NAPL saturations, and greater than 90% for the residual phase. Reactive tracer tests were conducted in both of the above chambers, and the same method was used to again map PCE saturations across the spatial domain [Chen and Jawitz, 2008]. DNAPL dissolution experiments were also conducted with a similar method in the smaller of the two chambers, and the ratio of PCE mass estimated from image analysis was between 89 – 103% of the known injection amount [Chen and Jawitz, 2009].

An Italian group used a 20 x 28 x 1cm flow cell packed with glass beads, transmitted light excitation, and a CCD camera to test the accuracy of image processing and calibration for the non-destructive determination of fluorescein concentration [Catania *et al.*, 2008]. Details of the method were presented and compared with past efforts at *in situ* solute mapping. Processing methodologies were presented and a pixel-by-pixel calibration was proposed as the requirement for removing nonuniform illumination. The concentration range over which calibration was conducted was 1-64mg/L, within which a linear relationship was determined between concentration and intensity below 20mg/L. Error analysis was conducted and asserted to be acceptable for the linear range of the calibration curve. In subsequent experiments, image analysis was not used due to its associated inaccuracies [Catania and Paladino, 2009].

After leaving Cornell, John Selker and his group in Oregon continued efforts in visualization. LNAPL distributions were observed via light transmission in a 50 x 60 x 0.95cm silica sand packed chamber and traced on plastic film taped to the front glass panel [Schroth *et al.*, 1995]. The same type of experiment was also conducted for flow over textural interfaces [Schroth *et al.*, 1998a] and accompanied by numerical simulation [Schroth *et al.*, 1998b]. The silica sands used in these experiments, as well as those to follow, were characterized in detail [Schroth *et al.*, 1996].

The light transmission system became quantitative with the use of a CCD camera to detect bioluminescence in 75mL flat-faced tissue culture flasks [Uesugi *et al.*, 2001]. The power and potential of the method were advanced by a physically based model and image processing protocol to determine liquid saturation in porous media via light transmission [Niemet and Selker, 2001]. This analysis was extended by quantification of gas-liquid interfacial area in a 45 x 45cm sand packed chamber, this time using a bandpass filter on the CCD camera [Niemet *et al.*, 2002]. The bandpass filter controlled the chromatic range of quantification of liquid saturation in a saline imbibition experiment [Weisbrod *et al.*, 2002]. Water vapor transport associated with saline imbibition was

quantified over layers of differing sand grades [Weisbrod *et al.*, 2003a]. Unstable fingering of saline solutions at a rate faster than pure water was observed in a 65 x 50 x 1.3cm sand packed chamber [Weisbrod *et al.*, 2004]. Gas flow was quantified in a 50 x 50 x 1cm sand packed chamber using pH indicator and a series of image processing steps relating dye color to CO<sub>2</sub> distribution [Parker *et al.*, 2006]. Physically based models explaining the geometry of gas injection were compared to experimental results [Selker *et al.*, 2007].

Bacterial growth was quantified via luminescence over four orders of magnitude using the same system [Yarwood *et al.*, 2002]. Colonization dynamics of bacteria in this system were observed and modeled [Rockhold *et al.*, 2007]. And the effect of microbial growth on water flow and solute transport were quantified using the addition of dye to trace flow paths [Yarwood *et al.*, 2006]. Transport of fluorescent colloids was observed in this system, using a gel filter sheet to control light exciting the particles [Weisbrod *et al.*, 2003b]. The technique used for observing fluorescent colloids in this system was improved to reduce noise by matching high quality bandpass filters to the light source [Kraft and Selker, 2005; Ochiai *et al.*, 2006]. These methods were further refined as presented in Chapter Three of this thesis.

Table 2.1 Summary of statistics pertinent to imaging system performance. Works cited are those that include quantification across the spatial domain.

Study	Dimensions (cm) <sup>3</sup>	Porous		Bit Depth	Resolution (mm <sup>2</sup> /pixel)	Component(s) Targeted	Detection Range	Prediction Error
		Media Type	Illumination Geometry					
<b>Non-Fluorescence</b>								
O'Carrol and Sleep, 2007 Ye et al. 2009	55 x 45 x 1.3	sand	transmission	n/r	n/r	NAPL saturation water saturation	0-1	n/r
Goswami et al., 2009	23 x 20 x 1.2	glass beads	transmission	8	0.027	red food dye	0-4mg/L	15-30%
Zinn et al., 2004	40 x 20 x 0.6	glass beads	transmission	14	0.16	FD&C Blue 1 dye	0.3 - 30mg/L	n/a
Oates et al., 2006	40 x 20 x 0.6	glass beads	transmission	14	0.1	colorimetric reaction	0.05 - 0.038M	<3%
Yu and Schwartz, 1999	183 x 61 x 10	glass beads	n/a	8	200dpi	Rhodamine dye	2 -97mg/L	n/a
Menand and Woods, 2005	34 x 15 x 1	glass beads	transmission	n/r	7pix/mm	red dye	0.1 - 0.5g/L	<5%
Lazik et al., 2008 Geistlinger et al., 2009	40 x 45 x 1.2	glass beads	reflection	12	0.23 1.6x10 <sup>-4</sup>	gas saturatioion	0 - 1	R <sup>2</sup> = 0.991
Kildsgaard and Engesgaard, 2002	30 x 44 x 3.8	sand	n/a	n/r	n/r	Brilliant Blue dye	0 - 180mg/L	n/r
Suchomel and Pennell, 2006	150 x 48 x 1.4	sand	transmission	n/r	n/r	PCE saturation	n/r	<5%
Bob et al., 2008	15 x 15 x 1.4 48 x 48 x 1.4	sand	transmission	16	0.5	PCE saturation	0.025 -	R <sup>2</sup> = 0.999
DiFilippo, 2008 DiFilippo et al., 2010	40 x 20 x 2.6	sand	reflection	n/r	n/r	TCE saturation	0 - 1	0 - 82%
Jaeger et al., 2009	78 x 15 x 1.1	glass beads	transmission	n/r	5mp	Acid Red 18 dye	0.5 - 100mg/L	<5%
Kechavarzi et al., 2008	180 x 120 x 8	sand	reflection	12	n/r	LNAPL saturation	0 - 1	8.7%
Glass et al., 2000	26 x 60 x 1	sand	transmission	12	0.25	TCE saturation	0 - 1	<12%
Darnault et al., 2002	62 x 52 x 1	sand	transmission	n/r	n/r	oil saturation water saturation	0 - 1	0.023 SD 0.037 SD
<b>Fluorescence</b>								
Bridge et al., 2006 Bridge et al., 2007	20 x 10 x 0.7	sand	reflection	8	0.5	fluorescein dye colloid	<1x10 <sup>-3</sup> M 2 - 200mg/L	26% 13%
Zhang and Wang, 2006	10 x 18 x 1	sand	reflection	14	4x10 <sup>-4</sup>	colloid concentration	2.5 x 10 <sup>5</sup> spheres/mL	<7%
Wang et al., 2008 Chen and Jawitz, 2009	30 x 20 x 1.7	sand	transmission	16	n/r	PCE saturation	0 - 1	<10% <11%
Catania et al., 2008	20 x 28 x 1	glass beads	transmission	10	n/r	fluorescein dye	1 - 64mg/L	R <sup>2</sup> = 0.87
Niemet and Selker, 2001	50 x 60 x 1.3	sand	transmission	14	1	water saturation	0 - 1	<2.3%
Weisbrod et al., 2003b	46 x 60 x 1	sand	transmission	14	1	colloids	>0.01% solids (>100ppm)	n/a
Kraft and Selker, 2005	47 x 55 x 1	sand	transmission	16	1	colloids	>0.6ppm	n/a

## Chapter Three: System Design, Construction, and Operation

### ***Objectives***

The light-transmission visualization system advanced in this work was originated by *Ho* [1981] and *Glass* [1989c; d] and developed by *Selker* [1992a; 1992b; 1992c]. The system was made quantitative for determination of water content by *Niemi* [2001]; *Weisbrod* [2003b] adapted the system for observation of colloid transport. While qualitative observation of colloid transport was demonstrated, quantification of colloid concentration over the spatial domain was not achieved. Additionally, these data were marked by optical noise which limited the detection of colloids to a concentration of  $10^2$  ppm (0.02% solids). No light-transmission system to date has been used to quantitatively observe colloids, water tracer, and water content in the same experiment. In light of this history, the objectives of the work presented in this thesis were four-fold.

- 1) Adapt the system for detection of multiple light spectra. The capability to image water content, water tracer, and colloid concentration over time and space allows for study of a broad range of colloid and solute transport phenomena. Colloid behavior can thus be observed separately from fluid flow. Few systems have matched visualization of fluorescent colloids with that of a conservative fluorescent solute [eg. *Bridge et al.*, 2006; 2007].
- 2) Expand the range of detection of solute and colloid concentrations. Extending the range of detection is important for studying contaminant transport, for example, as the ability to observe “trace” concentrations in the parts per million (ppm) to parts per billion (ppb) range is critical for the evaluation of processes that can limit successful clean-up of contaminated sites. However, detection of a tracer at low concentration is fundamentally limited by noise in the system. Enhancement of the signal-to-noise ratio allowed lower detection limits.

3) Develop the ability to use the system to quantify solute and colloid concentrations over the 54 x 43cm spatial domain. Maps of concentration allow for comparison of experimental results to model predictions. Image processing, system calibration, and application of calibration functions to image data allow for concentration quantification over the spatial domain.

4) Use the system to observe and quantify solute and colloid transport dynamics. Images collected of one and two dimensional transport, under one and two dimensional flow, in saturated conditions were analyzed for their transport characteristics. Addition of flow-through monitoring instruments in the chamber effluent line contributed to the system's ability to quantify transport phenomena.

### ***Light-Transmission Fundamentals***

Optical principles used to design this system are based on Beer's Law:

$$\log(I/I_0) = -\epsilon Cl, \tag{1}$$

where  $I$  (-) is the final intensity,  $I_0$  (-) is the incident intensity,  $\epsilon$  is the absorption coefficient ( $\text{ppm}^{-1} \text{cm}^{-1}$ ),  $C$  is the concentration of the absorbing substance (ppm), and  $l$  is the path length (cm) [DeRose and Kramer, 2005]. In light-transmission, light passes from one side of a plane of translucent medium to the other. When fluorescent dye is present in the medium, the light may excite the fluorescent dye molecules. Fluorescence emission then results. The intensity of that emission is collected by the detector on the opposite side of the medium from the light source.

In light-transmission systems for imaging fluorescent dye in porous media, diagrammed in Figure 3.1, molecules near the light source (a) are more highly excited than those far away (b), and emit more light, but the light they emit is attenuated more than the weakly excited molecules far from the light source. Therefore, the decrease of excitation intensity is balanced by the decrease of emission intensity for all particles equally the same. Both the excitation and emission are attenuated by solids and fluids in the porous medium equally for all dye molecules, regardless of their position.

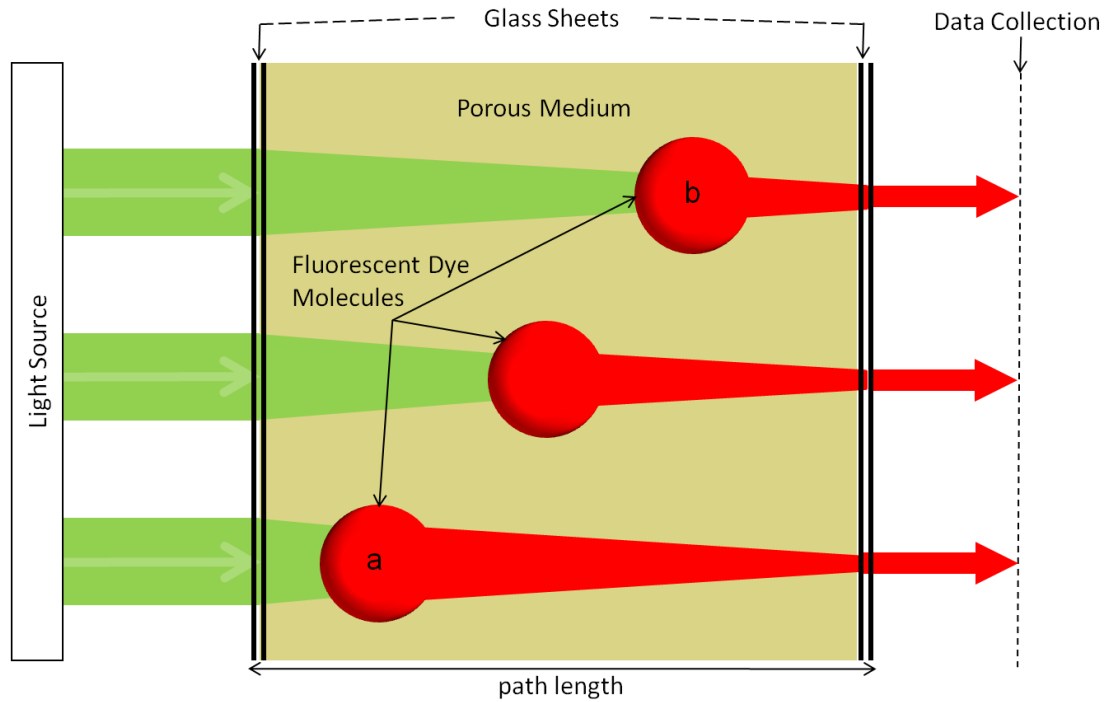


Figure 3.1 Light-transmission imaging system attenuation diagram. Three hypothetical fluorescent dye molecules are shown emplaced in a porous medium held between two glass sheets. Excitation light from the light source is shown on the left side of the fluorescent dye molecules. Emission light is shown on the right side of the fluorescent dye molecules. Detection and collection of emitted light (data) occurs at the plane represented by the vertical broken line. The detected intensity of molecules (a) and (b) are the same despite their position in the sand pack.

This arrangement is in contrast to reflexive-type systems where light source and data collection are on the same side of the medium [eg. *Bridge et al.*, 2006; *Zhang and Wang*, 2006]. In these systems (Figure 3.2), dye molecules near the illuminated surface (b) are excited more intensely and their emission is attenuated less than molecules far from the illuminated surface (a). Consequently, data collection in a reflexive system is biased with respect to sand pack depth.

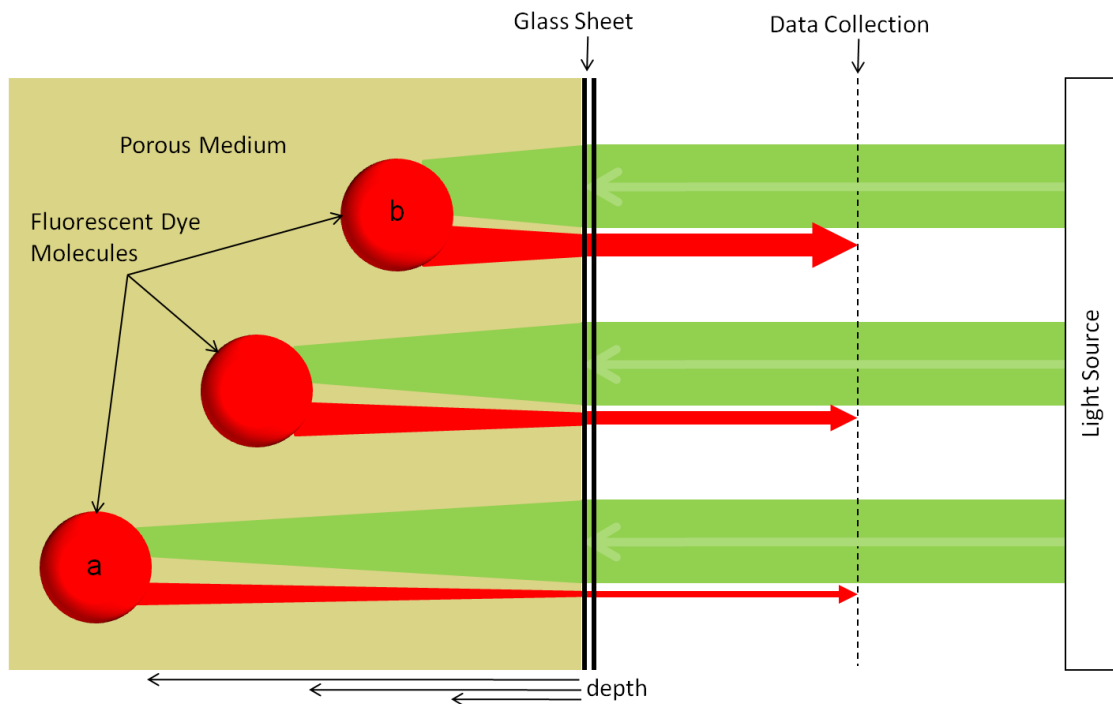


Figure 3.2 Reflexive imaging system attenuation diagram. Excitation light is shown as left-pointing arrows originating at the light source. Emitted light is shown as right-pointing arrows terminating at the plane of light detection and data collection. The detected intensity (thinner arrow) of a dye molecule deeper in the pack (a) is less bright than the detected intensity (thicker arrow) of a dye molecule closer to the active surface (b).

This principle can be demonstrated mathematically by comparing a plot of intensity vs. depth of a hypothetical molecule in the two system types. In transmission, the path length is fixed for all molecules regardless of position. In reflection, the path length is twice the depth of the molecule in the medium. The percent intensity as a function of depth in a 10mm-deep sand pack is shown in Figure 3.3. Calculations use a given initial intensity  $I_0 = 10,000(-)$ , absorption coefficient  $\epsilon = 100 (\text{ppm}^{-1} \text{cm}^{-1})$ , molar concentration  $C = 1 (\text{ppm})$ , path length  $l = 1(\text{cm})$ , and the depth  $d = 0.01-1 (\text{cm})$ . The intensity of observed light is calculated for transmission and reflexive systems by Equations 2 and 3 respectively.

$$I = I_0 10^{(-\epsilon Cl)} \quad (2)$$

$$I = I_0 10^{(-\epsilon C_2 d)} \quad (3)$$

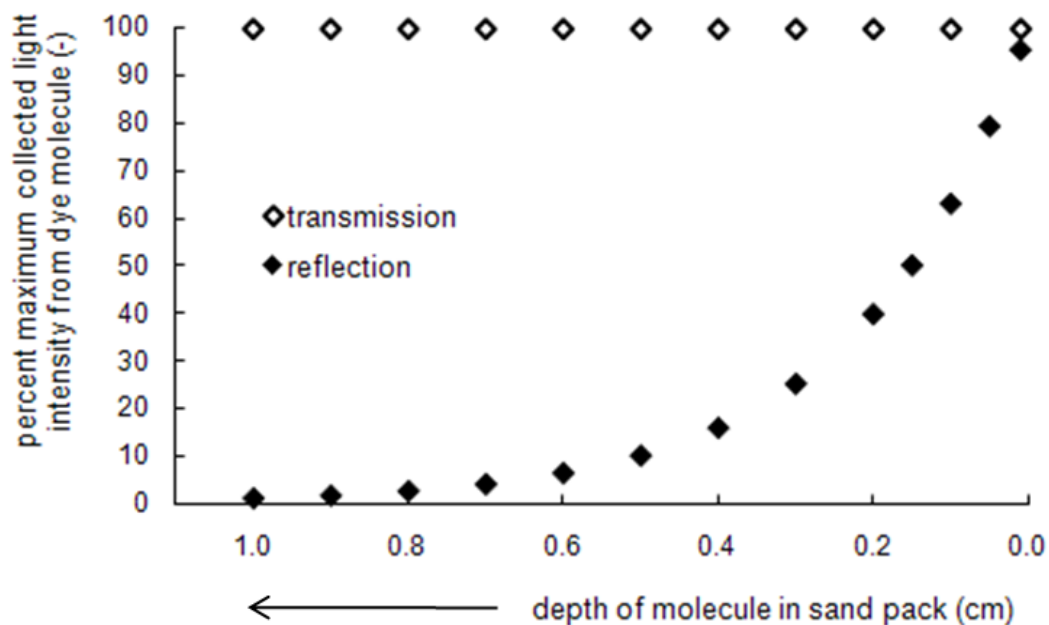


Figure 3.3 Intensity of emitted fluorescence reaching imaging detector in two system configurations. Light intensity collected from molecules as a function of depth is calculated for the two configurations according to Beer's Law. Calculated light intensity using light-transmission (open diamonds) is constant with depth. Calculated light intensity using light reflection (closed diamonds) declines logarithmically with depth.

### ***Light-Transmission System Components***

Optical components of a fluorescence light-transmission imaging system include a translucent porous medium, pore fluid, a light source, one or more fluorescent tracers (fluorescent dye molecules may be in solution or contained within colloidal particles that are suspended in the pore fluid), a detector, an enclosure curtain to isolate the system from ambient light, and a set of optical filters for control of excitation and emission light frequencies. Each component in the system carries with it a potential source of optical noise or experimental error. These include media autofluorescence, fluid leakage, chemical fluctuations affecting fluorescence intensity, variations in input intensity, degradation of the dye molecule, thermal noise, background light leakage, and spectral overlap.

The porous medium itself may demonstrate fluorescent properties (autofluorescence). Determination of signal contribution by the porous medium was accomplished by analysis of data collected without added fluorescent solutes or colloids. These data were also compared with those collected of illuminated craft paper, which is known to have an autofluorescence that far exceeds that of the porous medium used in these experiments [Billa, 1999]. The minimal autofluorescence of the porous medium was accounted for during data processing.

Creating a water-tight seal around the porous medium is required for water saturated experiments. Improper seal of the chamber can lead to flooding, as can improper regulation of flow rates. Control of the water table level inside the enclosed system requires exact matching of fluid inflow and outflow rates. A system was devised to check the chamber seal before packing, and flow rates were logged by change in mass of fluid contained on a balance.

The chemistry of the fluid affects the fluorescence of the dye. The intensity of dye fluorescence varies based partly on the pH of the solution [Diehl and Horchak-Morris, 1987; Smith and Pretorius, 2002]. The fluorescein molecule changes conformation with pH, and each form of the molecule has different fluorescent properties [Diehl and Markuszewski, 1989; Klonis and Sawyer, 1996]. Maintaining constant pH through use of a buffer solution eliminates this possible source of interference. Stability of solution pH was verified through use of an in-line pH meter.

Variations in input light intensity may be caused by fluctuations in the power supply. This variation was quantified by logging amperage and voltage generated by the power supply over time, and shown to be negligible.

Degradation of dye molecules may be caused by exposure to excitation light in a process called photodegradation [Song *et al.*, 1995]. Dye photodegradation was quantified in controlled experiments in a spectrofluorometer and in the light-transmission system. Reduction in emission intensity was

observed over time and was modeled as first order decay. Correction for this loss of intensity was not incorporated into data processing, and may account for error in concentration prediction.

Thermal noise is the generation of extraneous electrons on the imaging hardware as a function of chip temperature. Electron accumulation increases with increased temperature. The CCD chip is liquid-cooled to reduce thermal noise, but some noise will still be present in collected images. This noise was removed in image processing.

Background leakage of ambient light can limit the ability to detect low levels of fluorescence in an imaging system. An enclosure curtain was installed to prohibit ambient light from entering the imaging volume. Leakage into the enclosure was detected as intensity in images collected without system illumination, and may be quantified in pixel intensity above that detected in a fully blackened laboratory. This leakage noise was also removed during image processing.

### ***Selection of Optical Components***

The components through which light must pass in the light-transmission system are the light sources themselves, the air of the laboratory, the glass sheets that form the walls of the chamber, the porous medium, the fluid in the pores, and the lenses/filters on the camera. The fluid in the pore space may be liquid and/or gas, and may contain solutes and/or colloids.

The glass sheets are tempered borosilicate safety glass (ANSI Z97.1-1984). The index of refraction of this type of glass ranges from 1.51-1.55 across the visible range [eg. *El-Alaily and Mohamed*, 2003; *Tanio and Irie*, 1994]. The porous medium is crystalline quartz sand, which has an index of refraction near 1.55 [*Haynes*, 2011] and decreases as wavelength increases through the visible range [*Hecht*, 2002 pp 72, 343; *Zhang and Wang*, 2006]. The pore fluid in this system is reverse osmosis (RO) water, with or without phosphate buffer. Pure water has an index of refraction of 1.33 at 589nm [*Haynes*, 2011]. Potassium hydrogen phosphate and potassium dihydrogen phosphate were mixed to form the

buffer at a concentration of 0.5M. These two constituents in solution have an index of refraction ranging from 1.33 to 1.35 [Haynes, 2011], making their addition to the pore fluid inconsequential with respect to optics.

In order to design a system based on the detection of multiple optical signals at distinct light wavelengths the spectral absorption and emission properties of each component at each wavelength must be known. These properties may be used to limit spectral overlap and thus reduce noise in each signal. There are three signals to be detected with this system: water content, fluorescein concentration, and colloid concentration. The optical components associated with the detection of each of these will be presented with a justification for their use based on compatibility with the other optical components. Absorption and emission spectra are characterized by the wavelength at which light transmission is at half its maximum value—a unit termed the full width at half maximum (FWHM) [Geller, 2003].

The water content of the sand is determined by the degree of light attenuation without the use of any fluorophores. Because the index of refraction for a substance decreases as the wavelength of penetrating light increases, a long wavelength signal will most efficiently penetrate the sand. A long wavelength, 630nm, light-emitting diode (LED) was therefore used for detection of water content. This LED emits light at a peak of 635nm with typical dominant light at 628nm and a FWHM of 23nm. The range of this spectrum used in the system was limited by use of a long-pass filter, where only wavelengths greater than 630nm were allowed to pass. As a result, there was no effect of this light source on fluorescence processes or data collection at wavelengths smaller than 630nm. These sources are referred to as “630nm.” Light intensities transmitted from this source for the detection of water content were collected with no filter on the camera. The spectral curve and demarcations associated with detection of water content are shown in Figure 3.4.

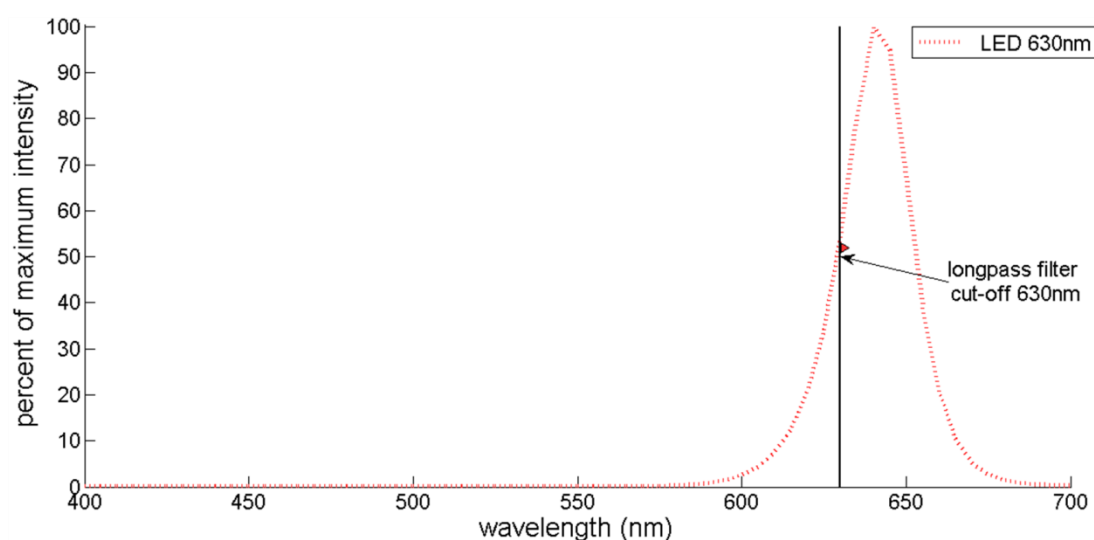


Figure 3.4 Optical properties of components used to determine water content. The dotted curve is the spectrum of light emitted by the 630nm LED. The spectrum is shown in terms of percent light intensity as a function of wavelength. The vertical black line represents the wavelength cut-off imposed on the 630nm LEDs by the long-pass filters. The right-pointing triangle indicates that wavelengths longer than 630nm are allowed to pass through the filter and penetrate the porous medium.

Fluorescent dyes were used in this system for the detection of two distinct signals—solute concentration and colloid concentration. The solute was dissolved directly into solution. The colloids had fluorescent dye incorporated into them during manufacturing. Collecting data on both of these signals over the same time allows comparison of colloid transport to fluid flow. Optical components were selected to control the natural spectra of the selected solute and colloids, allowing for refined detection of the two signals without optical interference or overlap.

Red FluoSpheres® polystyrene microspheres (Molecular Probes #F-13083), with a 1 $\mu$ m diameter were chosen as model colloids for this system. The composition of the red dye injected into these colloids is not disclosed by the manufacturer. The Stokes' shift (the difference between maximum excitation wavelength and the maximum emission wavelength) for the dye in these red fluorescent colloids is larger than any of the other dye colors used in colloids by the manufacturer. This larger wavelength gap between peaks increases the opportunity to choose optical filters to both effectively excite the dye, and to collect a strong fluorescence emission signal, without overlap. The Stokes' shift for the red colloids is shown as the horizontal distance between the excitation (closed stars) and emission (open

stars) peaks in Figure 3.5. Also shown in Figure 3.5 are two fine dotted lines; these are the excitation and emission wavelengths at which spectrofluorometer was set to collect in-line data on fluorescent intensity of colloids in experimental effluent.

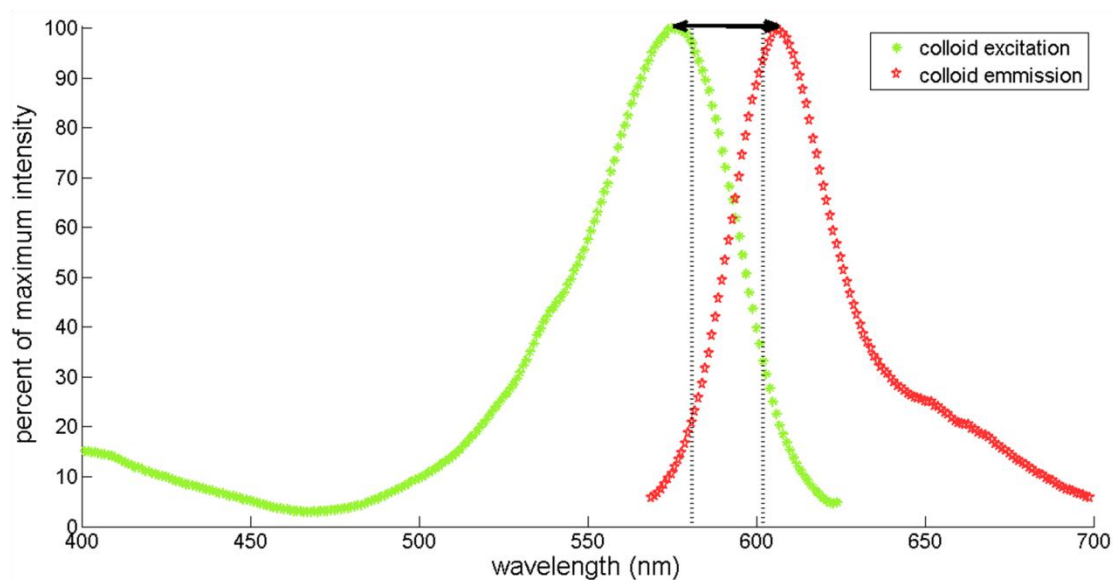


Figure 3.5 Excitation (closed stars) and emission (open stars) curves for red fluorescent colloids from manufacturer's data plotted as percent maximum intensity. The heavy arrow between plots designates the width of the Stoke's shift between maximum excitation and emission.

The manufacturer provided the data in Figure 3.5. In order to increase certainty of spectral characteristics, a spectrofluorometer was used to generate the spectral response of the colloids across the visible range. In this scan, a cuvette filled with colloid solution was excited from 300nm to 700nm at 10nm intervals. At each excitation, emission intensity values were recorded for all wavelengths between 500 and 700nm. A section was taken through the three-dimensional (excitation wavelength, emission wavelength, emission intensity) data where excitation was 580nm (Figure 3.6). The presence of the primary peak at the excitation wavelength indicates that the spectrofluorometer detects both the colloid emission signal and the colloid excitation signal as it is reflected off of the colloids. Figure 3.6 also shows the maximum emission from these colloids occurring at 601nm (at 14% the signal strength of the reflected signal). This is the wavelength around which the emission filter was centered to collect the maximum strength signal from the colloids.

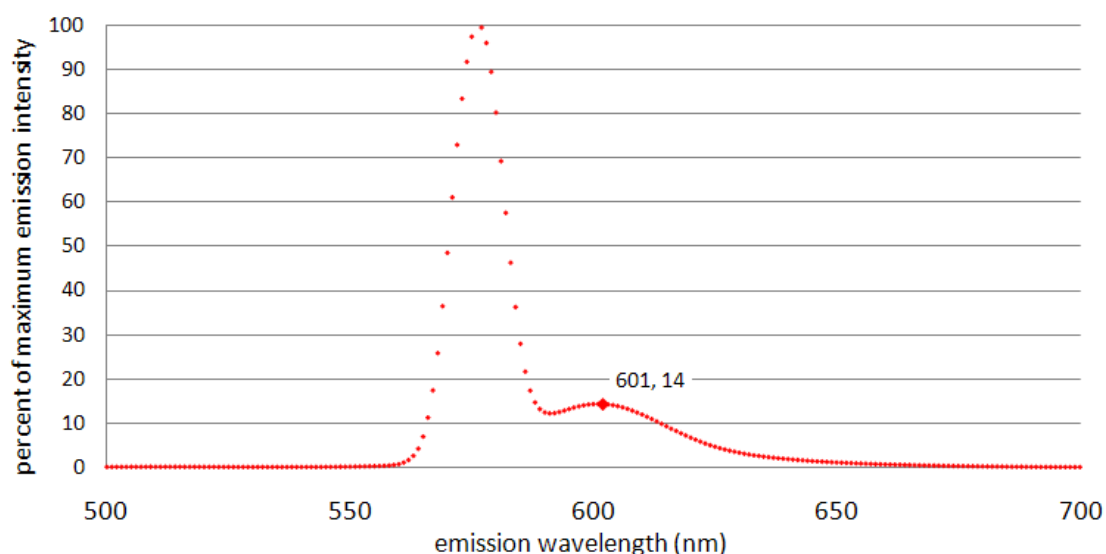


Figure 3.6 Spectrofluorometer scan of  $10^0$  ppm red fluorescent colloids in RO water excited at 580nm. The primary peak is the excitation spectrum reflecting off the colloidal particles. The secondary peak, with maximum at 601nm, is the emission spectrum of the red fluorescent dye.

A fluorescent dye was chosen as the water tracing solute that would be separate enough in spectral characteristics from the red colloids in order to have no signals overlap. Various fluorescent dyes were considered including several types of rhodamine and fluorescein. Published studies indicate that disodium fluorescein dye (fluorescein) would be least likely to bind to the sand, the tubing, or the glass walls [eg. *Smith and Pretorius, 2002*]. Scientific grade disodium fluorescein (Thermo Fisher Scientific Inc., Waltham, MA) was chosen based on this record of conservative behavior, and based on its excitation/emission characteristics which compliment well that of the red fluorescent colloids [eg. *Flury and Wai, 2003*]. Fluorescein excitation/emission characteristics include peak excitation/emission at 488/512nm. The peak excitation/emission of the red fluorescent colloids is 570/598nm. The 158nm gap between peak fluorescein emission at 412nm and peak colloid excitation at 570nm allows for the effective use of blocking filters between the two signals. Excitation and emission curves for fluorescein are shown plotted with those of the chosen colloids (Figure 3.7). Also on this plot are vertical lines indicating the wavelengths at which the fluorometer was set to excite and collect data on fluorescein and colloids in the effluent.

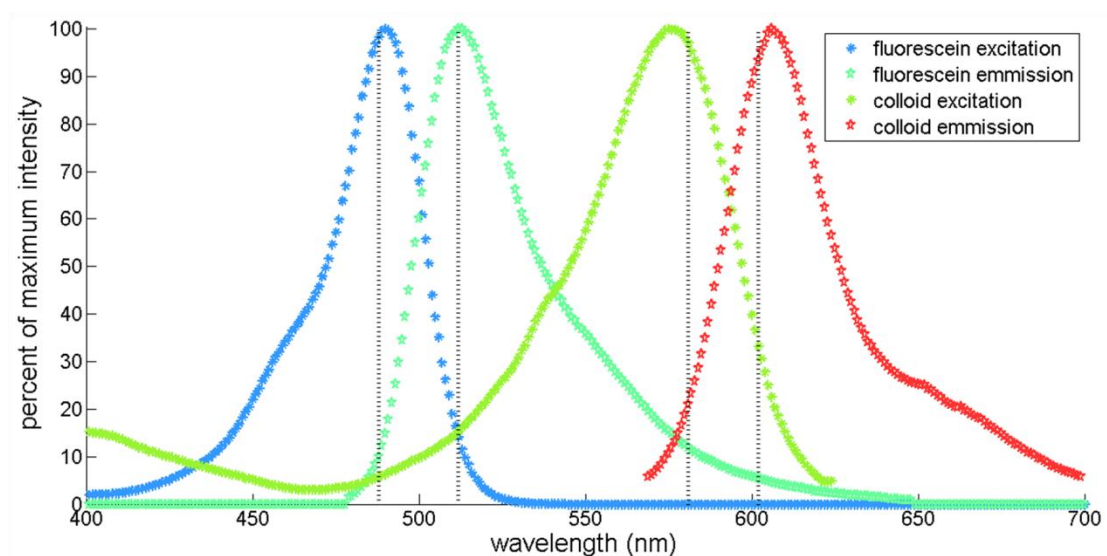


Figure 3.7 Excitation (closed stars) and emission (open stars) spectra for fluorescein dye (two on left) and colloids (two on right). The distance between all peaks was maximized in dye selection to allow for separation of fluorescein and colloid signals. Vertical black lines represent the excitation (488 and 581nm) and emission (512 and 602nm) settings of the spectrofluorometer used to further characterize the dye, and for in-line fluorescence breakthrough data collection.

Once the fluorescein and colloids were chosen, light sources were selected which had peak emission near the fluorescein and colloids excitation peaks. In selecting the light sources for excitation, the following desirable characteristics were considered: brightness, low heat load, temporal stability, tight bandpass, and availability of wavelengths needed. Light-emitting diodes are an increasingly useful semiconductor technology to generate bright light (up to 115 lumens/W), and can be selected to emit over a narrow bandwidth. LEDs better fit the needs than did other choices because their output intensity is greater, and their bandpass more narrow.

The light bank employed by *Weisbrod et al.* [2003b] was replaced by an array of 18 high flux density, solid-state 40-die monochromatic hex light sources (Norlux Corp., Carol Stream IL). Six sources at each of three frequencies were employed in order to spread the excitation light over the area of illumination. Blue LEDs (NHX470, Norlux Corp., Carol Stream IL) used to excite the fluorescein have a minimum radiant flux of 50mW, and peak intensity at 467nm with a 35nm full width at half maximum. Green LEDs (NHX530, Norlux Corp., Carol Stream IL) used to excite the colloids have a minimum

radiant flux of 33mW, and peak intensity at 520nm with a 35nm full width at half maximum. Red LEDs (NHX630, Norlux Corp., Carol Stream IL) used to detect water content have a minimum radiant flux of 280mW, and peak intensity at 635nm with a full width at half maximum of 23nm.

Each LED was fit with an optical reflector (NHXOPTIC040A, Norlux Corp.) to collimate the light, a short-pass or long-pass filter to constrain the wavelength of light illuminating the chamber (Intor Inc., Socorro NM), and a 60° holographic diffuser (NT55-444, Edmund Optics Inc., Barrington NJ) to spread the filtered light as uniformly as possible over the entire area of the sand pack. Cut-off filters were chosen to limit the bandwidth of light from the LEDs to that necessary to excite the dye, without interfering with emission. These 480nm short pass filters, 580nm short-pass filters, and 630nm long-pass filters measure 25mm across and are used on the blue, green and red LEDs respectively (480SWP, 580SWP, 630LWP, Intor Inc., Socorro NM). Designations throughout this thesis for LEDs and filters used will be “470nm” for fluorescein concentration, “530nm” for colloid concentration, and “630nm” for water content. The two excitation curves (closed stars) for fluorescein and colloids are shown in Figure 3.8 along with spectra of LED emission (dashed curves) and optical filter transmission (vertical lines) used to control the LED spectra.

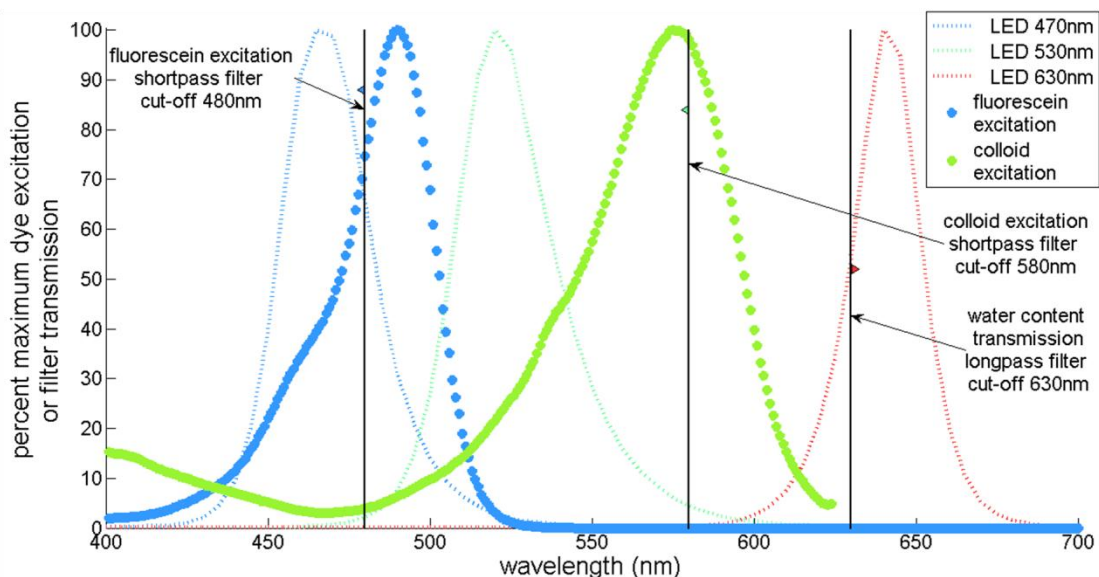


Figure 3.8 Excitation spectra for the light-transmission system (closed stars). Spectral curves for three sets of LEDs are shown in dashed lines. Black vertical lines show the cut-off wavelength for filters used on LEDs. The colored triangles on these lines point to the side of the line on which wavelengths are allowed to pass. Light is prevented from passing at wavelengths on the other side of the black line.

The excitation filters described above were used in conjunction with emission filters to effectively collect separate fluorescent signals for fluorescein and colloids. One high-grade 50mm bandpass filter was chosen to limit the band-width of light collected by the camera from fluorescein emission (Chroma Technology Corporation, Bellows Falls, VT, #D535/40m). And one high-grade 50mm bandpass filter was chosen to limit the band-width of light collected by the camera from colloid emission (Chroma Technology Corporation, Bellows Falls, VT, #D620/30m). These filters were placed in a five-slot filter wheel (CFW1-5, Finger Lakes Instrumentation, Lima, NY) and connected to the CCD camera by an AD1 adapter (FLI). Bandpass filters are described by their center wavelength (CWL) and their FWHM. The spectral data supplied by the manufacturer for these filters is shown in Figure 3.9.

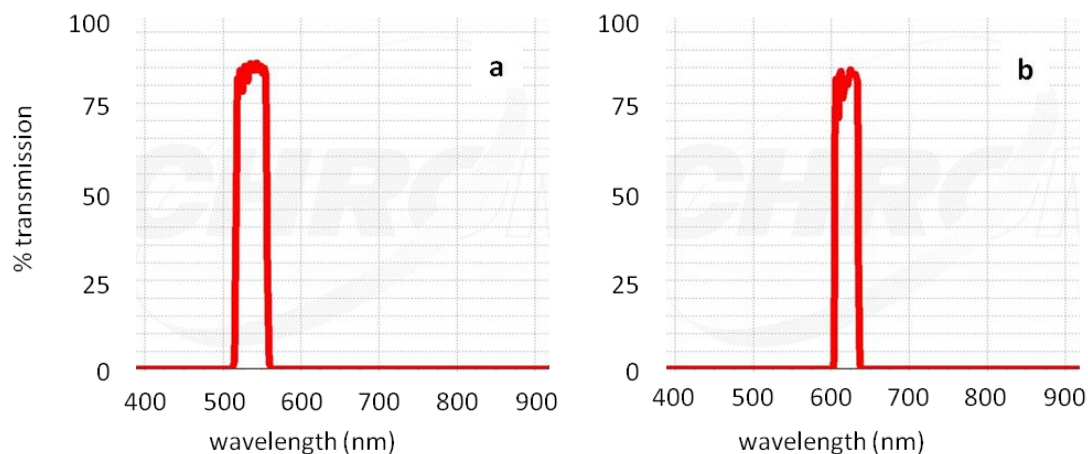


Figure 3.9 Spectral plots of bandpass emission filters #D535-40m (a) and #D620/30m (b) from Chroma Technology Corporation. These filters were used in front of the CCD camera for collection of fluorescein and colloid signals respectively.

Figure 3.9 shows sharp cut-off between maximum transmission of light and complete blocking (0% transmission) by the chosen emission filters. These bandpass filters are manufactured with thin film interference coatings which are put down in layers that are on the order of the thickness of one wavelength of light. These layers select by reflection against certain wavelengths of light with very high precision [Reichman, 2007]. Many bandpass filters are available to accommodate very specific optical needs. The best possible match was made between the arithmetic mean of the filter wavelengths at 50% peak transmission and the peak emission wavelength of the dye. The FWHM, the bandwidth at 50% of peak transmission, was minimized in filter selection in order to collect primarily only the light emitted as closely as possible to the peak wavelength. Figure 3.10 shows the spectra of the emission bandpass filters together with the fluorescein and colloid emission spectra they are employed to control.

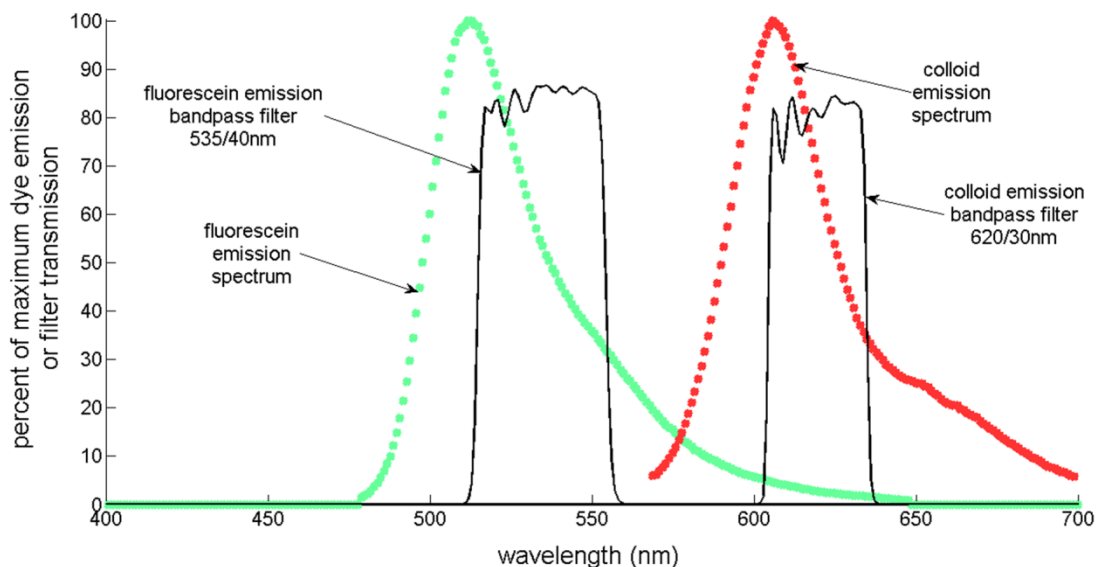


Figure 3.10 Emission spectra (closed stars) for fluorescein (left) and colloids (right). Solid lines show bandpass of emission filters used during collection of the fluorescein (left) and colloid (right) emission signals.

The effectiveness of the emission filters for blocking stray light was demonstrated by comparison of images of colloids taken with and without emission filters (Figure 3.11). These data, collected early in the process of system improvements, show improvement in signal strength vs. noise, as compared with the uncontrolled spectral data. The signal to noise ratio in each image may be compared as the ratio of the average off-peak intensity to the signal peak. This value is 2.8% for the unfiltered image and 15.8% for the image using optical filters—a five-fold improvement.

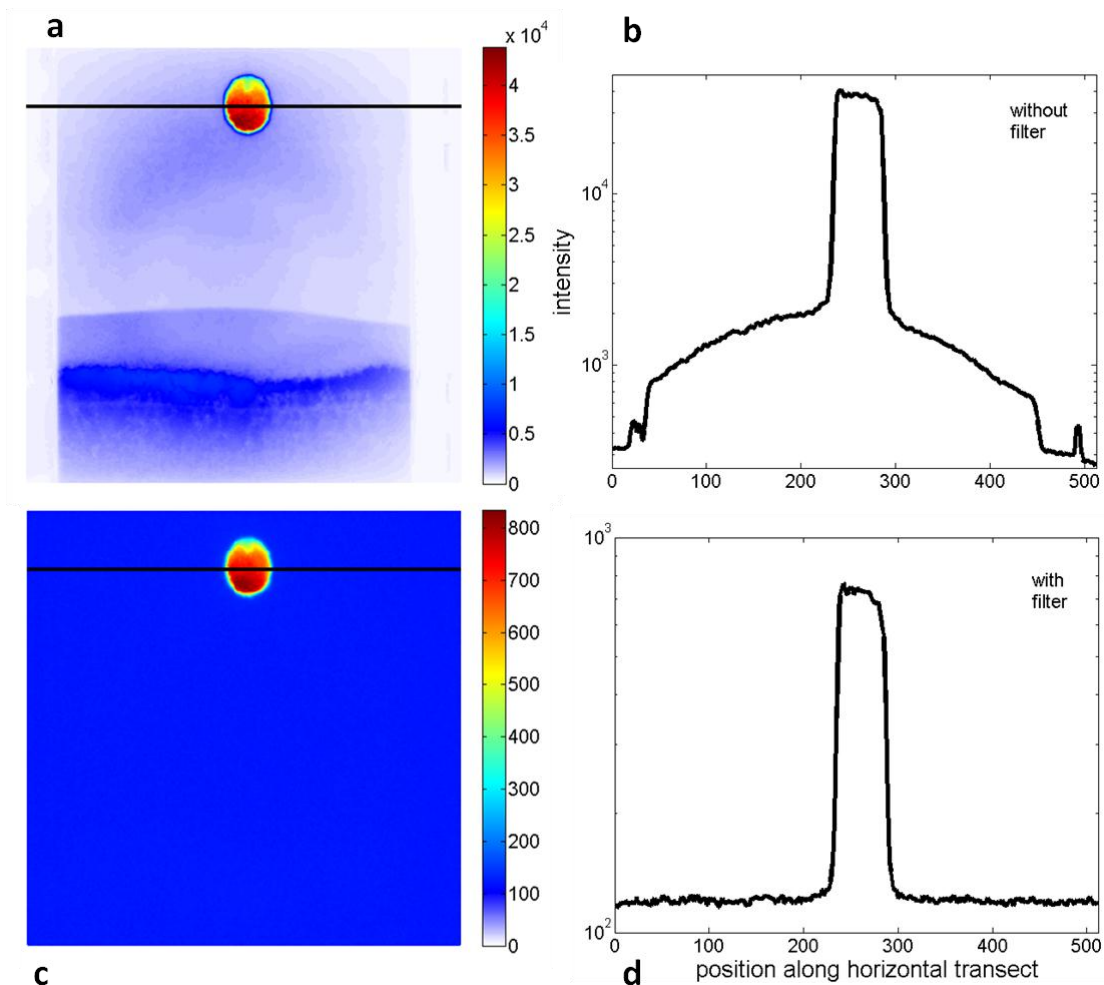


Figure 3.11 Reduction in noise in image of a 10mL, 2000ppm colloid plume by use of emission filter. Images were taken with 1s exposure time and were median-filtered to remove noise and colored for ease of viewing. A line has been superimposed on images to show transect location. (a) Image of plume without emission filter in place shows background noise and high intensities overall. (b) Transect of plume image without filter shows sloping transition between plume peak and zero values. (c) Image of plume with filter shows background reduced to a flat field and overall lower intensities. (d) Transect from plume image with filter shows improved sharpness of cut-off between plume and background values.

A complete evaluation of spectral data associated with each component was conducted. Plots showing all optical components associated with collection of the fluorescein signal, all optical components associated with collection of the colloid signal, and the full spectral match-up plot used to evaluate system components are included in Appendix A.

## ***System Construction***

To apply the optimization described above, LEDs were assembled with optical components into “collectives.” The eighteen optical collectives, six of each color light, consisted of an LED, an optical reflector (“optic”), an edge filter (short-pass or long-pass), and a 60° holographic diffuser (HOLO 60 DEG 8” SQ, Edmund Optics, Barrington, NJ). Optical collectives were installed in the system to improve the quality and distribution of light striking the sand surface. The 18 optical collectives were mounted to a 71 x 51cm x 3.05mm-thick anodized aluminum plate. This arrangement maximized uniformity of illumination over the chamber surface. A layer of thermal grease (ST-700, Roithner LaserTechnik, Vienna Austria) was used between the collectives and the plate, maximizing the heat sink properties of the metal, thereby cooling the LEDs during long periods of operation.

Power for the LEDs was provided by two programmable DC power supplies (3645A, Array Electronic Co., Ltd., Nanjing China) controlled through two USB Relay I/O Interfaces (ADU218, ADU200, Ontrak Control Systems, Sudbury Ontario Canada). Both these components have the capability for computer control and automation. Data from the power supplies can be logged over time, allowing system input monitoring. The green and blue sources were run at their maximum power settings of 19.5V and 400mA. The red sources used for straight transmission was run at a reduced power setting (10.5V from 13V and 310mA from 480mA). Red light most efficiently penetrates the media and no bandpass filter was employed for that signal oversaturation of the CCD chip would have resulted without this reduction of power.

Input to the light-transmission system is LED intensity, and output is grayscale intensity recorded by the CCD camera. A relationship exists between input from the power supply and LED intensity. To address this input, power supply data were logged for several experiments to evaluate the stability of the input to the system. Standard deviations of recorded volts, amps, and watts for both power

supplies, at all three settings, across multiple experiments showed a maximum of 3% deviation from the average.

To further address the stability of the power input, a series of experiments were conducted where power data was logged to the computer over the course of repetitive imaging of a static (no fluid flow) sand pack. Averages were taken of the image intensities and plotted alongside power data over time. This experiment revealed that while power input was stable, oscillations in image intensity occurred (although they were very small). Data collection of image intensity over longer time spans revealed a pattern that suggests building climate control as a component of imaging system variability. Hourly oscillations were observed (Figure 3.12), which correspond to the heating cycles in the building. The light emitting diodes are sensitive to temperature and thus changes in ambient conditions will result in concomitant change in LED intensity. Collected data showed that while the power feed to the light bank may be constant, collected image intensity varied with time. This oscillation is insignificant with respect to image quality, with its minimum value less than two percent different from its maximum value.

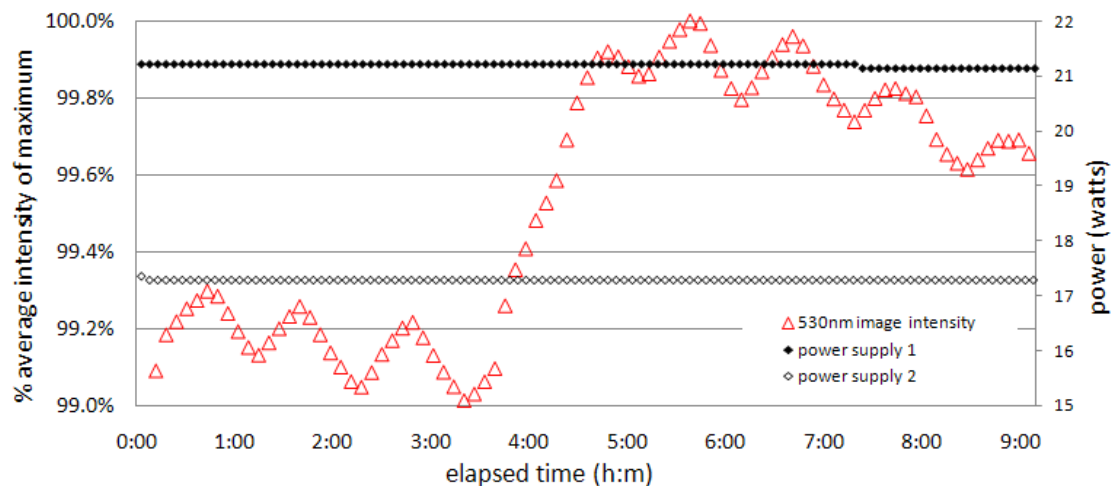


Figure 3.12 Percent average image intensity (-) variation from the maximum value (open triangles) of 530nm light travelling through a dry sand pack, with 76sec exposure, and no emission filter. Power (watts) data (diamonds) from the two power supplies running the 530nm LEDs at the time of image collection.

The anodized aluminum plate housing the optical “collectives” was mounted into the back opening of a four-sided sheet metal light box (71cm high by 51cm wide by 48cm deep). Weather-stripping at the seams allowed for a light-tight connection. The dimensions of the light box were chosen in association with the angle of the holographic diffusers to create a flat plane of light striking the chamber surface<sup>1</sup>. The light box was mounted to a wooden support frame by sturdy hasps with a weather-stripping interface to make a light-tight connection. The galvanized inside of the light box was left unpainted to allow for maximum retention of light intensity by light reflection off the inner walls. A schematic of the light box and the light array geometry are shown in Figure 3.13.

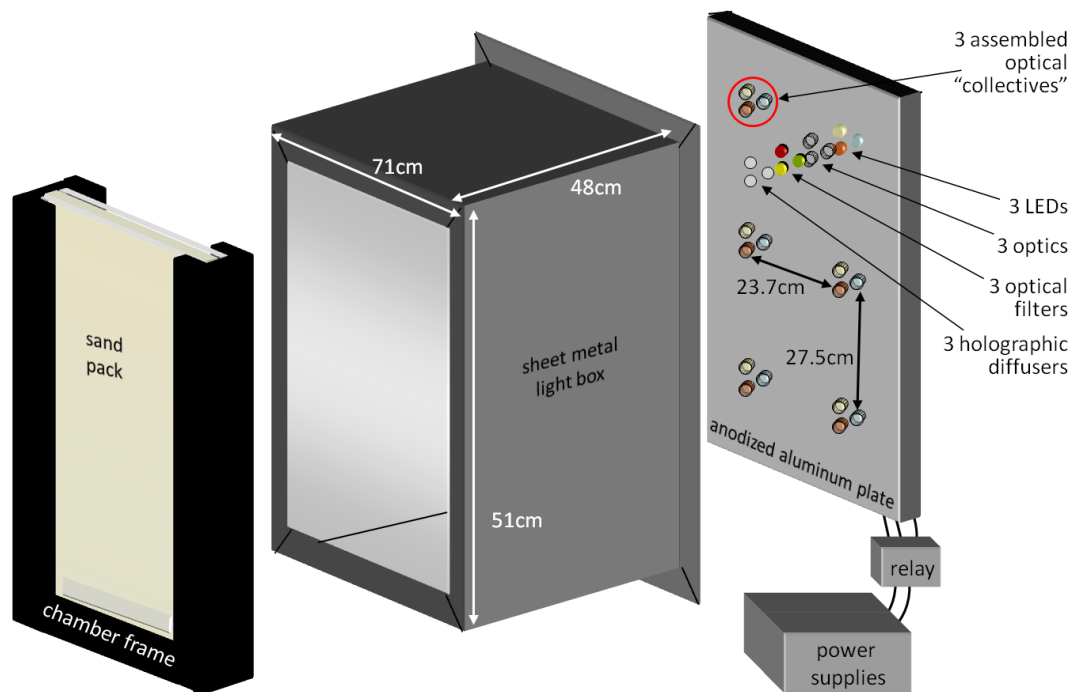


Figure 3.13 Schematic of light box and light array geometry. Exploded view of three optical “collectives” is shown in the upper right corner of the anodized aluminum plate; each collective includes an LED, an optic, an optical filter, and a holographic diffuser.

<sup>1</sup> The equations  $d = w/\tan\theta$  and  $d = h/\tan\theta$  were used to calculate light box dimensions where  $d$  (cm) is the distance between the plate and the sand pack,  $w$  and  $h$  are respectively the horizontal (23.67cm) and vertical (27.5cm) distance between the sources, and the angle  $\theta$  is  $30^\circ$ --half the value defined by the holographic diffuser. Calculations were made to optimize  $d$  for both equations and the result was  $d = 47.63$ cm. The box was therefore built to the depth 48cm.

The light-transmission system, while relatively inexpensive to operate and based on simple optical principles, does involve a number of structural components that require careful assembly for proper function. Two panes of glass are separated by a U-shaped spacer. The glass sheets are sealed to the U-shaped spacer using force against a continuous strip of o-ring stock. To prevent attrition of sand, the thickness of the o-ring stock and the pressure used to compress the o-ring against the u-shaped spacer must create a seal between the glass and the spacer.

The sand is placed between these glass sheets and supported at the bottom by a manifold. The manifold is covered with screening to support the sand while allowing unimpeded and even flow of water in and out of the system. To prevent sand attrition, this manifold must fill the gap between the glass sheets with less extra space than the diameter of the smallest sand grain, yet thin enough not to interfere with the seal made by the o-ring stock between the spacer and the glass.

The manifold originally used with this system was acrylic, with holes drilled for fluid to pass through, and wire mesh glued to its upper surface. Numerous experiments were marked by sand attrition. Areas having lost sand mass have higher intensities than the rest of the pack. Many experiments were rendered useless due to electronic oversaturation of the CCD chip caused by transmission of unattenuated light through areas affected by sand attrition (Figure 3.14a) Also, the area above the surface of the sand pack must be masked to prevent unattenuated light from reaching the CCD. An opaque card was placed in front of the glass, down to the level of the sand surface. The card was kept in place using electrical tape. Several experiments were marked by changes in the margin of this masking as the card and tape moved during an experiment (Figure 3.14b).

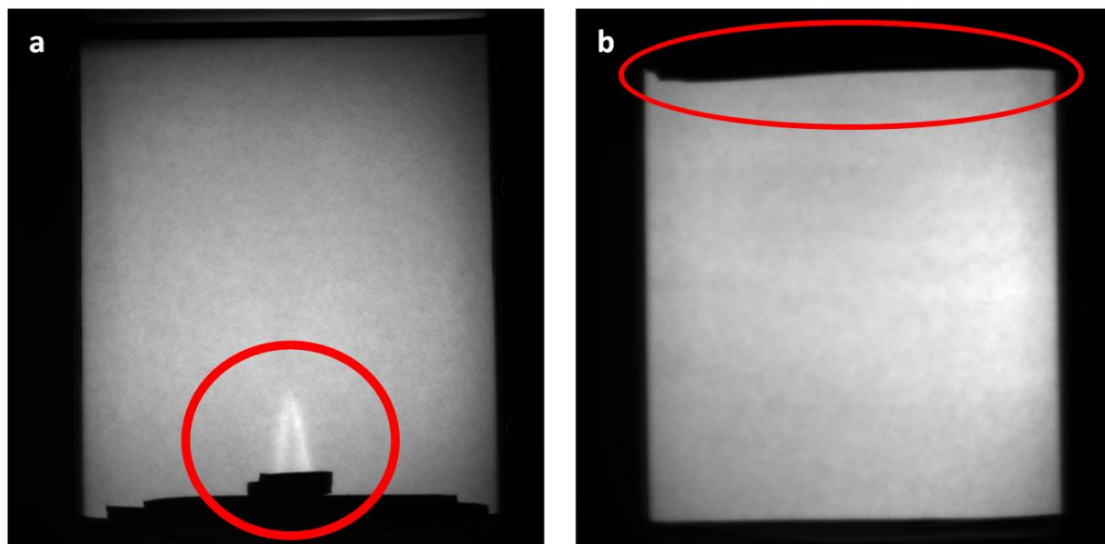


Figure 3.14 Light-transmission system images showing attrition from the sand pack as a result of poor function of the lower manifold (a) and an uneven margin as a result of poor upper mask (b). Image (a) was taken of  $10^1$  ppm fluorescein with a 0.5 second exposure time. Image (b) was taken of  $10^{-3}$  ppm fluorescein with a 191 second exposure time.

To prevent attrition and changing margins of the mask, a new manifold and mask were designed, constructed and installed. These parts were machined from aluminum, and anodized to minimize reflectance from their surfaces. Their opaque anodized quality and their contact with the sand pack prevented light from reaching the CCD camera unattenuated. These parts were designed to provide a permanent and unchangeable geometry of the lighted area, and to limit colloid sorption that may have occurred on the acrylic surfaces of the old manifold.

The new manifold corrected the problem of sand attrition and prevented light passage through the area below the sand pack. A groove was milled down the depth of the manifold and across its entire length for even application of fluid to the sand surface. A wire mesh of 178 micron stainless steel mesh (#MIC178T1, TWP, Berkeley CA) was fitted to the manifold over three sides, and fixed in place by two countersunk stainless steel flathead screws. The thickness of the mesh on both sides of the manifold filled the space between the aluminum and the glass to prevent passage of sand particles.

The new upper mask stopped electronic oversaturation of the chip by leaking light, and created consistent pack geometry between experiments. The upper mask was designed to slide inside the pack volume and press down on the surface of the sand. Grooves were milled into the U-shaped spacer so that the mask would overlap the spacer on both sides. Sand was packed into the chamber to a specific height so that installation of the mask results in a 2mm depression of the mask into the sand surface.

Behind the mask, Viton tubing terminated 1cm above the sand surface for application or withdrawal of fluids from the water layer above the sand surface. A dark enclosure made of 4 mil black polyethylene sheeting and lined with black velvet was sewn into a bellows and connected to the wall on one end with lathe strips and to the chamber on the other end. The front of the chamber was outfitted with a wood face that mounts to all-thread bolts extending out of the chamber frame. Wing nuts press the wood face to the chamber face compressing the black foam rubber cushion connected to the back of the wood face. This coupling allows the dark curtain to be sealed tightly to the chamber by squeezing steel press bars against the foam using a ratchet strap. The dark enclosure allowed for extended exposure time, up to five hours, before background light electronically oversaturated the chip in the CCD camera. A diagram of the full system assembly is shown in Figure 3.15.

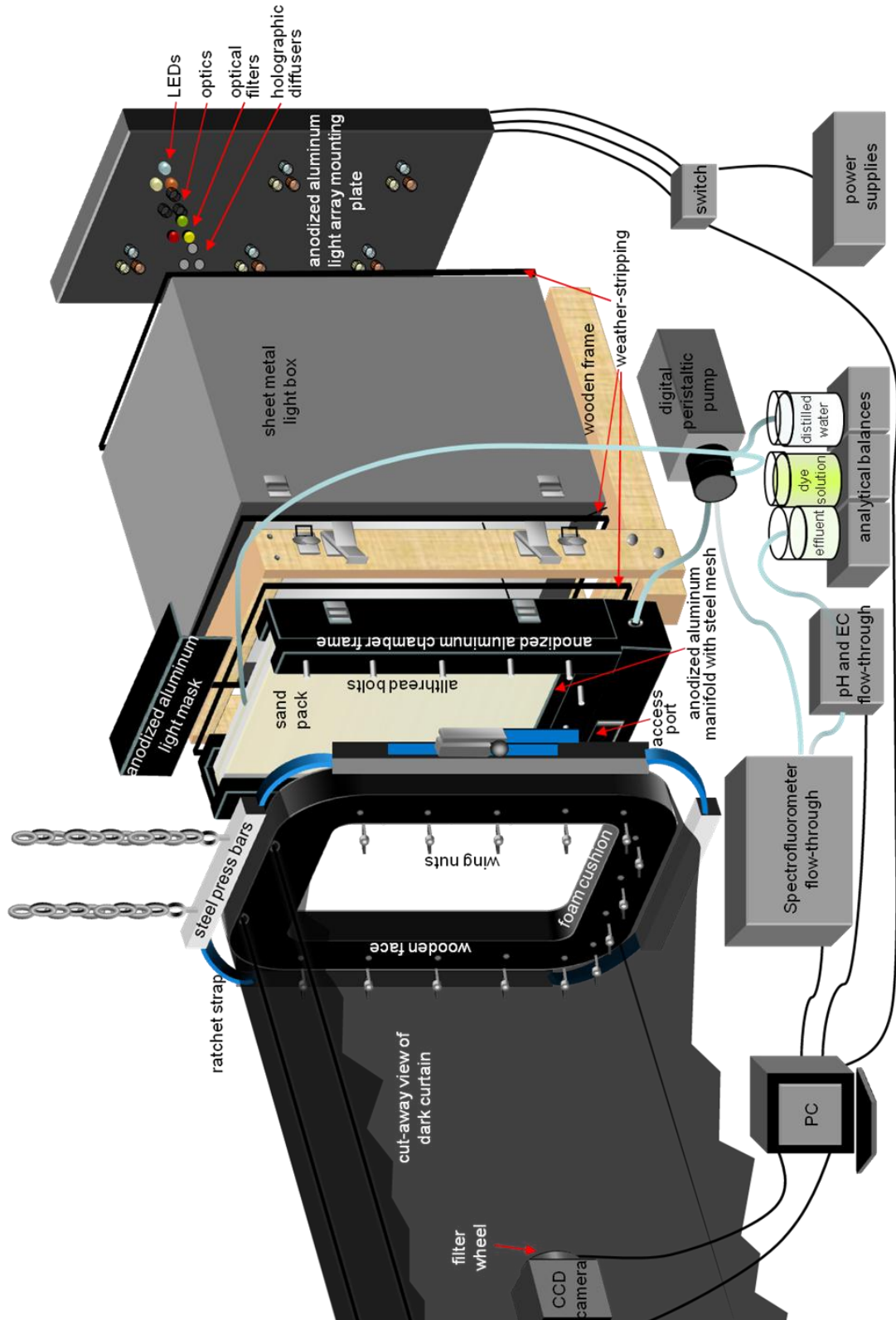


Figure 3.15 Full light-transmission system configuration.

## ***System Operation***

An experimental protocol was devised to ensure proper order of operations in setup and operation of the light-transmission visualization system. The protocol is presented here as it may be valuable to future researchers using this system, especially as more advanced and intricate instrumentation add levels of complexity to future versions of this system. The full experimental protocol is included in Appendix B, and will be described briefly here. The protocol for imaging and image processing are included in Appendices D and E respectively and will be described in more detail in the data collection and image processing sections of this chapter.

Before assembly, the glass sheets were cleaned with ammonia-based cleaner and wiped down with acetone using clean paper towels, or washed in a solution of 0.01M sulfuric acid ( $\text{H}_2\text{SO}_4$ ) followed by a RO water rinse, to prevent interaction with colloidal particles or generation of soap-based fluorescence. The glass sheets were installed in the chamber frame and ratcheted tight on all-thread bolts with double nuts to a prescribed separation distance. This separation distance was determined through a process of trial and error. Excessive tightening led to torque on the pressbars and subsequent non-uniformity of the o-ring seal. A caliper-measured distance of 1cm +/- 0.1cm, stopped short of causing torque, but supplied adequate pressure to seal the packing volume.

The chamber was then mounted to the wooden frame. Translucent silica Accusand<sup>®</sup> (Unimin Corporation, Lesueur MN) was packed into the assembled chamber using a prismatic hopper to generate random grain trajectories for even packing. Initial packing was extended above the fill line at the top of the experimental volume. The chamber frame was then tamped on the all-thread bolts with a small hammer to facilitate settling of the sand. The overburden was vacuumed off. This mass of overburden was weighed and subtracted from the total mass of sand used for packing to yield the pack mass. The porosity (generally ~0.32) was determined as the pack mass times the sand density ( $2.664 \text{ Mg/m}^3$  [Schroth *et al.*, 1996]) divided by the pack volume ( $62 \times 46 \times 1 \text{ cm}$ ).

Once the chamber was packed and mounted, the sand pack was purged of ambient air using compressed CO<sub>2</sub> gas supplied from the bottom, making the sand pack less likely to retain air bubbles when water-saturated (the higher solubility in water of CO<sub>2</sub> compared to air results in rapid dissolution and removal of any trapped CO<sub>2</sub> from the sand pack). Tubing was then connected to the system to deliver fluid to the sand pack. Inline monitoring instruments were also plumbed-in to the tubing system. Lengths of steel tubing were inserted into the sand pack from the top to allow for plume application. The wooden face with foam cushion was mounted to the ends of the all-thread bolts using wing nuts. The foam cushion was pressed tight to the chamber frame to create a light-tight seal. The dark enclosure was put in place by pressing the curtain to the foam cushion using steel press bars and a ratchet strap. Images of the dark and illuminated dry condition were collected.

The sand pack was saturated with clean fluid (RO water or buffer). A 4L flask filled with clean fluid was placed on an analytical balance (model 500L, Setra, Plainville CT). Initial mass, pH, and EC values were collected. Fluid was pumped into the chamber using a calibrated digital peristaltic pump (LS 7523-40 Masterflex/Cole-Parmer, Vernon Hills IL) with a dual-channel pump head (Easy-Load II Masterflex/Cole-Parmer HV-77200-60, Vernon Hills IL) via an access port at the base of the aluminum spacer at a flow rate between 10 and 184mL/min. Effluent mass was monitored on a second precision balance. The total fluid volume in the system was determined by logging mass change of the source flask. Multiple pore volumes of clean fluid were circulated through the sand pack, with the final pore volume left static in the pack. Effluent was tested for pH and electrical conductivity at pore volume intervals and typically showed initial increases in both pH and electrical conductivity that subsequently returned to near initial values. Images were collected of the saturated condition. Fluorescein and/or colloid solutions were then introduced into the system, and experimental images were collected.

Two methods were used to apply fluorescein and colloids to the system. In the uniform-concentration method, fluorescein and colloids were introduced to the sand pack via the same tubing used for bulk

fluid flow. This method allowed for complete saturation of the sand pack with known concentration of fluorescein and colloids. In the plume method, fluorescein and colloids were pushed into the sand pack through lengths of stainless steel HPLC tubing. The steel tubing was cut to a known length and fitted with leur lock end pieces cut from hypodermic syringe needles. Leur lock end pieces were fused to the tubing with StayBrite #8 silver solder and Stay Clean flux (Harris Products Group, Mason OH). Volume testing was conducted to determine the volume of each length of steel tubing to +/- 0.01mL accuracy. The steel tubing was bent to a geometry that closely fit the shape of the experimental chamber and inserted into packed chambers to a depth of 9cm below the sand surface. The position of the steel tubing was fixed to the outside of the light box using Velcro strips. During calibration experiments tubing lengths were filled with clean fluid either passively or by slow withdrawal using a syringe. Once the tubing volume was saturated, ends were capped and left static until plume application. Plumes were applied to the system using a 10mL glass syringe (Model #5127, Popper and Sons, New Hyde Park NY). This method allowed for the introduction of known fluorescein and colloid amounts into the sand pack, and made it possible to introduce and image the movement of plumes placed in multiple locations within the sand pack simultaneously.

The fluorescence efficiency of fluorescein in solution is affected by the pH of the solution [Diehl and Markuszewski, 1989]. Colloidal particles are affected by the pH of fluid in which they are suspended-- for the colloids used in this study, a pH above 5 is required to prevent agglomeration by attractive forces [Invitrogen, 2010]. Near neutral pH is achieved with RO water; however, pH measurements are highly unstable in pure water. It was necessary therefore to buffer the experimental fluid to allow for pH monitoring. Buffer used needed to have a limited effect on the colloids and provide little to no substrate for microbial growth. Concentration of buffer was kept as low as possible to minimize these effects, while still creating acceptable buffering capacity. 5mM sodium phosphate buffer at pH 7.1 was used (0.0254% monosodium phosphate, monohydrate; 0.0847% disodium phosphate, heptahydrate).

Solutions of fluorescein and colloids were prepared by serial dilution into either RO water or into buffer. Buffer was mixed using RO water, which contains less than 1.7ppm of any of the tested trace elements<sup>2</sup>. Disodium fluorescein powder was weighed on an analytical balance to prepare concentrated fluorescein stock solutions ( $\pm 10^{-4}$  g). Manufacturer's stock solution for colloids contained 2% solids ( $2 \times 10^4$  mg colloids per liter) in 2mM sodium azide was measured with a micro-pipettor ( $\pm 10^{-2}$  mL) into buffer to prepare concentrated colloid stock solutions. Before pipetting, the manufacturer's colloid stock solution was sonicated three times in 30 second bursts at 40-45kHz using an ultrasonic cleaner (Model B3, Branson Cleaning Equipment Co., Shelton CN) to assure that all colloids were separated and fully suspended. Fluorescein and colloids are reported in ppm in this thesis. For colloids,

$$ppm = \frac{mg}{L} = \frac{mg}{particle} \left( \frac{particles}{mL} \right) \left( \frac{1000mL}{L} \right) \quad (4)$$

where the colloid mass (mg/particle) is calculated using polystyrene density (1.05g/mL) and colloid volume per particle ( $cm^3$ ). Throughout this thesis, ppm will be used to convey both mg fluorescein/L solution and mg colloids/L solution. A unit conversion reference for colloids is shown in Table 3.1.

Table 3.1 Unit conversion reference for 1 $\mu$ m polystyrene colloids.

ppm	$10^{-6}$	$10^{-5}$	$10^{-4}$	$10^{-3}$	$10^{-2}$	$10^{-1}$	$10^0$	$10^1$	$10^2$	$10^3$	$10^4$
2*spheres/mL	$10^0$	$10^1$	$10^2$	$10^3$	$10^4$	$10^5$	$10^6$	$10^7$	$10^8$	$10^9$	$10^{10}$
% solids	$10^{-10}$	$10^{-9}$	$10^{-8}$	$10^{-7}$	$10^{-6}$	$10^{-5}$	$10^{-4}$	$10^{-3}$	$10^{-2}$	$10^{-1}$	$10^0$

To begin an experiment, flow was initiated in either the upward or downward direction. Upward flow was regulated by positioning the outflow tubing above the surface of the sand pack. By constant pumping at a flow rate equal or greater to that of the inflow rate, fluid above the level of the tubing termination was drawn off and a constant-elevation water reservoir was maintained. Flow in the

<sup>2</sup> Concentration of trace elements found in RO water. Data collected by OSU Central Analytical Lab on 9/21/10.

element	P	K	Ca	Mg	Mn	Cu	B	Zn	Fe
concentration(ppm)	0.1	1.7	0.9	<0.1	0.1	<0.1	0.1	<0.1	<0.1

downward direction required more careful matching of inflow and outflow rates. In some experiments overflow and flooding resulted from imperfect matching between inflow and outflow rates. The pump system was designed to use the same tubing and the same dual pump head for both inflow and outflow delivery. This was thought to be ideal for maintaining unity between the two rates. However, consistent discrepancy was observed that, if unattended, resulted in system overflow or inadvertent desaturation of the sand.

On several occasions the chamber data were marked by unexpected patterns in intensity. This intensity appeared in the field of view at various times over the course of calibration experiments and followed no predictable time course or form. One possible explanation was fluorescence from soap residues on chamber parts. Once this was understood as a possible source of fluorescence, all non-rubber chamber parts were prepared before assembly by a rinse with 0.01M sulfuric acid ( $H_2SO_4$ ) to eliminate any unwanted fluorescent signal from soap residues [Ingle and Crouch, 1988].

Despite the acid wash, the behavior referred to as “bleeding” continued. It generally arose from a chamber corner or edge, and extended out in a plume that grew as fluid was passed by. The cause of this behavior was thought to be contact between closed-cell foam rubber blocks and the pore fluid. As shown in the system configuration (Figure 3.15), foam rubber was used to create a light-proof seal between system components. The foam at the top of the chamber was pressed tightly to the upper surface of the glass sheets. When flow was initiated from above, there was difficulty in maintaining the same flow rate both in and out of the sand pack. This resulted in an overflow which was thought to saturate the foam with fluorescein and colloid solution. The fluorescein was likely held in the pores of the foam until water again contacted that storage volume. At that time, the stored fluorescein diffused into the system and traveled into the sand pack (Figure 3.16), corrupting some attempts to obtain calibration data.

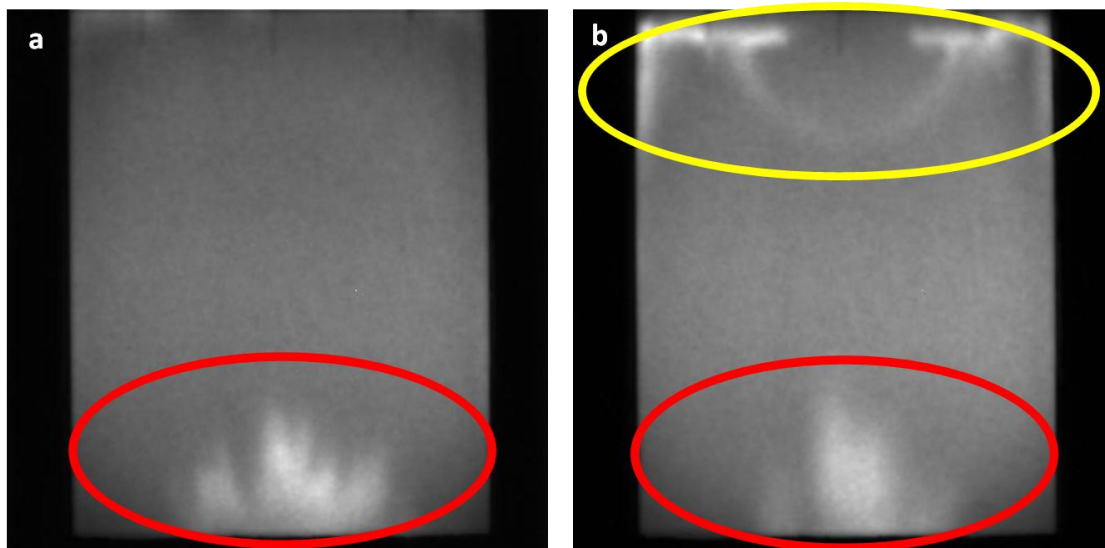


Figure 3.16 Examples of fluorescein bleeding. Images are from the same experiment with (a) having been taken four days prior to (b). Fluorescein bleeding upwards from the influent manifold during upward water flow is apparent in (a) and (b). Also shown in (b) is fluorescein bleeding from the sand surface—likely generated by retention in the foam blocks used around the upper mask for light containment, and caused by downward water flow and radial dispersion.

### ***Data Collection***

Several data streams were collected simultaneously during each experiment. Fluorescein and colloid fluorescence concentrations in sand pack effluent were collected using an inline spectrofluorometer (Model FP6200, Jasco Inc, Easton MD) fitted with a flow-through cuvette (Model #72F/Q/10, Starna Scientific Limited, Essex England), and plumbed to the outlet of the experimental system. Effluent was excited at 488nm and 581nm using the Spectra Manager™ software (Version 1.30, Jasco Inc, Easton MD) Dual Timecourse Measurement application (Model #4880-0576A, Jasco Inc, Easton MD). Fluorescence at 512nm and 602nm were collected as fluid left the chamber.

This instrument allowed for simultaneous generation of fluorescein and colloid breakthrough curves over certain ranges of concentration. Calibration of the spectrofluorometer was accomplished through use of experimental standards over a range of concentrations. The spectrofluorometer has three sensitivity settings, and calibrations for fluorescein and colloids were performed at all three sensitivities. Spectrofluorometer calibration data is presented in Appendix C. It must be noted that

only a single sensitivity setting could be used at any given time. Because the range of concentrations of fluorescein and colloids used in this research was so broad (nine orders of magnitude), multiple sensitivity settings were required to detect fluorescein and colloids across the full range of concentrations. Detection of both fluorescein and colloids in the effluent was often not possible at the given sensitivity, which prohibited simultaneous collection of data on both.

Because pH and ionic strength (measured indirectly via electrical conductivity) are critical to colloid interactions with surfaces [Saiers and Hornberger, 1999; Saiers and Lenhart, 2003] colloid transport is highly dependent on chemical conditions. Therefore, effluent pH and electrical conductivity were also monitored. A benchtop pH and electrical conductivity meter and electrodes (Model SB80PC, VWR International LLC, Bridgeport NJ) were used to record chemical data on solutions before and after pumping through the sand pack. This instrument was plumbed in-line (Figure 3.15) using universal flow-thru adapters (Catalog #61161-358, VWR International LLC, Bridgeport NJ).

Digital images (512x512 pixels) are the primary data collected during an experiment. A 16-bit, liquid-cooled CCD camera (Model TE/CCD detector, Model ST-130 controller, Princeton Instruments, Trenton NJ) was installed 1.4m from the chamber, fitted with an eight-slot 50mm filter wheel (Model C4W-1-5, Finger Lakes Instrumentation, Lima NY) and operated through WinView/32 (version 2.2) software (Princeton Instruments). Within the filter wheel, which was controlled through a computer interface, were housed the two high quality band-pass emission filters (Models D535/40m and D620/30m, Chroma Technology Corporation, Rockingham VT) described above, and a clear UV filter (52Hze Tiffen, Hauppauge, NY). The UV filter was used for collection of red light transmitted through the pack for water content analysis.

All images from all experiments were collected using the largest lens aperture (f-1.4) to allow for maximum light collection, and saved in 16-bit TIFF format. Dark images were taken with the shutter closed at all exposure times used in the experiment; these were used to remove background ambient

light, noise from the analog to digital converter (bias signal) and thermal noise (dark signal) from the data. In some cases the dark image was collected with the shutter open in a darkened room, or with the lens cap in place. Collection of these image with the shutter closed was optimum, as the shutter is controlled from outside the experimental system without disruption. Two images of the saturated sand pack without fluorescein and colloids were collected at each light source wavelength—one at short exposure time with no emission filter for use as the background reference condition in image processing, and one at long exposure time with the corresponding emission filter for use as the zero concentration condition.

Exposure time is a variable that is critical to success with this imaging technique. In the calibration experiments concentrations of fluorescein and colloids were used across the total possible range of detection. Appropriate exposure times were determined for each concentration, with the aim to make use of the full dynamic range of the CCD chip ( $2^{16}=65,536$  discrete intensity values). Exposure times ranged from 0.1s—the fastest shutter speed that produced consistent results to 5.17h, which was the maximum exposure before electronic overexposure of the CCD chip. The mean image intensity is linear with respect to exposure time (Figure 3.17) for exposures times  $> 0.1s$ .

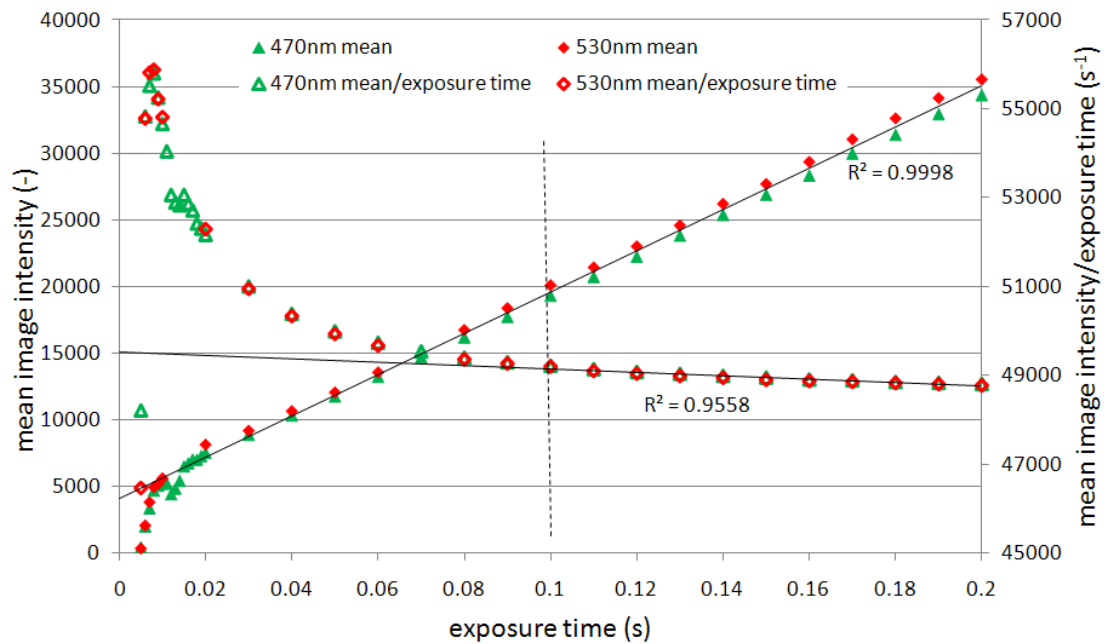


Figure 3.17 Mean image intensity (left axis) vs. exposure time is shown in closed symbols. Mean image intensity normalized to exposure time (right axis) is shown as open symbols. Images were collected on 2/26/07 of a static sand pack containing fluorescein and colloids at the end of a calibration experiment. Solid black lines are linear regression to the average of the 470 and 530 nm values for exposure time 0.1s (dashed line) and greater where image intensity is shown to be linear ( $R^2=0.99$ ,  $R^2=0.96$ ) with exposure time.

The CCD camera is the most sophisticated component of the system, and largely controls the quality of data that is collected. Noise from the camera is reduced by cooling the sensing CCD chip. A Peltier effect thermoelectric cooler [Princeton-Instruments, 1999], using cold ( $-45^{\circ}\text{C}$ ) flowing antifreeze, cools the CCD and leaves the data free of thermal noise. When cooling ceases the data become unusable. Experimental evidence showed that failure of the chip to stay at a constant temperature resulted in an excessive number of electrons accumulating and oversaturating the pixels in the image. An example of strips of false brightness caused by this mechanism is in Figure 3.18. These strips are problematic since the median filter algorithm used to remove single hot pixels from the data does not work when strips of hot pixels in the “filter neighborhood” are all oversaturated. Repair of the refrigeration system resolved this aberration in the data, and a series of experiments was conducted to determine the optimal temperature of the CCD chip and the effect of temperature on system data quality.

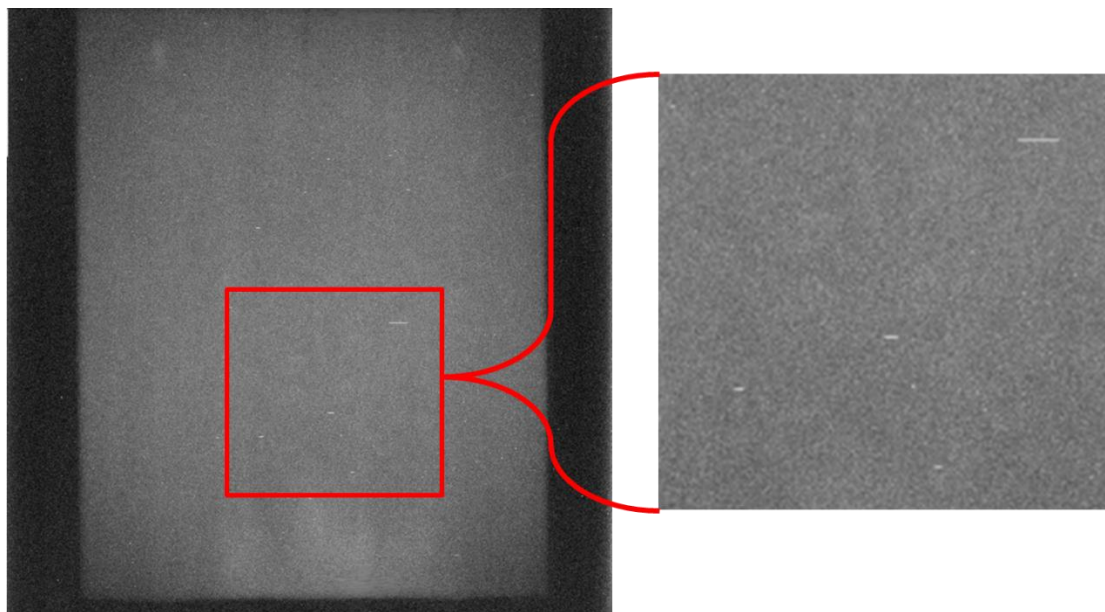


Figure 3.18 Example of horizontal striping from coolant failure. Image (left) is of water-saturated sand pack collected with a 5-hour exposure time using optical settings for colloid imaging (530nm). Zoom (right) of boxed area shows strips of bright pixels caused by coolant failure.

### ***Image Processing***

Images were collected:

- 1) without illumination
- 2) with illumination of the water-saturated sand pack, without fluorescein and colloids
- 3) with illumination of the sand pack, with fluorescein and colloids
- 4) with illumination, of the sand pack at residual water content

These images were processed according to the Image Processing Protocol included as Appendix E. This procedure will be summarized here. All images were first processed with a median filter (“m-f”) [Gonzalez *et al.*, 2004; Russ, 2007] to remove data outliers. The dark image was used to remove bias signal, dark signal, and background light. The saturated image was used to remove artifacts associated with inhomogeneous illumination. The images of fluorescein and colloids were corrected using the dark and saturated images. The residual water content image was used in conjunction with the saturated image to determine water content.

Calibration data of fluorescein and colloids over a known set of concentrations were processed and fit with calibration equations that relate the known concentration to the processed intensity. These calibration equations were then applied to images of 470nm and 530nm processed image intensity to determine respectively the fluorescein and colloid concentrations at each pixel (Figure 3.19).

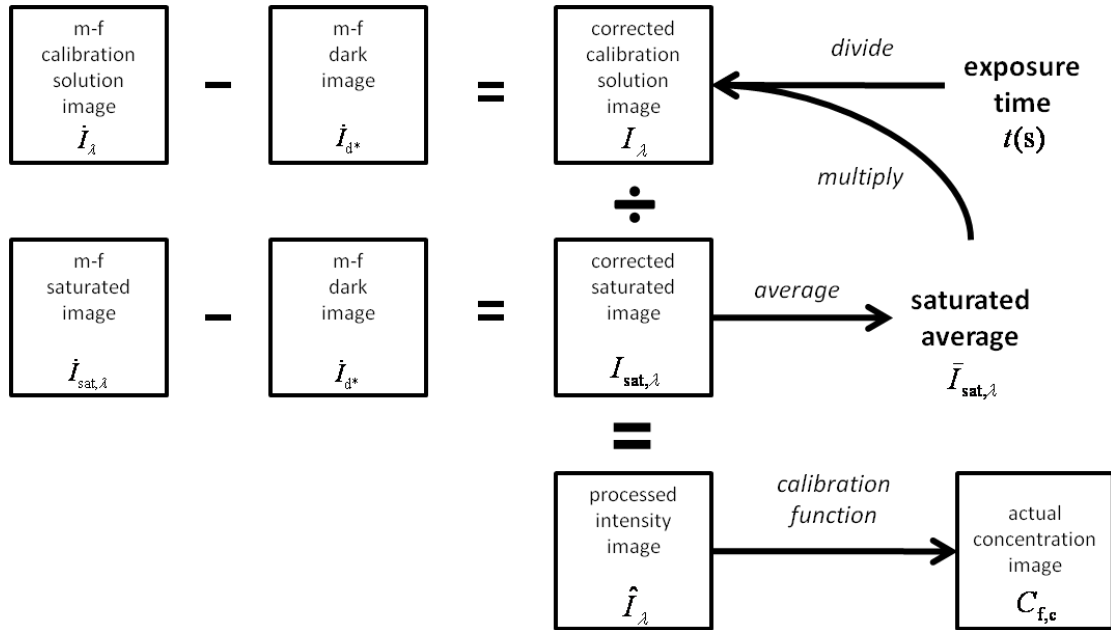


Figure 3.19 Image processing protocol. Images (two dimensional arrays) are shown as boxes. Scalar values are shown in bold font. Operations are shown in italics or with symbols. The subscript  $\lambda$  refers to the image having been taken at a specific wavelength. The subscript  $d^*$  refers to the dark image having been collected with an emission filter matching the image that it is being used to correct. The subscript  $f,c$  refers to the actual concentration image being specific to fluorescein or colloids.

The image processing protocol may be stated mathematically as:

$$\hat{I}_\lambda = \left( \frac{I_\lambda \bar{I}_{sat,\lambda}}{I_{sat,\lambda} t} \right) \quad (5)$$

where  $\hat{I}_\lambda (-)$  is the processed intensity image for 470 or 530nm,  $I_\lambda (-)$  is the corrected calibration solution image for 470 or 530nm,  $I_{sat,\lambda} (-)$  is the corrected saturated image,  $\bar{I}_{sat,\lambda} (-)$  is the mean value of the corrected saturated image, and  $t (s)$  is the exposure time of the raw calibration solution image. In this notation, bold font terms are images and regular font terms are scalar values. The calibration equations are presented in Chapter Four.

### ***Evaluation of System Modifications***

The success of system modification was gauged by the improvement in the signal-to-noise ratio (SNR), which is defined as “the ratio of the amplitude of a desired signal at any point to the amplitude of noise signals at that same point” [Geller, 2003]. The SNR is of interest in this system as it limits the lowest concentrations of fluorescein or colloids that can be quantified. Significant increases in SNR resulted from system improvements. In this thesis, the SNR was defined as:

$$SNR = \frac{\mu_{signal}}{\sigma_{signal}} \quad (6)$$

where  $\mu_{signal}$  is the mean pixel intensity value across the image (-), and  $\sigma_{signal}$  is the standard deviation of pixel values across the image (-) [Bushberg, 2002]. The SNR was calculated for 12 experiments that utilized a sand pack saturated with a uniform concentration of fluorescein and colloids. The mean pixel intensity was the average of all pixels in the processed image, and the standard deviation was the maximum of all standard deviation values computed for pixel rows of the processed image. The SNR for each calibration experiment are in Table 3.2. The largest SNR was achieved for fluorescein at low concentrations and for colloids at high concentrations. The maximum SNR achieved with this system using the method of uniform concentration was 21 for fluorescein and 58 for colloids.

Table 3.2 Summary of SNR statistics for all constant concentration experiments.

calibration experiment	experiment low concentration (ppm)	experiment high concentration (ppm)	maximum fluorescein SNR	fluorescein concentration (ppm) at maximum SNR	maximum colloid SNR	colloid concentration (ppm) at maximum SNR
1	$10^{-3}$	$10^1$	11.35	$10^{-1}$	10.20	$10^1$
2	$10^{-4}$	$10^0$	11.62	$10^{-4}$	5.29	$10^0$
3	$10^{-3}$	$10^1$	19.42	$10^{-3}$	19.05	$10^1$
5	$10^{-3}$	$10^1$	16.16	$10^{-3}$	10.25	$10^1$
6	$10^{-3}$	$10^1$	18.73	$10^{-3}$	7.42	$10^1$
7	$10^{-3}$	$10^1$	18.73	$10^{-3}$	7.42	$10^1$
8	$10^{-3}$	$10^1$	20.60	$10^{-2}$	22.80	$10^{-1}$
9	$10^{-3}$	$10^1$	16.53	$10^{-3}$	37.66	$10^{-1}$
10	$10^{-3}$	$10^1$	19.13	$10^{-2}$	11.51	$10^{-3}$
13	$10^{-6}$	$10^{-3}$	3.05	$10^{-5}$	3.67	$10^{-4}$
14	$10^{-6}$	$10^{-3}$	2.03	$10^{-6}$	3.53	$10^{-4}$
15	$10^{-6}$	$10^2$	8.55	$10^{-6}$	58.82	$10^0$

Other systems have been evaluated using a SNR computed by dividing the mean intensity value of an image by the standard deviation in that value over several replicate images [Bridge *et al.*, 2006]. This method of calculation evaluates only the noise associated with detector, source intensity and porous medium, and not the calibration method itself. Using this approach, SNR values ranged from 12 to 1764 for fluorescein and from 8 to 1042 for colloids (Figure 3.20). The limit of detection is defined as the concentration at which the SNR=3 [Bridge *et al.*, 2006; Pokhriyal *et al.*, 2010].

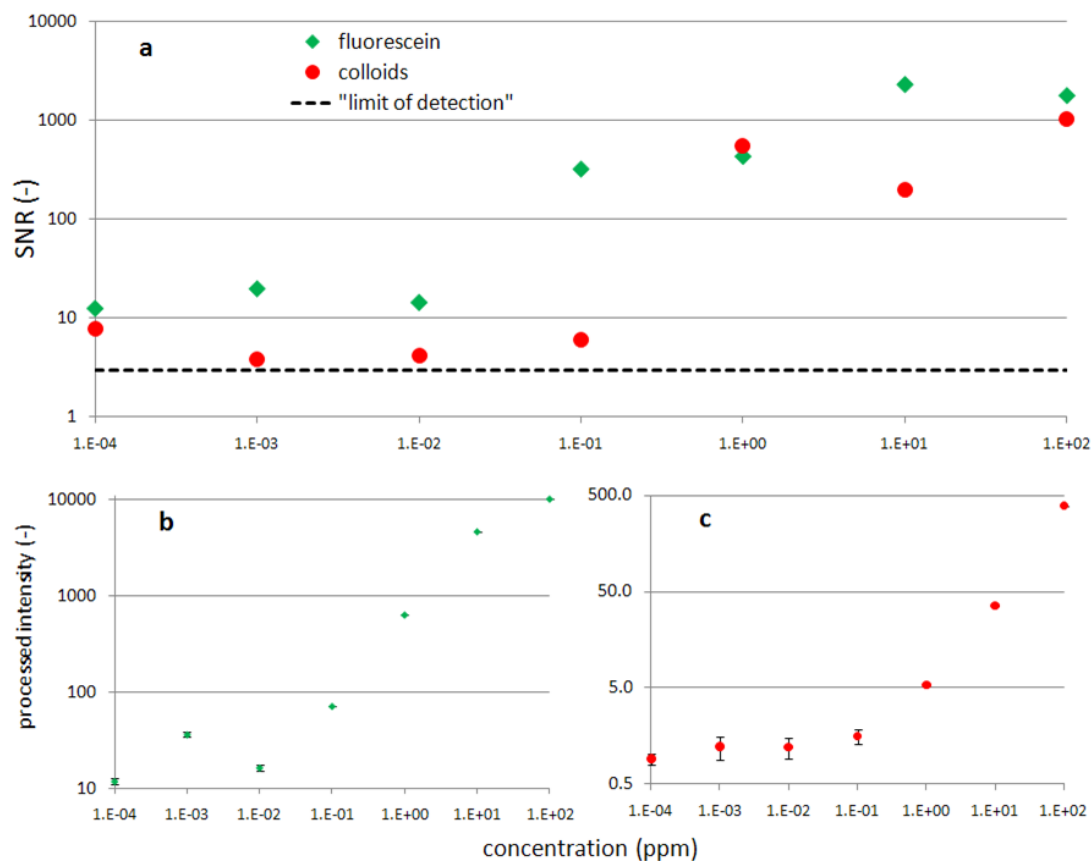


Figure 3.20 Signal-to-noise ratio for each of seven concentrations of fluorescein and colloids (a) plotted with “limit of detection” cutoff defined as  $SNR=3$ . Images of each concentration were collected three times during a calibration experiment (2/25/09). The maximum value was calculated for each image, and the mean and standard deviation were taken of the replicate maximum values. SNR was calculated as the mean divided by the standard deviation. Bottom plots show the mean of the three maximum processed intensity values for fluorescein (b) and colloids(c) plotted with the standard deviation around that mean.

The calculation of SNR presented above suggests no limit to detection down to  $10^{-4}$  ppm since SNR values never fall below 3. However, in light of the processed intensity data presented in Figure 3.20, we can say that we have developed a system that demonstrates detection of fluorescein to a concentration of  $10^{-2}$  ppm and of colloids to a concentration of  $10^{-1}$  ppm. Detection of fluorescein in a micro-scale imaging system was successful to a detection limit of  $5 \times 10^0$  ppm ( $5 \mu\text{g/mL}$ ) with a range of SNR values from 3 to 1000 [Pokhriyal et al., 2010]. A system similar to ours which used reflexive imaging reported reaching the limit of detection where  $SNR=3$  at  $7.6 \times 10^{-1}$  ppm ( $0.0023 \text{mM}$  converted using  $MW=332.306 \text{g/mol}$ ) for fluorescein and  $2.1 \times 10^0$  ppm for colloids [Bridge et al., 2006].

## Occlusion

Experiments that were conducted at very high concentrations were marked by a decrease in light intensity at the highest concentrations (Figure 3.21). This behavior was more marked for fluorescein than for colloids. In these highest concentration plumes, brightness decreased towards the center of the plume, where it was unaffected by dilution. This was not observed for plumes at lower concentrations. The occlusion behavior at high concentrations can be modeled, but transport experiments were conducted in the concentration range where occlusion was not significant.

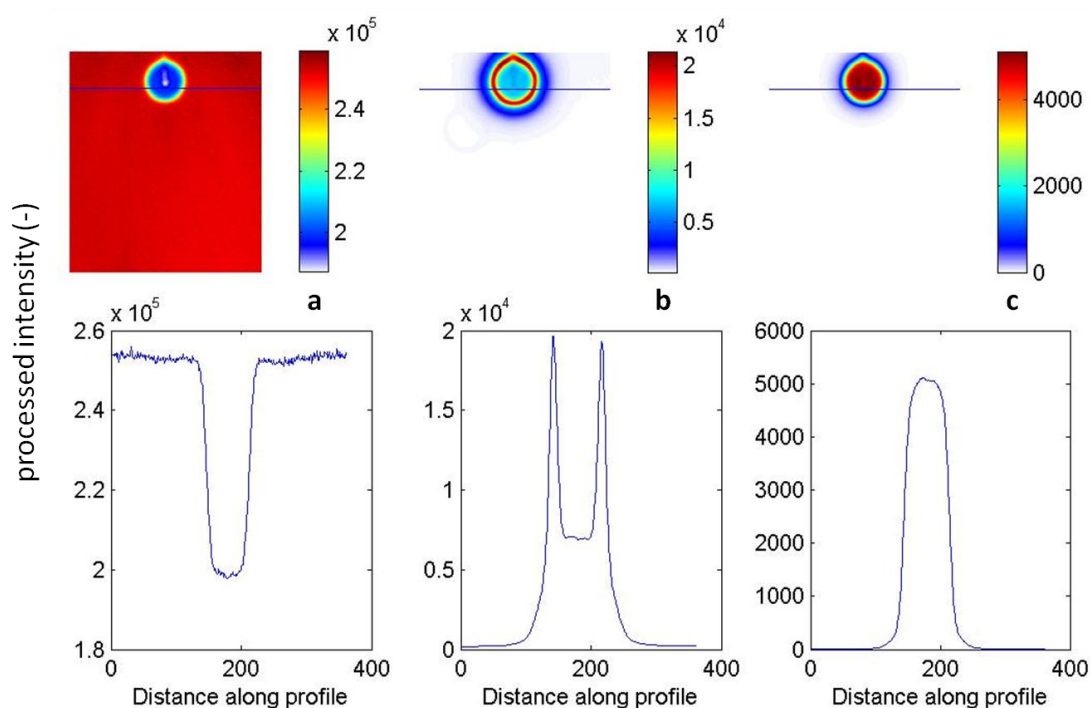


Figure 3.21 Occlusion by fluorescein at  $10^3$  ppm. Images are processed intensity of a  $10^3$  ppm plume during a calibration experiment (12/03/07) in a saturated sand pack. Images are collected at 630nm (a), 470nm (b), and 530nm (c) to quantify water content, fluorescein, and colloids respectively. Matching transects show that emission from fluorescein (b) is blocked, as is transmission of light at 630nm (a). High concentration colloids (b) show little effect of occlusion on fluorescein emission.

## Fluorescein Degradation

Since the 1970s, fluorescein has been used as a water tracer, largely in riverine environments. The tracer is actually particularly desirable for environmental applications because of its photodegradation behavior when exposed to light. Rapidly diminishing visibility of the green color in a natural water

body makes its use acceptable in places where public response to artificial color would be negative. It has been shown that degradation of fluorescein occurs more rapidly under UV light than it does under exposure to longer wavelengths [Smart and Laidlaw, 1977]. Work shown here by comparison evaluates photodegradation under controlled wavelengths of visible light. Colloids were not seen to be subject to photodegradation.

As fluorescent molecules are repeatedly excited and relaxed over time, some efficiency of emission is lost. The molecules undergo chemical degradation that makes them less efficient at emitting light upon relaxation to their lower energy state [Song *et al.*, 1995]. Fluorescein has been shown to be significantly affected by this type of photo-decay under natural sunlight [eg. Lindqvist, 1960]. We sought to quantify the possible error in experimental results from the light-transmission system as a result of this type of photo-decay. Experiments were conducted both in the sand-packed chamber and in the fluorometer that demonstrate the effect of time and light on fluorescein fluorescence.

Because the light used in this system to excite fluorescein is intentionally bright to exact maximum light energy output from the fluorescent molecules, it is also potentially particularly damaging to them. Additionally, since the calibration experiments endeavored to demonstrate a minimum detectable concentration, exposure times were extended to the maximum as defined by the noise threshold of the system. Long exposure (up to five hours) by bright light (up to 750 lumens) may well reduce the brightness of fluorescein emission during a calibration experiment.

In a sand pack saturated with uniform fluorescein concentration, fluorescein emission intensity decreased one percent under exposure to 162 lumens intensity light at 470nm over 13.5 minutes. A logarithmic trend was fit to the data (Figure 3.22).

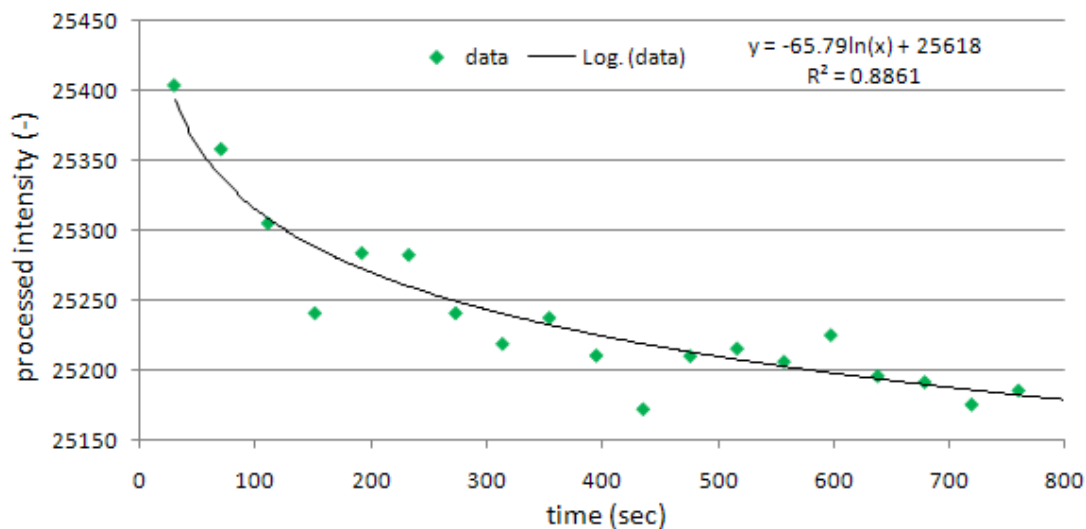


Figure 3.22 Photodegradation of fluorescein over time. Plotted data are the average of the processed intensity maxima of three  $10^0$  ppm fluorescein plumes from 2/25/09. Images were taken at 30.52s exposure time with a 10s delay.

The potential for degradation due to exposure was not uniform between or during experiments. The duration of exposure of fluorescein to light during imaging ranged from 0.1s to 50 min depending on the fluorescein concentration being used. In a similar way excitation light within the spectrofluorometer affected fluorescein as it passed through the sample cuvette. The duration of exposure was shorter, but the excitation light was brighter. In early experiments, calibration solutions were mixed and stored under fluorescent lighting in the laboratory. And translucent tubing was sometimes used, which allowed for ambient light to non-uniformly affect fluorescein-containing experimental fluid. The potential for fluorescein photodegradation was minimized in later experiments by storage of calibration solutions in a dark cooler and the use of opaque tubing. However photodegradation was never eliminated, and fluorescein photodegradation was included in transport modeling.

### ***Optical Noise***

While emission intensity at 470nm appeared to be decreased by degradation of fluorescein molecules, emission intensity at 530nm appeared to increase through spectral overlap in transmission by optical

filter. The system depends on clear optical separation of each signal. Fluorescein emission intensity leaking into colloid images (Figure 3.23) was seen to comprise up to 17% of colloid emission intensity. The leaking fluorescein signal was observed in this experiment due to the use of buffer which stimulated colloid deposition. In these colloid images, the fluorescein pattern was discernable while the colloids remained motionless. This observation led to an image processing step wherein a percentage of the intensity of each pixel in a fluorescein array was subtracted from the corresponding pixel in the colloid array (Figure 3.24). Limited success was achieved in correcting the signal overlap artifact. Further perfection of optical component matchup could resolve this source of error, but no compensations were made in calibration or modeling of transport behavior.

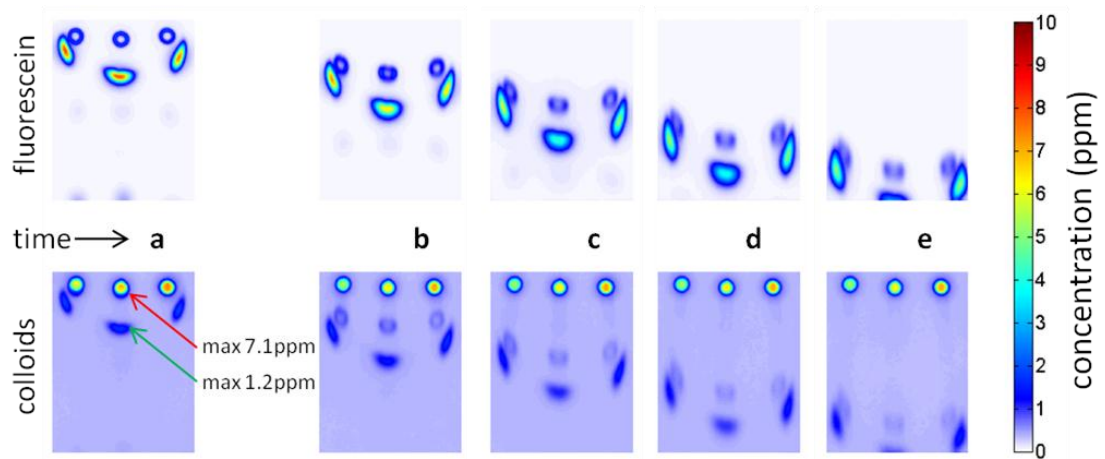


Figure 3.23 Fluorescein and colloid concentration images over time (a-e) at 10 mL/min downward flow. Images were taken with 5sec exposure for fluorescein and 3.2min exposure for colloids with flow stopped. Colloid images (bottom row) show evidence of the transport pattern expressed by fluorescein (top row). For the colloid image at time 1 (a), the maximum of the colloid plume is 7.1ppm, while the maximum concentration value generated by fluorescein intensity is 1.2ppm.

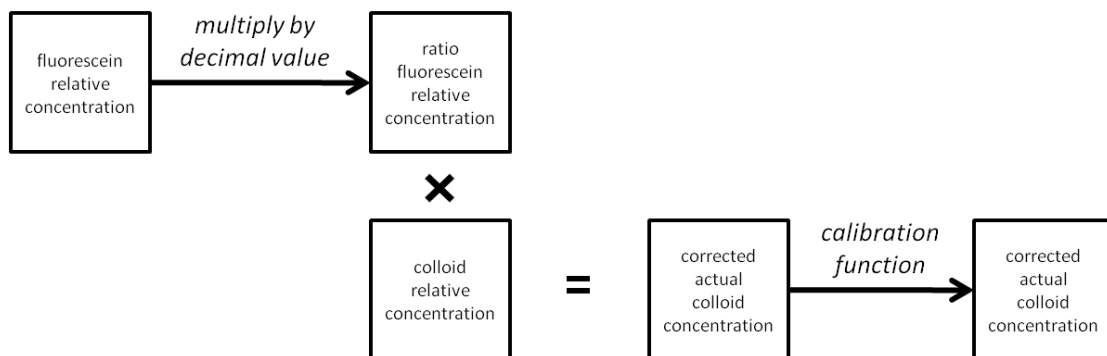


Figure 3.24 Flow chart of image processing step aimed at removing fluorescein signal from colloid images. Fluorescein relative concentration and colloid relative concentration arrays are those shown in the next to last processing step in Figure 3.19. The decimal value used to generate the ratio fluorescein relative concentration array was varied to find the value that would lead to the most accurate prediction of colloid mass.

### ***Autofluorescence***

Discrepancies between known and predicted concentrations could have resulted from fluorescence of the quartz sand, although quartz is known to have very low autofluorescence [Eckert *et al.*, 2000; Pokhriyal *et al.*, 2010; Udovich *et al.*, 2008]. The fluorescent signal contributed by the sand was determined and these levels were incorporated into the detection limit of this system. Paper, by contrast, exhibits significant autofluorescence [Billa *et al.*, 1999]. Craft paper is made from wood pulp, which is primarily cellulose whose autofluorescence has been demonstrated at 420nm [Smaghe *et al.*, 2007]. Images of a sand packed chamber were compared with those of an empty chamber masked with craft paper (Figure 3.25). It was shown that the autofluorescent intensities are higher at 470/535nm than at 530/620nm, and that they are two orders of magnitude higher for paper than for sand.

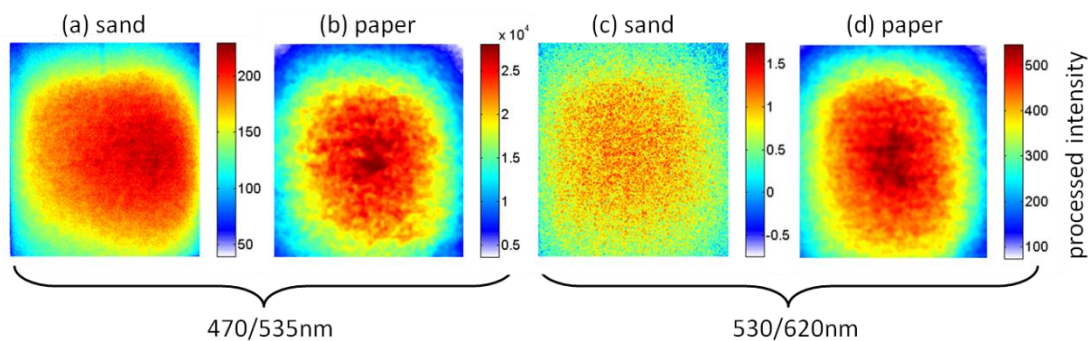


Figure 3.25 Processed intensity images of autofluorescence from quartz sand and craft paper. Images (a) and (b) were illuminated at 470nm and collected with emission filters centered at 535nm. Images (c) and (d) were illuminated at 530nm and collected with emission filters centered at 620nm. Autofluorescence at 470/535nm (a) and (b) is two orders of magnitude brighter than at 530/620nm (c) and (d). Autofluorescence of paper (b and d) is two orders of magnitude brighter than that of sand (a and c).

The average processed intensity values from the static saturated sand pack were small relative to the dynamic range of the camera. Autofluorescence is accounted for in the intercept term of the calibration equations presented in Chapter Four.

## Chapter Four: System Calibration

### ***Calibration Objectives***

The goal of this project was to observe and quantify colloid transport in porous media. Having built a system to observe colloids, conservative tracer, and water content changes over time and space, it was then necessary to create a set of calibration functions relating measured intensities at the three wavelengths to the actual physical quantities: water content, fluorescein concentration, and colloid concentration. Water content ( $\theta$ ) is expressed as a function of measured light intensity upon illumination at 630nm (Equation 7). Fluorescein concentration ( $C_f$ ) is expressed as a function of measured light intensity upon illumination at 470nm (Equation 8), and colloid concentration ( $C_c$ ) is expressed as a function of measured light intensity upon illumination at 530nm (Equation 9):

$$\theta(x, y, t) = f(\hat{I}_{630\text{nm}}(x, y, t)) \quad (7)$$

$$C(x, y, t)_f = f(\hat{I}_{470\text{nm}}(x, y, t)) \quad (8)$$

$$C(x, y, t)_c = f(\hat{I}_{530\text{nm}}(x, y, t)) \quad (9)$$

where  $\theta(-)$  is the volumetric water content,  $C_f$  and  $C_c$  (ppm) are the known concentrations of fluorescein and colloids respectively, and  $\hat{I}_{630\text{nm}}$ ,  $\hat{I}_{470\text{nm}}$ , and  $\hat{I}_{530\text{nm}}$  (-) are the processed intensity images collected under illumination by 630, 470 and 530 nm light respectively. The functional form for Equation 7 was previously developed by *Niemet and Selker* [2001]. In order to determine the functional form of Equations 8 and 9, calibration solutions of known concentrations of fluorescein and colloids were applied sequentially to a saturated sand pack. Statistics were taken from the measured intensities and plotted against known concentrations. The model and associated fitting parameters that best fit these curves are the sought after calibration functions.

This chapter describes the calibration process, and presents data from seventeen calibration experiments. Each calibration experiment had slightly different methodological details, as the system

and the experimental protocol were being continuously improved to extend the limits of detection for imaging of fluorescein and colloids at a wider range of concentrations.

### ***Calibration Data Collection***

Calibration experiments were conducted using two basic approaches: 1) uniform saturation of the sand pack with calibration solutions, or 2) application to the sand pack of discrete plumes of calibration solutions. In both approaches, calibration solutions were applied sequentially, starting with the lowest concentration calibration solution. In the case of uniform-saturation calibration, the goal was to achieve a homogeneous distribution of a known concentration of fluorescein and colloids throughout the sand pack. In the case of plume calibration, the goal was to achieve a known concentration at the center of the plume. After calibration solutions were employed in the sand pack, images were collected at the appropriate optical settings.

After imaging, flow was initiated to flush the fluorescein and colloids from the sand pack. In uniform-concentration experiments this was done by “flushing” one or multiple sand pack pore volumes of clean (fluorescein-free and colloid-free) fluid (RO water or buffer) or the next higher concentration calibration solution through the sand pack using upward flow. In plume calibration experiments flushing was always through downward flow. Flow rates varied between 10 and 184 mL/min, and flow was stopped at intervals for imaging. Flushing continued until plumes were removed from the sand pack. Determination of plume removal was based both on observation of the plume moving downwards and disappearing from collected images, and from inline measurements on the spectrofluorometer of fluorescein and colloid concentrations in sand pack effluent.

It was necessary to use a single sand pack for each calibration experiment, as subtle variations existed in sand pack and dark enclosure configuration between packings. It was shown to be acceptable to use a single pack for iterative application of multiple concentrations of calibration solutions as each sequential calibration solution was scaled to contain at least 10 times (one order of magnitude) more

fluorescein and colloids than the one that preceded it. Residue of earlier calibration solution would thereby contribute no greater than 10% to image intensity. The complete range of fluorescein and colloid concentrations applied over all experiments was  $10^{-6}$  to  $10^3$  ppm, but generally only a subset of this concentration range was used in any calibration experiment. The calibration protocol in Appendix B describes in detail each task executed to accomplish collection of data in a single calibration experiment.

### ***Calibration Experiments***

Calibration experiment 1 was conducted on 2/21/07, shortly after the installation of the dark enclosure. The uniform-concentration method was used, where the sand pack was saturated with calibration solutions of  $10^{-3}$ ,  $10^{-1}$ , and  $10^1$  ppm (Figure 4.1). Each calibration solution was flushed through the system for two pore volumes before imaging.

This experiment was marked by sand attrition from the lower portion of the sand pack due to a poor seal by the lower manifold. The collected data set did not include dark images or a saturated image. Dark and saturated images from subsequent experiments were used for data processing from this experiment. Processed images were cropped to exclude the lower part of the sand pack where sand attrition had occurred. In this experiment two sets of lights were available for colloid excitation, and they were used both together and separately to determine their relative utility in excitation. Data was collected at 470nm, 530nm, 530 and 570 nm together, and 630nm. These 570nm sources were used once more in calibration experiment 2 and not again thereafter due to their insufficient intensity for excitation.

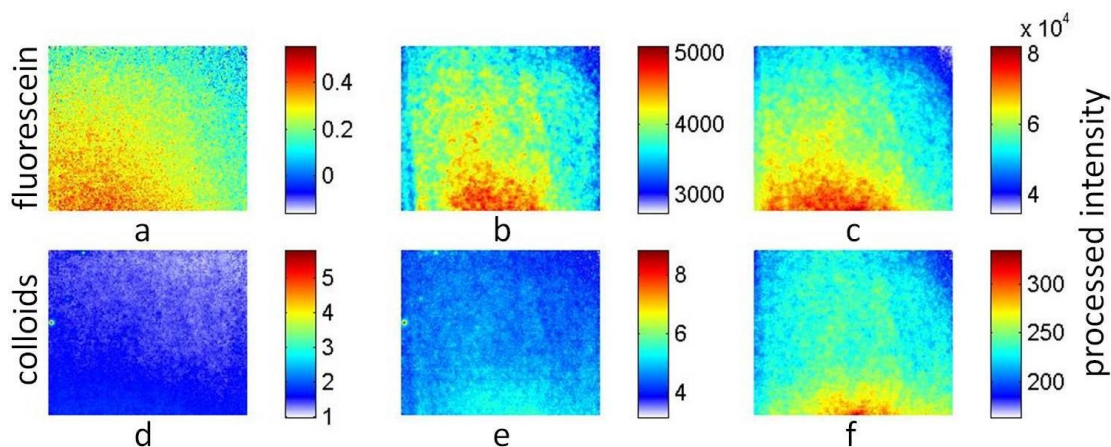


Figure 4.1 Images of processed intensity from calibration experiment 1. Concentrations are  $10^{-3}$  ppm (a, d)  $10^{-1}$  ppm (b, e), and  $10^1$  ppm (c, f). Images represent a physical area of 33.5 x 40.3cm.

Calibration experiment 2 was conducted on 3/2/07 to obtain data at additional concentrations.

Calibration solutions at concentrations  $10^{-4}$ ,  $10^{-2}$ , and  $10^0$  ppm were used (Figure 4.2). The manifold was improved for this experiment in order to prevent the sand attrition experienced in calibration experiment 1. The old mesh was removed and new woven wire 400mesh with  $38\mu\text{m}$  openings and  $25\mu\text{m}$  wire diameter (Screen Technology Group) was wrapped around the manifold to prevent sand attrition. All other experimental features were held constant. Saturated images from calibration experiment 2 were also used for processing images from calibration experiment 1. Dark images used in processing images from both of these calibration experiments were collected at a later date.

Flooding of the system occurred during application of the second calibration solution as a result of the effluent line coming out of the headspace. The images of fluorescein processed intensity from which global means were extracted were markedly inhomogeneous, with streaking particularly at high concentration ( $10^0$  ppm, Figure 4.2c). All three concentrations are below detection for colloids with this system configuration.

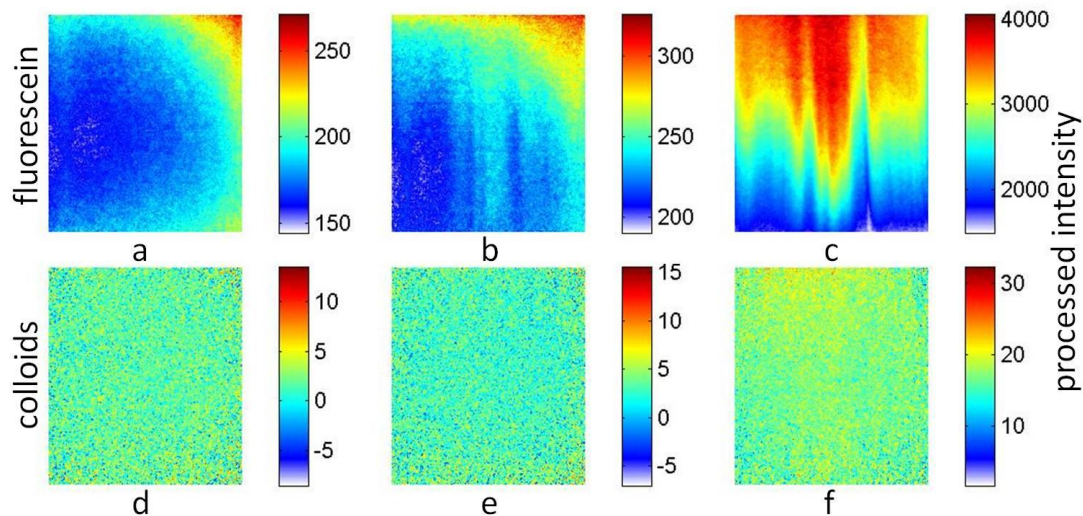


Figure 4.2 Images of processed intensity from calibration experiment 2. Concentrations are  $10^{-4}$  ppm (a, d),  $10^{-2}$  ppm (b, e), and  $10^0$  ppm (c, f). Images represent a physical area of 45.3 x 40.3cm.

Calibration experiment 3, conducted on 3/12/07, was the first experiment conducted using RO water flushes between the calibration solutions. Concentrations used were  $10^{-3}$ ,  $10^{-1}$ , and  $10^1$  ppm (Figure 4.3). Five pore volumes of RO water were flushed upwards through the pack after each concentration to remove the previous calibration solution. This experiment was marked by light leakage below the upper mask. Streaking for 470nm was pronounced with an intense streak at image left (Figure 4.3b and 3c). This calibration experiment raised questions regarding the cause inhomogeneous distribution of fluorescein throughout the sand pack. Colloids were detected at  $10^1$  ppm (Figure 4.3f).

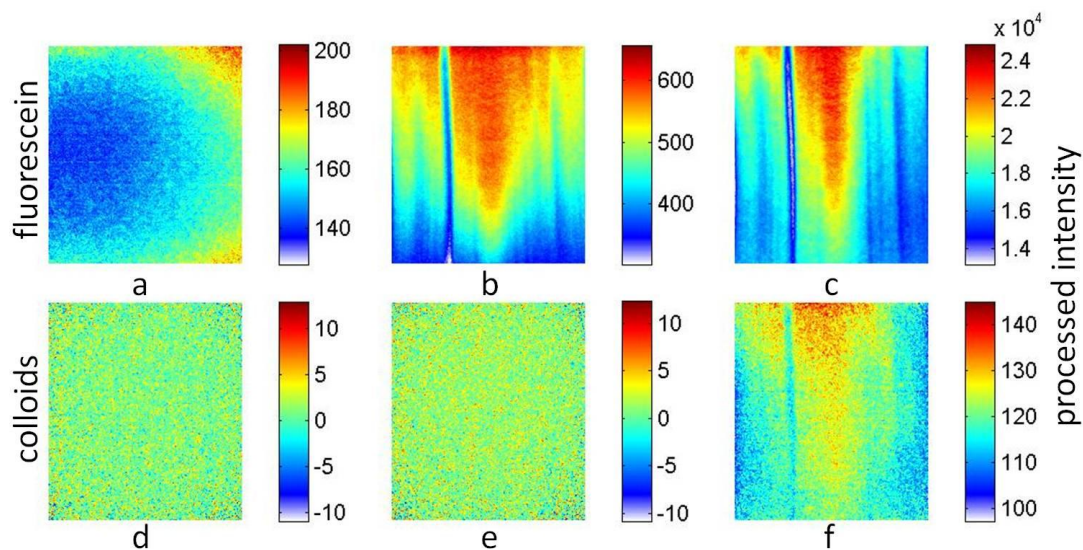


Figure 4.3 Images of processed intensity from calibration experiment 3. Concentrations are  $10^{-3}$  ppm (a, d),  $10^{-1}$  ppm (b, e), and  $10^1$  ppm (c, f). Images represent a physical area of 45.3 x 40.3cm.

Calibration experiment 4 was conducted on 8/31/07, with fluorescein alone, to determine the potential effect of colloid deposition on fluorescein transport and inhomogeneity in previous calibration experiments. A full pore volume of calibration solution at  $10^{-3}$ ,  $10^{-1}$ , and  $10^1$  ppm was iteratively pumped into the sand pack and imaged at 470nm (Figure 4.4). This experiment used RO water flushing of an inconsistent volume ranging from two to four pore volumes between calibration solutions. Prior to this experiment, the orientation of the emission filters was switched, which may affect comparison of these and subsequent data to those from earlier experiments.

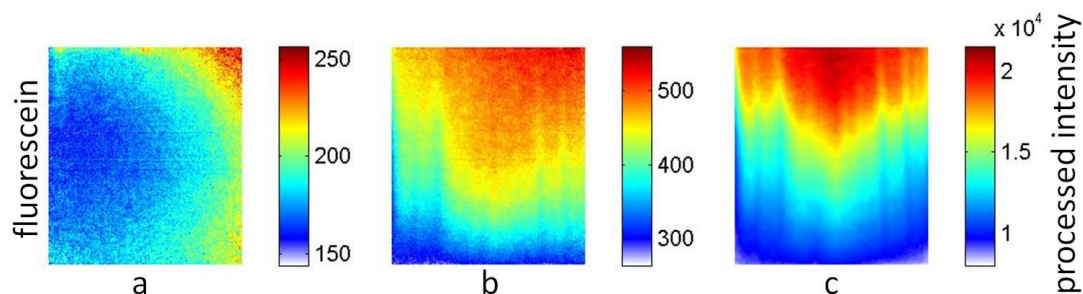


Figure 4.4 Images of processed intensity from calibration experiment 4. Concentrations are  $10^{-3}$  ppm (a),  $10^{-1}$  ppm (b), and  $10^1$  ppm (c). Images represent a physical area of 45.3 x 40.3cm.

Calibration experiment 5, collected on 9/10/07, was a replication of calibration experiment 1.

Calibration solutions with fluorescein and colloid concentrations of  $10^{-3}$ ,  $10^{-1}$ , and  $10^1$  ppm were used (Figure 4.5), and a full data set, including dark and saturated images, was collected. No clean fluid flushing was used. This experiment was marked by the non-optimal handling of calibration solutions, which were mixed over three weeks prior to application, and were moved in and out of the cooler several times. Exposure of these calibration solutions to light and heat may have affected the magnitude of collected fluorescent intensities. Colloids were detected at  $10^1$  ppm (Figure 4.5f).

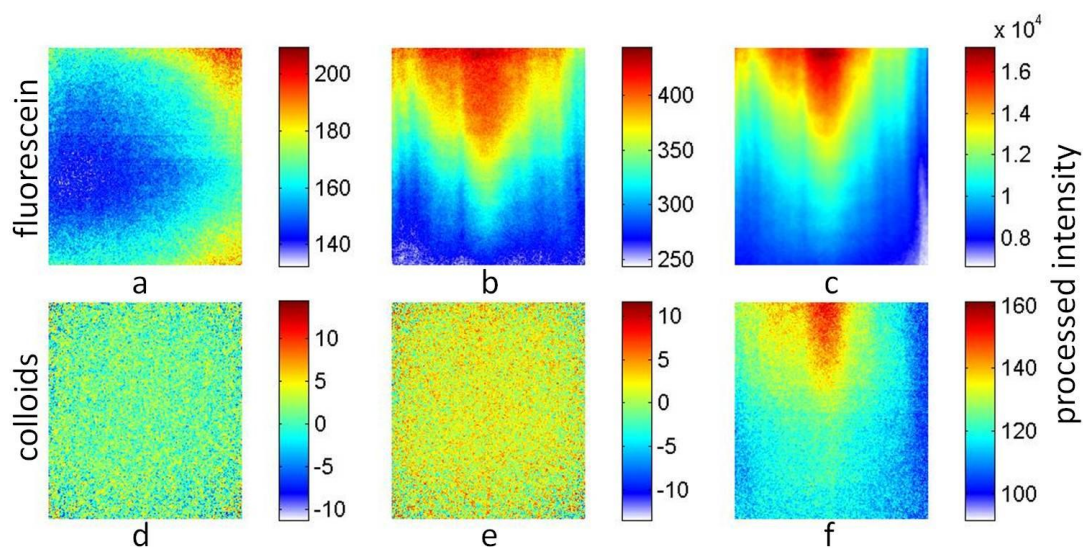


Figure 4.5 Images of processed intensity from calibration experiment 5. Concentrations are  $10^{-3}$  ppm (a, d),  $10^{-1}$  ppm (b, e), and  $10^1$  ppm (c, f). Images represent a physical area of 45.3 x 40.3 cm.

Calibration experiment 6 was conducted on 9/14/07 to replicate calibration experiment 5. Fresh calibration solutions were prepared. Significant streaking was observed in these images (Figure 4.6), especially for fluorescein.

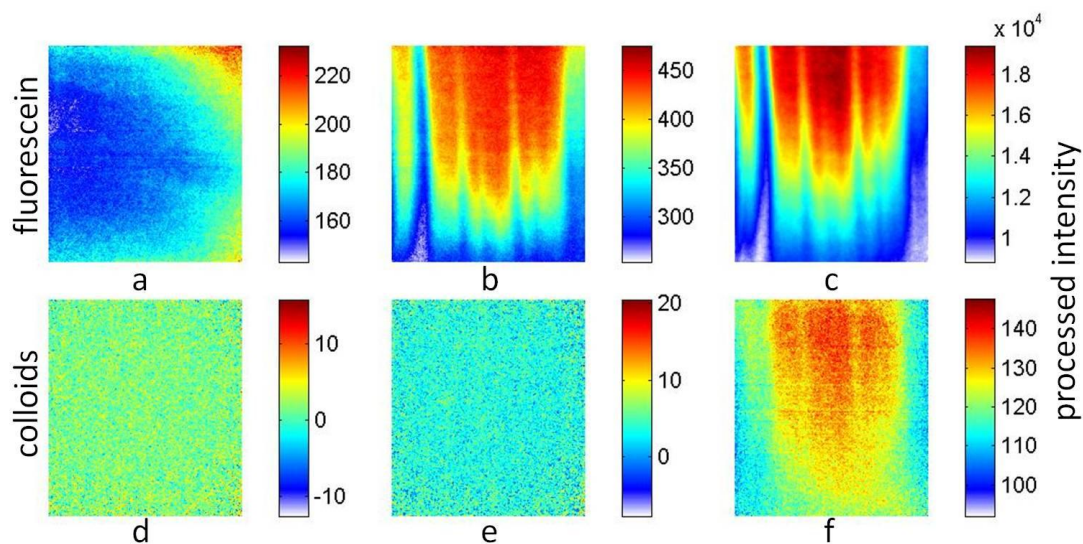


Figure 4.6 Images of processed intensity from calibration experiment 6. Concentrations are  $10^{-3}$ ppm (a, d),  $10^{-1}$ ppm (b, e), and  $10^1$ ppm (c, f). Images represent a physical area of 45.5 x 40.7cm.

Calibration experiment 7, conducted on 9/21/07, used more calibration solutions (five instead of three), closer together in concentration (one order of magnitude instead of two), than in previous calibration experiments (Figure 4.7). RO water flushing was used between calibration solutions. After imaging of the last calibration solution, a 250mL plume of  $10^1$ ppm fluorescein and colloids was applied to the surface of the sand pack, and flushed downwards at 100mL/min (Figure 4.8). By the end of this experiment, the sand pack had desaturated as a result of imperfect coordination of input and outlet flow rates. Inhomogeneity is noted in fluorescein images (Figure 4.8a-e). Colloids are detected at  $10^2$ ppm (Figure 4.8i,j).

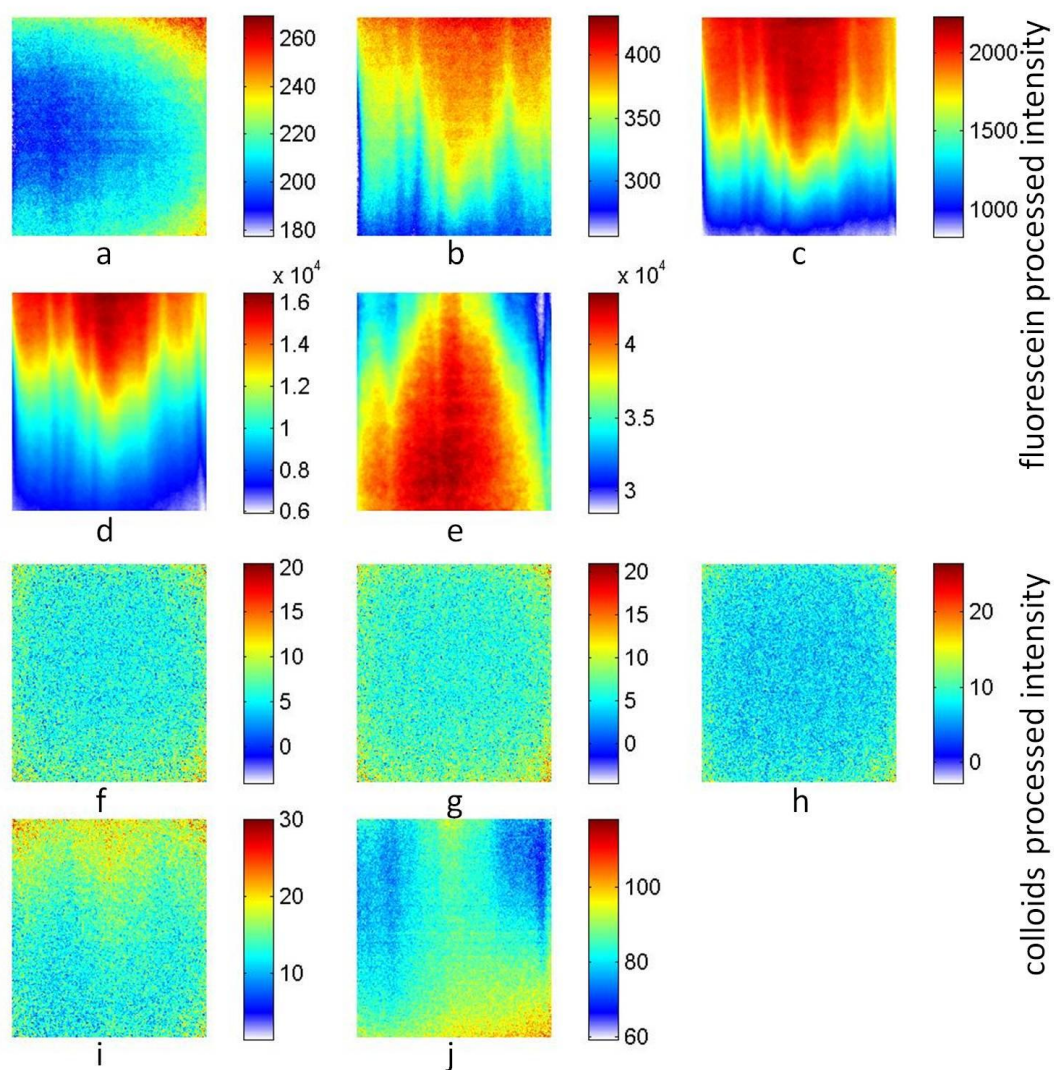


Figure 4.7 Images of processed intensity from calibration experiment 7. Concentrations are  $10^{-3}$  ppm (a, f),  $10^{-2}$  ppm (b, g),  $10^{-1}$  ppm (c, h),  $10^0$  ppm (d, i), and  $10^1$  ppm (e, j). Images represent a physical area of 45.3 x 40.3cm.

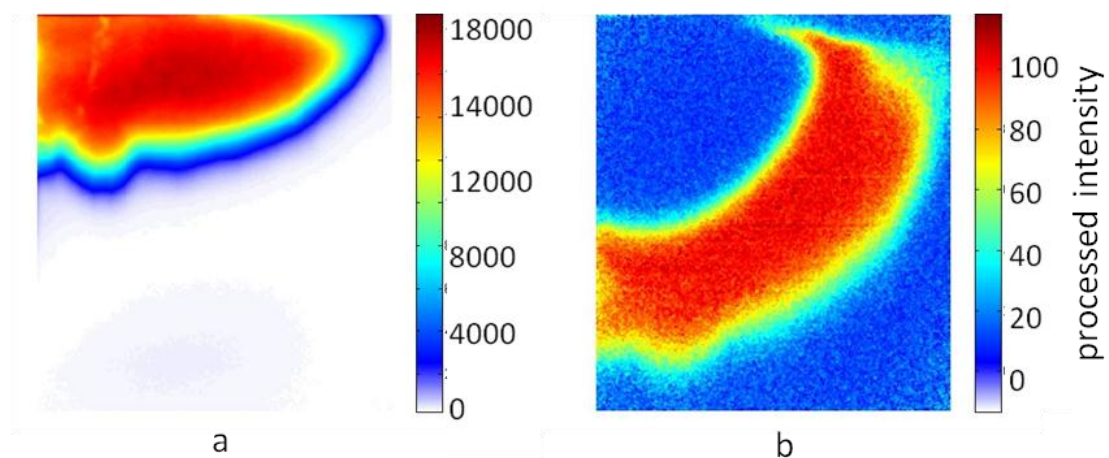


Figure 4.8 Images of processed intensity of plumes from calibration experiment 7. Static images taken during downward flushing were collected of fluorescein after seven minutes (a) and colloids after 13 minutes (b). Images represent a physical area of 45.3 x 40.3cm.

Calibration experiment 8 (Figure 4.9), conducted on 9/28/07, was a replication of calibration experiment 7. RO water flushing upwards was used between calibration solutions. After the last calibration solution, a 250mL plume of  $10^1$ ppm fluorescein and colloids was applied via the inlet tubing at the base of the sand pack (Figure 4.10). Plumes were flushed upwards at 100mL/min. This calibration experiment used an increased exposure time up to 150% of what was used in previous experiments. The result of this increase in exposure time was increased use of the dynamic range of the camera. Subsequent experiments would further maximize exposure time until all data registered a maximum value nearing but not exceeding the maximum possible intensity value of the 16-bit camera ( $2^{16} = 65536$ ). Colloids were detectable down to  $10^{-1}$ ppm (Figure 4.9, h) as a result of increased exposure time. This experiment was marked by poor masking at the top of the sand pack; the masking was cropped out of the images in processing. Patterns of fluorescein inhomogeneity are inconsistent with time (Figure 4.9a-e).

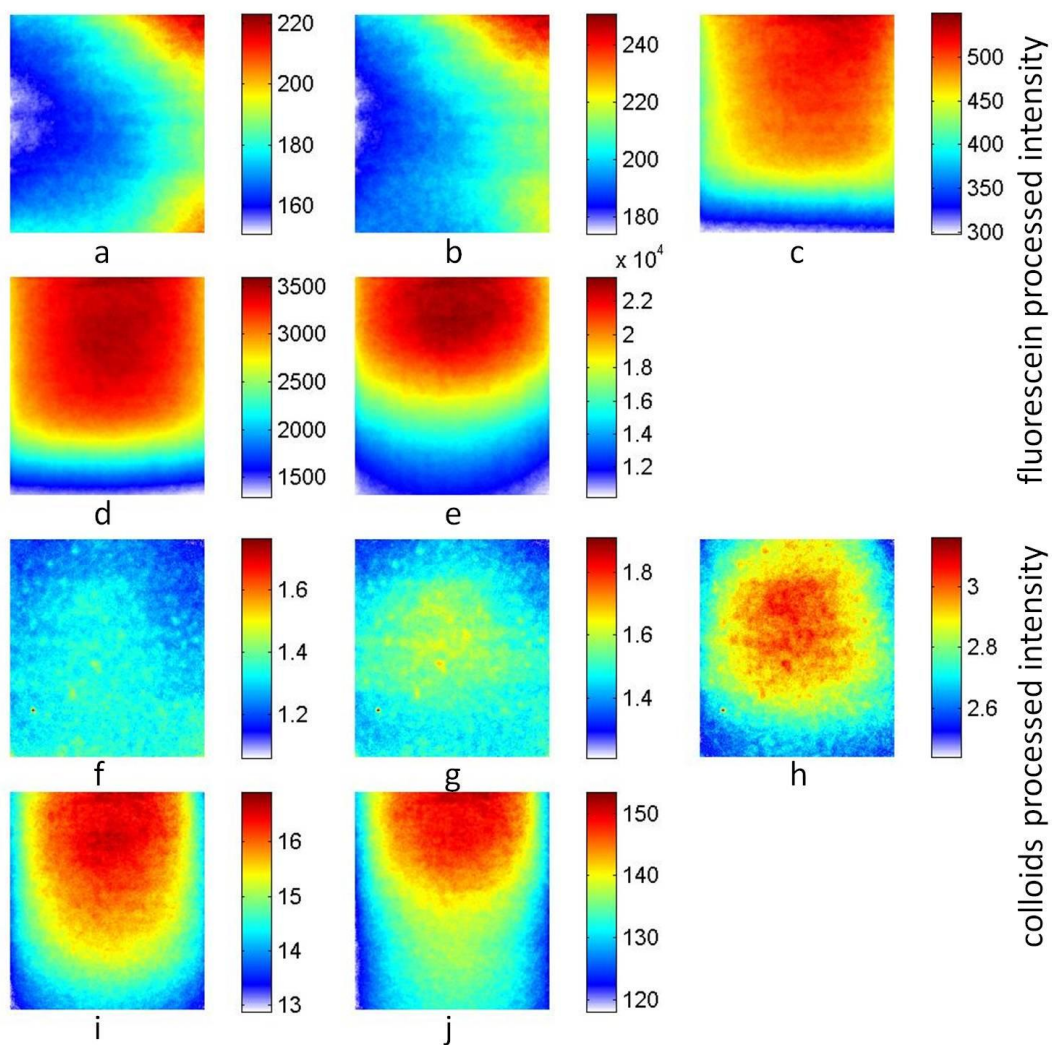


Figure 4.9 Images of processed intensity from calibration experiment 8. Concentrations are (a, f)  $10^{-3}$  ppm (a, f),  $10^{-2}$  ppm (b, g),  $10^{-1}$  ppm (c, h),  $10^0$  ppm (d, i), and  $10^1$  ppm (e, j). Images represent a physical area of 45.3 x 40.3cm.

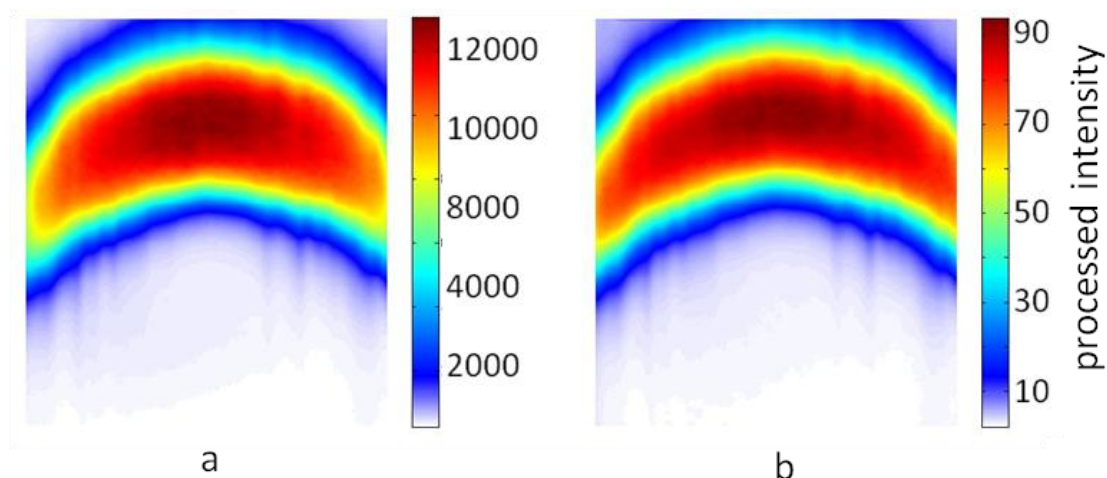


Figure 4.10 Images of processed intensity of plumes from calibration experiment 8 processed to relative concentration. Static images are of fluorescein (a) and colloids (b) taken after 600mL of flushing. Images represent a physical area of 45.3 x 40.3cm.

Calibration experiment 9 (Figure 4.11), conducted on 10/4/07, used exposure times up to 1000s to replicate experiment 8. The flow rate was 160mL/min in the upward direction. RO water flushing of two pore volumes was again used between calibration solutions. A 250mL plume of  $10^1$ ppm fluorescein and colloids was again applied via the inlet tubing at the base of the sand pack and flushed upward at 100mL/min (Figure 4.12). Streaking and inhomogeneity are still evident in the data (Figure 4.12a-e). Colloids were detectable down to  $10^{-1}$ ppm (Figure 4.12h).

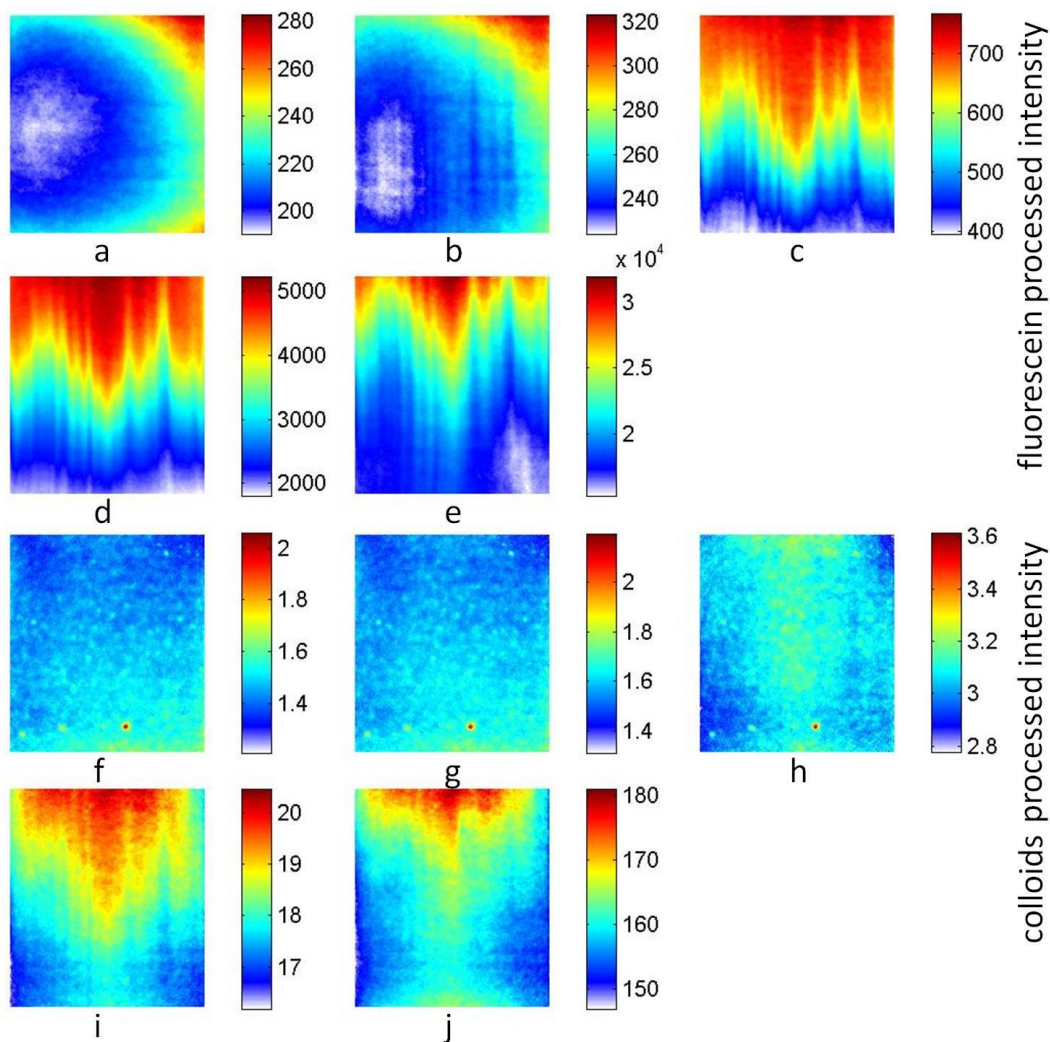


Figure 4.11 Images of processed intensity from calibration experiment 9. Concentrations are  $10^{-3}$  ppm (a, f),  $10^{-2}$  ppm (b, g),  $10^{-1}$  ppm (c, h),  $10^0$  ppm (d, i), and  $10^1$  ppm (e, j). Images represent a physical area of  $45.3 \times 40.3$  cm.

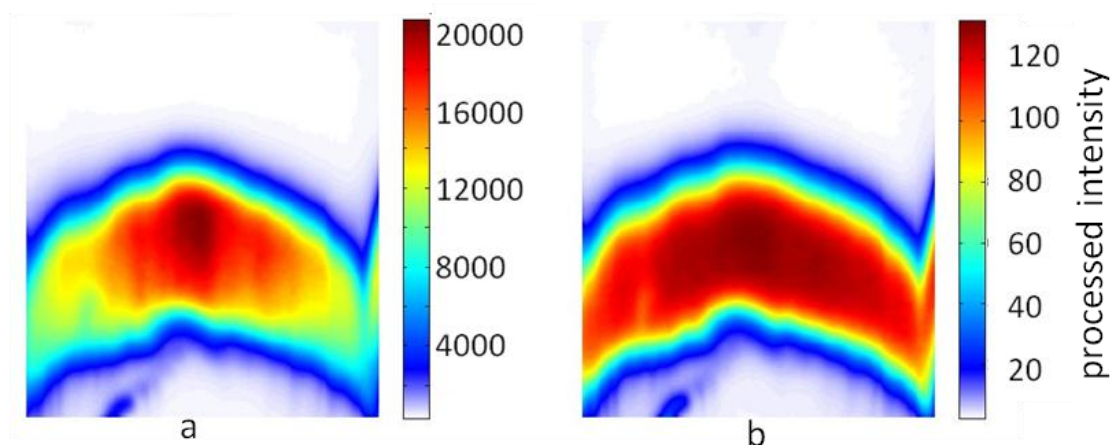


Figure 4.12 Images of processed intensity of plumes from calibration experiment 9. Static images are of fluorescein (a) and colloids (b) taken after 500mL had been pumped upwards after the plume. Images represent a physical area of 45.3 x 40.3cm.

Calibration experiment 10 (Figure 4.13), conducted 10/9/07, was replication of calibration experiments 8 and 9, with exposure time extended to the maximum for full use the camera's dynamic range. Images at a given setting were collected with increasing exposure time until the maximum pixel intensity value lay somewhere between 30,000 and 50,000. Incremental increases of 150% in exposure time made a series (included in Appendix D) that was used to guide imaging. Maximum intensity values were kept under 60,000 to prevent oversaturation and blooming caused by surpassing either the finite (full-well) charge capacity of individual photodiodes or the maximum charge transfer capacity of the CCD. In blooming, charge in excess of a pixel's full-well capacity spills over to adjoining pixels causing an artifact that significantly degrades image quality. Full exposure time was used for all subsequent experiments.

Flow in calibration experiment 10 was upward at 160mL/min. Two pore volumes of calibration solution were flushed through the sand pack at each concentration prior to imaging. Patterns of fluorescein and colloid distribution were variable (Figure 4.13). Colloids were detected at concentrations down to  $10^{-2}$  ppm (Figure 4.13g). After imaging of the last calibration solution, a 3.5L RO water flush at 311mL/min was used to cleanse the sand pack of the last calibration solution. A

250mL plume of  $10^1$ ppm fluorescein and colloids was then applied via the inlet tubing at the base of the sand pack and flushed upward at 160mL/min (Figure 4.14).

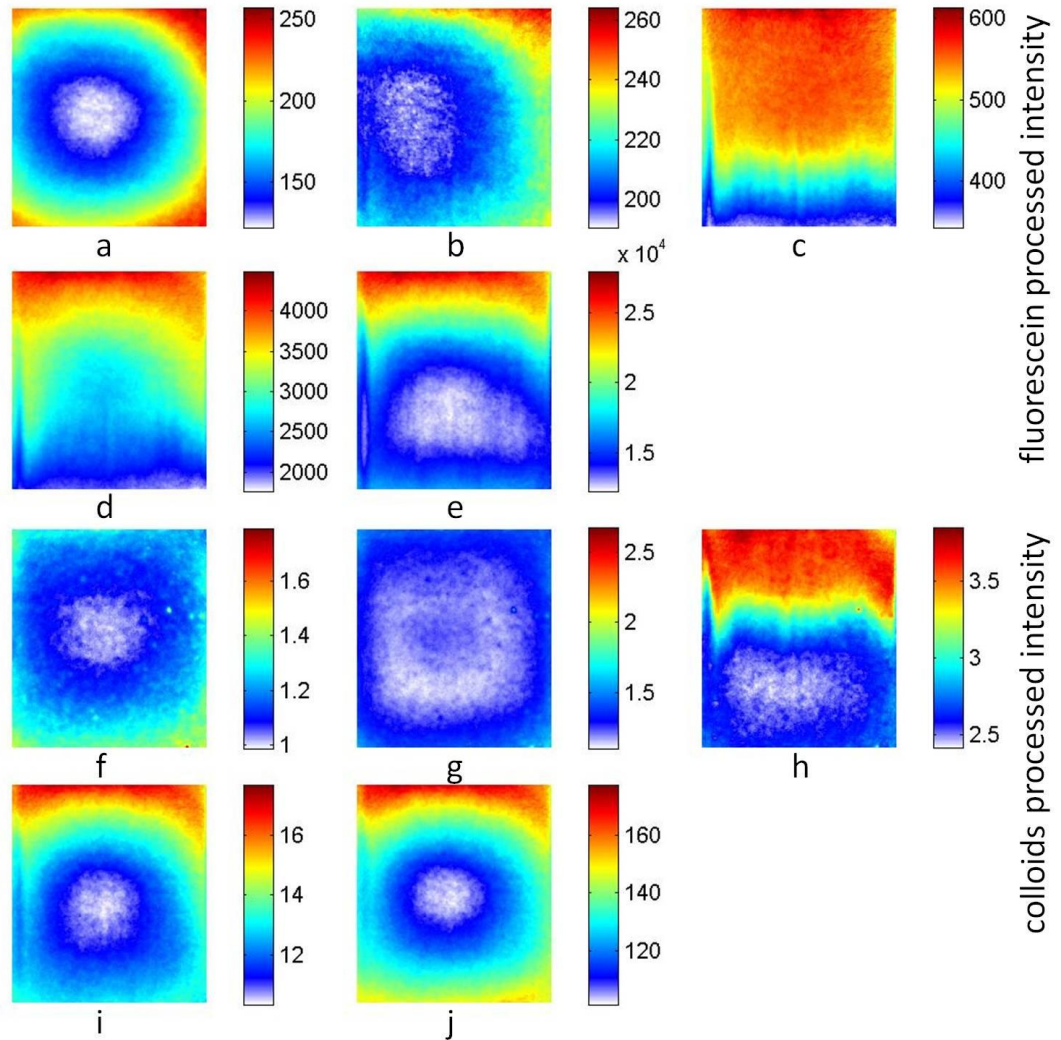


Figure 4.13 Images of processed intensity from calibration experiment 10. Concentrations are  $10^{-3}$  ppm (a, f),  $10^{-2}$  ppm (b, g),  $10^{-1}$  ppm (c, h),  $10^0$  ppm (d, i), and  $10^1$  ppm (e, j). Images represent a physical area of 45.3 x 40.3cm.

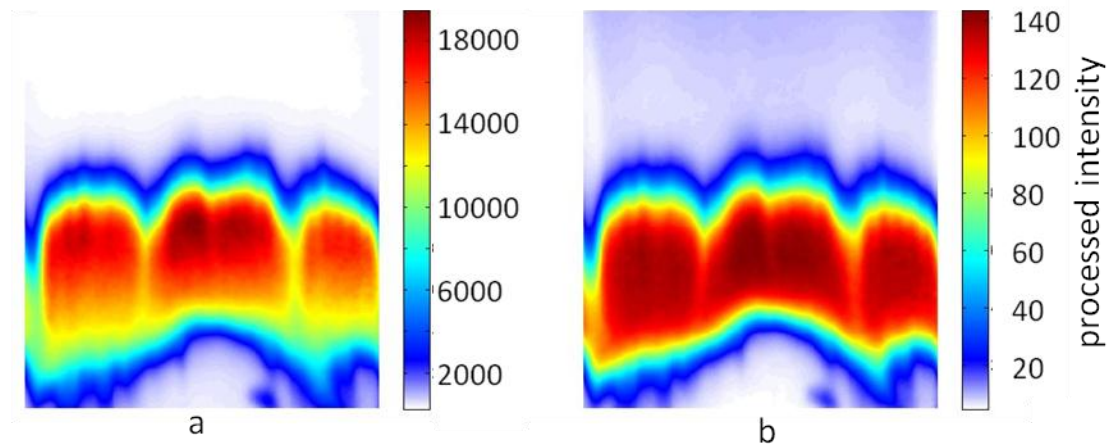


Figure 4.14 Images of processed intensity of plumes from calibration experiment 10. Static images are of fluorescein (a) and colloids (b) taken after 300mL flushing. Images represent a physical area of 45.3 x 40.3cm.

The calibration solutions in uniform-concentration experiments were expected to be distributed evenly through the sand pack, but distributions were repeatedly observed to be heterogeneous. The heterogeneity persisted even in experiments where several pore volumes of calibration solution were recirculated through the sand pack (e.g. Figure 4.13).

Images of processed intensity were divided into nine regions and averages from each region were compared. For calibration experiment 8 (Figure 4.9), the percent error between the average of a region and the average of the entire image was as much as 37% for fluorescein and 8% for colloids. For calibration experiment 9 (Figure 4.11), the maximum error was 52% for fluorescein and 16% for colloids. For calibration experiment 10 (Figure 4.13), the maximum error was 28% for fluorescein and 25% for colloids. The largest variation from the overall average was observed for fluorescein along the bottom of the sand pack. These calculations suggested the need for a different approach to calibration.

It was also believed that higher concentrations of fluorescein and colloids than had been used to this point might be detectable with this system. The uniform-concentration method employed to distribute fluorescein and colloids throughout the sand pack used large volumes of calibration

solution, and was cost-prohibitive for concentrations above  $10^1$  ppm. The plume calibration method was developed to attain data at higher concentrations, and to generate calibration data unaffected by heterogeneity in fluorescein and colloid distribution.

Calibration experiment 11 was conducted on 11/08/07 to determine the upper detection limit for fluorescein and colloids. Plumes of 20ml  $10^1$ ,  $10^2$  and  $10^3$  ppm calibration solutions (Figure 4.15) were applied sequentially to the sand pack using a hypodermic syringe. Images were collected of each calibration solution before the plume was flushed downward with RO water at 160mL/min. The inflow rate was in excess of the outflow rate, which resulted in flooding of the experimental system. The experimental system was disassembled between calibration solutions for investigation of the flooding. This experiment was also marked by poor masking across the upper edge of the sand pack, which was cropped out in processing. Image of fluorescein at  $10^3$  ppm (Figure 4.15a) was marked by occlusion—the center of the plume is the most concentrated but not brightest due to blockage of light. This phenomenon suggests an upper limit to detection.

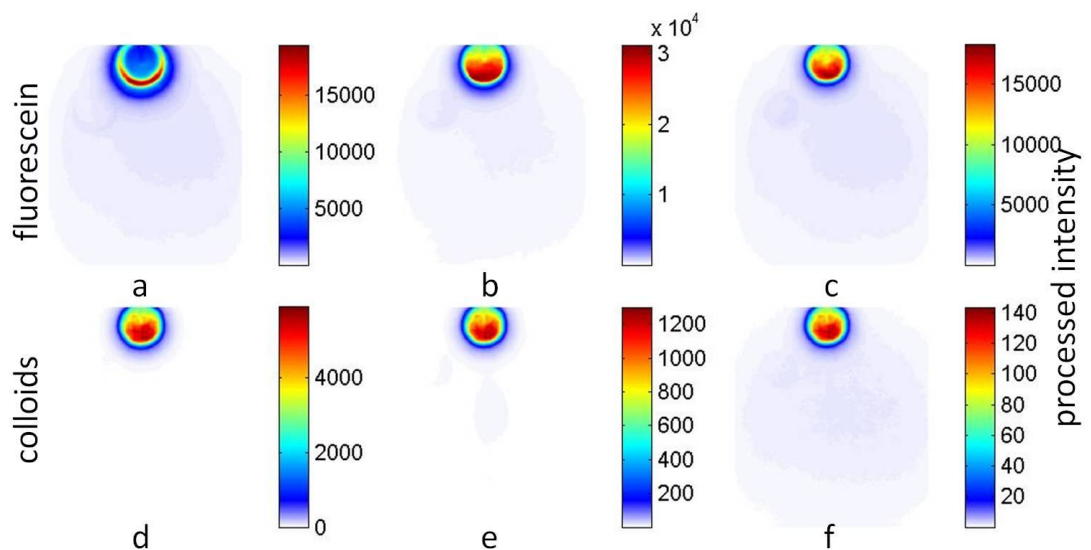


Figure 4.15 Images of processed intensity from calibration experiment 11. Concentrations are  $10^3$  ppm (a, d),  $10^2$  ppm (b, e), and  $10^1$  ppm (c, f). Images represent a physical area of 45.9 x 40.3cm.

Calibration experiment 12 was conducted on 12/03/07 to replicate calibration experiment 11--this time with an effort to curb flooding of the experimental system. Plumes of  $10^1$ ,  $10^2$  and  $10^3$  ppm (Figure 4.16) were applied to the sand pack and flushed downward with RO water. In this experiment the mask had been repaired, but the lower manifold was uneven. These features influenced the length of exposure possible due to light leakage, and were cropped from images during processing. The flow rates in this experiment were adjusted to prevent flooding; however, overcorrection resulted in higher outflow than inflow and subsequent desaturation of the sand pack. This desaturation occurred after imaging of the final plume. Data collection in this experiment was successful, yet inability to maintain a stable downward flow remained a problem. Occlusion of light (reduction of intensity at the center of the plume) by fluorescein concentration at  $10^3$  ppm (Figure 4.16a) indicated the high concentration detection limit for fluorescein in this system.

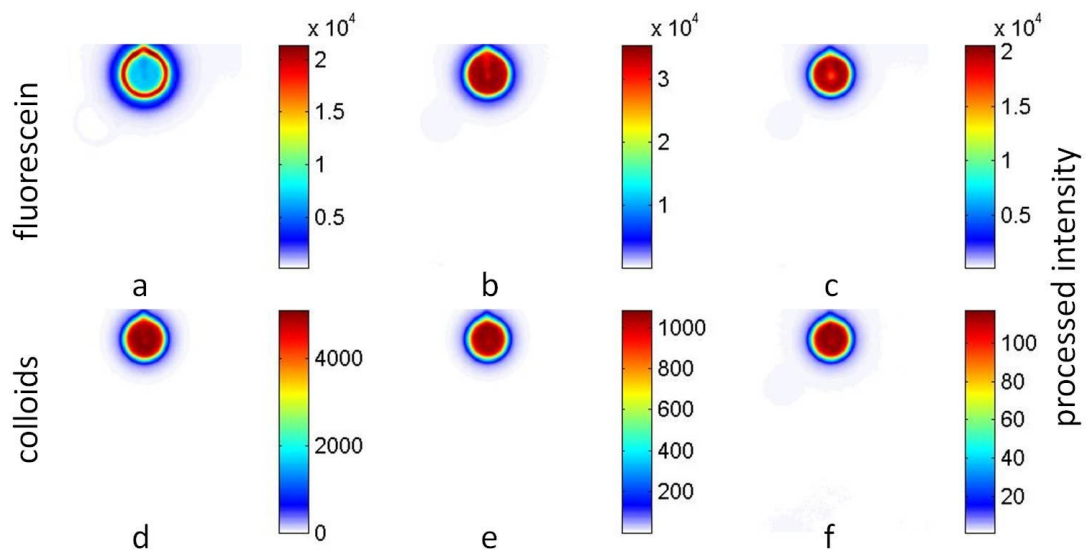


Figure 4.16 Images of processed intensity from calibration experiment 12. Concentrations are  $10^3$  ppm (a, d),  $10^2$  ppm (b, e), and  $10^1$  ppm (c, f). Images represent a physical area of  $46.3 \times 40.3$  cm.

Calibration experiment 13 was conducted on 12/19/07 to pursue the low-concentration detection limit. Calibration solutions used in this experiment ranged in concentration between  $10^{-6}$  and  $10^{-3}$  ppm. The method of uniform-concentration was utilized. Flow was in the upward direction at 160 mL/min.

Collection of initial images showed higher than normal intensity values, which were attributed to imperfect seal of the dark enclosure. Subtraction of dark images containing these elevated intensities was performed to normalize the data. Images of processed intensity (Figure 4.17) indicate that these concentrations are all within or near the noise level of the system. Fluorescein at  $10^{-3}$  ppm (Figure 4.17a) may be slightly detectable from the background noise, suggesting that  $10^{-3}$  ppm is near the lower detection limit for fluorescein, but above the lower limit for colloids. This may, however, be an underestimate of the capabilities of the system as this data set was affected by light leakage.

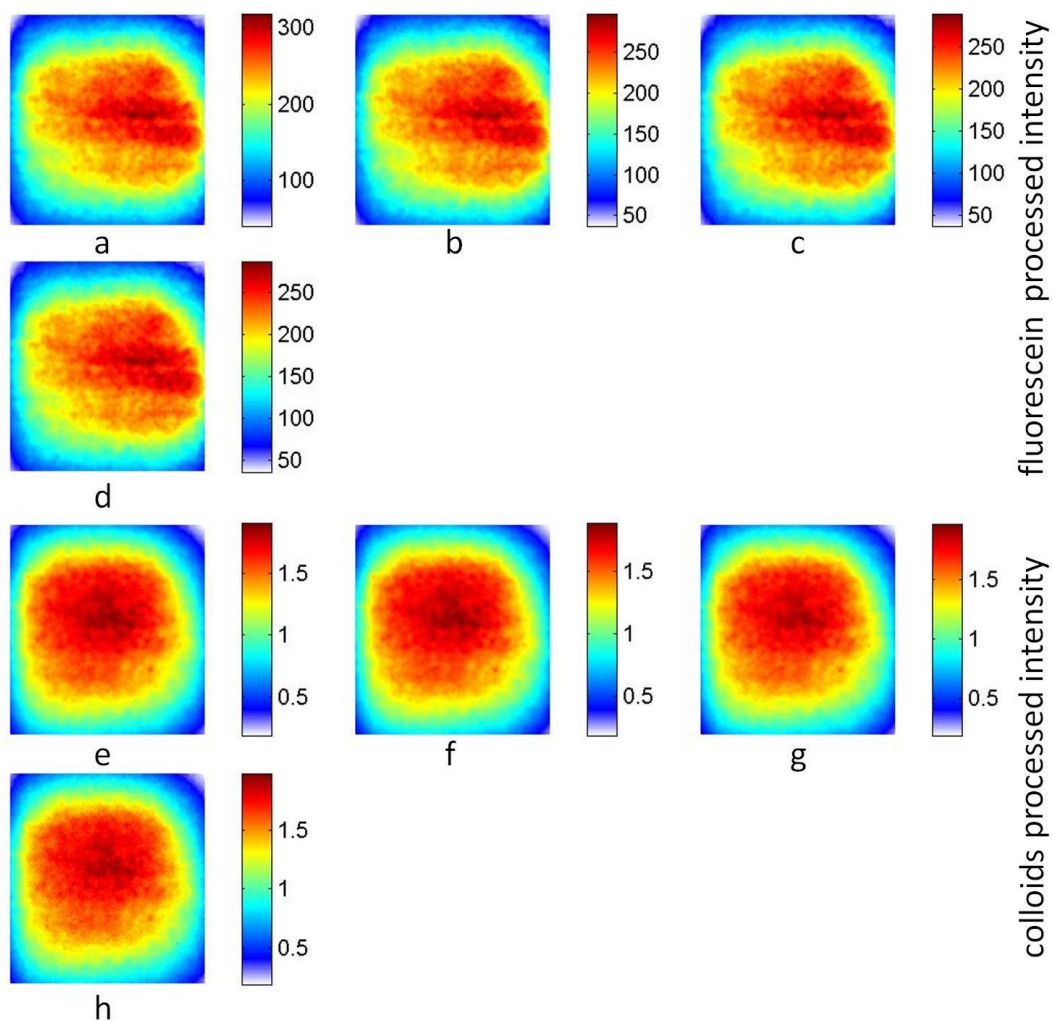


Figure 4.17 Images of processed intensity from calibration experiment 13. Concentrations are  $10^{-3}$  ppm (a, e),  $10^{-4}$  ppm (b, f),  $10^{-5}$  ppm (c, g), and  $10^{-6}$  ppm (d, h). Images represent a physical area of 43.5 x 40.3cm.

Calibration experiment 14, conducted on 1/8/08, was a replicate of calibration experiment 13. The dark enclosure had been repaired for improved light containment. The  $10^{-3}$  ppm concentration (Figure 4.18d,h) is detectable in comparison to calibration experiment 13 (Figure 17). Improved detection of low concentration in this experiment was due to improved light containment and enhancement of the signal to noise ratio.

The saturated images required for normalization of fluorescein calibration data in calibration experiment 14 was saved as an 8-bit image instead of 16-bit, making the image unusable in calibration. A proxy for that required image with slightly different optical settings was used. Experiments to this date used electrical tape to seal the cardboard mask to the glass but the location of the upper margin changed with time as the tape lost adhesion. This irregularity was again cropped out of the data.

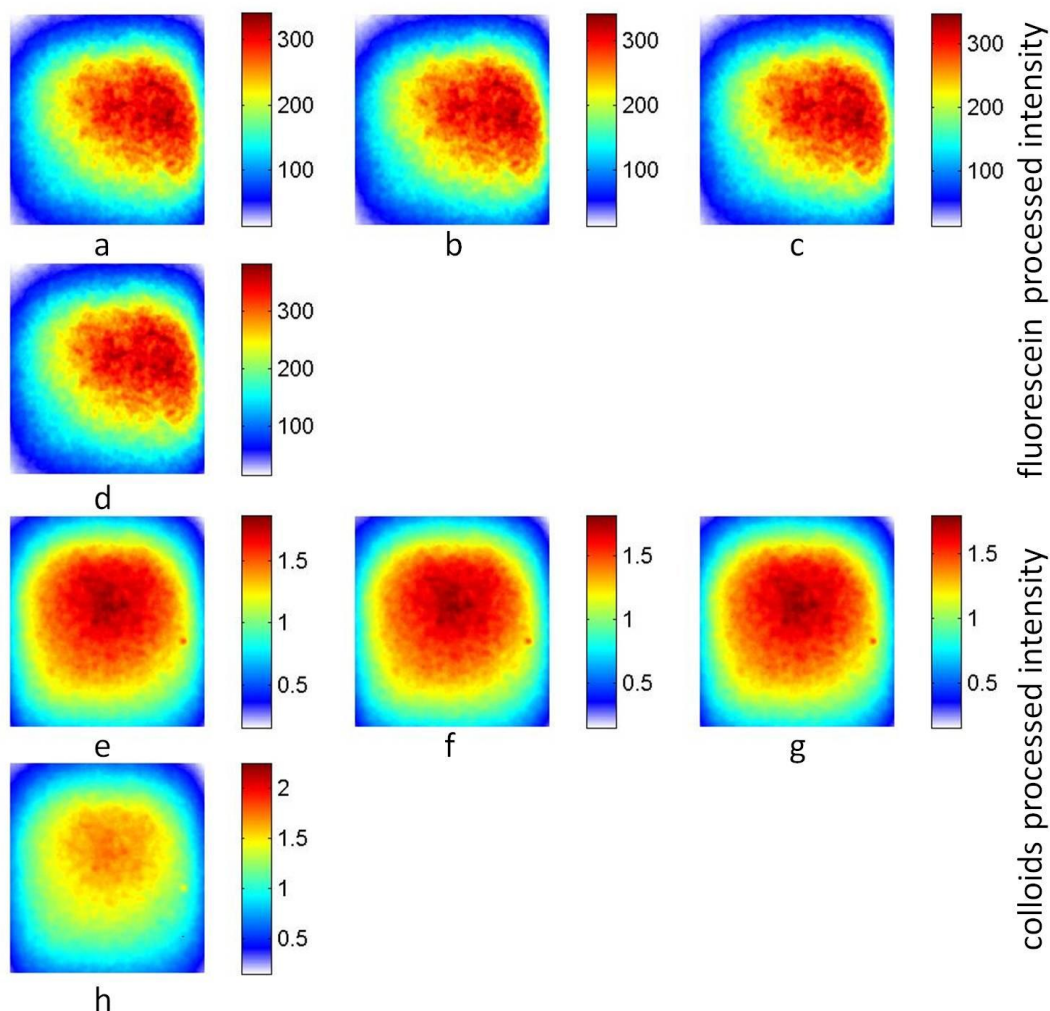


Figure 4.18 Images of processed intensity from calibration experiment 14. Concentrations are  $10^{-6}$  ppm (a, e),  $10^{-5}$  ppm (b, f),  $10^{-4}$  ppm (c, g), and  $10^{-3}$  ppm (d, h). Images represent a physical area of 43.5 x 40.3cm.

A comprehensive set of improvements to the system was made over five months time before the next calibration experiment. The aim of these improvements was to make it possible to collect fluorescein and colloid intensity data from nine calibration solutions ranging from  $10^{-6}$  to  $10^2$  ppm in a single calibration experiment. Improvements included use of higher purity fluorescein, the construction of an improved dark enclosure, optimized focus of the camera lens, the use of a newly designed and fabricated mask and manifold, new fluorescein excitation filters, and bubble traps to remove air bubbles from the fluid lines, initiating the use of a sonicator for dispersing colloids in stock solutions

before pipetting to prepare calibration solutions, the installation of an in-line cell to measure pH and EC in the chamber effluent, and the installation of new steel mesh for the lower manifold, the use of new fluid pump with a dual pump head to control the inflow and outflow simultaneously at the same flow rate, and installation of new Tygon tubing.

Calibration experiment 15 was conducted on 6/29/08 using calibration solutions ranging in concentrations from  $10^{-6}$  to  $10^2$  ppm. Each calibration solution was recirculated eight times in an effort to attain a homogeneous distribution of calibration solution throughout the sand pack. The flow rate was 1 pore volume per ten minutes or 92mL/min, and clean fluid flushing was not used between concentrations. Despite the efforts made to generate homogeneous distribution throughout the sand pack, the images were still marked by uneven fluorescein (Figure 4.19) and colloid (Figure 4.20) distribution, including an unexpected patch of high-concentration colloids (Figure 4.19b). These results reinforced the conclusion that a homogeneous distribution of fluorescein and colloids throughout the sand pack may not be attainable via the uniform-concentration approach. The use of clear tubing was noted as a possible source of error due to non-uniform degradation of fluorescein molecules. Tubing in calibration experiment 15 was covered with tin foil part way through data collection to reduce exposure of calibration solutions to ambient light.

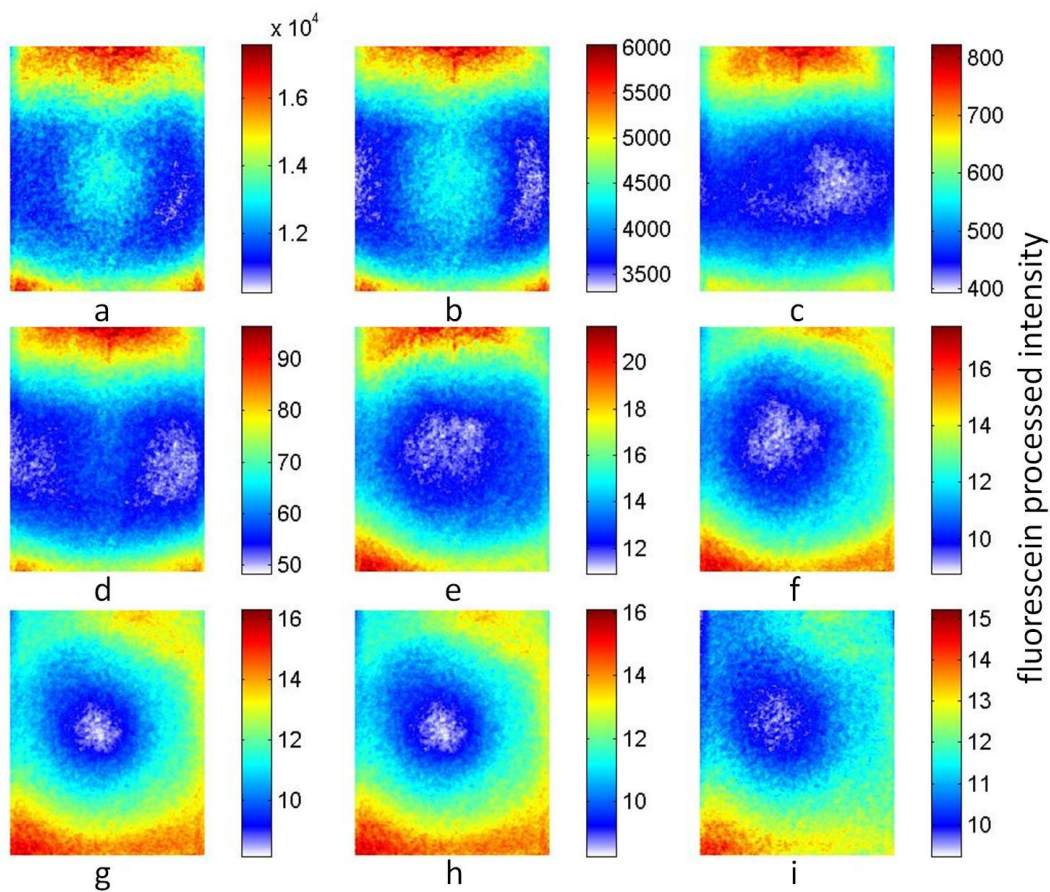


Figure 4.19 Images of fluorescein processed intensity from calibration experiment 15. Concentrations are  $10^2$  ppm (a),  $10^1$  ppm (b),  $10^0$  ppm (c),  $10^{-1}$  ppm (d),  $10^{-2}$  ppm (e),  $10^{-3}$  ppm (f),  $10^{-4}$  ppm (g),  $10^{-5}$  ppm (h), and  $10^{-6}$  ppm (i). Images represent a physical area of 53.8 x 42.6 cm.

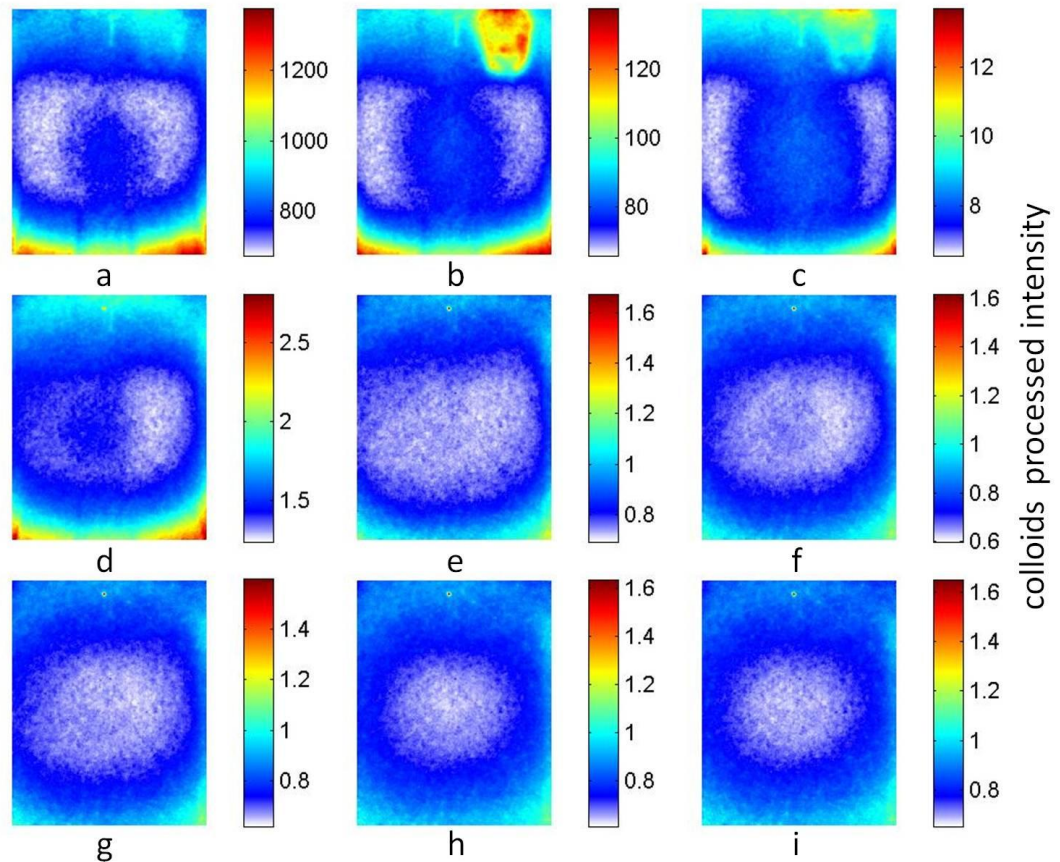


Figure 4.20 Images of colloid processed intensity from calibration experiment 15. Concentrations are  $10^2$  ppm (a),  $10^1$  ppm (b),  $10^0$  ppm (c),  $10^{-1}$  ppm (d),  $10^{-2}$  ppm (e),  $10^{-3}$  ppm (f),  $10^{-4}$  ppm (g),  $10^{-5}$  ppm (h), and  $10^{-6}$  ppm (i). Images represent a physical area of 53.8 x 42.6cm.

Flushing with RO water followed the highest concentration calibration solution, after which a single 20mL plume of  $10^1$  ppm fluorescein and colloids was applied to the sand pack (Figure 4.21). The plume appears as a ring due to RO water being pushed through the application tubing prior to imaging. Data were cropped to exclude residual  $10^1$  ppm fluorescein and colloids in the sand pack from the calibration solution (Figures 4.19a and 4.20a) used prior to plume application. Evidence of the unexpected colloid patch is visible in the colloid plume image (Figure 4.21b).

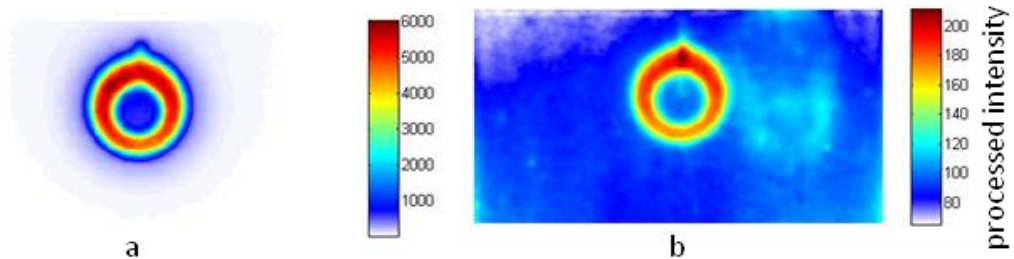


Figure 4.21 Images of processed intensity Processed plume images from calibration experiment 15. 20mL of  $10^1$ ppm fluorescein and colloids were imaged to view (a) fluorescein and (b) colloids. Images represent a physical area of 16.8 x 42.4cm.

Calibration experiment 16 was conducted on 2/25/09 using plumes of calibration solution applied in triplicate (Figures 4.22 and 4.23). Plumes of seven calibration solutions with concentrations ranging from  $10^{-4}$  to  $10^2$ ppm were applied sequentially via specially constructed application tubing.

Downwards flushing with clean fluid was performed in between each set of plumes.

The flow rate was reduced to 10mL/min, and bubble traps were removed due to poor performance.

Calibration experiment 16 was conducted eight months after completion of calibration experiment 15, and the prepared dry sand pack stood packed for three months prior to saturation. The delay was caused by failure of the camera chiller, whereby the temperature of the chip was rising above desired levels, resulting in data aberration. Once this problem was corrected, data collection was begun.

Maintenance of a constant head was challenging in calibration experiment 16. Buffer was added repeatedly to the headspace above the sand pack to prevent desaturation. This was the first experiment in which all chamber parts were acid washed to eliminate fluorescence from residual soap films. This experiment also utilized a new relay for improved control of the LEDs, new opaque tubing, and 5mM phosphate buffer as the clean fluid.

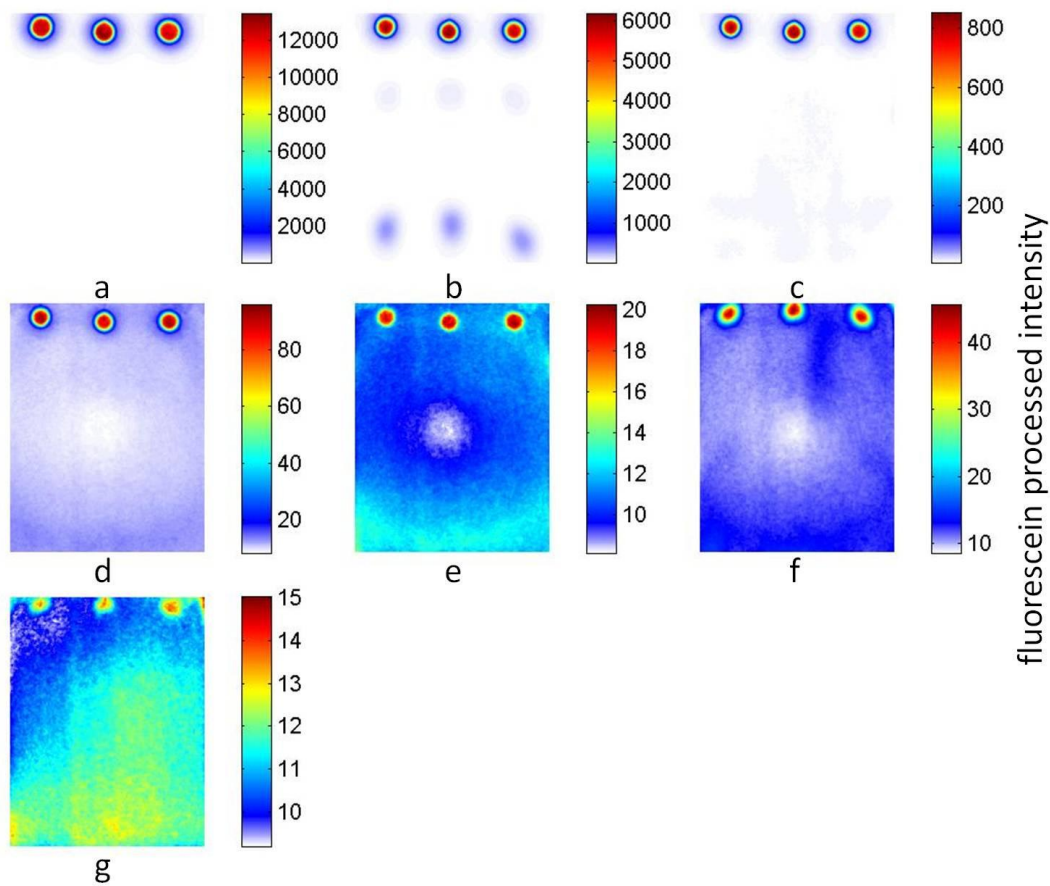


Figure 4.22 Images of fluorescein processed intensity from calibration experiment 16. Concentrations are  $10^2$  ppm (a),  $10^1$  ppm (b),  $10^0$  ppm (c),  $10^{-1}$  ppm (d),  $10^{-2}$  ppm (e),  $10^{-3}$  ppm (f), and  $10^{-4}$  ppm (g). Images represent a physical area of 54.1 x 42.4cm.

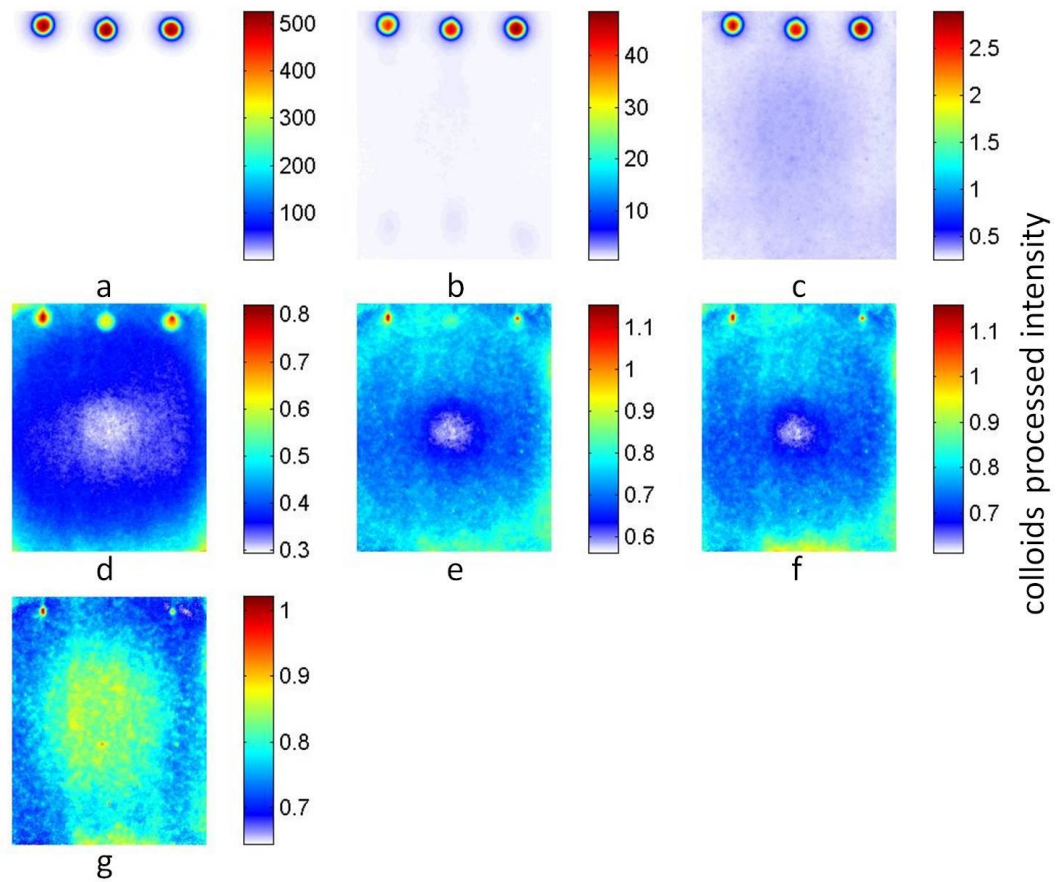


Figure 4.23 Images of colloid processed intensity from calibration experiment 16. Concentrations are  $10^2$  ppm (a),  $10^1$  ppm (b),  $10^0$  ppm (c),  $10^{-1}$  ppm (d),  $10^{-2}$  ppm (e),  $10^{-3}$  ppm (f), and  $10^{-4}$  ppm (g). Images represent a physical area of 54.1 x 42.4cm.

Calibration experiment 17 was conducted on 7/7/09. Four months passed between calibration experiments 16 and 17 due to problems maintaining the seal on the chamber containing the sand pack. Multiple sand packs during this time had to be repacked due to incomplete saturation and flooding of the experimental system. In an effort to prevent failed saturation, a drying system was devised to remove water films from the pack volume after a water fill of the assembled system without sand. This water fill allowed for checking of the seal before packing, which was made possible only by complete drying of the chamber after the check. A shaking table was also constructed to evenly agitate calibration solutions in a darkened cooler to keep calibration solutions in optimal condition during the long process of data collection.

Despite all precautions and improvements to the system and experimental protocol, images were still marked by confounding and unexpected artifacts. Bleeding of fluorescein from chamber parts was observed and caused significant delays in application of calibration solutions. Significant flushing of buffer through the sand pack was performed between calibration solutions in an effort to rid the system of the unanticipated fluorescein.

Plumes were applied in triplicate at increasing concentrations and flushed downwards at 10mL/min, as in experiment 16. Seven calibration solutions were used for fluorescein (Figure 4.24). High concentration areas in panel (g) are a result of fluorescein bleeding from chamber parts. Eight calibration solutions were used for colloids (Figure 4.25), as significant occlusion by colloids had not been observed in previous experiments as it had for fluorescein (Figure 4.15a, Figure 4.16a). It was thought the upper detection limit was higher for colloids than for fluorescein. The sand pack, however, was desaturated to below the plume application tubing before application of the highest concentration ( $10^3$  ppm) calibration solution. The capillary fringe was visible as a discontinuity in colloid processed intensity in Figure 4.25a.

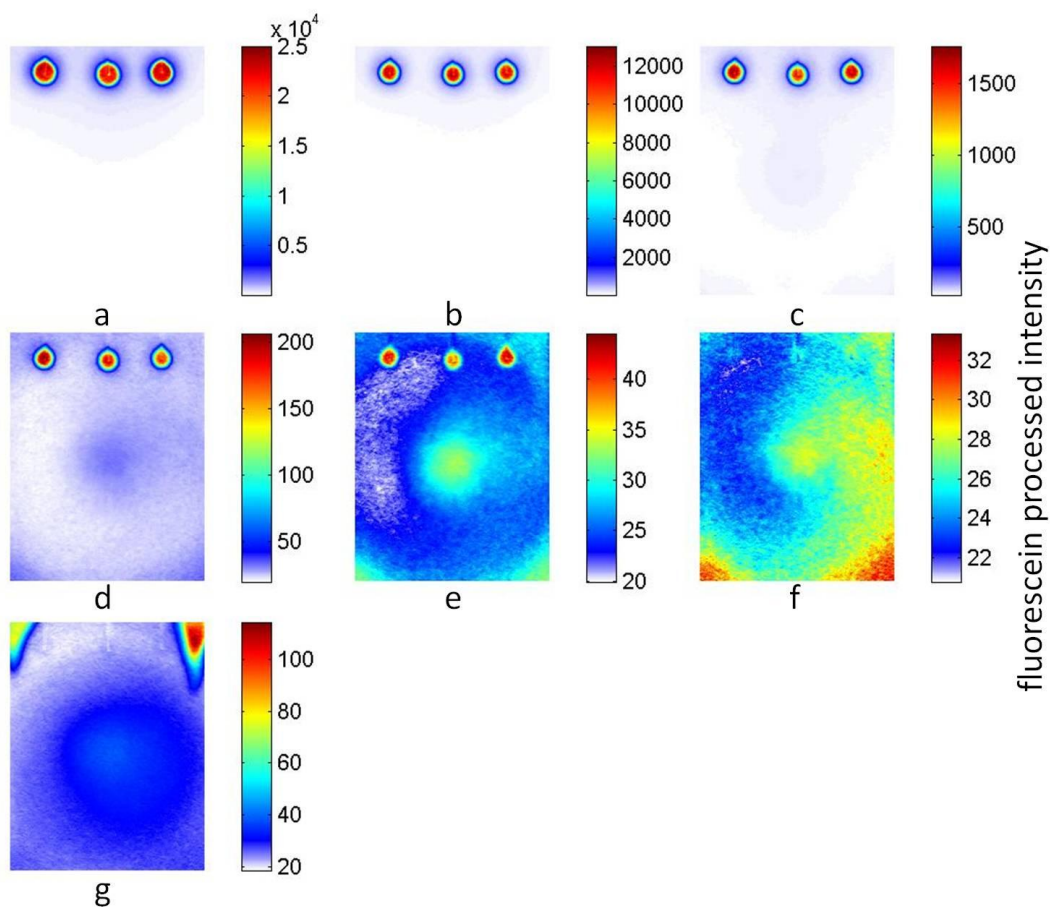


Figure 4.24 Images of processed intensity fluorescein from calibration experiment 17. Concentrations are  $10^2$  ppm (a),  $10^1$  ppm (b),  $10^0$  ppm (c),  $10^{-1}$  ppm (d),  $10^{-2}$  ppm (e),  $10^{-3}$  ppm (f), and  $10^{-4}$  ppm (g). Images represent a physical area of 54.1 x 42.4cm.

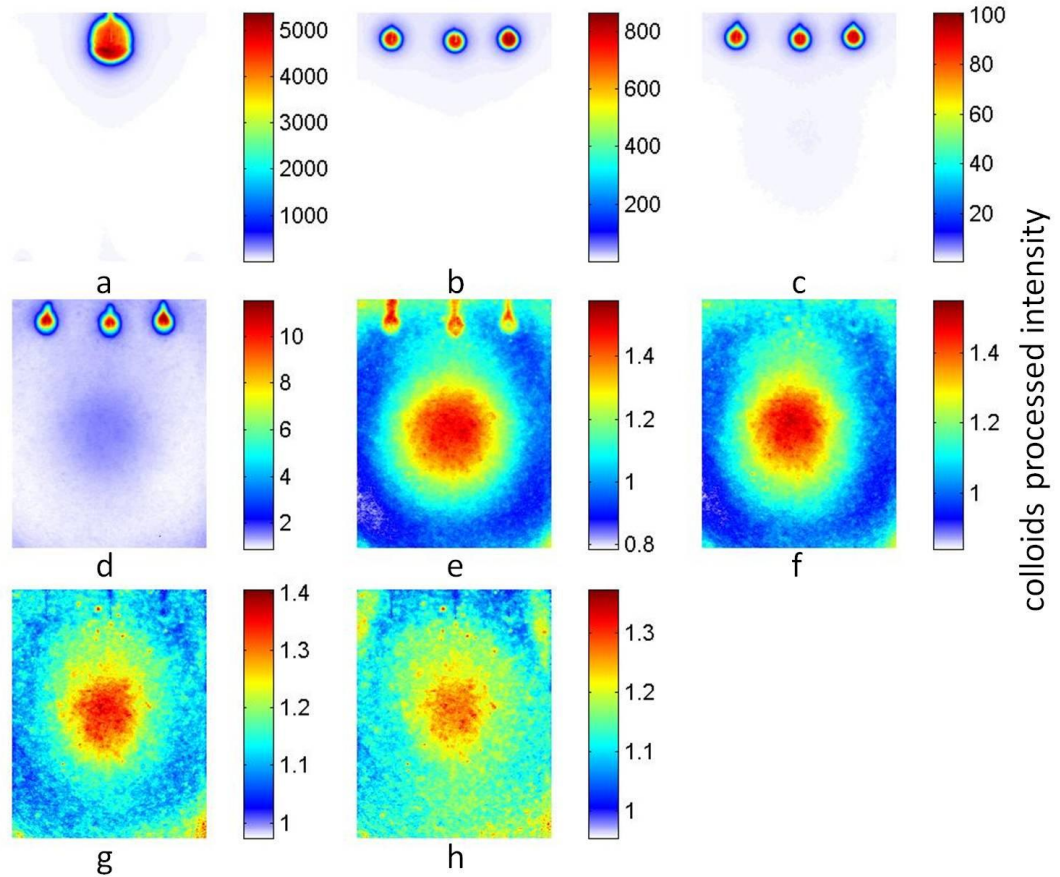


Figure 4.25 Images of colloid processed intensity from calibration experiment 17. Concentrations are  $10^3$  ppm (a),  $10^2$  ppm (b),  $10^1$  ppm (c),  $10^0$  ppm (d),  $10^{-1}$  ppm (e),  $10^{-2}$  ppm (f),  $10^{-3}$  ppm (g), and  $10^{-4}$  ppm (h). Images represent a physical area of 54.1 x 42.4cm.

### ***Statistics of Processed Intensities***

Data points used to generate a relationship between fluorescent intensity and fluorescein or colloid concentration were extracted from images of processed intensity ( $\hat{I}$ ). The values extracted from images were the statistics from the processed intensities ( $\hat{I}$ ) that best represented the actual physical concentration. The approach to choosing a statistic representative of the processed intensities was different for uniform-concentration calibration data and plume calibration data. For uniform-concentration calibration images, the mean value of the processed intensity image was used. For plume calibration images, the maximum value of the processed intensity image was used.

***Calibration Experiment Summary***

A summary of all calibration experiments is in Table 4.1.

Table 4.1 Summary of experimental details pertinent to data comparison. Color coding distinguishes similarities and differences among experiments.

calibration experiment	lowest concentration (ppm)	highest concentration (ppm)	number of calibration solutions	exposure time	calibration type	dye flow through	flow direction	clean fluid flushing	flow rate (cm/s)	optical filter version	light mask version	manifold version	buffer grade	sand grade	data set quality	plumes applied
1	10 <sup>-3</sup>	10 <sup>1</sup>	3	low	uniform concentration	2 pore volumes	up	no	0.182	1	old	1	no	30/40	no saturated image, poor dark image	no
2	10 <sup>-4</sup>	10 <sup>0</sup>	3	low	uniform concentration	2 pore volumes	up	no	0.182	1	old	2	no	30/40	poor dark image	no
3	10 <sup>-3</sup>	10 <sup>1</sup>	3	low	uniform concentration	2 pore volumes	up	5 pore volumes	0.182	1	old	2	no	30/40	full	no
4	10 <sup>-3</sup>	10 <sup>1</sup>	3	low	uniform concentration	2 pore volumes	up	2 pore volumes	0.182	2	old	2	no	30/40	full	no
5	10 <sup>-3</sup>	10 <sup>1</sup>	3	low	uniform concentration	2 pore volumes	up	no	0.182	2	old	2	no	30/40	full	no
6	10 <sup>-3</sup>	10 <sup>1</sup>	3	low	uniform concentration	2 pore volumes	up	no	0.182	2	old	2	no	30/40	full	no
7	10 <sup>-3</sup>	10 <sup>1</sup>	5	low	uniform concentration	2 pore volumes	up	2 pore volumes	0.182	2	old	2	no	30/40	full	yes
8	10 <sup>-3</sup>	10 <sup>1</sup>	5	med	uniform concentration	2 pore volumes	up	1 pore volume	0.182	2	old	2	no	30/40	full	yes
9	10 <sup>-3</sup>	10 <sup>1</sup>	5	med	uniform concentration	2 pore volumes	up	1 pore volume	0.182	2	old	2	no	30/40	full	yes
10	10 <sup>-3</sup>	10 <sup>1</sup>	5	full	uniform concentration	2 pore volumes	up	2 pore volumes	0.182	2	old	2	no	30/40	full	yes
11	10 <sup>1</sup>	10 <sup>3</sup>	3	full	single plume	n/a	down	2 pore volumes	0.182	2	old	2	no	30/40	full	yes
12	10 <sup>1</sup>	10 <sup>3</sup>	3	full	single plume	n/a	down	2 pore volumes	0.182	2	old	2	no	30/40	full	yes
13	10 <sup>-6</sup>	10 <sup>-3</sup>	4	full	uniform concentration	2 pore volumes	up	no	0.182	2	old	2	no	30/40	full	no
14	10 <sup>-6</sup>	10 <sup>-3</sup>	4	full	uniform concentration	2 pore volumes	up	1 pore volume	0.182	2	old	2	no	30/40	poor saturated image for	no
15	10 <sup>-6</sup>	10 <sup>2</sup>	9	full	uniform concentration	8 pore volumes	up	no	0.104	3	new	3	no	30/40	full	yes
16	10 <sup>-4</sup>	10 <sup>2</sup>	7	full	triplicate plume	n/a	down	1 pore volume	0.011	3	new	3	yes	30/40	full	yes
17	10 <sup>-4</sup>	10 <sup>3</sup>	7 (fluorescein) 8 (colloids)	full	triplicate plume	n/a	up	0.5 pore volume	0.011	3	new	3	yes	20/30 acid-wash	full	yes

Statistics of processed intensities (-) for fluorescein (Figure 4.26) and colloids (Figure 4.27) were plotted against known concentrations (ppm). Viewing fluorescein or colloid calibration data from all experiments on a single plot illustrates the overall reproducibility of the system. There is a general trend in the data between statistics of processed intensity and concentration. Variation in intensity of low concentrations is indicative noise in the experimental system which changed over the set of experiments. This variation in background noise is accounted for in calibration.

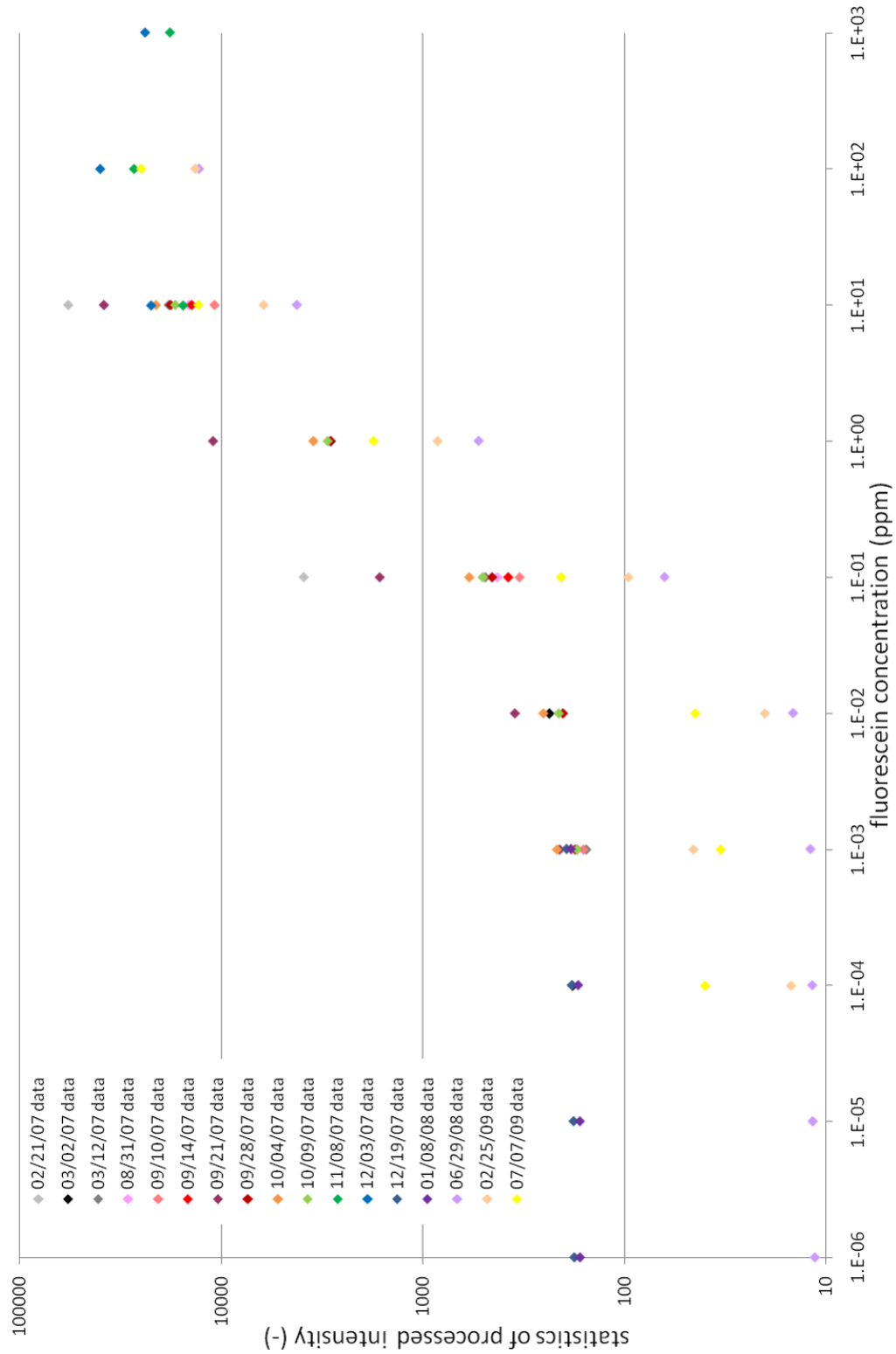


Figure 4.26 Fluorescein statistics of processed intensities from all 17 calibration experiments plotted against known concentration.

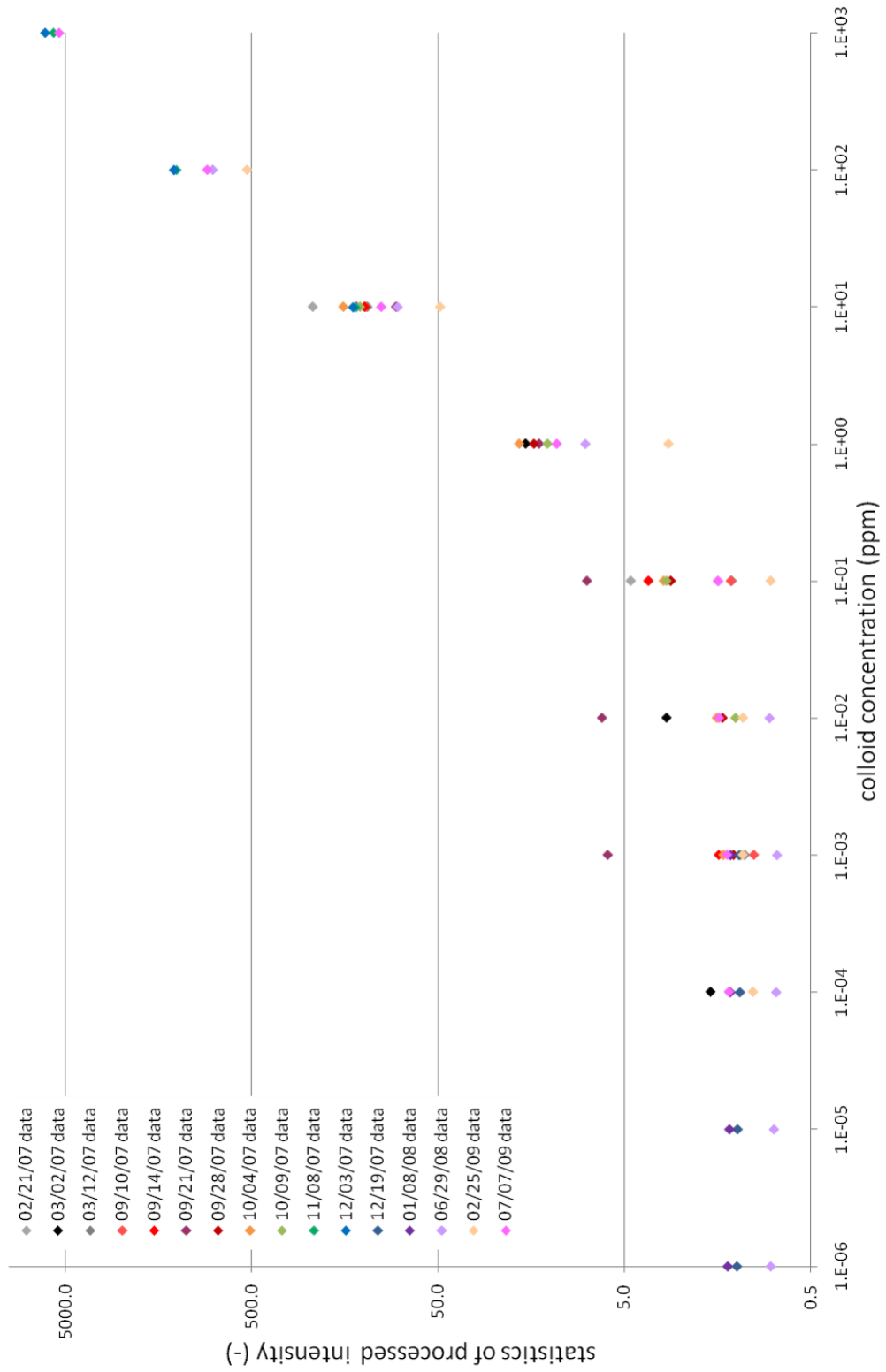


Figure 4.27 Colloid statistics of processed intensities from all 17 calibration experiments plotted against known concentration.

### **Calibration Functions**

Niemet and Selker [2001] previously developed a calibration equation for water content of the form:

$$\theta = \left( \frac{(\hat{I}_{630\text{nm}}/\hat{I}_{\text{sat},630\text{nm}}) - (\hat{I}_{\text{dry},630\text{nm}}/\hat{I}_{\text{sat},630\text{nm}})}{1 - (\hat{I}_{\text{dry},630\text{nm}}/\hat{I}_{\text{sat},630\text{nm}})} \right) \phi \quad (10)$$

where  $\theta(-)$  is the volumetric water content,  $\hat{I}_{630\text{nm}}(-)$  is the processed intensity at 630nm,  $\hat{I}_{\text{sat},630\text{nm}}(-)$  is the processed intensity of the saturated sand pack at 630nm,  $\hat{I}_{\text{dry},630\text{nm}}(-)$  is the processed intensity of the dry sand pack at 630nm, and  $\phi(-)$  is the porosity. Two additional calibration equations were developed.

The statistics of processed intensity ( $\hat{I}$ ) for fluorescein and colloids were described as a function of concentration (ppm) by a linear calibration model with an exponential term, which accounts for the decrease of intensity by occlusion at high concentration. The linear relationship (11) and Beer's Law (12) [DeRose and Kramer, 2005] were combined to produce the calibration model (13):

$$\hat{I} = mC + b \quad (11)$$

$$(I/I_0) = \exp(-C\epsilon l) \quad (12)$$

$$\hat{I} = b + mC\exp(-C/a) \quad (13)$$

where  $\hat{I}(-)$  is the statistic of processed intensity,  $b(-)$  is the y axis intercept,  $m(\text{ppm}^{-1})$  is the slope,  $C(\text{ppm})$  is the calibration solution concentration, and  $a(\text{ppm})$  is an occlusion parameter.  $a$  corresponds to the  $1/\epsilon l$  in Beer's Law where  $\epsilon$  ( $\text{ppm}\cdot\text{cm})^{-1}$  is the absorption coefficient<sup>3</sup> and  $l$  (cm) is the path length (a constant value).  $b$ , as mentioned previously, corresponds to the noise threshold of the system.

---

<sup>3</sup> The value reported for  $\epsilon$  for fluorescein at 491nm is  $8.71 \times 10^4$  ( $\text{kg}/\text{mol}\cdot\text{cm}$ ) [DeRose and Kramer (2005)].

The calibration model was fit to statistics of processed intensities from two experiments—the last one conducted using the uniform-concentration method (calibration experiment 15), and the last one conducted using the plume method (calibration experiment 17). These data sets were collected with the optimized system. A set of parameters was optimized to fit the calibration model to fluorescein statistics of processed intensities and colloid statistics of processed intensities for the two data sets. Equation 13 is used to predict intensity values based on known concentrations in the range  $10^{-3}$  to  $10^2$  ppm. The intercept parameter (b) was set to the value of the minimum statistic of processed intensity for the given data set. The slope (m) and occlusion (a) parameters for the model were fit to the statistics of processed intensities using Excel's solver to minimize the sum of squared error between the statistics of processed intensities and the model. Figure 4.28 shows the model results. Fluorescein and colloids (symbols) are plotted together for each of the two calibration experiments. Also on the plots are the calibration model (solid line, Equation 13), the linear model (broken line, Equation 11), and a table of parameter values used in the models.

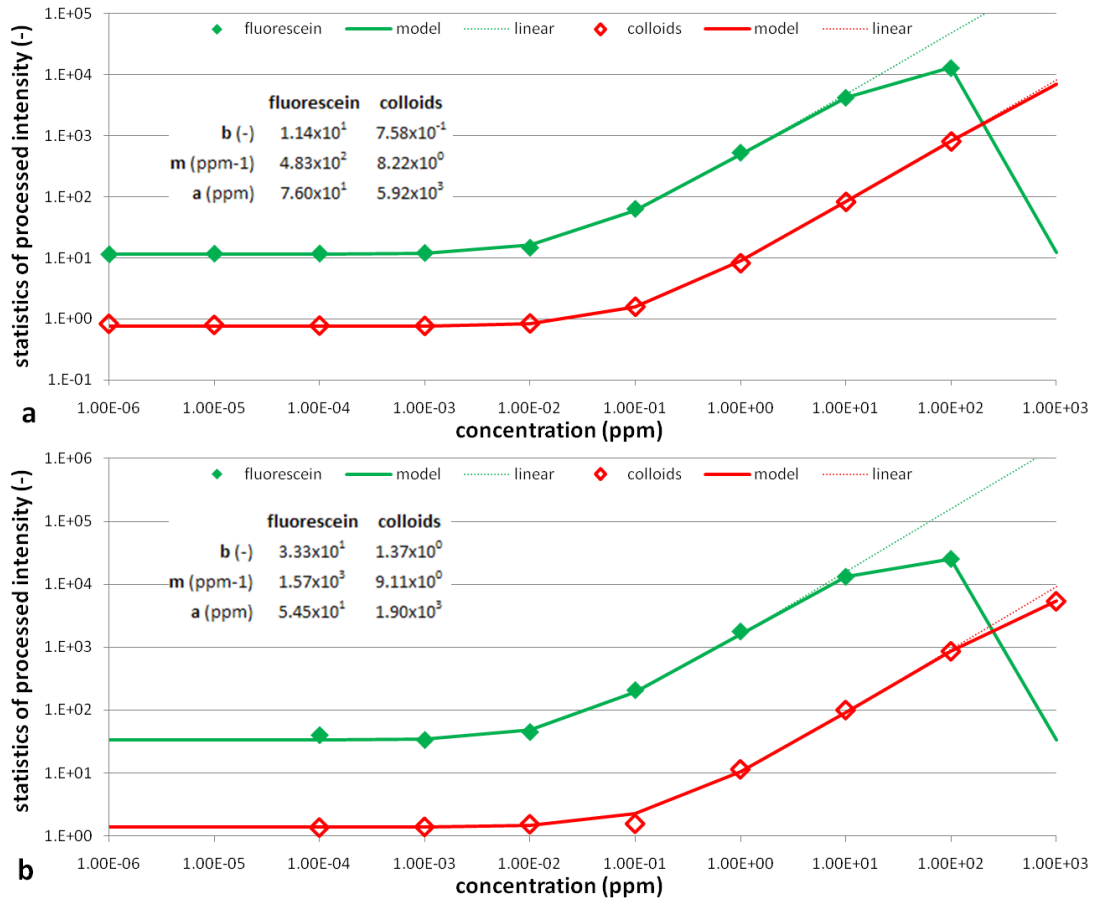


Figure 4.28 Model fitting to statistics of measured intensities from calibration experiment 15 (a) and calibration experiment 17 (b).

Figure 4.29 shows the model fitting for fluorescein data from two experiments separate from colloid data for the two data sets.

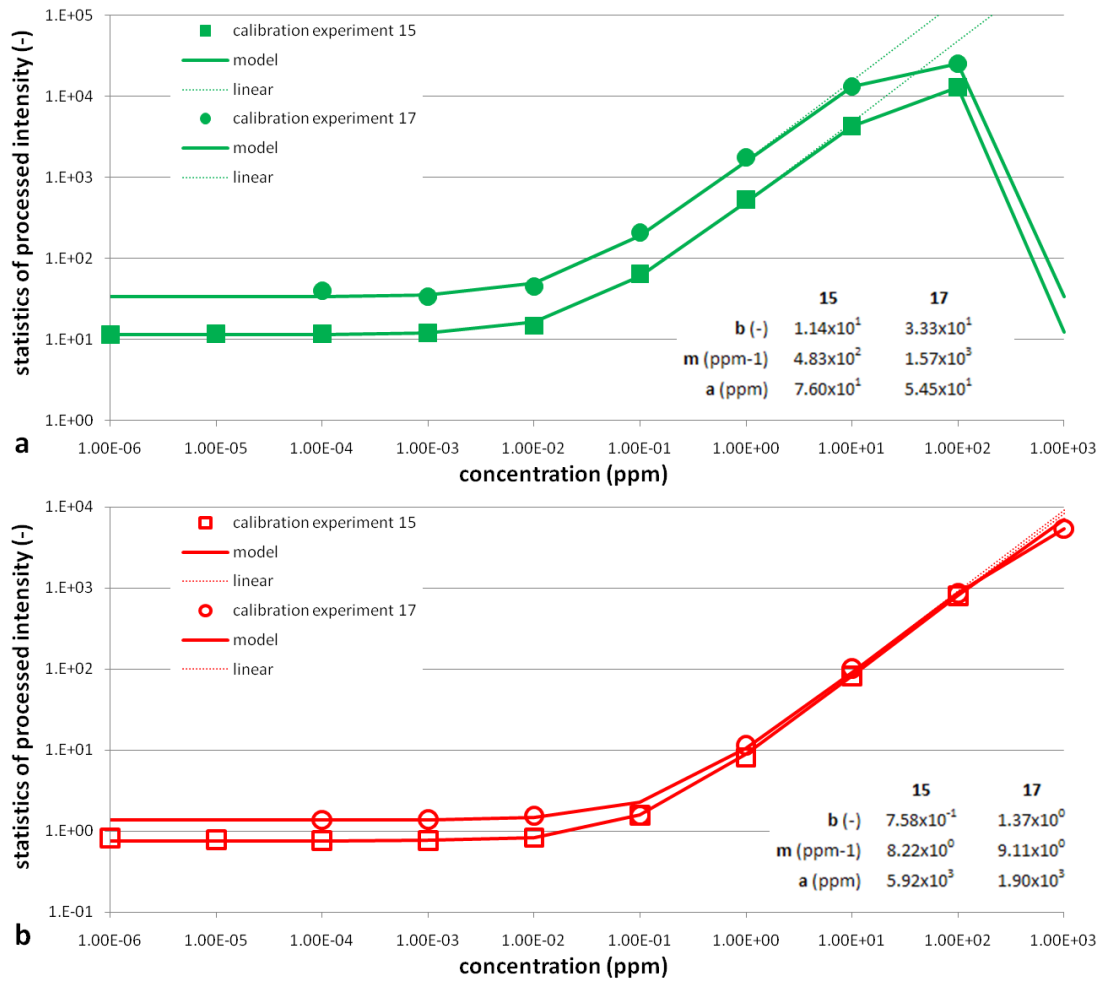


Figure 4.29 Model fitting to statistics of measured intensities for fluorescein (a) and colloids (b).

The optimized fitting parameters are shown in Table 4.2 with statistics from goodness of fit analysis.

The goodness of fit was determined using the coefficient of determination ( $R^2$ ), which is defined as:

$$R^2 = 1 - \frac{SS_{err}}{SS_{tot}} \quad (14)$$

using

$$SS_{err} = \sum_i (y_i - f_i)^2 \quad (15)$$

$$SS_{tot} = \sum_i (y_i - \bar{y})^2 \quad (16)$$

where  $y_i$  are the data values,  $f_i$  is the model values.  $\bar{y}$  is the mean value of the data defined as:

$$\bar{y} = \frac{1}{n} \sum_{i=1}^n y_i \quad (17)$$

where n is the number of data values.

Table 4.2 Estimated parameters for three calibration experiments with coefficients of determination.

calibration experiment	fluorescein parameters			goodness of fit		colloid parameters			goodness of fit	
	b(-)	m(ppm <sup>-1</sup> )	a(-)	R <sup>2</sup>	n	b(-)	m(ppm <sup>-1</sup> )	a(-)	R <sup>2</sup>	n
15	1.14x10 <sup>1</sup>	4.83x10 <sup>2</sup>	7.60x10 <sup>1</sup>	1.000	9	7.58x10 <sup>-1</sup>	8.22x10 <sup>0</sup>	5.92x10 <sup>3</sup>	1.000	9
17	3.33x10 <sup>1</sup>	1.57x10 <sup>3</sup>	5.45x10 <sup>1</sup>	1.000	7	1.37x10 <sup>0</sup>	9.11x10 <sup>0</sup>	1.90x10 <sup>3</sup>	1.000	8

The purpose of system calibration, stated in Equations (10) and (8), was to generate a function by which fluorescein concentration and colloid concentration could be mapped from experimental processed intensity images. No explicit solution to Equation (13) was found. Therefore, each set of parameters was used to create a “lookup table” for use in computation of fluorescein concentration and colloid concentration images from images of processed intensities. The “lookup tables” were generated in MatLab using linear interpolation. “Lookup tables” were applied to processed intensity images of 1x10<sup>1</sup>ppm calibration solutions from calibration experiment 15 (Figure 4.30) and calibration experiment 17 (Figure 4.31). These images of fluorescein and colloid concentration are cropped to a 17 x 42cm area corresponding to the middle region of Figure 4.19b and Figure 4.20b and the top region of Figure 4.25bFigure 4.26c.

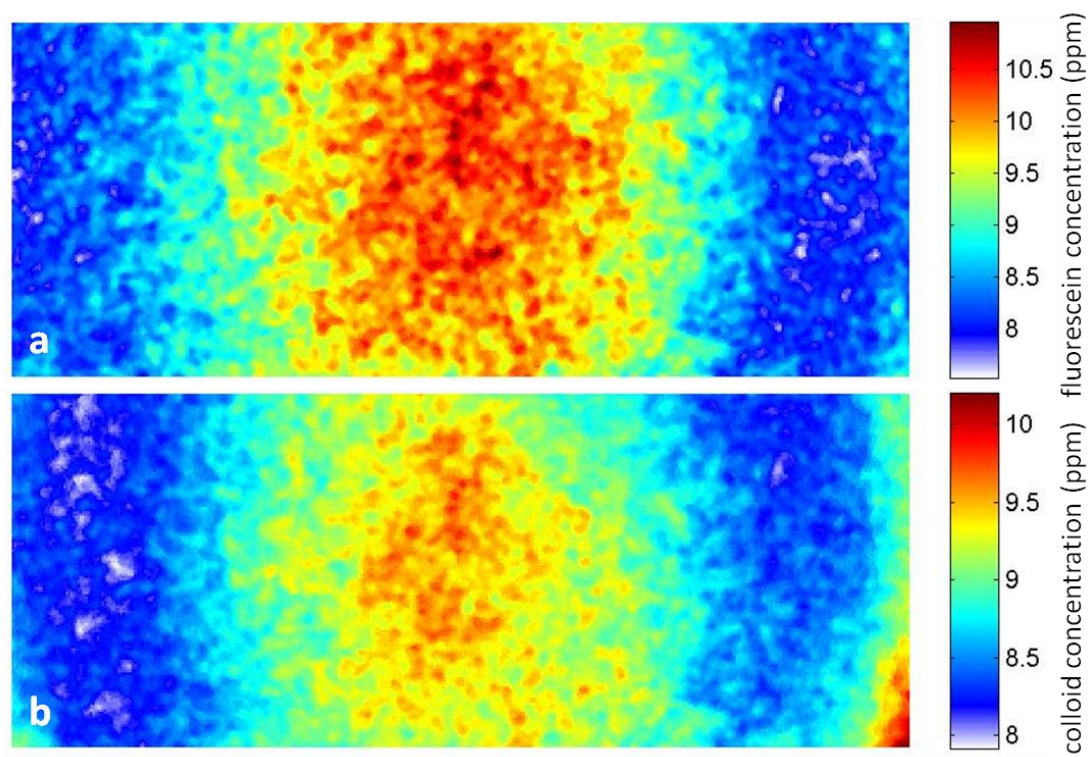


Figure 4.30 Fluorescein (a) and colloid (b) concentration values for  $1 \times 10^1$  ppm calibration solutions from calibration experiment 15 computed using derived calibration functions and fitted parameters. Images represent a physical area of 16.7 x 42.4 cm.

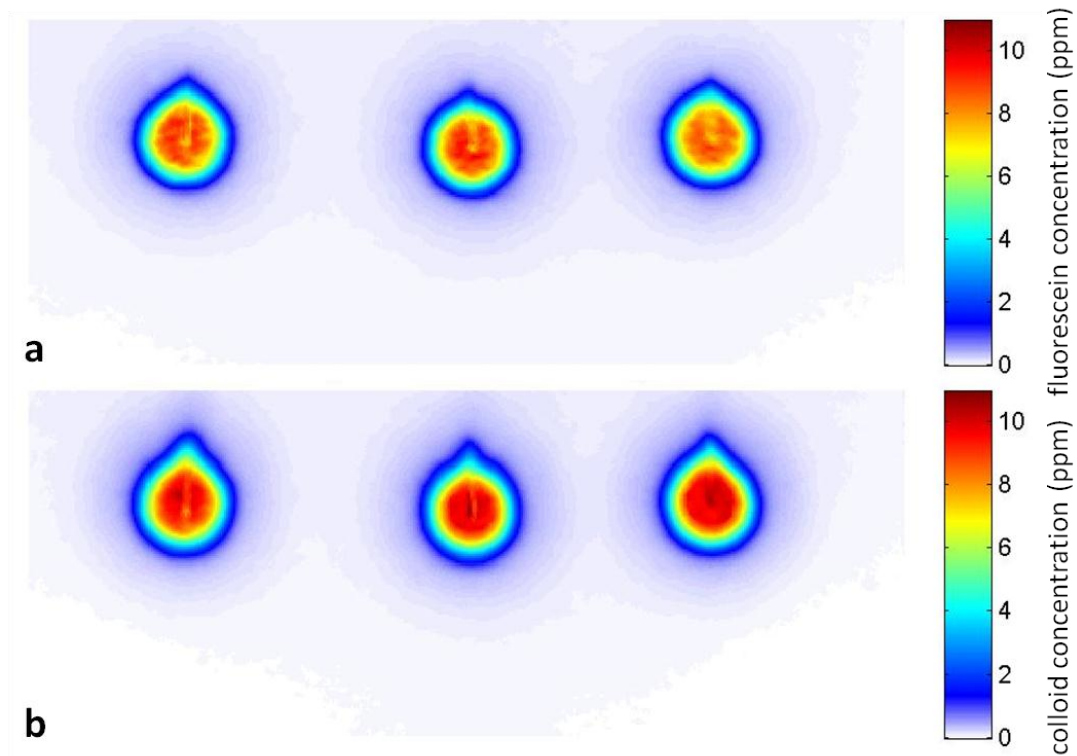


Figure 4.31 Fluorescein (a) and colloid (b) concentration values for  $1 \times 10^1$  ppm calibration solutions from calibration experiment 17 computed using derived calibration functions and fitted parameters. Images represent a physical area of  $16.8 \times 42.4$  cm.

### ***Conclusion***

Seventeen calibration experiments were conducted. Data quality improved over time due to system improvements. All data sets followed a similar trend. Models generated to fit the data performed well.

Fluorescein concentration may be quantitatively detected over the range  $10^{-2}$  to  $10^2$  ppm. Colloid concentration may be quantitatively detected over the range  $10^{-1}$  to  $10^3$  ppm. This imaging and data processing method may be used to address the transport behavior of fluorescein and colloids.

Calibration to multiple sand textures and to unsaturated conditions would further improve the utility of this system.

## Chapter Five: Fluorescein and Colloid Transport

### ***Objective***

The light-transmission imaging system described in Chapters Three and Four was developed as a tool for the observation and quantification of fluorescein and colloid transport in porous media. As a demonstration of the system's capabilities, a series of experiments was conducted to compare observed fluorescein and colloid concentrations to theoretical concentrations predicted using analytical and numerical solutions to transport equations that included processes of diffusion, advection, and dispersion (fluorescein and colloids), retardation (colloids only), photodegradation (fluorescein only), and deposition (colloids only) for conditions of (a) no flow with two dimensional transport by diffusion only, (b) one-dimensional flow with one-dimensional transport, (c) one-dimensional flow with two-dimensional transport in a homogeneous sand pack, and (d) two-dimensional flow with two-dimensional transport in a heterogeneous sand pack (Table 5.1). Experiments were conducted with a range of fluorescein and colloid concentrations; light intensities in images were converted to concentrations for comparison with model predictions using calibration data and the methods presented in Chapter Four.

Table 5.1 Summary of transport experiments.

flow field	transport	description	calibration experiment	date performed	fluorescein concentration (ppm)	colloid concentration (ppm)
no flow	2D	plume diffusion	16	2/25/09	$1 \times 10^2$	$1 \times 10^2$
1D	1D	uniform- concentration flush	10	10/9/07	$1 \times 10^{-1}$	$1 \times 10^0$
1D	1D	uniform- concentration flush	15	6/29/08	$1 \times 10^{-1}$	$1 \times 10^0$
1D	2D	plume flush with clean fluid	12	12/3/07	$1 \times 10^1$	$1 \times 10^1$
2D	2D	plume flush across textural inclusion	n/a	8/17/06	n/a	$5 \times 10^0$

### ***No Flow, Two-Dimensional Transport***

In the absence of fluid flow, molecular diffusion is the principal solute transport mechanism in porous media. For the case of radial diffusion, Fick's Law can be written [Crank, 1975]:

$$F = -D^* \frac{\partial C}{\partial r} \quad (18)$$

where  $F(\text{mg}/\text{cm}^2\text{s})$  is the mass flux per unit area time,  $C(\text{ppm})$  is the concentration of the diffusing substance,  $r(\text{cm})$  is the space coordinate measured radially outward, and  $D^*(\text{cm}^2/\text{s})$  is the effective diffusion coefficient [Fetter, 1993]. In porous media, the effective diffusion coefficient is smaller than the molecular diffusion coefficient in bulk liquids, and is computed by [Cussler, 1991]:

$$D^* = D_a/\tau \quad (19)$$

where,  $D_a(\text{cm}^2/\text{s})$  is the molecular diffusion coefficient in the bulk liquid, and  $\tau(-)$  is the tortuosity defined as ratio of the average flow path distance through the pore space to the straight path distance between two points, which is always greater than 1 and may exceed 2 [Hillel, 1998]. The tortuosity may be estimated using [Dias et al., 2008]:

$$\tau = 1/\phi^{\varpi} \quad (20)$$

where  $\phi(-)$  is the porosity, and  $\varpi(-)$  is a coefficient of porous medium packing density that ranges from 0.4 (loose packing) to 0.5 (dense packing) [Dias *et al.*, 2008]. The effective diffusion coefficients for fluorescein and colloids were computed from experimental data using [de Josselin de Jong, 1958]:

$$D^* = \frac{\Delta\sigma^2}{2\Delta t} \quad (21)$$

where  $\sigma^2$  (cm<sup>2</sup>) is the variance of the fluorescein or colloid concentration distribution, and  $t$  (s) is time.

The variance of the concentration distribution was computed using spatial moments [Freyberg, 1986; Goltz and Roberts, 1987]:

$$M_j = \int_{-\infty}^{\infty} \int_{-\infty}^{\infty} x^j y^j C(x, y) dx dy \quad (22)$$

where  $M_j$  is the  $j^{\text{th}}$  spatial moment, and  $x$  and  $y$  (cm) are coordinates in the  $x$  and  $y$  directions. For the image data,  $C$  (ppm) was computed from light intensity measurements at individual pixels as described in Chapter Four, and the integrals in Equation 22 were performed numerically:

$$M_j = \sum_{i=1}^{N_i} \sum_{k=1}^{N_k} x_i^j y_k^j C(x_i y_k) \phi V \quad (23)$$

where  $N_i$  and  $N_k$  (-) are the number of pixels in the image in the  $x$  and  $y$  directions, respectively,  $\phi(-)$  is the porosity, and  $V = 0.124$ (cm<sup>3</sup>) is the volume of sand pack represented by a single pixel (constant for all pixels).

The mass of fluorescein or colloids in the sand pack is equal to the zeroth spatial moment  $M_0$ (mg). The variance  $\sigma^2$ (cm<sup>2</sup>) of the concentration distribution used in Equation 21 is:

$$\sigma^2 = M_2(\text{cm}^2 \cdot \text{mg})/M_0(\text{mg}) \quad (24)$$

After the last plume application ( $10^2$  ppm) in calibration experiment 16 (early time = 0s), the sand pack was allowed to sit with no flow for a period of 15 days (late time =  $1.296 \times 10^6$  s) at  $20^\circ\text{C}$ . During this time fluorescein and colloid concentrations changed due to diffusion. Two plumes were evaluated for their diffusion behavior, and are referred to in this section as the left and right plumes. Images of water content from this experiment are shown for early time and late time (Figures 5.1 and 5.2) (all images shown for this experiment were for the same  $27.4 \times 14.0$  cm region of the sand pack). Water content images serve as a frame of reference for the diffusion behavior shown in the fluorescein and colloid images, and provide a check on values of porosity ( $\phi$ ) used in spatial moment calculations. Volumetric water content is equal to porosity in water-saturated porous media. The porosity of this sand pack determined gravimetrically was  $\phi = 0.323$ (-).

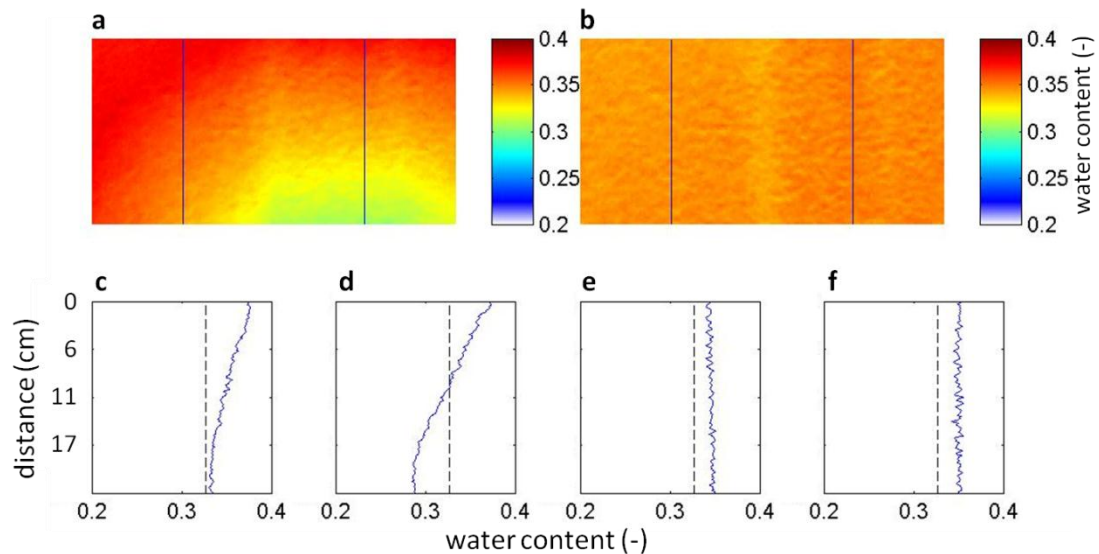


Figure 5.1 Water content images from the 2/25/09 sand pack for early time (a) and late time (b), where vertical lines in the images indicate transect locations. Transects are shown for early time left (c) and right (d) and late time left (e) and right (f). Dashed lines indicate the reference value for porosity.

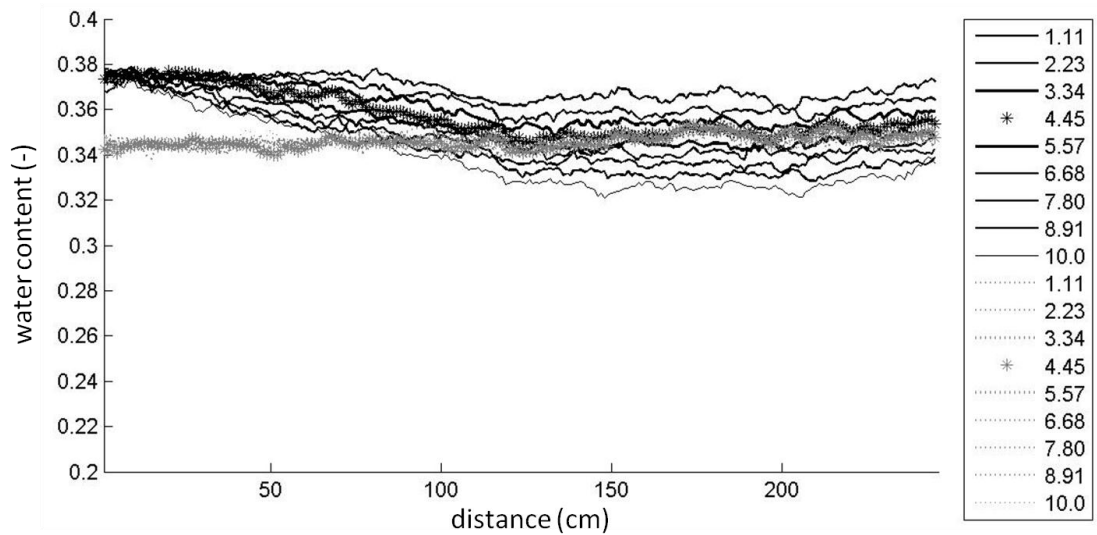


Figure 5.2 Horizontal transects of water content across the region shown in Figure 5.1 at early time (black lines) and late time (grey lines). Legend shows vertical elevation (cm) of transects from the sand surface. Stars indicate transect elevation used in diffusion calculations.

Figure 5.3 shows the effect of molecular diffusion on fluorescein concentrations. The initially compact plumes emplaced in the sand pack at early time (a) have spread considerably by late time (b). Vertical and horizontal transects from the images show patterns of spreading typical of diffusion.

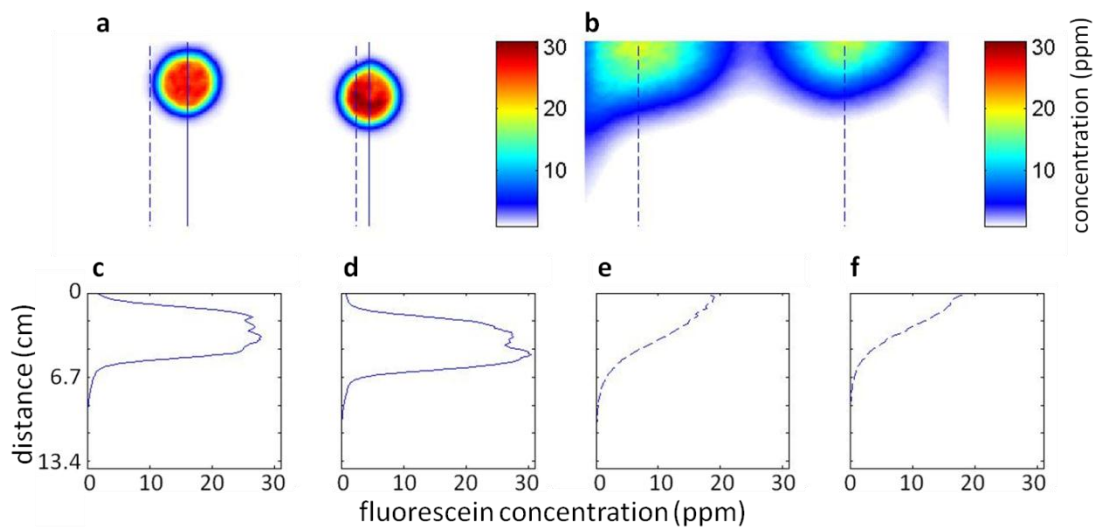


Figure 5.3 Fluorescein concentrations at early time (a) and late time (b) with corresponding transect plots (c-f). Dashed lines indicate location of late time transects.

Spatial moments were computed for the right plume in Figure 5.3d and f and used to calculate the effective diffusion coefficient. In this analysis we ignored the effects of advection and assumed that

photodegradation of the fluorescein was negligible because the chamber was dark during the experiment. Spreading of fluorescein at late time (Figure 5.3b) extended beyond the limit of the image. Therefore, transects were taken from the center of mass outwards at early and late times (Figure 5.4) and these data were used for the spatial moment calculations.

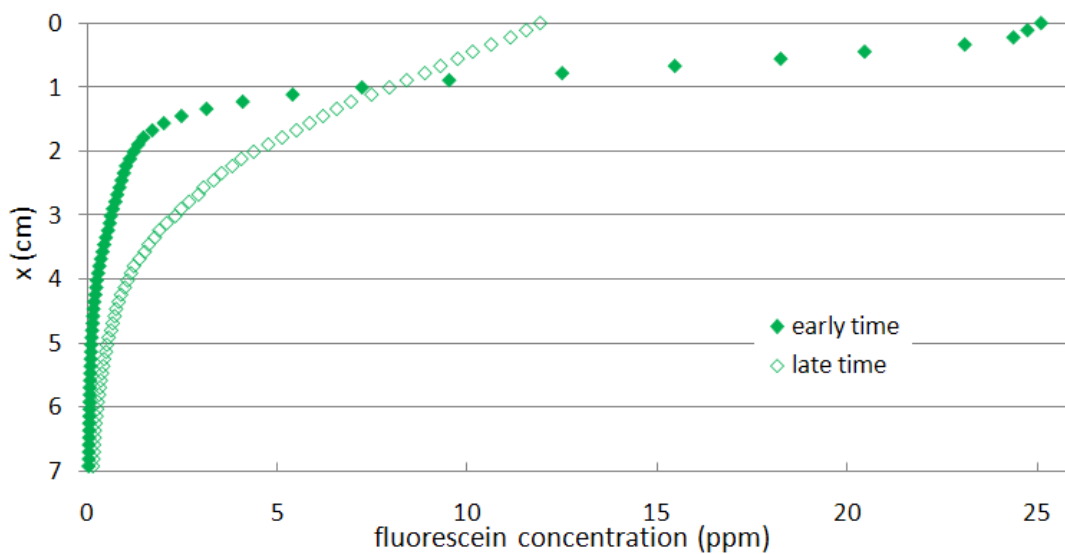


Figure 5.4 Vertical fluorescein transects through plume at early and late time from the center of mass outwards.

Horizontal transects (Figure 5.5) were analyzed in a similar fashion to obtain replicate estimates for the fluorescein diffusion coefficient.

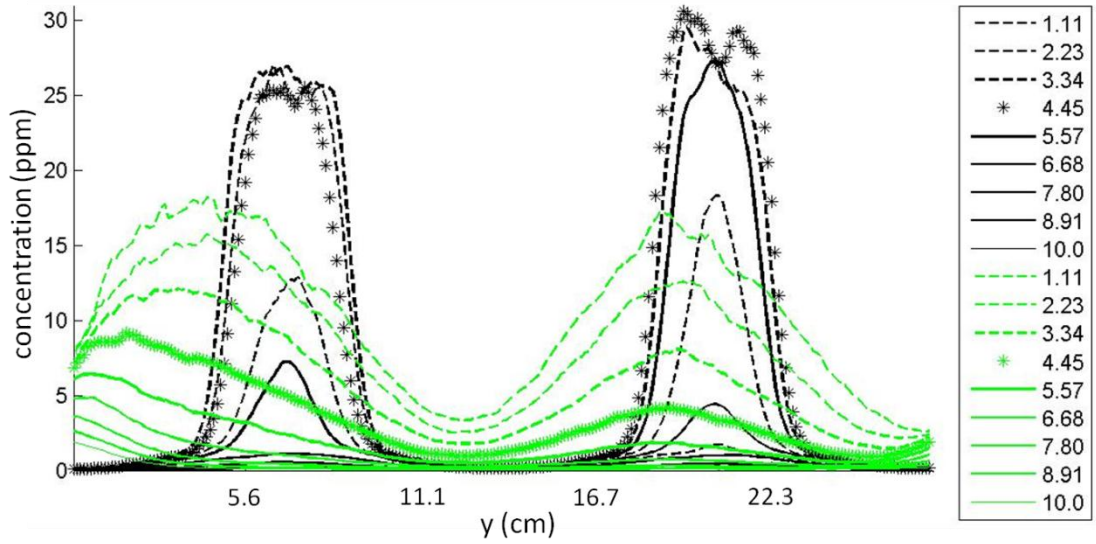


Figure 5.5 Horizontal transects of fluorescein concentration at early time (black) and late time (green). Legend shows vertical elevation of transects (cm). Stars indicate data used for analysis.

The early and late time transects from Figure 5.5 at  $x = 4.45\text{cm}$  were plotted together (Figure 5.6) and also used to compute a replicate colloid diffusion coefficient (Table 5.2, horizontal). The transect for model fitting was taken from the peak concentration out towards the edge of the sand pack to avoid data that blended with concentrations from the left plume.

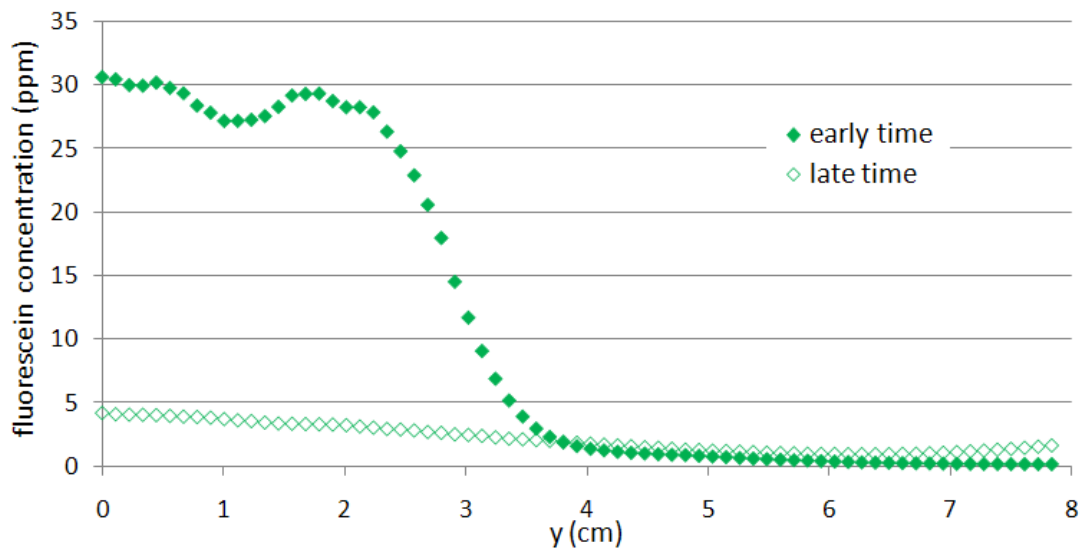


Figure 5.6 Horizontal fluorescein transects from Figure 5.5 (stars, right plume) at early and late times used to calculate diffusion coefficient in Table 5.2.

Table 5.2 Computed spatial moments, spatial variance, and effective diffusion coefficients for fluorescein.

	time 1			time2			$D^*(\text{cm}^2/\text{s})$
	$M_0(\text{mg})$	$M_2(\text{cm}^2\text{mg})$	$\sigma^2(\text{cm}^2)$	$M_0(\text{mg})$	$M_2(\text{cm}^2\text{mg})$	$\sigma^2(\text{cm}^2)$	
<b>vertical</b>	$9.38 \times 10^{-4}$	$1.10 \times 10^{-3}$	$1.17 \times 10^{-0}$	$8.91 \times 10^{-4}$	$3.67 \times 10^{-3}$	$4.11 \times 10^0$	$1.14 \times 10^{-6}$
<b>horizontal</b>	$3.42 \times 10^{-3}$	$1.22 \times 10^{-2}$	$3.56 \times 10^0$	$6.33 \times 10^{-4}$	$6.93 \times 10^{-3}$	$1.10 \times 10^1$	$2.85 \times 10^{-6}$

The effect of diffusion on colloid concentrations in this experiment was much smaller than for fluorescein as indicated by the tight, round appearance of the colloid plumes that persisted to late time (Figure 5.7b).

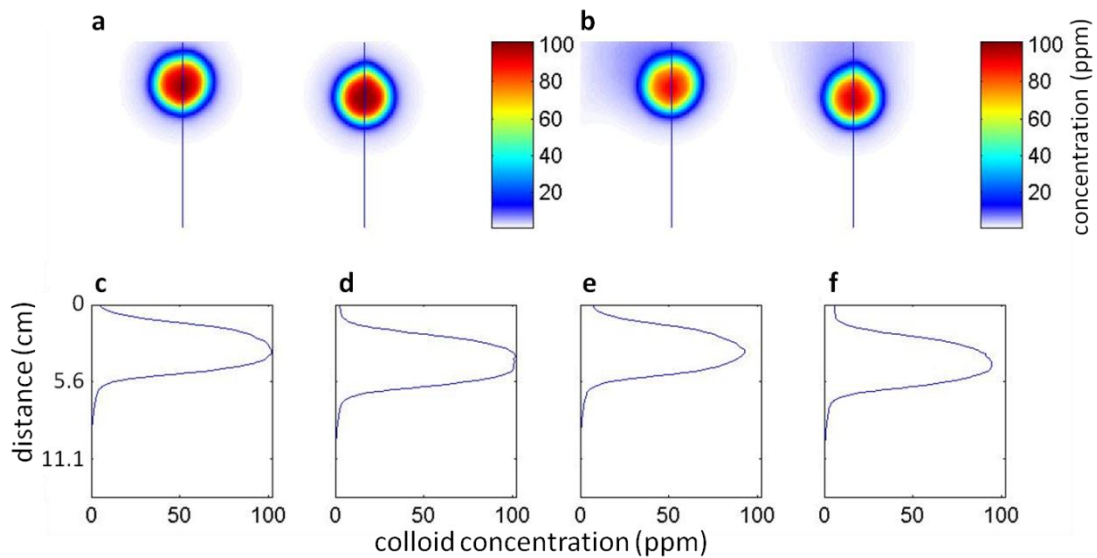


Figure 5.7 Colloid concentrations at early time (a) and late time (b), and vertical transects (c-f).

Spatial moments were computed for the vertical transects in Figure 5.7d and f, and used to calculate the effective diffusion coefficients for colloids (Table 5.3). In this analysis we ignored the effects of advection. Analysis was conducted on transects as was done for fluorescein. Transects were also used that spanned the entire plume; this was possible for colloids due to their limited spreading. Results are compared between the two approaches in Table 5.3.

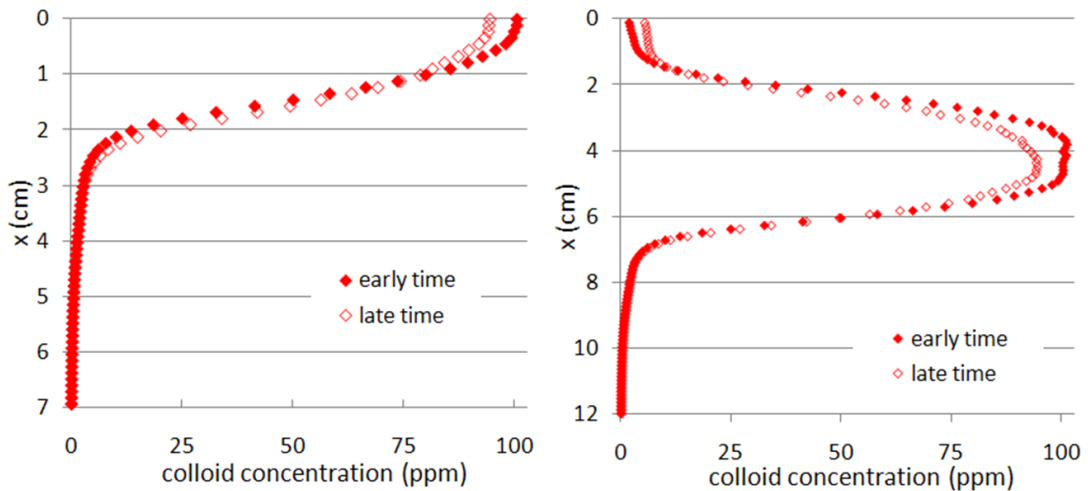


Figure 5.8 Vertical transects through colloid plume in Figure 5.7b and d. Analyses were conducted on data where  $0 < x < 7.4$ cm (a) and where  $0 < x < 22$  (b). Colloid concentration values in the range  $12 < x < 22$ cm that are not included in (b) decline from a maximum of 0.23ppm to a minimum of 0.010ppm.

Transects taken through the plumes horizontally show for colloids (Figure 5.9) very little lateral spreading, but some reduction in peak concentrations in the central region of the plumes.

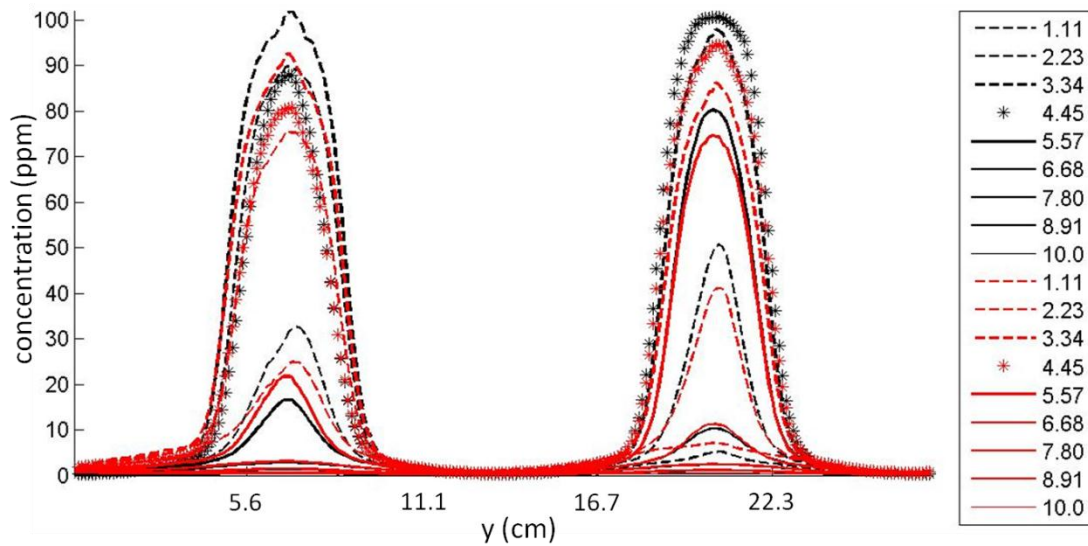


Figure 5.9 Horizontal transects of colloids at early time (black) and late time (red). Legend shows vertical elevation of transects (cm). Stars indicate data used for modeling.

The early and late time transects from Figure 5.9 at  $x = 4.45$ cm were plotted together (Figure 5.10) and also used to compute a replicate colloid diffusion coefficient (Table 5.3, horizontal).

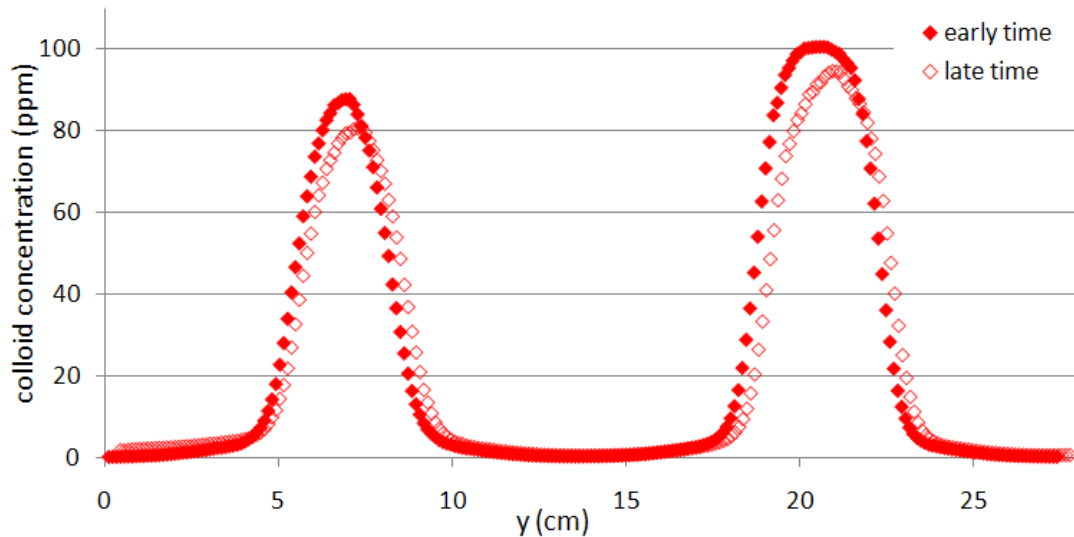


Figure 5.10 Horizontal colloid transects from Figure 5.9 at early and late times used to calculate diffusion coefficient in Table 5.3.

The colloid effective diffusion coefficients derived from the four data sets did vary, but showed generally good agreement, ranging from  $1.70$  to  $5.42 \times 10^{-7} \text{ cm}^2/\text{s}$  (Table 5.3).

Table 5.3 Computed spatial moments, variance, and effective diffusion coefficients for colloids.

	early time			late time			D* (cm <sup>2</sup> /s)
	M <sub>0</sub> (mg)	M <sub>2</sub> (cm <sup>2</sup> mg)	σ <sup>2</sup> (cm <sup>2</sup> )	M <sub>0</sub> (mg)	M <sub>2</sub> (cm <sup>2</sup> mg)	σ <sup>2</sup> (cm <sup>2</sup> )	
<b>vertical</b> <b>0&lt;x&lt;7.4cm</b>	$5.68 \times 10^{-3}$	$1.13 \times 10^{-2}$	$1.99 \times 10^0$	$5.68 \times 10^{-3}$	$8.78 \times 10^{-3}$	$1.55 \times 10^0$	<b><math>1.70 \times 10^{-7}</math></b>
<b>vertical</b> <b>0&lt;x&lt;22cm</b>	$1.41 \times 10^{-2}$	$2.75 \times 10^{-1}$	$1.95 \times 10^1$	$1.31 \times 10^{-2}$	$2.73 \times 10^{-1}$	$2.09 \times 10^1$	<b><math>5.42 \times 10^{-7}</math></b>
<b>horizontal</b>	$2.43 \times 10^{-2}$	$6.41 \times 10^0$	$2.64 \times 10^2$	$2.30 \times 10^{-2}$	$6.06 \times 10^0$	$2.64 \times 10^2$	<b><math>1.93 \times 10^{-7}</math></b>

### ***One-Dimensional Flow, One Dimensional Transport***

One-dimensional solute transport in homogeneous porous media may be described by the one-dimensional form of the advection-dispersion equation [Selker *et al.*, 1999]:

$$\frac{\partial \theta C}{\partial t} = \frac{D_L}{R} \frac{\partial^2 \theta C}{\partial x^2} - \frac{u}{R} \frac{\partial \theta C}{\partial x} - \lambda \theta C \quad (25)$$

where  $\theta(-)$  is the volumetric water content,  $C(\text{ppm})$  is concentration,  $t(\text{s})$  is time,  $x(\text{cm})$  is distance, and  $\lambda(\text{s}^{-1})$  is the decay coefficient.  $D_L(\text{cm}^2/\text{s})$  is the longitudinal dispersion coefficient defined as

$$D_L = \alpha_L u + D^* \quad (26)$$

where  $\alpha_L(\text{cm})$  is the longitudinal dispersivity,  $u(\text{cm/s})$  is the average pore water velocity, and  $D^*(\text{cm}^2/\text{s})$  is the effective diffusion coefficient.  $R(-)$  is the retardation factor defined as the ratio of the water velocity to the solute velocity, and is used here to describe sorption. For the case of equilibrium sorption with a linear isotherm, the retardation factor can be written:

$$R = 1 + (\rho_b K_d / \theta) \quad (27)$$

where  $\rho_b(\text{mg/L})$  is the bulk density, and  $K_d(\text{L/mg})$  is the distribution coefficient, which describes partitioning of a solute between liquid and solid phases.

Given continuous solute injection with solute concentration  $C_0$  (ppm) at  $x = 0\text{cm}$  into an infinite porous medium with zero initial solute concentration, an analytical solution of Equation 25 is [Selker *et al.*, 1999]:

$$C(x, t) = \frac{C_0}{2} \exp\left(\frac{x}{2\alpha_L}\right) \left[ \exp\left(\frac{-x\gamma}{2\alpha_L}\right) \text{erfc}\left(\frac{x - ut\gamma/R}{2\sqrt{D_L t/R}}\right) - \exp\left(\frac{x\gamma}{2\alpha_L}\right) \text{erfc}\left(\frac{x + ut\gamma/R}{2\sqrt{D_L t/R}}\right) \right] \quad (28)$$

where

$$\gamma = \sqrt{1 + 4\lambda\alpha_L R/u} \quad (29)$$

$\lambda(\text{s}^{-1})$  is the first order decay coefficient defined by:

$$C = C_0 \exp(-\lambda t) \quad (30)$$

A value for the fluorescein decay coefficient was attained through analysis of image data (Figure 3.22) collected to address photodegradation. In that experiment, a sand pack was saturated with known concentration of fluorescein and then held under no flow conditions. After the fluorescein was emplaced, the sand pack was imaged repeatedly under continuous illumination to quantify the rate of fluorescein photodegradation. Equation 30 was fit to the photodegradation data to obtain  $\lambda = 3.30 \times 10^{-5} \text{ s}^{-1}$  for  $0 < t < 60 \text{ s}$ , and  $\lambda = 2.60 \times 10^{-5} \text{ s}^{-1}$  for  $0 < t < 268 \text{ s}$ . (In the transport experiments presented in this chapter, the duration of fluorescein illumination ranged from 60 to 268s.) This parameter also was derived by fitting fluorescein concentrations from transport experiments, and these will be compared to the value obtained from the experiment shown in Figure 5.11.

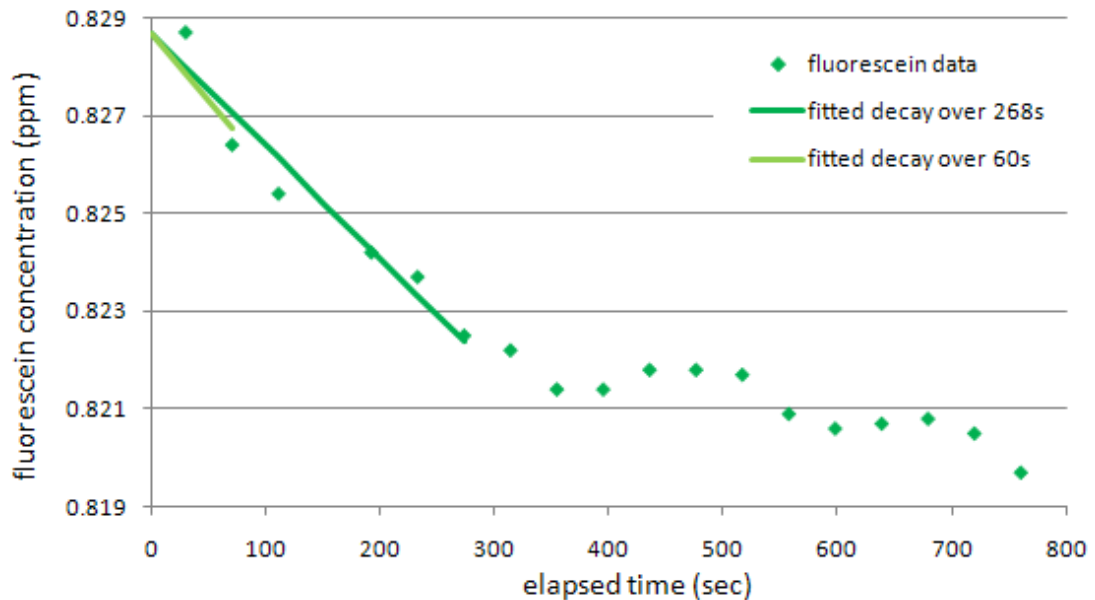


Figure 5.11 Photodegradation of fluorescein fit with a first order exponential decay model.

The rest of the data in this section are uniform-concentration saturation events used to analyze one-dimensional transport under one dimensional flow. Data presentation includes the full image under consideration followed by a cropped image and a transect (eg. Figure 5.12a-c). Full images (a) were 53.5 x 42.6cm and were overlain by a 33.4 x 22.3cm rectangle used to define the dimensions of the

cropped image (b). The transect data were extracted from the cropped images by averaging values across each row in the cropped region and plotting the result against distance (c).

Calibration experiment 10 utilized the uniform-concentration method to emplace fluorescein and colloids into the sand pack at a flow rate of 0.182cm/s. Images of water content after emplacement of the  $10^{-3}$  ppm calibration solution (Figure 5.12) matched closely the water content prior to emplacement of the  $10^{-2}$  ppm calibration solution (Figure 5.13), which occurred 22hours later. The volumetric water content obtained from both images corresponded closely to the value of porosity  $\phi=0.327(-)$  reported for similar sand packs by *Niemet and Selker* [2001] (gravimetric determination of sand pack porosity was not conducted for this experiment). Slight deviations from this value seen in the images are attributed to small differences in illumination.

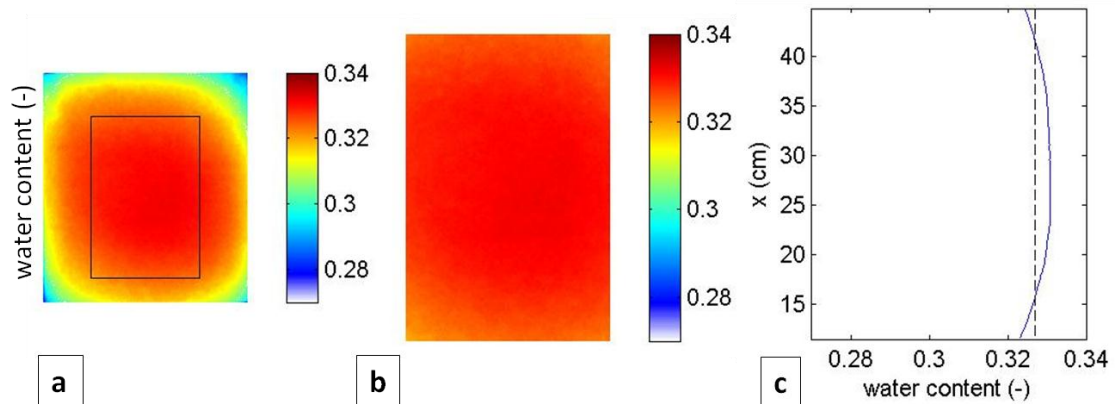


Figure 5.12 Water content full image (a), cropped area (b), and transect (c) of 10/9/07 sand pack after emplacement of  $10^{-3}$  ppm calibration solution in calibration experiment 10.

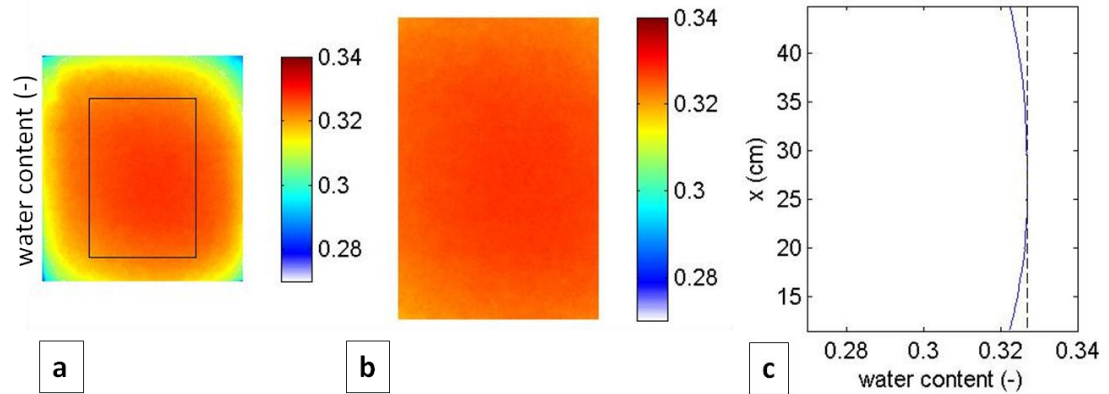


Figure 5.13 Water content full image (a), cropped area (b), and transect (c) of 10/9/07 sand pack prior to emplacement of  $10^{-2}$  ppm calibration solution in calibration experiment 10.

Fluorescein concentration images show the advancing fluorescein front (Figure 5.14) and a vertical transect through the images shows the progress of the front as it moved vertically upward; the decreased concentration computed at the bottom edge of the sand pack ( $x < 10$  cm) was attributed to decreased light intensities caused by edge effects in the image (Figure 5.14).

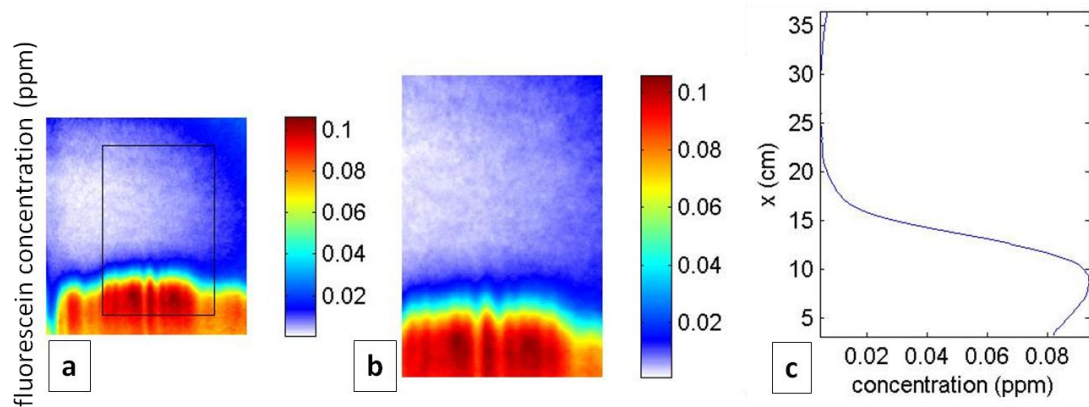


Figure 5.14 Fluorescein concentration full image (a), cropped area (b), and transect (c) of 10/9/07 sand pack after 60s upward pumping with  $10^{-1}$  ppm calibration solution.

Figure 5.15 shows the result of using  $C_0 = 9.40 \times 10^{-2}$  ppm,  $t = 60$  s, and  $R = 1$ , in Equation 28 to fit the transect from Figure 5.14c. Minimizing least squares yielded  $u = 0.228$  cm/s,  $\alpha_L = 0.203$  cm, and  $\lambda = 2.23 \times 10^{-4}$  s $^{-1}$ . The minimum data value was added to the model prediction to account for background fluorescence from residual dye.

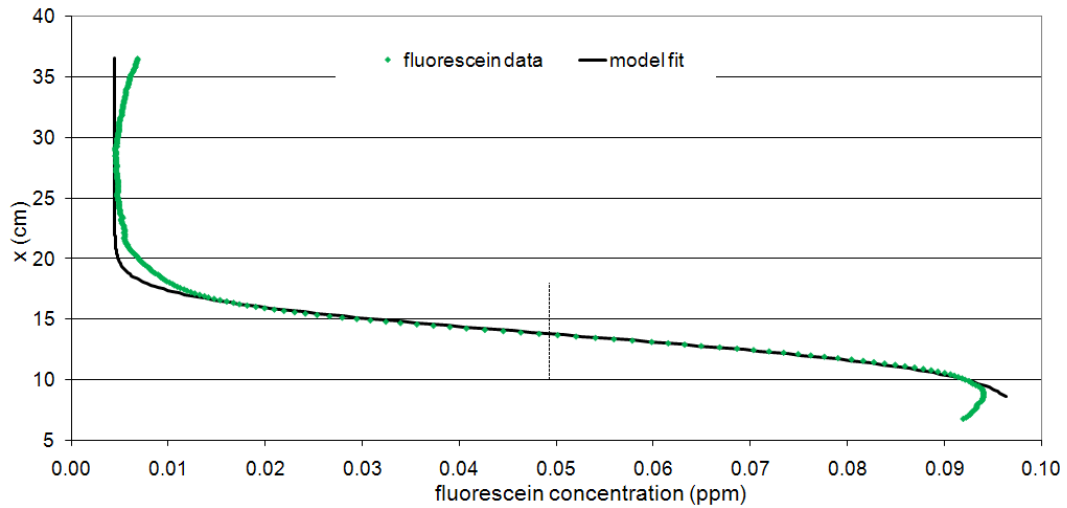


Figure 5.15 Equation 28 fit to fluorescein data transect in Figure 5.14c.

A second data set of the same nature was analyzed in the same manner to generate replicate values of transport parameters. Calibration experiment 15 utilized the uniform-concentration method to emplace fluorescein and colloids into the sand pack at 0.105cm/s. The porosity of this sand pack calculated from chamber dimensions and sand mass was  $\phi = 0.326(-)$ . The water content calculated from image data deviates from the gravimetrically-calculated reference value due to imperfections in image processing, but image-derived values are fairly homogeneous indicating a water-saturated condition (Figure 5.16).

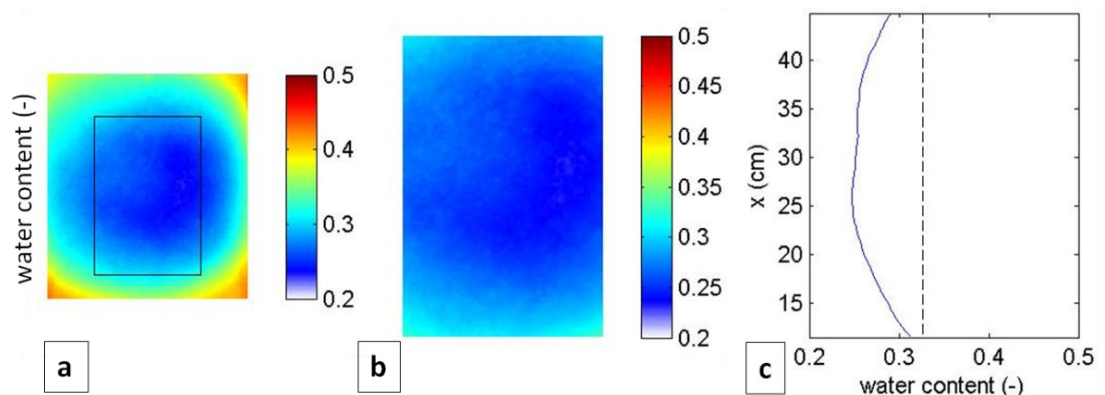


Figure 5.16 Water content full image (a), cropped area (b), and transect (c) of 6/29/08 sand pack while saturated with  $10^{-1}$  ppm calibration solution. Dashed line represents the value for porosity.

Images of  $10^{-1}$ ppm calibration solution emplacement were captured in a time series. Images and transects of fluorescein concentration (Figure 5.17) are shown when the solution has been pumped half way up the sand pack.

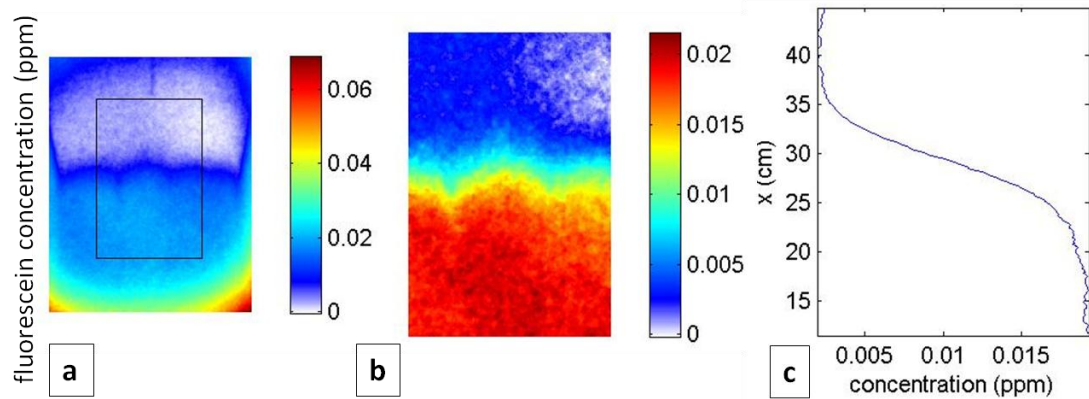


Figure 5.17 Fluorescein concentration full image (a), cropped area (b), and transect (c) of 6/29/08 sand pack after 269s upward pumping with  $10^{-1}$ ppm calibration solution.

Figure 5.18 shows the result of using  $C_0 = 1.93 \times 10^{-2}$ ppm,  $t = 268$ s, and  $R = 1$  in Equation 28 to fit the transect from Figure 5.17c. Minimizing least squares yielded  $u = 0.110$ cm/s,  $\alpha_L = 0.190$ cm, and  $\lambda = 8.45 \times 10^{-4}$ s $^{-1}$ . The minimum data value was added to the model prediction to account for background fluorescence from residual dye.

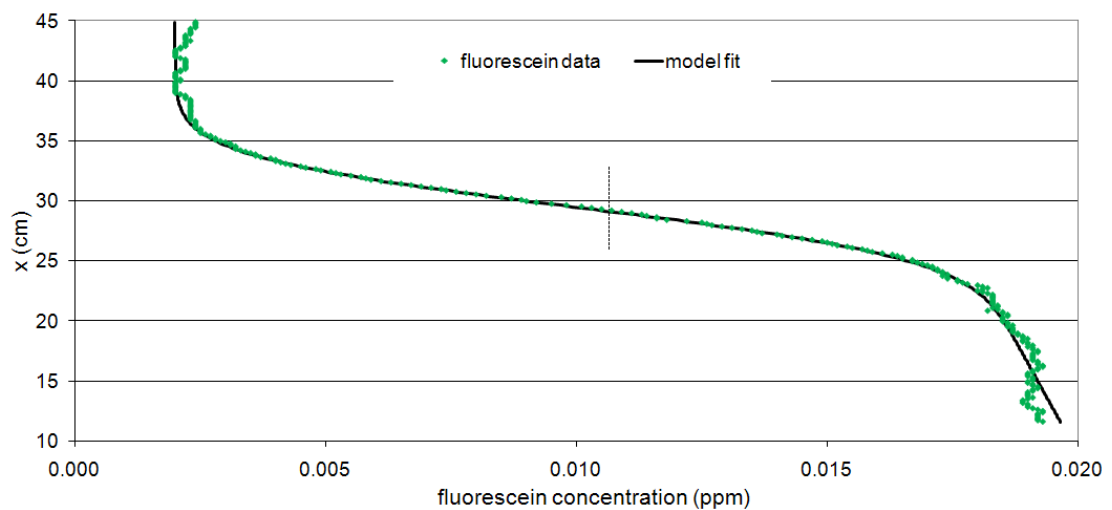


Figure 5.18 Equation 28 fit to 6/29/08  $10^{-1}$ ppm fluorescein transect from Figure 5.17c.

Generally good agreement was demonstrated between longitudinal dispersivities and decay coefficients estimated from the two data sets (Table 5.4).

Table 5.4 Fluorescein fitted parameters.

fluorescein image transect date	initial concentration, $C_0$ (ppm)	fluid velocity, $u$ (cm/s)	longitudinal dispersivity, $\alpha_L$ (cm)	decay coefficient, $\lambda$ ( $s^{-1}$ )	error, sse ( $\text{ppm}^2$ )	number of data points, n (-)
<b>10/9/07</b>	$9.40 \times 10^{-2}$	$2.28 \times 10^{-1}$	$2.03 \times 10^{-1}$	$2.32 \times 10^{-4}$	$3.94 \times 10^{-4}$	252
<b>6/29/08</b>	$1.93 \times 10^{-2}$	$1.10 \times 10^{-1}$	$1.90 \times 10^{-1}$	$8.45 \times 10^{-4}$	$9.22 \times 10^{-5}$	300

Deviation of colloids from fluorescein transport behavior was addressed through fitting the retardation factor and modifying the interpretation of the decay coefficient. For fluorescein, it was assumed that the retardation factor was one, but this parameter was estimated for colloid data. The decay coefficient in models fit to colloid data does not represent photodegradation, but rather depositional processes that lead to loss of colloids from the mobile aqueous phase. The same functional form used for fluorescein will also be used for colloids, but with the substitution of  $\mathcal{K}$  ( $s^{-1}$ ) for  $\lambda$  ( $s^{-1}$ ):

$$C(x, t) = \frac{C_0}{2} \exp\left(\frac{x}{2\alpha_L}\right) \left[ \exp\left(\frac{-x\gamma}{2\alpha_L}\right) \operatorname{erfc}\left(\frac{x - ut\gamma/R}{2\sqrt{D_L t/R}}\right) - \exp\left(\frac{x\gamma}{2\alpha_L}\right) \operatorname{erfc}\left(\frac{x + ut\gamma/R}{2\sqrt{D_L t/R}}\right) \right] \quad (31)$$

where

$$\gamma = \sqrt{1 + 4\mathcal{K}\alpha_L R/u} \quad (32)$$

and  $\mathcal{K}$  ( $s^{-1}$ ) is a first order deposition coefficient:

$$C = C_0 \exp(-\mathcal{K}t) \quad (33)$$

A time series of images was taken of the colloid signal in calibration experiment 10 during the emplacement of the  $10^0$  calibration solution (Figure 5.19) at 0.185cm/s.

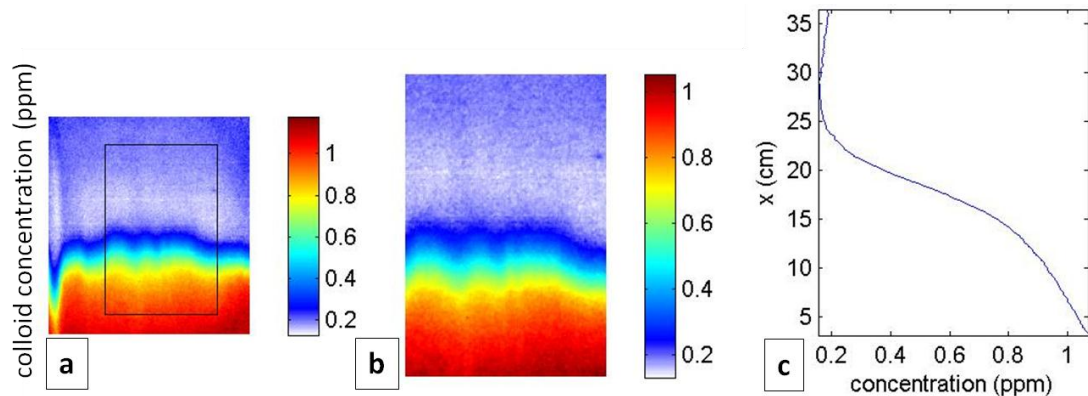


Figure 5.19 Colloid concentration full image (a), cropped area (b), and transect (c) of 10/9/07 sand pack after 93s upward pumping of  $10^0$  ppm calibration solution.

Transects of the colloid data were taken from Figure 5.19c and fitted (Figure 5.20) by Equation 31 using  $C_0 = 1.07 \times 10^0$  ppm,  $t = 93$  s, and  $u = 2.28 \times 10^{-1}$  cm/s to estimate the longitudinal dispersivity for colloids. Minimizing least squares yielded  $\alpha_L = 0.237$  cm,  $R = 1.11(-)$ , and  $\mathcal{K} = 6.87 \times 10^{-3} \text{ s}^{-1}$ . The minimum data value was added to the model prediction to account for background fluorescence from residual dye.

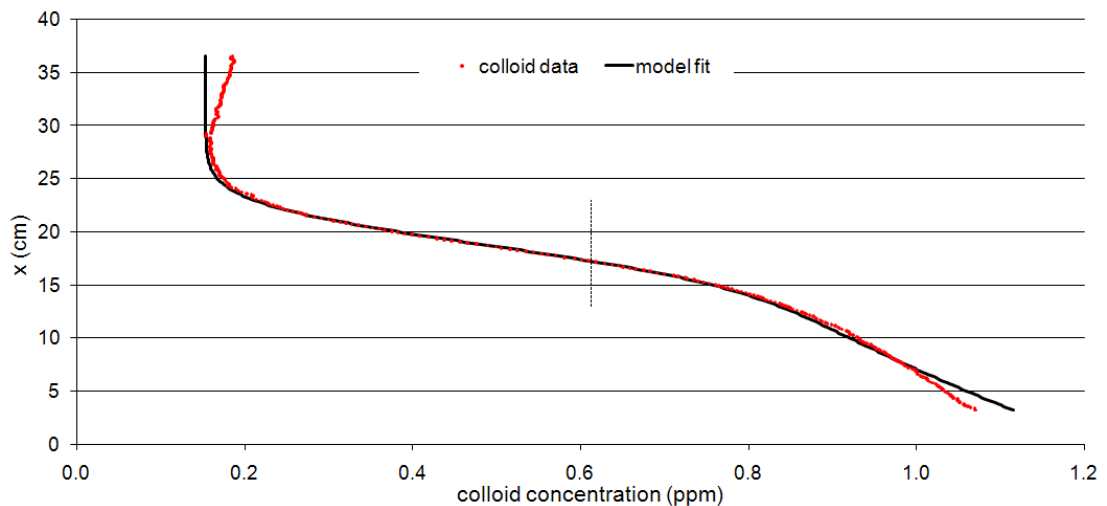


Figure 5.20 Equation 31 fit to colloid transect in Figure 5.19c.

The same analysis for colloids was conducted on a second similar experiment. A time series was taken of the colloid signal in calibration experiment 15 during the emplacement of the  $10^0$  ppm calibration solution at 0.105 cm/s. Water content of the sand pack while emplaced with  $10^0$  ppm calibration

solution (Figure 5.21) was nearly homogeneous, but lower than that expected from the porosity ( $\phi = 0.326(-)$ ). This discrepancy is thought to be due to small variations in illumination.

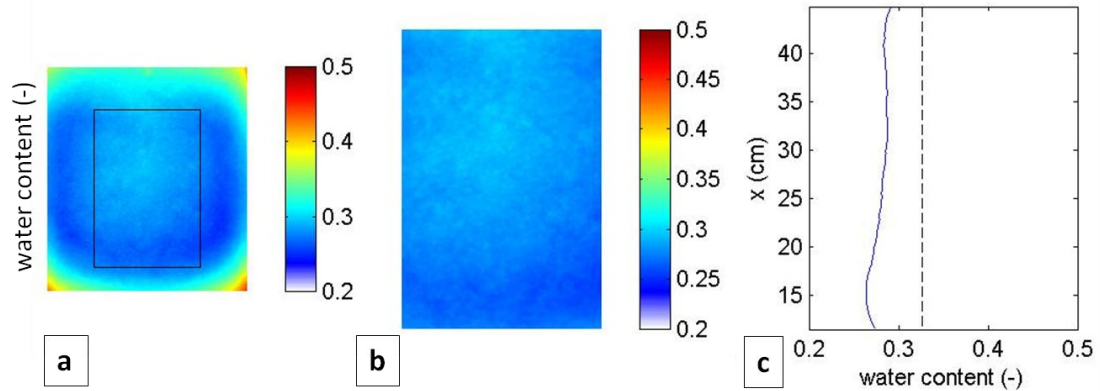


Figure 5.21 Water content full image (a), cropped area (b), and transect (c) of 6/29/08 sand pack while saturated with  $10^0$  ppm calibration solution. Dashed line is the gravimetrically calculated value for porosity.

Images of  $10^0$  ppm calibration solution emplacement during calibration experiment 15 were captured in a time series. Images and transects of colloid concentration (Figure 5.22) are shown when the solution has been pumped half way up the sand pack.

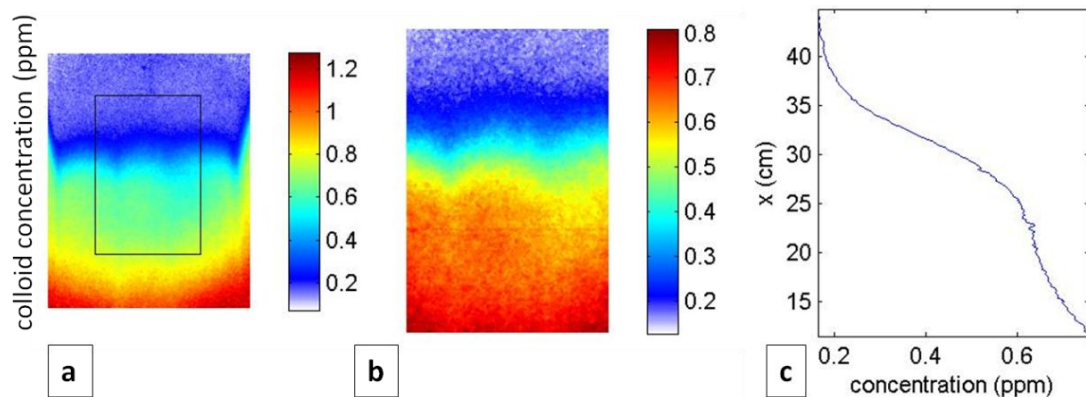


Figure 5.22 Colloid concentration full image (a), cropped area (b), and transect (c) of 6/29/08 sand pack after 388s upward pumping with  $10^0$  ppm calibration solution during calibration experiment 15.

The longitudinal dispersivity, retardation factor, and deposition coefficient were fit to colloid data; pore water velocity and time were held constant to values determined from fitting fluorescein data.

Using  $C_0 = 7.56 \times 10^{-1}$  ppm,  $t = 388$  s, and  $u = 1.10 \times 10^{-1}$  cm/s, Equation 28 was fit (Figure 5.23) to the transect in Figure 5.22c. Minimizing least squares yielded  $\alpha_L = 0.202$  cm,  $R = 1.31(-)$ , and  $\mathcal{K} = 1.87 \times 10^{-3}$

$s^{-1}$  (Table 5.5). The minimum data value was added to the model prediction to account for background fluorescence from residual dye.

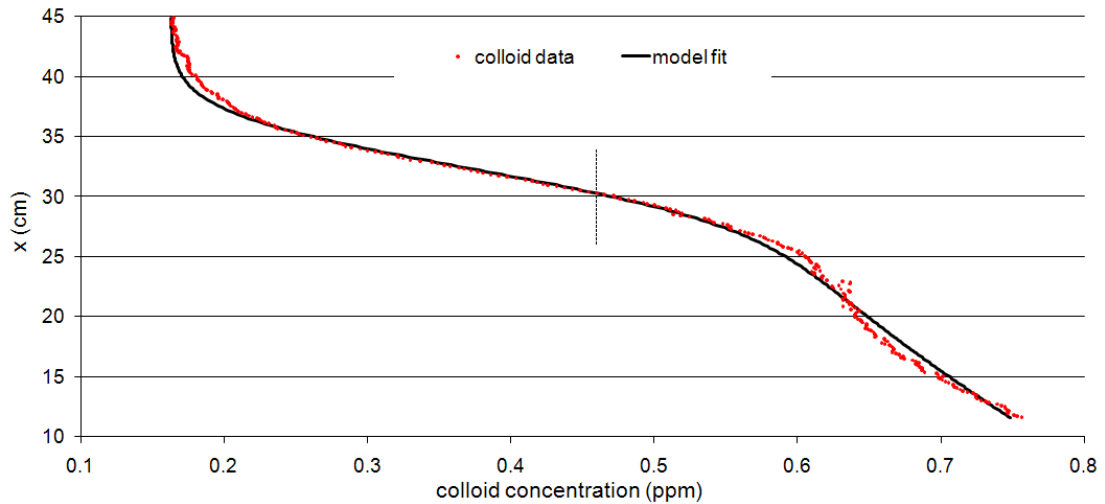


Figure 5.23 Equation 28 fit to colloid concentration transect in Figure 5.22c.

Generally good agreement was demonstrated between estimation of longitudinal dispersivities and deposition coefficients for colloids between the two experiments (Table 5.5).

Table 5.5 Colloid fitted parameters

colloid image transect date	initial concentration, $C_0$ (ppm)	fluid velocity, $u$ (cm/s)	longitudinal dispersivity, $\alpha_L$ (cm)	retardation factor, $R$ (-)	deposition coefficient, $\mathcal{K}$ ( $s^{-1}$ )	error, sse ( $\text{ppm}^2$ )	number of data points, $n$ (-)
<b>10/9/07</b>	$1.07 \times 10^0$	$2.28 \times 10^{-1}$	$2.37 \times 10^{-1}$	$1.11 \times 10^0$	$6.87 \times 10^{-3}$	$6.69 \times 10^{-2}$	300
<b>6/29/08</b>	$7.56 \times 10^{-1}$	$1.10 \times 10^{-1}$	$2.02 \times 10^{-1}$	$1.31 \times 10^0$	$1.87 \times 10^{-3}$	$1.78 \times 10^{-2}$	300

The in-line fluorometer described in Chapter Three (Figure 3.15) was installed as a tool to monitor concentrations of fluorescein and colloids as water followed out of the sand pack. Using  $x = 247\text{cm}$ , and  $u = 9.00 \times 10^{-2}\text{cm/s}$ , Equation 28 was fit to fluorescein data collected by the fluorometer of chamber effluent from 6/29/08. Good agreement of the model with both fluorescein and colloid data was achieved using  $\alpha_L = 2.16\text{cm}$ ,  $R = 1(-)$ , and  $\lambda = \mathcal{K} = 9.25 \times 10^{-6}\text{s}^{-1}$  (Figure 5.24). These data demonstrate the ability of the fluorometer to provide validation of breakthrough behavior, but

parameters obtained may not be compared to those from image data due to the drastically different geometries involved. (The images show concentrations within the sand pack but the concentrations measured with the fluorometer include transport within the sand pack as well as within the inlet and outlet manifolds and tubing and the fluorometer flow cell.)

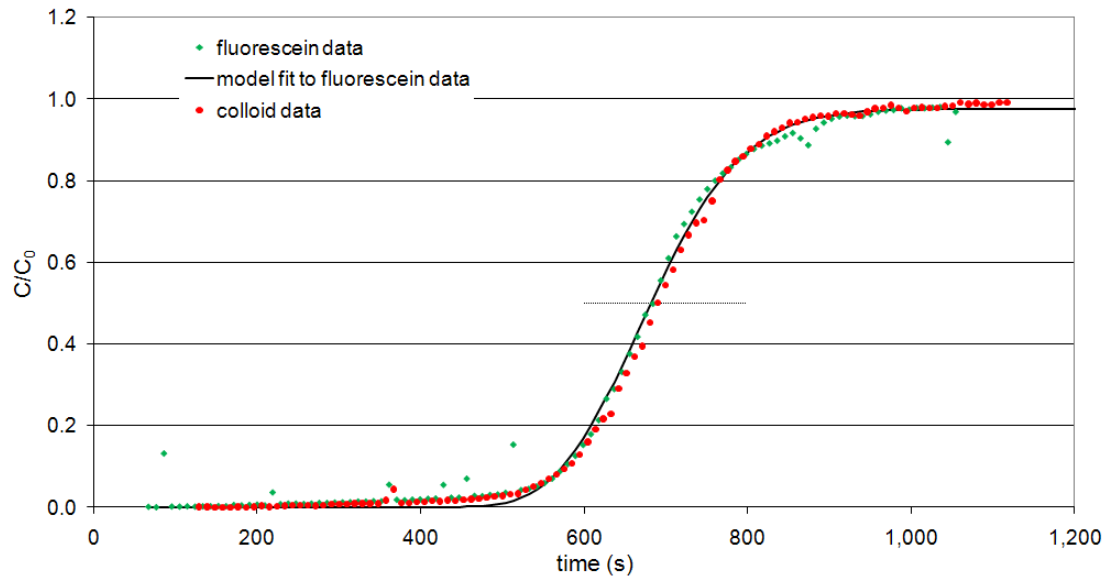


Figure 5.24 In-line fluorometer readings of fluorescein at  $10^{-3}$  ppm and colloids at  $10^0$  ppm from 6/29/08 experiment. Equation 28 is fit to the fluorescein data.

### ***One-Dimensional Flow, Two-Dimensional Transport***

The advection-dispersion equation for two dimensional transport in a one dimensional flow field may be written [Selker *et al.*, 1999]:

$$\frac{\partial \theta C}{\partial t} = \frac{D_L}{R} \frac{\partial^2 \theta C}{\partial x^2} + \frac{D_T}{R} \frac{\partial^2 \theta C}{\partial y^2} - \frac{u}{R} \frac{\partial \theta C}{\partial x} - \lambda \theta C \quad (34)$$

where  $x(\text{cm})$  and  $y(\text{cm})$  are the distance along the  $x$  (longitudinal) and  $y$  (transverse) axes

respectively,  $D_T(\text{cm}^2/\text{s})$  is the transverse dispersion coefficient

$$D_T = \alpha_T u + D^*, \quad (35)$$

$\alpha_T$  (cm) is the transverse dispersivity,  $u$ (cm/s) is the pore fluid velocity, and  $D^*$ (cm<sup>2</sup>/s) is the effective diffusion coefficient. The solution to Equation 34 for instantaneous injection, flow in the x direction, zero initial concentration, is [Selker *et al.*, 1999]:

$$C(x, y, t) = \frac{M \exp(-\lambda t)}{4\pi t \theta \sqrt{D_L D_T}} \exp\left(-\frac{(x - ut/R)^2}{4D_L t/R} - \frac{y^2}{4D_T t/R}\right) \quad (36)$$

where  $M$ (mg/cm) is the solute mass applied per length perpendicular to the x-y plane. This solution therefore assumes a zero initial radius of the plume. With sufficient time and spreading of the plume the solution will begin to fit the data despite the discrepancy at early time.

Image data used to demonstrate two-dimensional transport, under one-dimensional flow, were collected on 12/3/07 as part of calibration experiment 12. A single 10<sup>1</sup> ppm plume of fluorescein and colloids was applied to a 30/40 sand pack and RO water was used to transport the plume vertically downward (+ x direction). The plume had an initial radius of 6cm. The porosity of this sand pack was not determined gravimetrically, but was estimated by the value of  $\phi = 0.327$ (-) reported for similar sand packs by *Niemi and Selker* [2001]. Images and longitudinal transects of water content (Figure 5.25) (obtained and presented in the same manner as in the previous section) demonstrate the utility of water content images, even in water-saturated experiments. The dark blue region at the top of panel (a) indicates partial desaturation of the sand likely due to inadvertent withdrawal of water from the sand pack at the tip of the plume application tubing. This area of variable saturation is expected to affect transport of fluorescein only for early times, but may lead to sustained deposition for colloids.

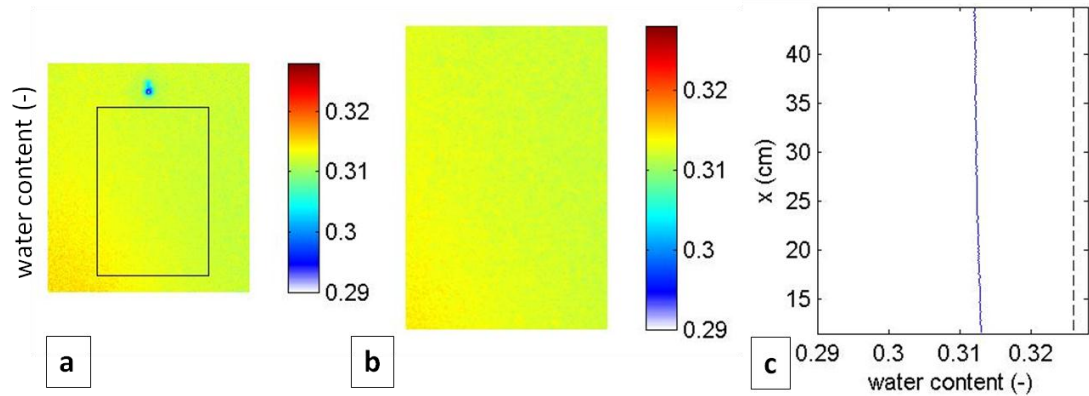


Figure 5.25 Water content full image (a), cropped area (b), and transect (c) of 12/3/07 sand pack while emplaced with  $10^1$  ppm calibration plume. The cropped area measures 22.3cm wide by 27.3cm long.

Fluorescein concentrations in calibration experiment 12 are shown at three times (Figure 5.26) under downward flow, where (a) is taken at the same condition as shown in Figure 5.25a. Data images in this section measure 40.2cm wide x 45.1cm long, and transects were extracted from single value image profiles in the location of diagrammed lines (not averages across the cropped image as was done in the previous section).

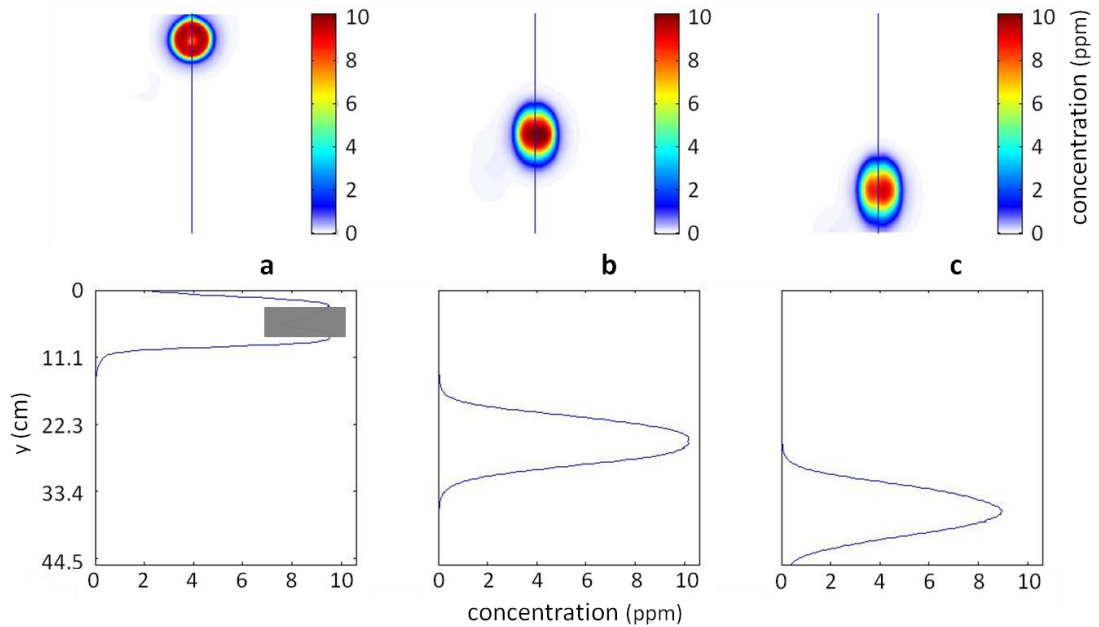


Figure 5.26 Longitudinal transects through 10ppm fluorescein plume at three time steps (a-c) under downward flow. Shaded rectangle is area of data where concentration measurements were affected by the plume application tubing.

Using  $t = 138\text{s}$  and  $u = 0.182$ , Equation 36 was fit (Figure 5.27) to the transect in Figure 5.26b.  $D_L$ ,  $D_T$ , and  $\lambda$  were obtained by minimizing least squares error (Table 5.6). Calculations of  $\alpha_L$  and  $\alpha_T$  by Equation 26 are included in the table for comparison to previous experiments.

Table 5.6 Fitted parameters from 12/3/07 fluorescein transects modeled using Equation 36.

initial mass per length, $M$ (mg/cm)	longitudinal dispersion coefficient, $D_L$ ( $\text{cm}^2/\text{s}$ )	longitudinal dispersivity, $\alpha_L$ (cm)	transverse dispersion coefficient, $D_T$ ( $\text{cm}^2/\text{s}$ )	transverse dispersivity, $\alpha_T$ (cm)	retardation factor, $R$ (-)	decay coefficient, $\lambda$ ( $\text{s}^{-1}$ )
0.200	$3.70 \times 10^{-2}$	$6.75 \times 10^{-3}$	$2.50 \times 10^{-2}$	$4.56 \times 10^{-3}$	1	$2.20 \times 10^{-4}$

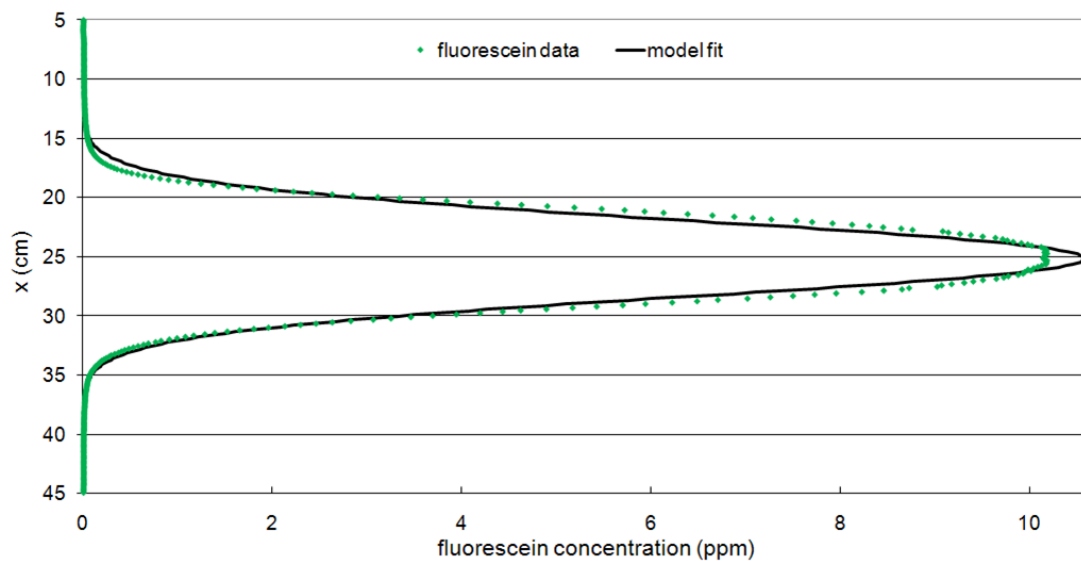


Figure 5.27 Longitudinal transect of fluorescein concentrations fit using Equation 36.

Transverse transects of fluorescein concentration were taken through images from the same experiment (Figure 5.28) in order to obtain replicate parameter estimates. The two-dimensional solution has the capacity to predict spreading both longitudinally and transversely and good agreement between the two fits increases confidence in the fitted parameters. Discrepancies in the fit are due to the assumption of zero plume radius at time = 0.

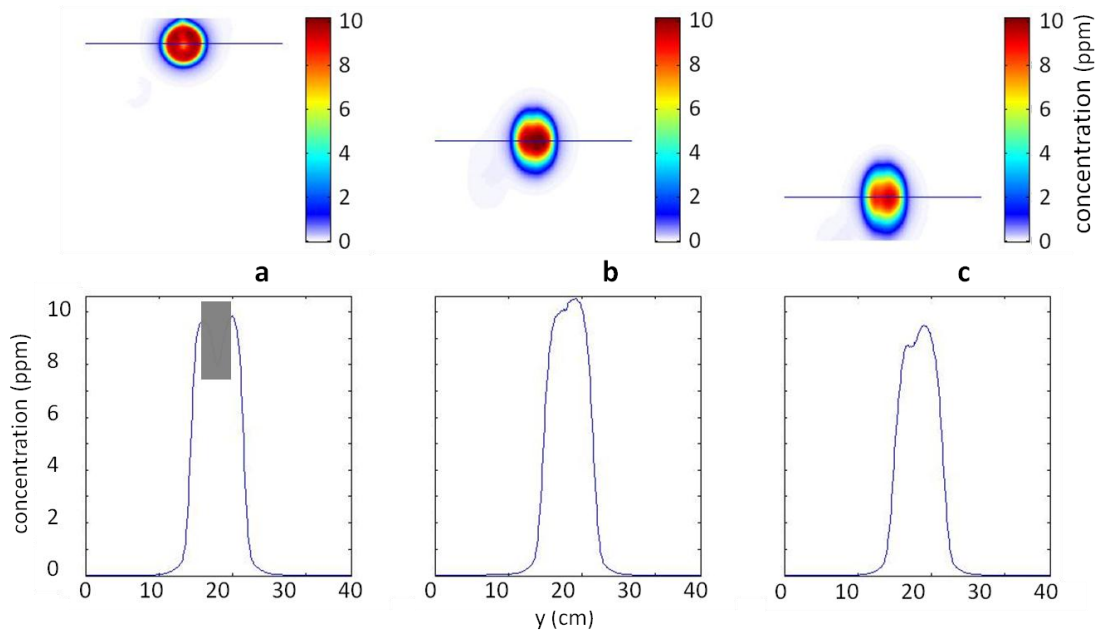


Figure 5.28 Transverse fluorescein concentration transects through the longitudinal center of mass of the 12/3/07 10ppm calibration plume at three time steps (a-c) under downward flow. Shaded rectangle is area of data where concentration measurements were affected by the plume application tubing.

Using model parameters fit to the longitudinal data (Table 5.6), Equation 36 was fit (Figure 5.29) to the transect in Figure 5.28b. The sum of squared errors was smaller for the longitudinal data than for the transverse data (Table 5.8).

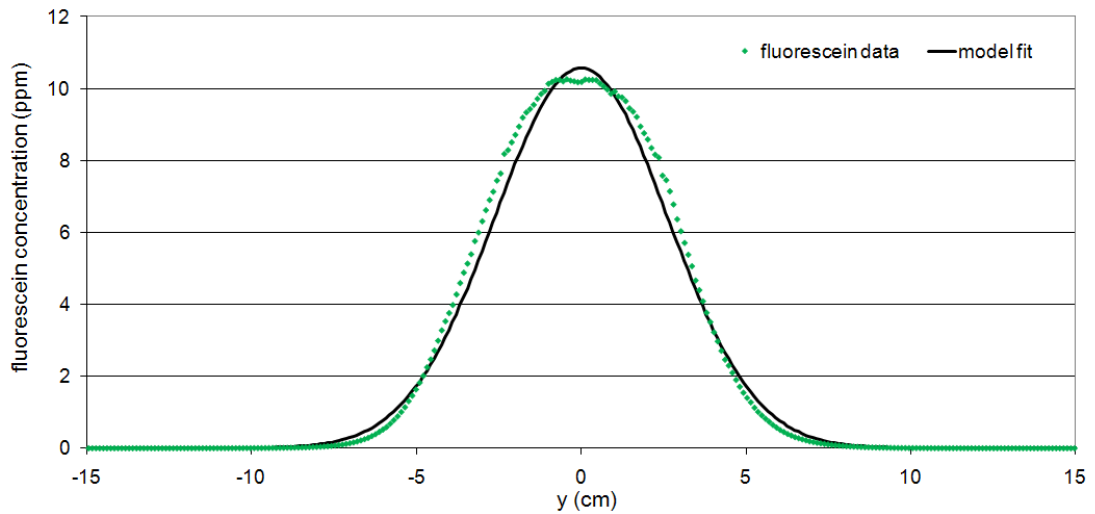


Figure 5.29 Transverse transect of fluorescein concentration fit using Equation 36.

Images and longitudinal transects of colloid concentration from 12/3/07 at three times (Figure 5.30) showed colloid deposition that may be a result of unsaturated conditions in the sand pack at the tubing outlet (seen as the faint bluish-grey shading above the bulk of the plume).

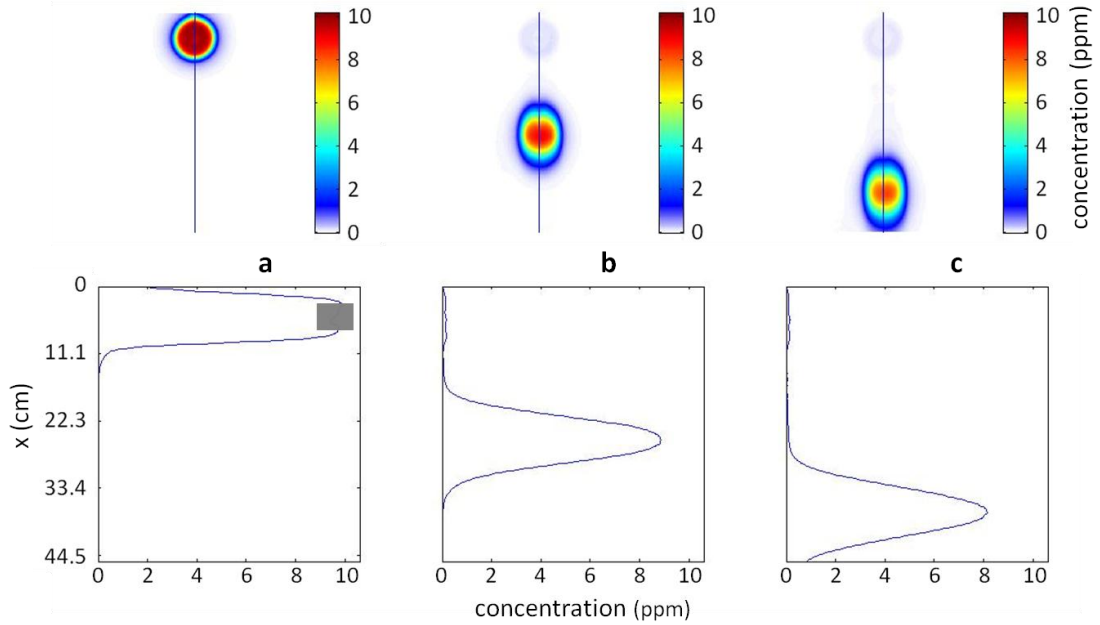


Figure 5.30 Longitudinal transects through 10ppm colloid plume at three time steps (a-c) under downward flow. Shaded rectangle is area of data where concentration measurements were affected by the plume application tubing. Deposition for colloids is seen in the bluish grey shading above the plume in b and c.

In the same fashion as was done for the one-dimensional solution, the deposition coefficient  $\mathcal{K}(\text{s}^{-1})$  was used in place of the fluorescein decay coefficient  $\lambda(\text{s}^{-1})$  in Equation 36 yielding:

$$C(x, y, t) = \frac{M \exp(-Kt)}{4\pi t \theta \sqrt{D_L D_T}} \exp\left(-\frac{(x - ut/R)^2}{4D_L t/R} - \frac{y^2}{4D_T t/R}\right) \quad (37)$$

Using the model parameters nearly identical to those shown in Table 5.7, Equation 37 was fit (Figure 5.31) to the transect in Figure 5.30b. The parameters used were the same as for fluorescein (Table 5.6) with the exception of  $R$  and  $\mathcal{K}$  which help to explain the deposition of colloids visible in Figure 5.30b.

Table 5.7 Fitted parameters from 12/3/07 colloid transects modeled using Equation 37.

initial mass per length, $M$ (mg/cm)	longitudinal dispersion coefficient, $D_L$ (cm <sup>2</sup> /s)	longitudinal dispersivity, $\alpha_L$ (cm)	transverse dispersion coefficient, $D_T$ (cm <sup>2</sup> /s)	transverse dispersivity, $\alpha_T$ (cm)	retardation factor, $R$ (-)	deposition coefficient, $\mathcal{K}$ (s <sup>-1</sup> )
0.200	$3.70 \times 10^{-2}$	$6.93 \times 10^{-3}$	$2.50 \times 10^{-2}$	$4.56 \times 10^{-3}$	$9.84 \times 10^{-1}$	$2.20 \times 10^{-2}$

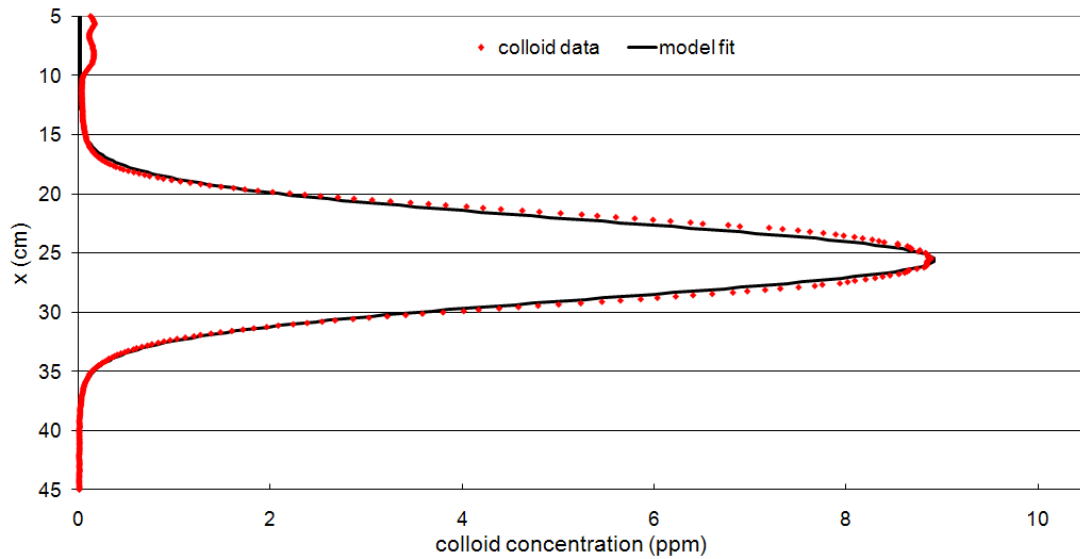


Figure 5.31 Longitudinal colloid concentration transect fit by Equation 36.

Transverse transects of colloid concentration were taken through the center of mass in the same images (Figure 5.32) in order to obtain replicate parameter estimates.

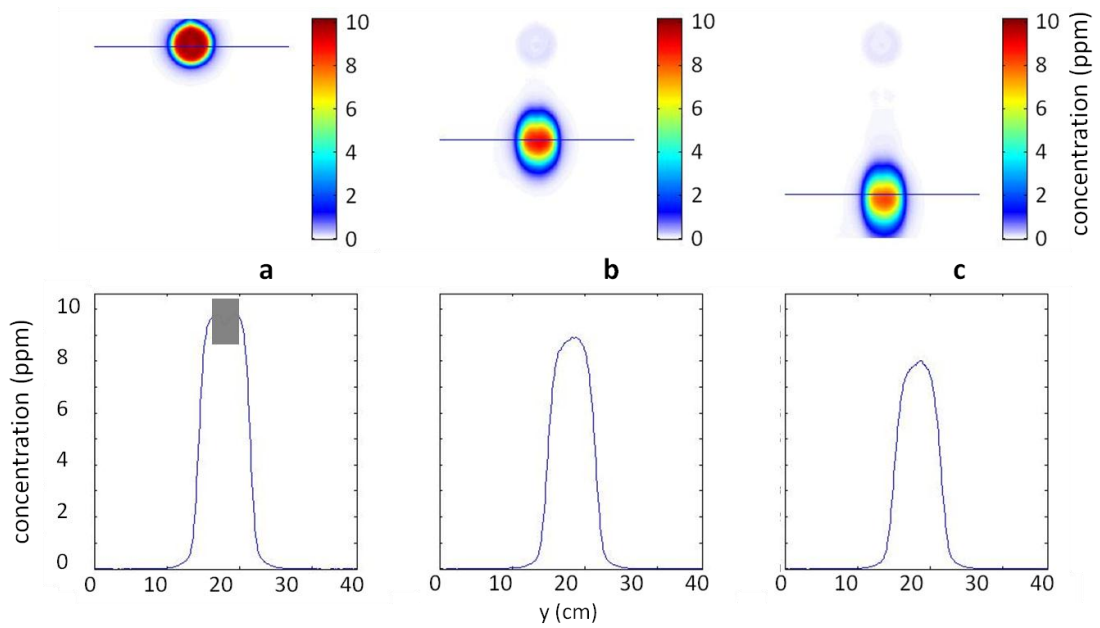


Figure 5.32 Transverse colloid concentration transects through the longitudinal center of mass of the 12/3/07 10ppm calibration plume at three time steps (a-c) under downward flow. Shaded rectangle is area of data where concentration measurements were affected by the plume application tubing.

Using the same model parameters as were used for the longitudinal data (Table 5.7), Equation 37 was fit to the transect data in Figure 5.32b. The model fits the peak, minimum, and middle concentrations of the curve, but represents less well the transitions from high to low concentrations (Figure 5.33).

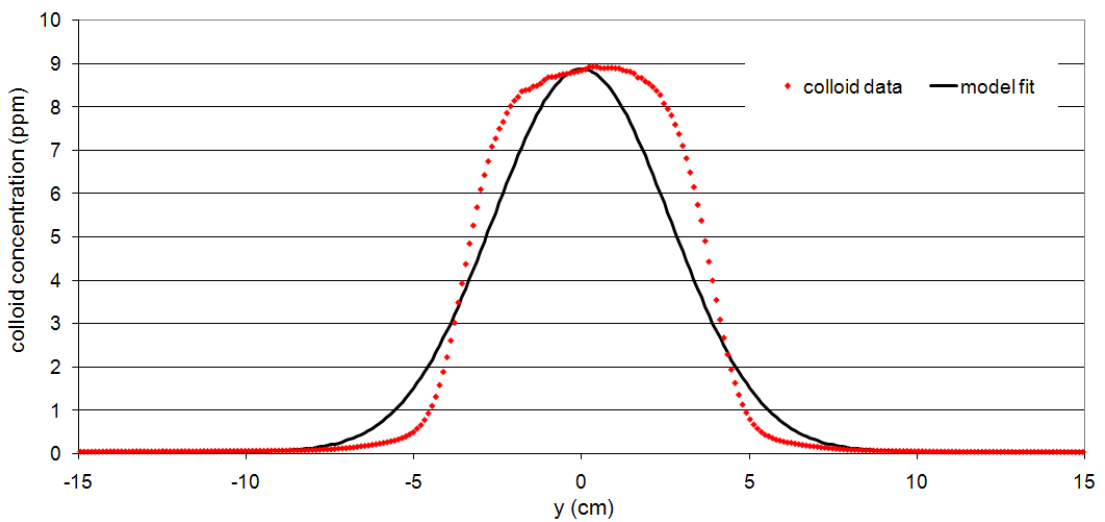


Figure 5.33 Transverse transect of colloid concentration fit by Equation 36.

The same input parameter values were used to model both fluorescein and colloids for this experiment. The sum of squared errors was smaller for the model fit to the longitudinal transect data than for the transverse transect data, both for fluorescein and for colloids (Table 5.8). The fit to the transverse data is worse than the fit to the longitudinal data because transverse dispersion is roughly ten times less than longitudinal dispersion. The assumption of zero plume radius at time = 0 became acceptable over time as the plume spread along the direction of flow. Dispersion had smoothed the flat central area of the plume. However, after this duration of transport, the correct plume shape was not achieved in the y-direction. The solution could be modified to better fit these data through convolution over the area of the plume.

Table 5.8 Error associated with fit of the two-dimensional models (Equation 36 for fluorescein, Equation 37 for colloids) to 12/3/07 transport data.

	fluorescein longitudinal	fluorescein transverse	colloids longitudinal	colloids transverse
error, sse (ppm <sup>2</sup> )	4.85x10 <sup>1</sup>	5.75x10 <sup>3</sup>	2.15x10 <sup>1</sup>	1.54x10 <sup>2</sup>
number of data points, n (-)	408	361	408	361

### ***Discussion of Derived Parameters***

Table 5.9 shows the range of fitted values obtained for transport experiments presented in this chapter. The computed colloid diffusion coefficients were smaller than those for fluorescein due to the colloid particles larger size. A literature value for fluorescein molecular diffusion in water at 21.5°C is  $D_{d,f} = 4.9 \times 10^{-6} \text{ cm}^2/\text{s}$  [Rani *et al.*, 2005]. A literature value for 1µm diameter colloids diffusion coefficient in bulk water is  $D_{d,c} = 3.2 \times 10^{-9} \text{ cm}^2/\text{s}$  [Baumann *et al.*, 2010]. Another researcher found diffusion coefficients for 0.5µm latex colloids in water to range from 1 to  $3 \times 10^{-8} \text{ cm}^2/\text{s}$  depending on temperature [Carlsson, 2004]. For comparison to our experimentally derived values, these values must be converted to effective diffusion coefficients to account for the physical effect of the pore network on diffusion. The literature value for fluorescein molecular diffusion was used to solve for  $\tau$  by setting it's effective value equal to our experimentally-derived value giving  $\tau = 4.3$  by Equation 19. This value

was then used to convert the literature value for colloids to an effective diffusion coefficient giving  $D^* = 7.44 \times 10^{-10} \text{ cm}^2/\text{s}$ . This value is almost three orders of magnitude smaller than our experimentally derived value. The reason for this large discrepancy is unknown.

Longitudinal dispersivities calculated by model fitting with Equations 28 and 31 (one-dimensional solution) ranged from  $1.10 \times 10^{-1}$  to  $2.37 \times 10^{-1} \text{ cm}$  (Table 5.9). Longitudinal and transverse dispersion coefficients ( $\text{cm}^2/\text{s}$ ) calculated by model fitting with Equations 36 and 37 (two-dimensional solution) (Table 5.6) were divided by the pore fluid velocity ( $\text{cm}/\text{s}$ ) to attain longitudinal and transverse dispersivities ( $\text{cm}$ ) by Equation 35. The longitudinal dispersivities thus attained ( $\alpha_L = 6.75\text{-}6.93 \times 10^{-3} \text{ cm}$ ) were smaller than the values calculated by fitting the one-dimensional model. The corresponding transverse dispersivity ( $\alpha_T = 4.56 \times 10^{-3} \text{ cm}$ ) was  $\sim 67\%$  of  $\alpha_L$  for the same experiment. In field experiments, transverse dispersivities are generally expected to be lower than longitudinal dispersivities by a factor of 5-20 [Freeze and Cherry, 1979], but our value is not unreasonable.

Dispersivities in general for sandy homogeneous materials range from 0.01 to 1cm [Freeze and Cherry, 1979]. A literature value for dispersivity in 30/40 Accusand is  $\alpha_L = 2 \times 10^{-2} \text{ cm}$  [Cortis et al., 2006]. In packed columns, the dispersivity may be taken as equal to the representative grain size [Appelo and Postma, 2005]. For reference then, the mean diameter of the sand grains used in our experiments was  $5.32 \times 10^{-2} \text{ cm}$  [Schroth et al., 1996]. The discrepancy between our calculated values and those cited from the literature is not a concern as it varies widely, and it is scale-dependant [Maidment, 1993].

As several previous studies have shown that fluorescein is a conservative (i.e. nonsorbing) solute [eg. Smart and Laidlaw, 1977], the retardation factor for fluorescein was assumed throughout this chapter to be one. The retardation factor was used as a fitting parameter for colloid data and found to range from  $9.84 \times 10^{-1}$  to  $1.31 \times 10^0$ . Colloid retardation values have been reported in the literature to range from  $4.6 \times 10^{-1}$  to  $3.3 \times 10^0$  due to the broad range of processes affecting colloid transport [Powelson et al., 1993]. Colloids are capable of travelling slower than the bulk fluid ( $R > 1$ ) due to their

large size and propensity for deposition. And, when negatively charged (as in these experiments), they are also capable of travelling faster than the bulk fluid ( $R < 1$ ) due to charge exclusion

[*Sirivithayapakorn and Keller, 2003a*]

The fluorescein decay coefficient derived in this work is difficult to compare with literature findings due to the very specific nature of the illumination. The coefficient was attained several times in this chapter and was the smallest for the photodegradation experiment (Figure 5.11). Image data of the photodegradation process yielded decay coefficients for fluorescein that were smaller than the other estimates, which may be due differences between constant or intermittent illumination on fluorescein photodegradation or to the very different number of data points used in the various fits .

The fitted colloid deposition coefficients had a fairly narrow range, and the ability of  $R$  and  $\mathcal{K}$  to describe colloid depositional processes has some interesting implications. Many studies have been conducted to model the transport of colloids in porous media, and the deposition process has been described using combinations of several difficult-to-measure parameters [eg. *Johnson and Elimelech, 1995*]. The effect of deposition may be seen in these data, especially in the deviation of the data from the model in Figure 5.33. The use of the retardation factor and the coefficient  $\mathcal{K}$  in these analyses makes accessible the measurement and coarse prediction of colloid deposition. More complex solutions could be used in future experiments to interpret transport images with greater precision.

Table 5.9 Summary of fitted parameters obtained from transport experiments.

	diffusion coefficient, $D^*$ ( $\text{cm}^2/\text{s}$ )	longitudinal dispersivity, $\alpha_L$ (cm)	transverse dispersivity, $\alpha_T$ (cm)	retardation factor, $R$ (-)	decay coefficient, $\lambda$ ( $\text{s}^{-1}$ )	deposition coefficient, $\mathcal{K}$ ( $\text{s}^{-1}$ )
<b>fluorescein</b>	1.14x10 <sup>-6</sup> to 2.85x10 <sup>-6</sup>	6.75x10 <sup>-3</sup> to 2.03x10 <sup>-1</sup>	4.56x10 <sup>-3</sup>	1	2.60x10 <sup>-5</sup> to 8.45x10 <sup>-4</sup>	--
<b>colloids</b>	1.70x10 <sup>-7</sup> to 5.42x10 <sup>-7</sup>	6.93x10 <sup>-3</sup> to 2.37x10 <sup>-1</sup>	4.56x10 <sup>-3</sup>	9.84x10 <sup>-1</sup> to 1.31x10 <sup>0</sup>	--	1.87x10 <sup>-3</sup> to 2.20x10 <sup>-2</sup>

The flow rate for each experiment was measured through the use of a calibrated peristaltic pump. The volumetric flow rates (mL/min) were converted to pore water velocities using sand pack cross sectional area and porosity. These velocities are compared to the derived values attained through fitting of the transport model to the image data and were in close agreement (Table 5.10).

Table 5.10 Flow rate comparison for transport experiments.

	10/9/07	6/29/08	12/3/07
peristaltic pump measured flow rate, $\tilde{u}$ (cm/s)	0.182	0.105	0.182
fitted pore water velocity, $u$ (cm/s)	0.228	0.110	0.182

### ***Two-Dimensional Flow, Two-dimensional Transport***

When the sand pack is heterogeneous, i.e. contains more than one porous medium, assumptions used to derive analytical solutions to the advection-dispersion equation presented above are violated and the solutions cannot be used to model transport behavior. Instead, fluorescein and colloid concentrations obtained during the experiment described below were compared with a numerical simulation performed using Hydrus2D software [Šimůnek *et al.*, 1996]. In Hydrus2D, the flow and transport equations are solved numerically using Galerkin-type linear finite element schemes [Šimůnek *et al.*, 2006]. The governing equation used for solute transport is:

$$\frac{\partial \theta C}{\partial t} = \frac{\partial}{\partial x_i} \left( \frac{D_{ij}}{R} \frac{\partial \theta C}{\partial x_j} \right) - \frac{u_i}{R} \frac{\partial C}{\partial x_i} - \lambda \theta C \quad (38)$$

where  $D_{ij}$  (cm<sup>2</sup>/s) is an effective dispersion coefficient tensor, and  $u_i$ (cm/s) are the velocities in the  $i$  directions.

On 8/17/06, a plume of 5ppm colloids was applied to a 40/50 grade Accusand sand pack (matrix) containing a sloping inclusion of 12/20 grade Accusand. Flow was initiated downwards at 0.182cm/s

and sequential images were collected. A simulation was created to model water flow and solute transport through the fine matrix and across the coarse inclusion, using geometry identical to the experiment. Average values of transport parameters obtained above from fluorescein experimental data were used in the model, and the same values were used for both sand grades. The longitudinal dispersivity was 0.196cm, the transverse dispersivity was 0.137cm, and the diffusion coefficient was  $2 \times 10^{-6} \text{ cm}^2/\text{s}$ . The simulation was run for 100s using  $R = 1$ , and no reaction or deposition. The vanGenuchten-Mualem hydraulic model was used to simulate water flow. Parameters relevant to saturated flow are shown in Table 5.11, where  $\theta_s(-)$  is the saturated water content,  $K_{\text{sat}}$  (cm/s) is the saturated hydraulic conductivity,  $d$ (mm) is the sand grain diameter, and  $\rho_b(\text{g}/\text{cm}^3)$  is the bulk density.

Table 5.11 Input parameters relevant to saturated flow for materials Hydrus2D simulation.

	$\theta_s(-)$	$K_{\text{sat}}$ (cm/s)	$d$ (mm)	$\rho_b(\text{g}/\text{cm}^3)$
matrix	0.348	$7.22 \times 10^{-2}$	0.359	2.663
inclusion	0.348	$5.03 \times 10^{-1}$	1.11	2.665

The simulation was set up to model transport of a nonsorbing ( $R = 1$ ), non-decaying ( $\lambda = 0$ ) tracer, and we are comparing the results to colloid data. The differences between colloid data and simulated tracer concentrations can be seen clearly even at early time where colloids are deposited in the sand and are left behind plume as it moves downward. By Figure 5.34c, there is a significant area of dark blue remaining at the point of injections, as compared with Figure 5.34f. At the interface of the two sand layers, colloids appeared to respond similarly to the simulated tracer with an initial divergence towards the coarse sand, perhaps due to a high local velocity, and subsequent redirection along the interface. Colloids also appear to be moving ahead of the simulated tracer plume by panel (c).

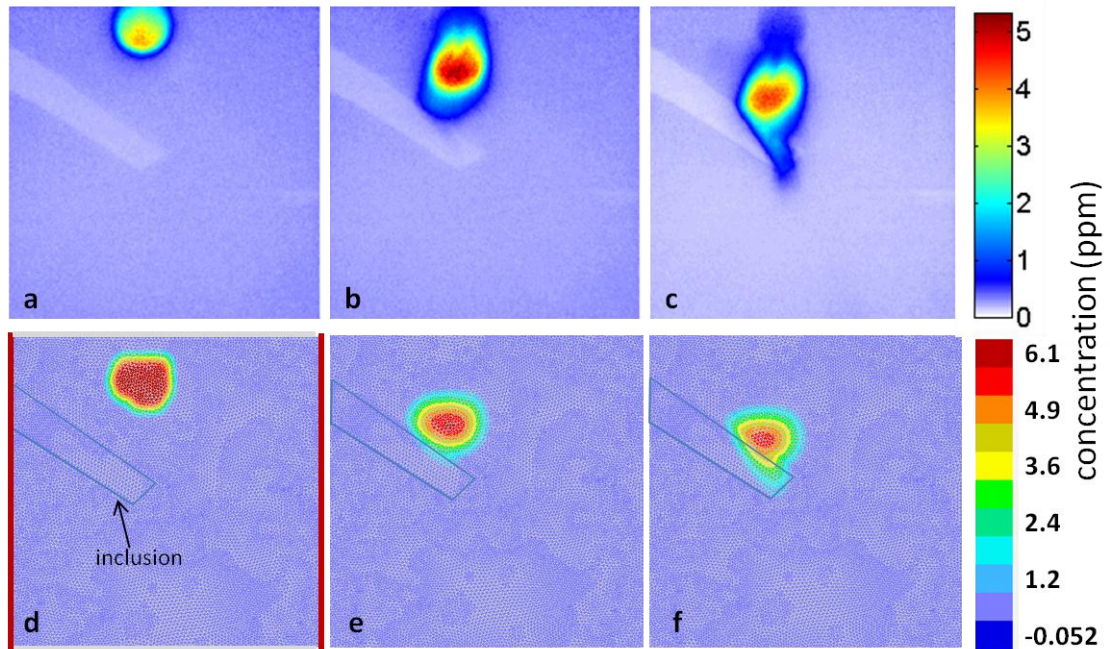


Figure 5.34 Colloid concentration images (a-c) matched morphologically with simulated tracer concentrations (d-f) at three early times. Panel d shows boundary conditions-- vertical edges (red bars) are no flux, and horizontal edges (grey bars) are 0.182 and -0.182 constant flux boundaries on top and bottom respectively.

Experimental images of colloid concentration compared with simulated tracer concentrations at three late times (Figure 5.35) show colloid data demonstrating larger longitudinal spreading than the simulated plume. Deposition is observed at the top of panels a-c, where none exists in panels d-f. Less transverse spreading is observed in the data than in the simulation, where the tracer plume appears broader than the colloid plume. Behavior through the inclusion appear similar for colloids and solute, yet deposition and subsequent straining would be expected for colloids at the transition from inclusion (coarse) to matrix (fine) [Silliman, 1995]. This would likely be evident at late time, but not possible to analyze quantitatively here as calibration equations were not developed in this work for multiple sand grades.

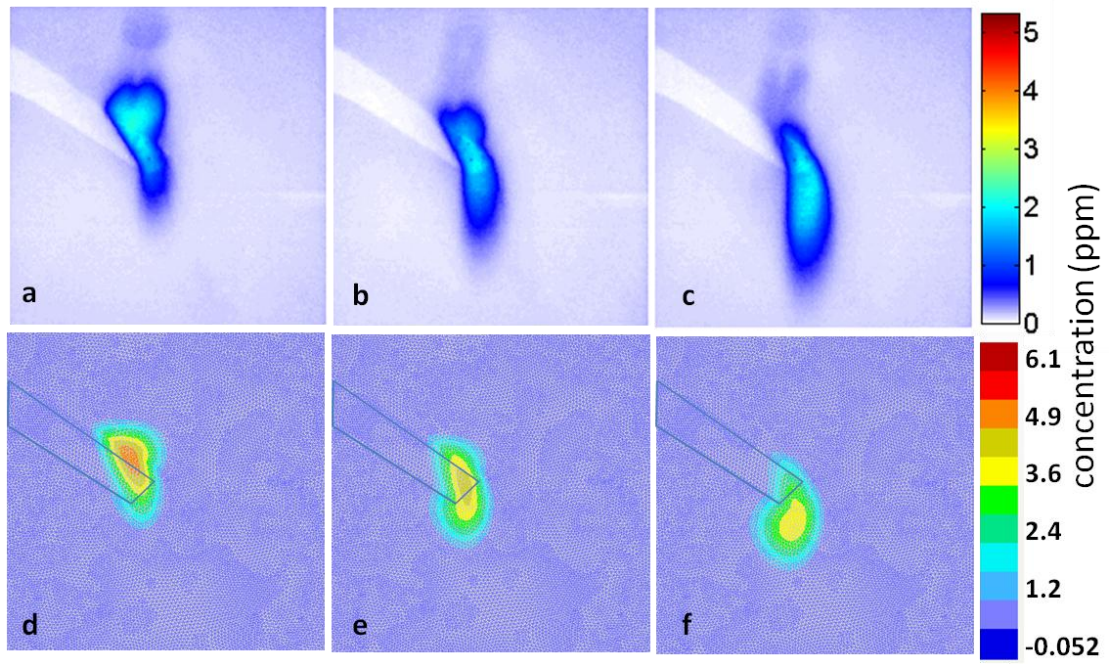


Figure 5.35 Colloid concentration images (a-c) matched with simulated tracer concentrations (d-f) at three late times.

## Chapter Six: Conclusions

Contaminant transport is an area of hydrology research that is important to human health; contamination comes from many sources and takes many forms [Freeze and Cherry, 1979]. Many contaminants are dissolved species (eg. radionuclides) and colloids are sometimes considered contaminants (eg. pathogens). Additionally, colloids are known to act as carriers for the transport of toxic species bound to their surfaces [McCarthy and Zachara, 1989]. The synthetic latex colloids used in this work may be used as an analog for certain types of colloidal contaminants. Colloid transport behavior deviates from that of a nonsorbing tracer like fluorescein due to the interaction of colloids with the surfaces of the porous media [Elimelech and O'Melia, 1990]. Latex colloids and fluorescein are good models to demonstrate this deviation, but predicting transport of naturally occurring solutes and colloids, especially microorganisms, must be expected to require additional levels of complexity.

A visualization system was built that could collect images used to quantify volumetric water content, fluorescein concentrations, and colloid concentrations during transport experiments in prepared sand packs. Technical improvements to the system made the method more powerful than previous versions. The adaptation of the system to multiple spectra allowed for imaging and analysis of a variety of transport scenarios involving water tracer, colloids, and variable saturation. These improvements were made possible through the use of specialized optical components. Multiple dye signals, multiple wavelengths of LEDs, and optical filters allowed detection of light and fluorescence at specific wavelengths sensitive to water content or dye concentration. Housing the entire system in a dark enclosure reduced background noise and allowed for longer exposure times, facilitating detection of fluorescein and colloids at much lower concentrations than in previous systems.

In a series of calibration experiments, detection was demonstrated of fluorescein over the concentration range  $10^{-2}$  to  $10^2$  ppm and of colloids over the concentration range  $10^{-1}$  to  $10^3$  ppm. By contrast, the detection limit for fluorescein in a micro-scale imaging system was  $5 \times 10^0$  ppm [Pokhriyal

*et al.*, 2010], and a meso-scale system similar to ours, which used reflexive imaging, reported a detection limit of  $7.6 \times 10^{-1}$  ppm for fluorescein and  $2.1 \times 10^0$  ppm for colloids [Bridge *et al.*, 2006]. The lower detection limit for colloid concentration in this work was improved three orders of magnitude from  $10^2$  ppm achieved by the previous system developed in our laboratory [Weisbrod *et al.*, 2003b]. Detection at these low concentrations is largely due to the improvement in signal to noise ratio. For colloids at a concentration of  $10^0$  ppm, the signal to noise ratio was increased over the course of the system developments reported here from 5.29 (3/2/07) to 58.82 (6/29/08)—a 91% improvement in the strength of the colloid signal vs. the background noise.

Calibration of this system over the broad range of concentrations was demonstrated seventeen times, and shown to produce a consistent trend in the relationship between processed intensity and concentration. A calibration equation was developed that can be used to compute fluorescein and colloid concentrations from images collected from the large central area of the sand pack. This system can detect a wider range of concentrations than any other system, in addition to which it can detect multiple signals and quantify them over larger spatial areas. This capability allows for research on process occurring over Darcy-scale heterogeneities. Imperfections in image processing remain, but the central region of the image area yields high-quality data. Improvements in data quality may be achievable through ray tracing and consideration of optical distortion potentially caused by bidirectional reflectance distributions.

Several transport experiments were conducted to demonstrate the utility of this system. Diffusion coefficients were determined using the method of moments on data from a no-flow experiment. Dispersivities were determined for fluorescein and colloids using advection-dispersion model fitting to data from a one-dimensional flow, one-dimensional transport experiment. Dispersivities were checked by fitting of the two-dimensional advection-dispersion model to longitudinal and transverse transects through data from a one-dimensional flow, two-dimensional transport experiment. Decay coefficients

were calculated to represent loss of fluorescein concentrations due to photodegradation. Retardation factors and deposition coefficients were used to represent the difference between fluorescein and colloid transport behavior. Parameters derived through model fits to these experiments were used as input parameters to a numerical simulation of a two-dimensional flow, two-dimensional transport experiment. A qualitative comparison was drawn between colloid transport data and the simulation of a conservative tracer. Calibration of fluorescein and colloids in multiple textures of sand would allow for quantitative comparison between data and simulated concentrations over textural inclusions such as that used in this experiment. Calibration of fluorescein and colloid concentration in unsaturated media also remains a practical goal, which would allow for hypothesis testing in the area of vadose zone transport.

Future research with this system could include a broad array of transport experiments including more complex sand pack heterogeneities, variation of solution chemistry, transport in unsaturated porous media, and use of a variety of colloid sizes and surface properties. This work advances the capabilities of quantitative, two-dimensional, meso-scale, optical imaging, which in turn allows for more powerful study of contaminant transport. Through increased knowledge of this subject, water quality and human and environmental health may be improved. Testing of pore-scale theories is possible with this system, and may serve as a link between fundamental behavior and bulk transport. Demonstration at the field scale of predictions generated using light-transmission imaging system data must however take into consideration the idealized nature of the imaging system. Natural systems will always be infinitely more complex than what can be understood in the laboratory, and care must always be taken in extrapolation.

## BIBLIOGRAPHY

- Abarca, E., and T. P. Clement (2009), A novel approach for characterizing the mixing zone of a saltwater wedge, *Geophysical Research Letters*, 36, 5.
- Aeby, P., et al. (1997), Image analysis for determination of dye tracer concentrations in sand columns, *Soil Science Society of America Journal*, 61(1), 33-35.
- Aeby, P. (1998), Quantitative Fluorescence Imaging of Tracer Distributions in Soil Profiles, ETH.
- Aeby, P., et al. (2001), Fluorescence Imaging of Tracer Distributions in Soil Profiles, *Environmental Science & Technology*, 35(4), 753-760.
- Albrecht, A., et al. (2003), Behavior of a surface applied radionuclide and a dye tracer in structured and repacked soil monoliths, *J. Environ. Radioact.*, 68(1), 47-64.
- Altman, S. J., et al. (2005), Evaluation of synchrotron X-ray computerized microtomography for the visualization of transport processes in low-porosity materials, *Journal of Contaminant Hydrology*, 78(3), 167-183.
- Amitay-Rosen, T., et al. (2005), Magnetic resonance imaging and quantitative analysis of particle deposition in porous media, *Environmental Science & Technology*, 39(18), 7208-7216.
- Anderson, J. L., and J. Bouma (1973), Relationships Between Saturated Hydraulic Conductivity and Morphometric Data of an Argillic Horizon, *Soil Sci Soc Am J*, 37(3), 408-413.
- Andreini, M. S., and T. S. Steenhuis (1990), Preferential paths of flow under conventional and conservation tillage, *Geoderma*, 46(1-3), 85-102.
- Appelo, C. A. J., and D. Postma (2005), *Geochemistry, groundwater and pollution*, Balkema, Leiden; New York.
- Auset, M., and A. A. Keller (2004), Pore-scale processes that control dispersion of colloids in saturated porous media, *Water Resources Research*, 40(3), Art. No. W03503.
- Auset, M., et al. (2005), Intermittent filtration of bacteria and colloids in porous media, *Water Resources Research*, 41(9).
- Auset, M., and A. A. Keller (2006), Pore-scale visualization of colloid straining and filtration in saturated porous media using micromodels, *Water Resources Research*, 42(12).
- Auzerais, F., et al. (1996), Transport in sandstone: a study based on three dimensional microtomography, *Geophysical Research Letters*, 23, 705-708.
- Banninger, D. (2004), Remote soil texture recognition, ETH, Zurich.
- Banninger, D., et al. (2005), Effect of water saturation on radiative transfer, *Vadose Zone Journal*, 4(4), 1152-1160.
- Banninger, D., et al. (2006), Modelling the effect of soil water content and sorption on dye-tracer fluorescence, *European Journal of Soil Science*, 57(6), 808-815.
- Barataud, F., et al. (1999), Measurement of soil water diffusivity of an undisturbed forest soil using dual-energy gamma radiation technique, *Soil Science*, 164(7), 493-502.
- Barth, G. R., et al. (2001a), Predictive modeling of flow and transport in a two-dimensional intermediate-scale, heterogeneous porous medium, *Water Resources Research*, 37(10), 2503-2512.

- Barth, G. R., et al. (2001b), A new tracer-density criterion for heterogeneous porous media, *Water Resources Research*, 37(1), 21-31.
- Bauer, R. D., et al. (2008), Mixing-controlled biodegradation in a toluene plume - Results from two-dimensional laboratory experiments, *Journal of Contaminant Hydrology*, 96(1-4), 150-168.
- Bauer, R. D., et al. (2009a), Enhanced biodegradation by hydraulic heterogeneities in petroleum hydrocarbon plumes, *Journal of Contaminant Hydrology*, 105(1-2), 56-68.
- Bauer, R. D., et al. (2009b), Two-dimensional flow-through microcosms - Versatile test systems to study biodegradation processes in porous aquifers, *Journal of Hydrology*, 369(3-4), 284-295.
- Baumann, T., and C. J. Werth (2004), Visualization and Modeling of Polystyrol Colloid Transport in a Silicon Micromodel, *Vadose Zone Journal*, 3(2), 434-443.
- Baumann, T., and C. J. Werth (2005), Visualization of colloid transport through heterogeneous porous media using magnetic resonance imaging, *Colloids and Surfaces a-Physicochemical and Engineering Aspects*, 265(1-3), 2-10.
- Baumann, T., and R. Niessner (2006), Micromodel study on repartitioning phenomena of a strongly hydrophobic fluorophore at a colloid/1-octanol interface, *Water Resources Research*, 42(12), 9.
- Baumann, T., et al. (2010), Colloid dispersion on the pore scale, *Water Research*, 44(4), 1246-1254.
- Baveye, P. (2010), Comment on "Comparison of bioclogging effects in saturated porous media within one- and two-dimensional flow systems" by Martin Thullner, *Ecol. Eng.*, 36(6), 835-836.
- Bell, J., et al. (1990), Rapid moisture measurements in thin sand slab, paper presented at International Meeting of the American Society of Agricultural Engineers, Chicago, IL.
- Berkowitz, B., et al. (2004), Impact of the Capillary Fringe on Local Flow, Chemical Migration, and Microbiology, *Vadose Zone Journal*, 3, 534-548.
- Billa, E., et al. (1999), Fluorescence analysis of paper pulps, *Bioresource Technology*, 67(1), 25-33.
- Blume, T., et al. (2002), Permeability changes in layered sediments: Impact of particle release, *Ground Water*, 40(5), 466-474.
- Bob, M. M., et al. (2008), A modified light transmission visualization method for DNAPL saturation measurements in 2-D models, *Advances in Water Resources*, 31(5), 727-742.
- Booltink, H. W. G., and J. Bouma (1991), Physical and morphological characterization of bypass flow in a well-structured clay soil, *Soil Science Society of America Journal*, 55(5), 1249-1254.
- Bouma, J., et al. (1977), The Function of Different Types of Macropores During Saturated Flow through Four Swelling Soil Horizons, *Soil Sci Soc Am J*, 41(5), 945-950.
- Bradford, S., and M. Bettahar (2006), Concentration dependent transport of colloids in saturated porous media, *Journal of Contaminant Hydrology*, 82, 99-117.
- Bridge, J. W., et al. (2006), Noninvasive quantitative measurement of colloid transport in mesoscale porous media using time lapse fluorescence imaging, *Environmental Science & Technology*, 40(19), 5930-5936.
- Bridge, J. W., et al. (2007), High-resolution measurement of pore saturation and colloid removal efficiency in quartz sand using fluorescence Imaging, *Environmental Science & Technology*, 41(24), 8288-8294.
- Bridge, J. W., and S. A. Banwart (2009), Monitoring cell transport, biofilm evolution and movement of genetic material in porous media: potential of cm-scale fluorescence imaging, *Geochimica Et Cosmochimica Acta*, 73(13), A160-A160.

- Bridge, J. W., et al. (2009), Measurement of Colloid Mobilization and Redeposition during Drainage in Quartz Sand, *Environmental Science & Technology*, 43(15), 5769-5775.
- Brovelli, A., et al. (2009), Bioclogging in porous media: Model development and sensitivity to initial conditions, *Environmental Modelling & Software*, 24(5), 611-626.
- Brown, S., et al. (1998), Experimental observation of fluid flow channels in a single fracture, *J. Geophys. Res.-Solid Earth*, 103(B3), 5125-5132.
- Brusseau, M. L., et al. (2000), Influence of heterogeneity and sampling method on aqueous concentrations associated with NAPL dissolution, *Environmental Science & Technology*, 34(17), 3657-3664.
- Brusseau, M. L., et al. (2002), Dissolution of nonuniformly distributed immiscible liquid: Intermediate-scale experiments and mathematical modeling, *Environmental Science & Technology*, 36(5), 1033-1041.
- Burns, S. E., and M. Zhang (1999), Digital image analysis to assess microbubble behavior in porous media, *J. Comput. Civil. Eng.*, 13(1), 43-48.
- Bushberg, J. T. (2002), *The essential physics of medical imaging*, Lippincott Williams & Wilkins, Philadelphia [u.a.].
- Carlsson, G. (2004), Latex Colloid Dynamics in Complex Dispersions, Dissertation thesis, Karlstad University, Karlstad, SWEDEN.
- Caruana, A., and R. A. Dawe (1996), Flow behaviour in the presence of wettability heterogeneities, *Transport in Porous Media*, 25(2), 217-233.
- Catania, F., et al. (2008), Assessment of quantitative imaging of contaminant distributions in porous media, *Experiments in Fluids*, 44(1), 167-177.
- Catania, F., and O. Paladino (2009), Optimal sampling for the estimation of dispersion parameters in soil columns using an Iterative Genetic Algorithm, *Environmental Modelling & Software*, 24(1), 115-123.
- Chao, W.-L., et al. (2000), An Analysis of the Movement of Wetting and Nonwetting Fluids in Homogeneous Porous Media, *Transport in Porous Media*, 41(2), 121-135.
- Chen, G., and M. Flury (2005), Retention of mineral colloids in unsaturated porous media as related to their surface properties, *Colloids and Surfaces a-Physicochemical and Engineering Aspects*, 256(2-3), 207-216.
- Chen, J., and B. Koopman (1997), Effect of fluorochromes on bacterial surface properties and interaction with granular media, *Applied and Environmental Microbiology*, 63, 3941-3945.
- Chen, J. D., and N. Wada (1986), Visualization of immiscible displacement in a 3-dimensional transparent porous-medium, *Experiments in Fluids*, 4(6), 336-338.
- Chen, M. R., et al. (1996), Computed tomography imaging of air sparging in porous media, *Water Resources Research*, 32(10), 3013-3024.
- Chen, Q., et al. (2002), Nuclear magnetic resonance imaging for studies of flow and transport in porous media, *Journal of Environmental Quality*, 31(2), 477-486.
- Chen, X., and J. W. Jawitz (2008), Reactive tracer tests to predict dense nonaqueous phase liquid dissolution dynamics in laboratory flow chambers, *Environmental Science & Technology*, 42(14), 5285-5291.
- Chen, X., and J. W. Jawitz (2009), Convergence of DNAPL Source Strength Functions with Site Age, *Environmental Science & Technology*, 43(24), 9374-9379.

- Chevalier, L. R., and J. Petersen (1999), Literature review of 2-D laboratory experiments in NAPL flow, transport, and remediation, *J. Soil Contam.*, 8(1), 149-167.
- Ciobanu, L., et al. (2002), 3D MR microscopy with resolution 3.7  $\mu$ m by 3.3  $\mu$ m by 3.3  $\mu$ m, *Journal of Magnetic Resonance*, 158, 178-182.
- Clausnitzer, V., and J. W. Hopmans (2000), Pore-scale measurements of solute breakthrough using microfocus X-ray computed tomography, *Water Resources Research*, 36(8), 2067-2079.
- Coles, M., et al. (1998), Pore level imaging fluid transport using synchrotron X-ray microtomography, *Journal of Petroleum Science and Engineering*, 19, 55-63.
- Conrad, S. H., et al. (2002), Bench-scale visualization of DNAPL remediation processes in analog heterogeneous aquifers: surfactant floods and in situ oxidation using permanganate, *Journal of Contaminant Hydrology*, 58(1-2), 13-49.
- Corapcioglu, M. Y., and S. Jiang (1993), Colloid-facilitated groundwater contaminant transport, *Water Resources Research*, 29(7), 2215-2226.
- Cortis, A., et al. (2006), Transport of *Cryptosporidium parvum* in porous media: Long-term elution experiments and continuous time random walk filtration modeling, *Water Resources Research*, 42(12).
- Crank, J. (1975), *The mathematics of diffusion*, Clarendon Press, Oxford.
- Crestana, S., et al. (1985), Static and dynamic 3-dimensional studies of water in soil using computed tomographic scanning, *Soil Science*, 140(5), 326-332.
- Crist, J. T., et al. (2004), Pore-scale visualization of colloid transport and retention in partly saturated porous media, *Vadose Zone Journal*, 3(2), 444-450.
- Crist, J. T., et al. (2005), Transport and retention mechanisms of colloids in partially saturated porous media, *Vadose Zone Journal*, 4(1), 184-195.
- Culligan, K. A., et al. (2004), Interfacial area measurements for unsaturated flow through a porous medium, *Water Resources Research*, 40(12).
- Cumbie, D. H., and L. D. McKay (1999), Influence of diameter on particle transport in a fractured shale saprolite, *Journal of Contaminant Hydrology*, 37(1-2), 139-157.
- Cussler, E. L. (1991), *Diffusion, mass transfer in fluid systems*, Cambridge University Press, Cambridge [Cambridgeshire]; New York.
- Darnault, C. J. G., et al. (1998), Visualization by light transmission of oil and water contents in transient two-phase flow fields, *Journal of Contaminant Hydrology*, 31(3-4), 337-348.
- Darnault, C. J. G., et al. (2001), Measurement of fluid contents by light transmission in transient three-phase oil-water-air systems in sand, *Water Resources Research*, 37(7), 1859-1868.
- Darnault, C. J. G., et al. (2002), Visualization and measurement of multiphase flow in porous media using light transmission and synchrotron X-rays, in *Ann Ny Acad Sci*, edited, pp. 103-110.
- Dathe, A., et al. (2001), The surface fractal dimension of the soil-pore interface as measured by image analysis, *Geoderma*, 103(1-2), 203-229.
- Dawe, R., et al. (2010), Microscale Visual Study of End Effects at Permeability Discontinuities, *Transport in Porous Media*, 1-16.
- Dawe, R. A., et al. (1992), Experimental investigation of capillary-pressure effects on immiscible displacement in lensed and layered porous media, *Transport in Porous Media*, 7(1), 83-101.

- de Jonge, L. W., et al. (2004a), Colloids and colloid-facilitated transport of contaminants in soils: An introduction, *Vadose Zone Journal*, 3(2), 321-325.
- de Jonge, L. W., et al. (2004b), Particle leaching and particle-facilitated transport of phosphorus at field scale, *Vadose Zone J*, 3(2), 462-470.
- de Josselin de Jong, G. (1958), Longitudinal and transverse diffusion in granular deposits, *Transactions American Geophysical Union*, 39(1), 67-74.
- Deinert, M. R., et al. (2004), Measurement of fluid contents and wetting front profiles by real-time neutron radiography, *Journal of Hydrology*, 290(3-4), 192-201.
- DeRose, P. C., and G. W. Kramer (2005), Bias in the absorption coefficient determination of a fluorescent dye, standard reference material 1932 fluorescein solution, *Journal of Luminescence*, 113(3-4), 314-320.
- Detwiler, R. L., et al. (1999), Measurement of fracture aperture fields using transmitted light: An evaluation of measurement errors and their influence on simulations of flow and transport through a single fracture, *Water Resources Research*, 35(9), 2605-2617.
- Dias, R. P., et al. (2008), Permeability analysis in bisized porous media: Wall effect between particles of different size, *Journal of Hydrology*, 349(3-4), 470-474.
- DiCarlo, D. A., et al. (1999), Lateral expansion of preferential flow paths in sands, *Water Resources Research*, 35(2), 427-434.
- DiCarlo, D. A., et al. (2006), In situ measurements of colloid transport and retention using synchrotron X-ray fluorescence, *Water Resources Research*, 42(12).
- DiCarlo, D. A., et al. (2010), Tomographic measurements of pore filling at infiltration fronts, *Advances in Water Resources*, 33(4), 485-492.
- Diehl, H., and N. Horchak-Morris (1987), Studies on fluorescein--V The absorbance of fluorescein in the ultraviolet, as a function of pH, *Talanta*, 34(8), 739-741.
- Diehl, H., and R. Markuszewski (1989), Studies on fluorescein--VII : The fluorescence of fluorescein as a function of pH, *Talanta*, 36(3), 416-418.
- DiFilippo, E. L. (2008), Investigation of Mass Flux Reduction as a Function of Source-Zone Mass Removal for Immiscible-Liquid Contaminated Aquifers University of Arivona, Tuscon, Tuscon, AZ.
- DiFilippo, E. L., et al. (2010), Impact of organic-liquid distribution and flow-field heterogeneity on reductions in mass flux, *Journal of Contaminant Hydrology*, 115(1-4), 14-25.
- Dirksen, C. (1978), Transient and steady flow from subsurface line sources at constant hydraulic head in anisotropic soil, *Trans. ASAE*, 21(5), 913-919.
- Dirksen, C., and M. J. Huber (1978), Soil-water flow model with 2-dimensional automatic gamma-ray attenuation scanner, *Water Resources Research*, 14(4), 611-614.
- Dong, W. J., and A. R. S. Selvadurai (2006), Image processing technique for determining the concentration of a chemical in a fluid-saturated porous medium, *Geotech. Test. J.*, 29(5), 385-391.
- Dror, I., et al. (2004), Effects of air injection on flow through porous media: Observations and analyses of laboratory-scale processes, *Water Resources Research*, 40(9).
- Dunn, A. M., and S. E. Silliman (2003), Air and water entrapment in the vicinity of the water table, *Ground Water*, 41(6), 729-734.
- Dunn, A. M., et al. (2005), Demonstration of microbial transport into the capillary fringe via advection from below the water table, *Journal of Hydrology*, 306(1-4), 50-58.

- Duwig, C., et al. (2008), Quantifying fluorescent tracer distribution in allophanic soils to image solute transport, *European Journal of Soil Science*, 59(1), 94-102.
- Eckert, R., et al. (2000), Near-field fluorescence imaging with 32 nm resolution based on microfabricated cantilevered probes, *Applied Physics Letters*, 77(23), 3695-3697.
- El-Alaily, N. A., and R. M. Mohamed (2003), Effect of irradiation on some optical properties and density of lithium borate glass, *Mater. Sci. Eng. B-Solid State Mater. Adv. Technol.*, 98(3), 193-203.
- Elimelech, M., and C. O'Melia (1990), Kinetics of deposition of colloidal particles in porous media, *Environmental Science & Technology*, 24(10), 1528-1536.
- Er, V., and T. Babadagli (2010), Miscible Interaction Between Matrix and Fracture: A Visualization and Simulation Study, *Spe Reservoir Evaluation & Engineering*, 13(1), 109-117.
- Ewing, R. P., and R. Horton (1999a), Quantitative color image analysis of agronomic images, *Agronomy Journal*, 91(1), 148-153.
- Ewing, R. P., and R. Horton (1999b), Discriminating dyes in soil with color image analysis, *Soil Science Society of America Journal*, 63(1), 18-24.
- Ferrand, L. A., et al. (1986), Dual-gamma attenuation for the determination of porous-medium saturation with respect to 3 fluids, *Water Resources Research*, 22(12), 1657-1663.
- Fetter, C. W. (1993), *Contaminant hydrogeology*, Macmillan, New York.
- Finno, R. J., et al. (1996), Strain localization and undrained steady state of sand, *J. Geotech. Eng.-ASCE*, 122(6), 462-473.
- Flury, M., and N. N. Wai (2003), Dyes as tracers for vadose zone hydrology, *Rev. Geophys.*, 41(1), 1002.
- Forrer, I. (1997), Solute Transport in an Unsaturated Field Soil: Visualization and Quantification of Flow Patterns Using Image Analysis, ETH.
- Forrer, I., et al. (1999), Longitudinal and lateral dispersion in an unsaturated field soil, *Water Resources Research*, 35(10), 3049-3060.
- Forrer, I., et al. (2000), Quantifying dye tracers in soil profiles by image processing, *European Journal of Soil Science*, 51(2), 313-322.
- Freeze, R. A., and J. A. Cherry (1979), *Groundwater*, Prentice-Hall, Englewood Cliffs, N.J.
- Freyberg, D. L. (1986), A natural gradient experiment on solute transport in a sand aquifer, 2. Spatial moments and the advection and dispersion of nonreactive tracers, *Water Resources Research*, 22(13), 2031-2046.
- Friendly, M. (2008), The Golden Age of Statistical Graphics, *Stat. Sci.*, 23(4), 502-535.
- Fure, A. D., et al. (2006), DNAPL source depletion: Linking architecture and flux response, *Journal of Contaminant Hydrology*, 85(3-4), 118-140.
- Gaganis, P., et al. (2005), On the evaluation of dispersion coefficients from visualization experiments in artificial porous media, *Journal of Hydrology*, 307(1-4), 79-91.
- Gao, B., et al. (2006), Pore-scale mechanisms of colloid deposition and mobilization during steady and transient flow through unsaturated granular media, *Water Resources Research*, 42.
- Gao, B., et al. (2009), Visualization of unstable water flow in a fuel cell gas diffusion layer, *Journal of Power Sources*, 190(2), 493-498.
- Garnier, P., et al. (1998), Dual-energy synchrotron X ray measurements of rapid soil density and water content changes in swelling soils during infiltration, *Water Resources Research*, 34(11), 2837-2842.

- Geistlinger, H., et al. (2006), Direct gas injection into saturated glass beads: Transition from incoherent to coherent gas flow pattern, *Water Resour. Res.*, 42(7), W07403.
- Geistlinger, H., et al. (2009), Pore-scale and continuum modeling of gas flow pattern obtained by high-resolution optical bench-scale experiments, *Water Resources Research*, 45, 15.
- Geller, E. (Ed.) (2003), *McGraw-Hill Dictionary of Scientific and Technical Terms*, 6th ed., McGraw-Hill, New York, NY.
- Ghodrati, M., and W. A. Jury (1990), A field-study using dyes to characterize preferential flow of water, *Soil Science Society of America Journal*, 54(6), 1558-1563.
- Ghodrati, M. (1999), Point measurement of solute transport processes in soil using fiber optic sensors, *Soil Science Society of America Journal*, 63(3), 471-479.
- Gimmi, T., and N. Ursino (2004), Mapping material distribution in a heterogeneous sand tank by image analysis, *Soil Science Society of America Journal*, 68(5), 1508-1514.
- Glass, R. J. (1985), A study of wetting front instability in layered porous media, Cornell, Ithaca, NY.
- Glass, R. J., et al. (1988), Wetting front instability as a rapid and far-reaching hydrologic process in the vadose zone, *Journal of Contaminant Hydrology*, 3(2-4), 207-226.
- Glass, R. J., et al. (1989a), Preferential solute transport in layered homogeneous sands as a consequence of wetting front instability, *Journal of Hydrology*, 110(1-2), 87-105.
- Glass, R. J., et al. (1989b), Wetting front instability 1. theoretical discussion and dimensional analysis, *Water Resources Research*, 25(6), 1187-1194.
- Glass, R. J., et al. (1989c), Wetting front instability 2. experimental determination of relationships between parameters and two-dimensional unstable flow field behavior in initially dry porous media, *Water Resources Research*, 25(6), 1195-1207.
- Glass, R. J., et al. (1989d), Mechanism for finger persistence in homogeneous, unsaturated porous-media--theory and verification, *Soil Science*, 148(1), 60-70.
- Glass, R. J., et al. (1990), Wetting front instability in unsaturated porous media--a 3-dimensional study in initially dry sand, *Transport in Porous Media*, 5(3), 247-268.
- Glass, R. J., and M. J. Nicholl (1995), Quantitative visualization of entrapped phase dissolution within a horizontal flowing fracture, *Geophysical Research Letters*, 22(11), 1413-1416.
- Glass, R. J., and M. J. Nicholl (1996), Physics of gravity fingering of immiscible fluids within porous media: An overview of current understanding and selected complicating factors, *Geoderma*, 70(2-4), 133-163.
- Glass, R. J., et al. (2000), Gravity-destabilized nonwetting phase invasion in macroheterogeneous porous media: Experimental observations of invasion dynamics and scale analysis, *Water Resources Research*, 36(11), 3121-3137.
- Glass, R. J., et al. (2001), Gravity-destabilized nonwetting phase invasion in macroheterogeneous porous media: Near-pore-scale macro modified invasion percolation simulation of experiments, *Water Resources Research*, 37(5), 1197-1207.
- Glass, R. J., and L. Yarrington (2003), Mechanistic modeling of fingering, nonmonotonicity, fragmentation, and pulsation within gravity/buoyant destabilized two-phase/unsaturated flow, *Water Resources Research*, 39(3), 10.
- Goltz, M. N., and P. V. Roberts (1987), Using the method of moments to analyze three-dimensional diffusion-limited solute transport from temporal and spatial perspectives, *Water Resour. Res.*, 23(8), 1575-1585.

- Gonzalez, R. C., et al. (2004), *Digital Image processing using MATLAB*, Pearson Prentice Hall, Upper Saddle River, N.J.
- Goswami, R. R., and T. P. Clement (2007), Laboratory-scale investigation of saltwater intrusion dynamics, *Water Resources Research*, 43(4), 11.
- Goswami, R. R., et al. (2009), Estimating Errors in Concentration Measurements Obtained from Image Analysis, *Vadose Zone Journal*, 8(1), 108-118.
- Gotz, J., et al. (2002), Visualisation of flow processes in packed beds with NMR imaging: determination of the local porosity, velocity vector and local dispersion coefficients, *Chem. Eng. Process.*, 41(7), 611-629.
- Gramling, C. M., et al. (2002), Reactive transport in porous media: A comparison of model prediction with laboratory visualization, *Environmental Science & Technology*, 36(11), 2508-2514.
- Grolimund, D., et al. (1998), Transport of in situ mobilized colloidal particles in packed soil columns, *Environmental Science & Technology*, 32(22), 3562-3569.
- Hainsworth, J. M., and L. A. G. Aylmore (1983), The use of computer-assisted tomography to determine spatial-distribution of soil-water content, *Australian Journal of Soil Research*, 21(4), 435-443.
- Hall, L. D., et al. (1997), MR properties of water in saturated soils and resulting loss of MRI signal in water content detection at 2 tesla, *Geoderma*, 80(3-4), 431-448.
- Hangen, E., et al. (2004), Flow path visualization in a lignitic mine soil using iodine-starch staining, *Geoderma*, 120(1-2), 121-135.
- Harris, W. W., et al. (1995), Use of stereophotogrammetry to analyze the development of shear bands in sand, *Geotech. Test. J.*, 18(4), 405-420.
- Hatano, R., and H. W. G. Boutilik (1992), Using fractal dimensions of stained flow patterns in a clay soil to predict bypass flow, *Journal of Hydrology*, 135(1-4), 121-131.
- Hatano, R., et al. (1992), Evaluation of the effect of morphological features of flow paths on solute transport by using fractal dimensions of methylene-blue staining pattern, *Geoderma*, 53(1-2), 31-44.
- Hatiboglu, C., and T. Babadagli (2008), Diffusion Mass Transfer in Miscible Oil Recovery: Visual Experiments and Simulation, *Transport in Porous Media*, 74(2), 169-184.
- Hatiboglu, C. U., and T. Babadagli (2010a), Experimental and visual analysis of co- and counter-current spontaneous imbibition for different viscosity ratios, interfacial tensions, and wettabilities, *Journal of Petroleum Science and Engineering*, 70(3-4), 214-228.
- Hatiboglu, C. U., and T. Babadagli (2010b), Experimental and visual analysis of diffusive mass transfer between matrix and fracture under static conditions, *Journal of Petroleum Science and Engineering*, 74(1-2), 31-40.
- Haynes, W. M. (Ed.) (2011), *CRC handbook of chemistry and physics*, 91st ed., CRC Press, Cleveland, Ohio.
- Hecht, E. (2002), *Optics*, 4th ed., Pearson Education, San Francisco, CA.
- Hill, D. E., and J. Y. Parlange (1972), Wetting front instability in layered soils, *Soil Science Society of America Proceedings*, 36(5), 697-&.
- Hillel, D. (1998), *Environmental soil physics*, Acad. Press, San Diego [u.a.

- Hoang, N. T., et al. (1977), Influence of hysteresis effect on transient flows in saturated-unsaturated porous media, *Water Resources Research*, 13(6), 992-996.
- Hoang, N. T. (1981), A new method allowing the measurement of rapid variations of the water-content in sandy porous-media, *Water Resources Research*, 17(1), 41-48.
- Hopmans, J. W., and J. H. Dane (1986), Calibration of a dual-energy gamma-radiation system for multiple point measurements in a soil, *Water Resources Research*, 22(7), 1109-1114.
- Hsieh, H., et al. (1998), Measurement of porous media component content and heterogeneity using gamma ray tomography, *Water Resources Research*, 34(3), 365-372.
- Huang, A. Y. L., et al. (2008), Optical measurements of pore geometry and fluid velocity in a bed of irregularly packed spheres, *Experiments in Fluids*, 45(2), 309-321.
- Huang, W. E., et al. (2002), Physical modelling of solute transport in porous media: evaluation of an imaging technique using UV excited fluorescent dye, *Water Research*, 36(7), 1843-1853.
- Huang, W. E., et al. (2003), Dissolved oxygen imaging in a porous medium to investigate biodegradation in a plume with limited electron acceptor supply, *Environmental Science & Technology*, 37(9), 1905-1911.
- Iassonov, P., and M. Tuller (2010), Application of Segmentation for Correction of Intensity Bias in X-Ray Computed Tomography Images, *Vadose Zone J*, 9(1), 187-191.
- Ibaraki, M., et al. (2000), Modeling instability development in layered systems, *Journal of Contaminant Hydrology*, 42(2-4), 337-352.
- Illangasekare, T. H., et al. (1995a), Non-aqueous-phase fluids in heterogeneous aquifers - experimental study, *Journal of Environmental Engineering-Asce*, 121(8), 571-579.
- Illangasekare, T. H., et al. (1995b), Experimental study of movement and distribution of dense organic contaminants in heterogeneous aquifers, *Journal of Contaminant Hydrology*, 20(1-2), 1-25.
- Ingle, J. D., and S. R. Crouch (1988), *Spectrochemical Analysis*, Prentice-Hall, Englewood Cliffs, NJ.
- Invitrogen (2010), *Molecular Probes Handbook, A guide to fluorescent probes and labeling technologies*, 11th ed.
- Iskander, M., and J. Y. Liu (2010), Spatial Deformation Measurement Using Transparent Soil, *Geotech. Test. J.*, 33(4), 314-321.
- Iskander, M. G., et al. (2002), Transparent amorphous silica to model clay, *Journal of Geotechnical and Geoenvironmental Engineering*, 128(3), 262-273.
- Istok, J. D., et al. (2007), An experimental investigation of nitrogen gas produced during denitrification, *Ground Water*, 45(4), 461-467.
- Jaeger, S., et al. (2009), CCD camera image analysis for mapping solute concentrations in saturated porous media, *Analytical and Bioanalytical Chemistry*, 395(6), 1867-1876.
- Jawitz, J. W., et al. (1998), Miscible fluid displacement stability in unconfined porous media: Two-dimensional flow experiments and simulations, *Journal of Contaminant Hydrology*, 31(3-4), 211-230.
- Jawitz, J. W., et al. (2003), Estimating nonaqueous phase liquid spatial variability using partitioning tracer higher temporal moments, *Water Resources Research*, 39(7), 19.
- Jeong, S.-W., et al. (2000), Micromodel Study of Surfactant Foam Remediation of Residual Trichloroethylene, *Environmental Science & Technology*, 34(16), 3456-3461.

- Ji, W., et al. (1993), Laboratory study of air sparging - air-flow visualization, *Ground Water Monitoring and Remediation*, 13(4), 115-126.
- Jia, C., et al. (1999), Visualization and simulation of non-aqueous phase liquids solubilization in pore networks, *Journal of Contaminant Hydrology*, 35(4), 363-387.
- Johnson, P. R., and M. Elimelech (1995), Dynamics of colloid deposition in porous media: blocking based on random sequential adsorption, *Langmuir*, 11(3), 801-812.
- Johnson, P. R., et al. (1996), Colloid transport in geochemically heterogeneous porous media: Modeling and measurements, *Environmental Science & Technology*, 30(11), 3284-3293.
- Jones, E. H., and C. C. Smith (2005), Non-equilibrium partitioning tracer transport in porous media: 2-D physical modelling and imaging using a partitioning fluorescent dye, *Water Research*, 39(20), 5099-5111.
- Jose, S. C., et al. (2004), Large-scale sandbox experiment on longitudinal effective dispersion in heterogeneous porous media, *Water Resources Research*, 40(12).
- Kaiser, L. G., et al. (2000), Visualization of gas flow and diffusion in porous media, *Proc. Natl. Acad. Sci. U. S. A.*, 97(6), 2414-2418.
- Kanel, S. R., et al. (2008), Two dimensional transport characteristics of surface stabilized zero-valent iron nanoparticles in porous media, *Environmental Science & Technology*, 42(3), 896-900.
- Kantzas, A., et al. (1992), Computer-assisted tomography - from qualitative visualization to quantitative core analysis, *J. Can. Pet. Technol.*, 31(9), 48-56.
- Kasteel, R., et al. (2000), From local hydraulic properties to effective transport in soil, *European Journal of Soil Science*, 51(1), 81-91.
- Kaye, A. J., et al. (2008), Laboratory investigation of flux reduction from dense non-aqueous phase liquid (DNAPL) partial source zone remediation by enhanced dissolution, *Journal of Contaminant Hydrology*, 102(1-2), 17-28.
- Kechavarzi, C., et al. (2000), Multispectral image analysis method to determine dynamic fluid saturation distribution in two-dimensional three-fluid phase flow laboratory experiments, *Journal of Contaminant Hydrology*, 46(3-4), 265-293.
- Kechavarzi, C., et al. (2005), Two-dimensional laboratory simulation of LNAPL infiltration and redistribution in the vadose zone, *Journal of Contaminant Hydrology*, 76(3-4), 211-233.
- Kechavarzi, C., et al. (2008), Laboratory Study of Immiscible Contaminant Flow in Unsaturated Layered Sands, *Vadose Zone J*, 7(1), 1-9.
- Keller, A. A., and M. Auset (2007), A review of visualization techniques of biocolloid transport processes at the pore scale under saturated and unsaturated conditions, *Advances in Water Resources*, 30(6-7), 1392-1407.
- Khalili, A., et al. (1998), Flow visualization in porous media via Positron Emission Tomography, *Physics of Fluids*, 10(4), 1031-1033.
- Khalili, A., et al. (1999), An experimental study of recirculating flow through fluid-sediment interfaces, *J. Fluid Mech.*, 383, 229-247.
- Kildsgaard, J., and P. Engesgaard (2001), Numerical analysis of biological clogging in two-dimensional sand box experiments, *Journal of Contaminant Hydrology*, 50(3-4), 261-285.
- Kildsgaard, J., and P. Engesgaard (2002), Tracer tests and image analysis of biological clogging in a two-dimensional sandbox experiment, *Ground Water Monitoring and Remediation*, 22(2), 60-67.

- Kim, J., et al. (2006), Tracer transport test in simple fractured media, *Geosci. J.*, 10(2), 131-136.
- Klauth, P., et al. (2007), Fluorescence macrophotography as a tool to visualise and quantify spatial distribution of deposited colloid tracers in porous media, *Colloids and Surfaces a-Physicochemical and Engineering Aspects*, 306(1-3), 118-125.
- Klise, K. A., et al. (2008), Comparison of laboratory-scale solute transport visualization experiments with numerical simulation using cross-bedded sandstone, *Advances in Water Resources*, 31(12), 1731-1741.
- Klonis, N., and W. H. Sawyer (1996), Spectral properties of the prototropic forms of fluorescein in aqueous solution, *Journal of Fluorescence*, 6(3), 147-157.
- Kneafsey, T. J., and K. Pruess (1998), Laboratory experiments on heat-driven two-phase flows in natural and artificial rock fractures, *Water Resources Research*, 34(12), 3349-3367.
- Kong, X. Z., et al. (2009), Migration of air channels: An instability of air flow in mobile saturated porous media, *Chemical Engineering Science*, 64(7), 1528-1535.
- Kong, X. Z., et al. (2010a), Morphodynamics during air injection into water-saturated movable spherical granulates, *Chemical Engineering Science*, 65(16), 4652-4660.
- Kong, X. Z., et al. (2010b), Compaction and size segregation in a liquid-saturated grain packing due to pulsation effect during air injection, *Chemical Engineering Science*, 65(9), 2680-2688.
- Konz, M., et al. (2008), On the measurement of solute concentrations in 2-D flow tank experiments, *Hydrology and Earth System Sciences*, 12(3), 727-738.
- Konz, M., et al. (2009a), Comparison of light transmission and reflection techniques to determine concentrations in flow tank experiments, *Experiments in Fluids*, 47(1), 85-93.
- Konz, M., et al. (2009b), Two-dimensional stable-layered laboratory-scale experiments for testing density-coupled flow models, *Water Resources Research*, 45, 14.
- Konz, M., et al. (2009c), Variable-density flow in heterogeneous porous media - Laboratory experiments and numerical simulations, *Journal of Contaminant Hydrology*, 108(3-4), 168-175.
- Kraft, E. L., and J. S. Selker (2005), Methodological developments in in-situ measurement and visualization of colloid transport processes in the subsurface, paper presented at GSA Annual Meeting and Exposition, Salt Lake City UT.
- Kuester, F., et al. (2005), Image centric finite element simulation, *Comput. Graph.-UK*, 29(3), 379-392.
- Lanning, L. M., and R. M. Ford (2002), Glass micromodel study of bacterial dispersion in spatially periodic porous networks, *Biotechnology and Bioengineering*, 78(5), 556-566.
- Lazik, D., et al. (2008), Multi-scale optical analyses of dynamic gas saturation during air sparging into glass beads, *Transport in Porous Media*, 74(1), 87-104.
- Lenhart, J. J., and J. E. Saiers (2004), Adsorption of natural organic matter to air-water interfaces during transport through unsaturated porous media, *Environmental Science & Technology*, 38(1), 120-126.
- Levy, M., and B. Berkowitz (2003), Measurement and analysis of non-Fickian dispersion in heterogeneous porous media, *Journal of Contaminant Hydrology*, 64(3-4), 203-226.
- Li, X. Q., et al. (2006), Pore-scale observation of microsphere deposition at grain-to-grain contacts over assemblage-scale porous media domains using X-ray microtomography, *Environmental Science & Technology*, 40(12), 3762-3768.

- Li, Y., et al. (2004), Fluorescence microscopy for visualization of soil microorganisms - a review, *Biology and Fertility of Soils*, 39(5), 301-311.
- Lindqvist, L. (1960), A flash photolysis study of fluorescein, *Arkiv for Kemi*, 16(8), 79-138.
- Liu, J. Y., et al. (2003), Consolidation and permeability of transparent amorphous silica, *Geotech. Test. J.*, 26(4), 390-401.
- Liu, J. Y., and M. Iskander (2004), Adaptive cross correlation for imaging displacements in soils, *J. Comput. Civil. Eng.*, 18(1), 46-57.
- Liu, J. Y., and M. G. Iskander (2010), Modelling capacity of transparent soil, *Canadian Geotechnical Journal*, 47(4), 451-460.
- Liu, S. Y., et al. (2002), Effectiveness of hydraulic tomography: Sandbox experiments, *Water Resources Research*, 38(4), 9.
- Liu, Y., et al. (1991), Hysteretic finger phenomena in dry and wetted sands, paper presented at Preferential flow; proceedings of the national symposium, Chicago, IL.
- Liu, Y. P., et al. (1993), High-intensity X-ray and tensiometer measurements in rapidly changing preferential flow-fields, *Soil Science Society of America Journal*, 57(5), 1188-1192.
- Lo, H. C., et al. (2010), A Transparent Water-Based Polymer for Simulating Multiphase Flow, *Geotech. Test. J.*, 33(1), 1-13.
- Loggia, D., et al. (2009), Experimental Study of Upward Oil Migration in a Fracture, *Transport in Porous Media*, 80(1), 1-16.
- Lu, T. X., et al. (1994a), Water movement in glass bead porous media 1. Experiments of capillary rise and hysteresis, *Water Resources Research*, 30(12), 3275-3281.
- Lu, T. X., et al. (1994b), Water movement in glass bead porous media 2. Experiments of infiltration and finger flow, *Water Resources Research*, 30(12), 3283-3290.
- Lunati, I., et al. (2003), Effects of pore volume-transmissivity correlation on transport phenomena, *Journal of Contaminant Hydrology*, 67(1-4), 195-217.
- Macari, E. J., et al. (1997), Measurement of volume changes in triaxial tests using digital imaging techniques, *Geotech. Test. J.*, 20(1), 103-109.
- Maidment, D. R. (1993), *Handbook of hydrology*, McGraw-Hill, New York.
- Majdalani, S., et al. (2007), Mobilization and preferential transport of soil particles during infiltration: A core-scale modeling approach, *Water Resources Research*, 43(5).
- Mandoli, D. F., et al. (1990), SOME SPECTRAL PROPERTIES OF SEVERAL SOIL TYPES - IMPLICATIONS FOR PHOTOMORPHOGENESIS, *Plant Cell Environ.*, 13(3), 287-294.
- Manz, B., et al. (2003), Measuring local flow velocities and biofilm structure in biofilm systems with magnetic resonance imaging (MRI), *Biotechnology and Bioengineering*, 84, 424-432.
- McCarthy, J. F., and J. M. Zachara (1989), Subsurface transport of contaminants, *Environmental Science & Technology*, 23, 496-502.
- McCarthy, J. F., and L. Shevenell (1998), Processes controlling colloid composition in a fractured and karstic aquifer in eastern Tennessee, USA, *Journal of Hydrology*, 206(3-4), 191-218.
- McDowell, C. J., et al. (2003), Behavior of gasoline pools following a denatured ethanol spill, *Ground Water*, 41(6), 746-757.

- McDowell, C. J., and S. E. Powers (2003), Mechanisms affecting the infiltration and distribution of ethanol-blended gasoline in the vadose zone, *Environmental Science & Technology*, 37(9), 1803-1810.
- McNeil, J. D., et al. (2006), Quantitative imaging of contaminant distributions in heterogeneous porous media laboratory experiments, *Journal of Contaminant Hydrology*, 84(1-2), 36-54.
- Menand, T., et al. (2003), Thermal inertia and reversing buoyancy in flow in porous media, *Geophysical Research Letters*, 30(6), 3.
- Menand, T., and A. W. Woods (2005), Dispersion, scale, and time dependence of mixing zones under gravitationally stable and unstable displacements in porous media, *Water Resources Research*, 41(5), 14.
- Montemagno, C. D., and W. G. Gray (1995), Photoluminescent volumetric imaging - a technique for the exploration of multiphase flow and transport in porous media, *Geophysical Research Letters*, 22(4), 425-428.
- Mooney, S. J., et al. (1999), Morphological observations of dye tracer infiltration and by-pass flow in milled peat, *Plant Soil*, 208(2), 167-178.
- Mooney, S. J., and W. Nipattasuk (2003), Quantification of the effects of soil compaction on water flow using dye tracers and image analysis, *Soil Use Manage.*, 19(4), 356-363.
- Mooney, S. J., and C. Morris (2008), Morphological approach to understanding preferential flow using image analysis with dye tracers and X-ray computed tomography, *Catena*, 73(2), 204-211.
- Morales, V. L., et al. (2009), Grain Surface-Roughness Effects on Colloidal Retention in the Vadose Zone, *Vadose Zone J*, 8(1), 11-20.
- Morris, C., and S. J. Mooney (2004), A high-resolution system for the quantification of preferential flow in undisturbed soil using observations of tracers, *Geoderma*, 118(1-2), 133-143.
- Mortensen, A. P., et al. (2001), Visualization of microscale phase displacement processes in retention and outflow experiments: Nonuniqueness of unsaturated flow properties, *Water Resources Research*, 37(6), 1627-1640.
- Mumford, K. G., et al. (2009a), Slow gas expansion in saturated natural porous media by gas injection and partitioning with non-aqueous phase liquids, *Advances in Water Resources*, 32(1), 29-40.
- Mumford, K. G., et al. (2009b), New Observations of Gas-Phase Expansion above a Dense Nonaqueous Phase Liquid Pool, *Vadose Zone Journal*, 8(2), 404-410.
- Mumford, K. G., et al. (2010), The effect of spontaneous gas expansion and mobilization on the aqueous-phase concentrations above a dense non-aqueous phase liquid pool, *Advances in Water Resources*, 33(4), 504-513.
- Nambi, I. M., and S. E. Powers (2000), NAPL dissolution in heterogeneous systems: an experimental investigation in a simple heterogeneous system, *Journal of Contaminant Hydrology*, 44(2), 161-184.
- Nambi, I. M., and S. E. Powers (2003), Mass transfer correlations for nonaqueous phase liquid dissolution from regions with high initial saturations, *Water Resources Research*, 39(2).
- Neethirajan, S., and D. Jayas (2008), Analysis of Pore Network in Three-dimensional (3D) Grain Bulks Using X-ray CT Images, *Transport in Porous Media*, 73(3), 319-332.
- Ng, K. M., et al. (1978), Visualization of blob mechanics in flow through porous media, *Chemical Engineering Science*, 33(8), 1009-1017.
- Nicholl, M. J., et al. (1994), Gravity-driven infiltration instability in initially dry nonhorizontal fractures, *Water Resources Research*, 30(9), 2533-2546.

- Niehren, S., et al. (1995), An all-solid-state flow cytometer for counting fluorescent microspheres, *Analytical Chemistry*, 67(15), 2666-2671.
- Niemet, M. R., and J. S. Selker (2001), A new method for quantification of liquid saturation in 2D translucent porous media systems using light transmission, *Advances in Water Resources*, 24(6), 651-666.
- Niemet, M. R., et al. (2002), Relationships between gas-liquid interfacial surface area, liquid saturation, and light transmission in variably saturated porous media, *Water Resources Research*, 38(8).
- Nobles, M. M., et al. (2004), Pathways of dye tracer movement through structured soils on a macroscopic scale, *Soil Science*, 169(4), 229-242.
- O'Carroll, D. M., et al. (2004), Infiltration of PCE in a system containing spatial wettability variations, *Journal of Contaminant Hydrology*, 73(1-4), 39-63.
- O'Carroll, D. M., and B. E. Sleep (2007), Hot water flushing for immiscible displacement of a viscous NAPL, *Journal of Contaminant Hydrology*, 91(3-4), 247-266.
- Oates, P. M., et al. (2005), Illuminating reactive microbial transport in saturated porous media: Demonstration of a visualization method and conceptual transport model, *Journal of Contaminant Hydrology*, 77(4), 233-245.
- Oates, P. M., and C. F. Harvey (2006), A colorimetric reaction to quantify fluid mixing, *Experiments in Fluids*, 41(5), 673-683.
- Ochiai, N., et al. (2005), Use of rectangular capillary chambers for nondestructive microscopic observation of biofilm on sand, paper presented at AGU Fall Meeting, San Francisco, CA.
- Ochiai, N., et al. (2006), Methods for colloid transport visualization in pore networks, *Water Resources Research*, 42(12).
- Ochiai, N., et al. (2010), Three-Dimensional Tracking of Colloids at the Pore Scale Using Epifluorescence Microscopy, *Vadose Zone Journal*, 9(3), 576-587.
- Olson, M. S., et al. (2004), Quantification of bacterial chemotaxis in porous media using magnetic resonance imaging, *Environmental Science & Technology*, 38(14), 3864-3870.
- Olson, M. S., et al. (2005), Analysis of column tortuosity for MnCl<sub>2</sub> and bacterial diffusion using magnetic resonance imaging, *Environmental Science & Technology*, 39(1), 149-154.
- Oltean, C., et al. (2004), Transport with a very low density contrast in Hele-Shaw cell and porous medium: Evolution of the mixing zone, *Transport in Porous Media*, 55(3), 339-360.
- Oostrom, M., et al. (1992), Behavior of dense aqueous phase leachate plumes in homogeneous porous-media, *Water Resources Research*, 28(8), 2123-2134.
- Oostrom, M., et al. (1995), Error analysis of dual-energy gamma-radiation measurements, *Soil Science*, 160(1), 28-42.
- Oostrom, M., et al. (1997), Light nonaqueous-phase liquid movement in a variably saturated sand, *Soil Science Society of America Journal*, 61(6), 1547-1554.
- Oostrom, M., et al. (1998), Single-source gamma radiation procedures for improved calibration and measurements in porous media, *Soil Science*, 163(8), 646-656.
- Oostrom, M., and R. J. Lenhard (1998), Comparison of relative permeability-saturation-pressure parametric models for infiltration and redistribution of a light nonaqueous-phase liquid in sandy porous media, *Advances in Water Resources*, 21(2), 145-157.

- Oostrom, M., et al. (2007), A review of multidimensional, multifluid, intermediate-scale experiments: Flow behavior, saturation imaging, and tracer detection and quantification, *Vadose Zone Journal*, 6(3), 610-637.
- Oswald, S. E., et al. (2002), Time-Dependent Measurement of Strongly Density-Dependent Flow in a Porous Medium via Nuclear Magnetic Resonance Imaging, *Transport in Porous Media*, 47(2), 169-193.
- Pang, L., et al. (2008), Modeling Transport of Microbes in Ten Undisturbed Soils under Effluent Irrigation, *Vadose Zone J*, 7(1), 97-111.
- Pantazidou, M., and N. Sitar (1993), Emplacement of nonaqueous liquids in the vadose zone, *Water Resources Research*, 29(3), 705-722.
- Parker, L., et al. (2006), Observations of gas flow in porous media using a light transmission technique, *Water Resources Research*, 42(5).
- Persoff, P., and K. Pruess (1995), Two-phase flow visualization and relative permeability measurement in natural rough-walled rock fractures, *Water Resources Research*, 31(5), 1175-1186.
- Persson, M., et al. (2001), Modeling plot scale dye penetration by a diffusion limited aggregation (DLA) model, *Journal of Hydrology*, 250(1-4), 98-105.
- Persson, M. (2005a), Accurate dye tracer concentration estimations using image analysis, *Soil Science Society of America Journal*, 69(4), 967-975.
- Persson, M. (2005b), Estimating surface soil moisture from soil color using image analysis, *Vadose Zone Journal*, 4(4), 1119-1122.
- Persson, M., et al. (2005), Solute transport dynamics by high-resolution dye tracer experiments - Image analysis and time moments, *Vadose Zone Journal*, 4(3), 856-865.
- Petersen, C. T., et al. (1997), Tillage-induced horizontal periodicity of preferential flow in the root zone, *Soil Science Society of America Journal*, 61(2), 586-594.
- Peterson, J. W., et al. (1999), Effect of sediment size on area of influence during groundwater remediation by air sparging: a laboratory approach, *Environmental Geology*, 38(1), 1-6.
- Peterson, J. W., et al. (2000), A laboratory simulation of toluene cleanup by air sparging of water-saturated sands, *Journal of Hazardous Materials*, 72(2-3), 167-178.
- Peterson, J. W., et al. (2001), Airflow geometry in air sparging of fine-grained sands, *Hydrogeology Journal*, 9(2), 168-176.
- Petrovic, A. M., et al. (1982), Soil bulk-density analysis in 3 dimensions by computed tomographic scanning, *Soil Science Society of America Journal*, 46(3), 445-450.
- Pokhriyal, A., et al. (2010), Photonic crystal enhanced fluorescence using a quartz substrate to reduce limits of detection, *Opt. Express*, 18(24), 24793-24808.
- Polak, A., et al. (2003), Tracer diffusion from a horizontal fracture into the surrounding matrix: measurement by computed tomography, *Journal of Contaminant Hydrology*, 67(1-4), 95-112.
- Post, V. E. A., and C. T. Simmons (2010), Free convective controls on sequestration of salts into low-permeability strata: insights from sand tank laboratory experiments and numerical modelling, *Hydrogeology Journal*, 18(1), 39-54.
- Potter, K., et al. (1996), Assay for bacteria in porous media by diffusion-weighted NMR, *Journal of Magnetic Resonance Series B*, 113(1), 9-15.

- Powelson, D. K., et al. (1993), Virus transport and removal in wastewater during aquifer recharge, *Water Research*, 27(4), 583-590.
- Powers, S. E., et al. (1998), Non-aqueous phase liquid dissolution in heterogeneous systems: Mechanisms and a local equilibrium modeling approach, *Water Resources Research*, 34(12), 3293-3302.
- Prado, B., et al. (2009), Image processing-based study of soil porosity and its effect on water movement through Andosol intact columns, *Agricultural Water Management*, 96(10), 1377-1386.
- Princeton-Instruments (1999), TE/CCD Detector, edited, Roper Scientific.
- Ptak, T., and G. Schmid (1996), Dual-tracer transport experiments in a physically and chemically heterogeneous porous aquifer: Effective transport parameters and spatial variability, *Journal of Hydrology*, 183(1-2), 117-138.
- Rahman, M. A., et al. (2005), Experiments on vertical transverse mixing in a large-scale heterogeneous model aquifer, *Journal of Contaminant Hydrology*, 80(3-4), 130-148.
- Rangel-German, E. R., and A. R. Kovscek (2006), A micromodel investigation of two-phase matrix-fracture transfer mechanisms, *Water Resources Research*, 42(3).
- Rani, S. A., et al. (2005), Rapid Diffusion of Fluorescent Tracers into Staphylococcus epidermidis Biofilms Visualized by Time Lapse Microscopy, *Antimicrob. Agents Chemother.*, 49(2), 728-732.
- Rathfelder, K. M., et al. (2003), Influence of surfactant-facilitated interfacial tension reduction on chlorinated solvent migration in porous media: observations and numerical simulation, *Journal of Contaminant Hydrology*, 64(3-4), 227-252.
- Rechenmacher, A. L., and R. J. Finno (2004), Digital image correlation to evaluate shear banding in dilative sands, *Geotech. Test. J.*, 27(1), 13-22.
- Rees, H. C., et al. (2007), Biodegradation processes in a laboratory-scale groundwater contaminant plume assessed by fluorescence imaging and microbial analysis, *Applied and Environmental Microbiology*, 73(12), 3865-3876.
- Reichman, J. (2007), Handbook of optical filters for fluorescence microscopy, edited by C. T. Group, Chroma Technology Corp., Rockingham, VT.
- Reinecke, N., et al. (1998), Tomographic measurement techniques - Visualization of multiphase flows, *Chemical Engineering & Technology*, 21(1), 7-18.
- Reylea, J. F. (1982), Theoretical and experimental considerations for the use of the column method for determining retardation factors, *Radioact. Waste Manage. Nucl. Fuel Cycle*, 3(2), 151-166.
- Rimmer, A., et al. (1998), Rapid fluid content measurement method for fingered flow in an oil-water-sand system using synchrotron X-rays, *Journal of Contaminant Hydrology*, 31(3-4), 315-335.
- Rockhold, M. L., et al. (2007), Visualization and modeling of the colonization dynamics of a bioluminescent bacterium in variably saturated, translucent quartz sand, *Advances in Water Resources*, 30(6-7), 1593-1607.
- Roosevelt, S. E., and M. Y. Corapcioglu (1998), Air bubble migration in a granular porous medium: Experimental studies, *Water Resources Research*, 34(5), 1131-1142.
- Rossi, M., et al. (2007), Solute mixing during imbibition and drainage in a macroscopically heterogeneous medium, *Water Resources Research*, 43(4), 13.
- Rossi, M., et al. (2008), Solute dilution under imbibition and drainage conditions in a heterogeneous structure: Modeling of a sand tank experiment, *Advances in Water Resources*, 31(9), 1242-1252.

- Russ, J. C. (2007), *The image processing handbook*, edited, CRC/Taylor and Francis, Boca Raton.
- Sadek, S., et al. (2002), Geotechnical properties of transparent silica, *Canadian Geotechnical Journal*, 39(1), 111-124.
- Sadek, S., et al. (2003), Accuracy of digital image correlation for measuring deformations in transparent media, *J. Comput. Civil. Eng.*, 17(2), 88-96.
- Saiers, J. E., and G. M. Hornberger (1999), The influence of ionic strength on the facilitated transport of cesium by kaolinite colloids, *Water Resources Research*, 35(6), 1713-1721.
- Saiers, J. E., and J. J. Lenhart (2003), Ionic-strength effects on colloid transport and interfacial reactions in partially saturated porous media, *Water Resources Research*, 39(9).
- Schena, G., and S. Favretto (2007), Pore space network characterization with sub-voxel definition, *Transport in Porous Media*, 70(2), 181-190.
- Schincariol, R. A. (1989), Migration of dense aqueous phase liquids in homogeneous and heterogeneous porous media, University of Alberta, Edmonton, Alberta.
- Schincariol, R. A., and F. W. Schwartz (1990), An experimental investigation of variable density flow and mixing in homogeneous and heterogeneous media, *Water Resources Research*, 26(10), 2317-2329.
- Schincariol, R. A., et al. (1993), On the application of image-analysis to determine concentration distributions in laboratory experiments, *Journal of Contaminant Hydrology*, 12(3), 197-215.
- Schroth, M. H., et al. (1995), Geometry and position of light nonaqueous-phase liquid lenses in water-wetted porous-media, *Journal of Contaminant Hydrology*, 19(4), 269-287.
- Schroth, M. H., et al. (1996), Characterization of miller-similar silica sands for laboratory hydrologic studies, *Soil Science Society of America Journal*, 60, 1331-1339.
- Schroth, M. H., et al. (1998a), Three-phase immiscible fluid movement in the vicinity of textural interfaces, *Journal of Contaminant Hydrology*, 32(1-2), 1-23.
- Schroth, M. H., et al. (1998b), Multifluid flow in bedded porous media: laboratory experiments and numerical simulations, *Advances in Water Resources*, 22(2), 169-183.
- Schwille, F. (1988), *Dense Chlorinated Solvents in Porous and Fractured Media*, Lewis Publishers, Chelsea, Michigan.
- Sederman, A. J., et al. (1997), Magnetic resonance imaging of liquid flow and pore structure within packed beds, *Chemical Engineering Science*, 52(14), 2239-2250.
- Sederman, A. J., and L. F. Gladden (2001), Magnetic resonance visualisation of single- and two-phase flow in porous media, *Magnetic Resonance Imaging*, 19(3-4), 339-343.
- Selker, J. S., et al. (1992a), Fingered flow in two dimensions, 1, Measurement of matric potential, *Water Resources Research*, 28(9), 2513-2521.
- Selker, J. S., et al. (1992b), Fingered flow in two dimensions, 2, predicting finger moisture profile, *Water Resources Research*, 28(9), 2523-2528.
- Selker, J. S., et al. (1992c), Wetting front instability in homogeneous sandy soils under continuous infiltration, *Soil Science Society of America Journal*, 56(5), 1346-1350.
- Selker, J. S., et al. (1999), *Vadose zone processes*, Lewis Publishers, Boca Raton, Fla.
- Selker, J. S., et al. (2007), The local geometry of gas injection into saturated homogeneous porous media, *Transport in Porous Media*, 68(1), 107-127.

- Selker, J. S. (2010), edited, Corvallis, OR.
- Seol, Y., et al. (2001), Oxidation of binary DNAPL mixtures using potassium permanganate with a phase transfer catalyst, *Ground Water Monitoring and Remediation*, 21(2), 124-132.
- Seyfried, M. S., and P. S. C. Rao (1987), Solute transport in undisturbed columns of an aggregated tropical soil - preferential flow effects, *Soil Science Society of America Journal*, 51(6), 1434-1444.
- Seymour, J. D., et al. (2004), Magnetic resonance microscopy of biofilm structure and impact on transport in a capillary bioreactor, *Journal of Magnetic Resonance*, 167(2), 322-327.
- Seymour, J. D., et al. (2007), Magnetic resonance microscopy of biofouling induced scale dependent transport in porous media, *Advances in Water Resources*, 30(6-7), 1408-1420.
- Sharp, R. R., et al. (1999), Observation of thick biofilm accumulation and structure in porous media and corresponding hydrodynamic and mass transfer effects, *Water Science and Technology*, 39(7), 195-201.
- Sharp, R. R., et al. (2005), Visualization and characterization of dynamic patterns of flow, growth and activity of biofilms growing in porous media, *Water Science and Technology*, 52(7), 85-90.
- Sherwood, J. L., et al. (2003), Analysis of bacterial random motility in a porous medium using magnetic resonance imaging and immunomagnetic labeling, *Environmental Science & Technology*, 37(4), 781-785.
- Shonnard, D. R., et al. (1994), Injection-attachment of *methylosinus-trichosporium* OB3B in a 2-dimensional miniature sand-filled aquifer simulator, *Water Resources Research*, 30(1), 25-35.
- Silliman, S. E., et al. (1987), Laboratory investigation of longitudinal dispersion in anisotropic porous-media, *Water Resources Research*, 23(11), 2145-2151.
- Silliman, S. E., and E. S. Simpson (1987), Laboratory evidence of the scale effect in dispersion of solutes in porous-media, *Water Resources Research*, 23(8), 1667-1673.
- Silliman, S. E., et al. (1994), Application of a UV-curing resin to hydrodynamic studies in porous-media, *Industrial & Engineering Chemistry Research*, 33(8), 1997-2001.
- Silliman, S. E. (1995), Particle transport through two-dimensional, saturated porous media: influence of physical structure of the medium, *Journal of Hydrology*, 167(1-4), 79-98.
- Silliman, S. E., et al. (1998), The use of laboratory experiments for the study of conservative solute transport in heterogeneous porous media, *Hydrogeology Journal*, 6(1), 166-177.
- Silliman, S. E., et al. (2001), Bacterial transport in heterogeneous porous media: Observations from laboratory experiments, *Water Resources Research*, 37(11), 2699-2707.
- Silliman, S. E., et al. (2002), Fluid flow and solute migration within the capillary fringe, *Ground Water*, 40(1), 76-84.
- Simantiraki, F., et al. (2009), Implementation of an image analysis technique to determine LNAPL infiltration and distribution in unsaturated porous media, *Desalination*, 248(1-3), 705-715.
- Simmons, C. T., et al. (2002), Laboratory Investigation of Variable-Density Flow and Solute Transport in Unsaturated-Saturated Porous Media, *Transport in Porous Media*, 47(2), 215-244.
- Šimůnek, J., et al. (1996), The HYDRUS-2D software package for simulating water flow and solute transport in two-dimensional variably saturated media, edited, International Ground Water Modeling Center, Colorado School of Mines, Golden, Colorado.

- Šimůnek, J., et al. (2006), The HYDRUS-2D software package for simulating two- and three-dimensional movement of water, heat, and multiple solutes in variably saturated media, edited, p. Technical Manual, PC Progress, Prague, Czech Republic.
- Sinai, G., and C. Dirksen (2006), Experimental evidence of lateral flow in unsaturated homogeneous isotropic sloping soil due to rainfall, *Water Resources Research*, 42(12), 12.
- Sirivithayapakorn, S., and A. Keller (2003a), Transport of colloids in saturated porous media: A pore-scale observation of the size exclusion effect and colloid acceleration, *Water Resources Research*, 39(4).
- Sirivithayapakorn, S., and A. Keller (2003b), Transport of colloids in unsaturated porous media: A pore-scale observation of processes during the dissolution of air-water interface, *Water Resources Research*, 39(12).
- Smagghe, B. J., et al. (2007), Immunolocalization of non-symbiotic hemoglobins during somatic embryogenesis in chicory, *Plant Signal Behav.*, 2(1), 43-49.
- Smart, P. L., and I. M. S. Laidlaw (1977), An Evaluation of Some Fluorescent Dyes for Water Tracing, *Water Resour. Res.*, 13.
- Smith, J., et al. (2008), Pore-scale quantification of colloid transport in saturated porous media, *Environmental Science & Technology*, 42(2), 517-523.
- Smith, J. E., and Z. F. Zhang (2001), Determining effective interfacial tension and predicting finger spacing for DNAPL penetration into water-saturated porous media, *Journal of Contaminant Hydrology*, 48(1-2), 167-183.
- Smith, S., and W. Pretorius (2002), The conservative behaviour of fluorescein, *Water SA*, 28(4).
- Soltani, A., et al. (2010), Three-Dimensional Characterization of Permeability at the Core Scale, *Transport in Porous Media*, 84(2), 285-305.
- Song, L., et al. (1995), Photobleaching kinetics of fluorescein in quantitative fluorescence microscopy, *Biophysical Journal*, 68(6), 2588-2600.
- Spanne, P., et al. (1994), Synchrotron computed microtomography of porous-media - topology and transports, *Physical Review Letters*, 73(14), 2001-2004.
- Stadler, D., et al. (2000), Dye tracing and image analysis for quantifying water infiltration into frozen soils, *Soil Science Society of America Journal*, 64(2), 505-516.
- Steenhuis, T. S., et al. (2005), Reply to "Comments on 'Pore-scale visualization of colloid transport and retention in partly saturated porous media'", *Vadose Zone Journal*, 4(4), 957-958.
- Stock, S. R. (1999), X-ray microtomography of materials, *International Materials Reviews*, 44(4), 141-164.
- Su, G. W., et al. (1999), Experimental studies of water seepage and intermittent flow in unsaturated, rough-walled fractures, *Water Resources Research*, 35(4), 1019-1037.
- Su, G. W., et al. (2003), Effect of isolated fractures on accelerated flow in unsaturated porous rock, *Water Resources Research*, 39(12).
- Su, H. C., and W. Kinzelbach (2001), Application of 2-D random generators to the study of solute transport in fractures, *Journal of the Chinese Institute of Engineers*, 24(3), 397-403.
- Suchomel, E. J., and K. D. Pennell (2006), Reductions in contaminant mass discharge following partial mass removal from DNAPL source zones, *Environmental Science & Technology*, 40(19), 6110-6116.

- Sun, N., et al. (2001), A novel two-dimensional model for colloid transport in physically and geochemically heterogeneous porous media, *Journal of Contaminant Hydrology*, 49(3-4), 173-199.
- Swartz, C. H. (1993), An experimental investigation of variable-density-driven flow in layered porous media, Ohio State University.
- Swartz, C. H., and F. W. Schwartz (1998), An experimental study of mixing and instability development in variable-density systems, *Journal of Contaminant Hydrology*, 34(3), 169-189.
- Tanio, N., and M. Irie (1994), Refractive index of organic photochromic dye amorphous polymer composites, *Jpn. J. Appl. Phys. Part 1 - Regul. Pap. Short Notes Rev. Pap.*, 33(7A), 3942-3946.
- Tester, M., and C. Morris (1987), The penetration of light through soil, *Plant Cell Environ.*, 10(4), 281-286.
- Theodoropoulou, M. A., et al. (2003), A new visualization technique for the study of solute dispersion in model porous media, *Journal of Hydrology*, 274(1-4), 176-197.
- Thieme, J., et al. (2003), X-ray tomography of a microhabitat of bacteria and other soil colloids with sub-100 nm resolution, *Micron*, 34(6-7), 339-344.
- Thullner, M., et al. (2002a), Interaction between water flow and spatial distribution of microbial growth in a two-dimensional flow field in saturated porous media, *Journal of Contaminant Hydrology*, 58(3-4), 169-189.
- Thullner, M., et al. (2002b), Influence of Microbial Growth on Hydraulic Properties of Pore Networks, *Transport in Porous Media*, 49(1), 99-122.
- Thullner, M. (2010a), Comment on "Comparison of bioclogging effects in saturated porous media within one- and two-dimensional flow systems" by Martin Thullner Response, *Ecol. Eng.*, 36(6), 837-838.
- Thullner, M. (2010b), Comparison of bioclogging effects in saturated porous media within one- and two-dimensional flow systems, *Ecol. Eng.*, 36(2), 176-196.
- Tidwell, V. C., and R. J. Glass (1994), X ray and visible light transmission for laboratory measurement of two-dimensional saturation fields in thin-slab systems, *Water Resources Research*, 30(11), 2873-2882.
- Tidwell, V. C., et al. (2003), Visualization experiment to investigate capillary barrier performance in the context of a Yucca Mountain emplacement drift, *Journal of Contaminant Hydrology*, 62-3, 287-301.
- Udovich, J. A., et al. (2008), Spectral background and transmission characteristics of fiber optic imaging bundles, *Appl. Opt.*, 47(25), 4560-4568.
- Uesugi, S. L., et al. (2001), A model that uses the induction phase of lux gene-dependent bioluminescence in *Pseudomonas fluorescens* HK44 to quantify cell density in translucent porous media, *Journal of Microbiological Methods*, 47(3), 315-322.
- Ursino, N., et al. (2001a), Combined effects of heterogeneity, anisotropy, and saturation on steady state flow and transport: A laboratory sand tank experiment, *Water Resources Research*, 37(2), 201-208.
- Ursino, N., et al. (2001b), Dilution of non-reactive tracers in variably saturated sandy structures, *Advances in Water Resources*, 24(8), 877-885.
- Ursino, N., and T. Gimmi (2004), Combined effect of heterogeneity, anisotropy and saturation on steady state flow and transport: Structure recognition and numerical simulation, *Water Resources Research*, 40(1), 12.

- Vanderborght, J., et al. (2002a), Identification of transport processes in soil cores using fluorescent tracers, *Soil Science Society of America Journal*, 66(3), 774-787.
- Vanderborght, J., et al. (2002b), Imaging Fluorescent Dye Concentrations on Soil Surfaces: Uncertainty of Concentration Estimates, *Soil Sci Soc Am J*, 66(3), 760-773.
- Vangeel, P. J., and J. F. Sykes (1994), LABORATORY AND MODEL SIMULATIONS OF A LNAPL SPILL IN A VARIABLY-SATURATED SAND .1. LABORATORY EXPERIMENT AND IMAGE-ANALYSIS TECHNIQUES, *Journal of Contaminant Hydrology*, 17(1), 1-25.
- Vanommen, H. C., et al. (1988), A new technique for evaluating the presence of preferential flow paths in nonstructured soils, *Soil Science Society of America Journal*, 52(4), 1192-1193.
- Verdon, J., and A. W. Woods (2007), Gravity-driven reacting flows in a confined porous aquifer, *J. Fluid Mech.*, 588, 29-41.
- Vinegar, H. J., and S. L. Wellington (1987), Tomographic imaging of 3-phase flow experiments, *Rev. Sci. Instrum.*, 58(1), 96-107.
- Vogel, H. J., and K. Roth (2001), Quantitative morphology and network representation of soil pore structure, *Advances in Water Resources*, 24(3-4), 233-242.
- von Wandruska, R., and J. D. Wineforder (1986), Fluorescence in thin liquid films, *Talanta*, 33(11), 871-874.
- Walker, R. C., et al. (1998), Surfactant enhanced removal of PCE in a nominally two-dimensional, saturated, stratified porous medium, *Journal of Contaminant Hydrology*, 34(1-2), 17-30.
- Walter, M. T., et al. (2000), Funneled flow mechanisms in a sloping layered soil: Laboratory investigation, *Water Resources Research*, 36(4), 841-849.
- Wan, J., et al. (1994), Influence of the gas-water interface on transport of microorganisms through unsaturated porous media, *Applied and Environmental Microbiology*, 60(2), 509-516.
- Wan, J., and J. L. Wilson (1994a), Visualization of the role of the gas-water interface on the fate and transport of colloids in porous media, *Water Resources Research*, 30(1), 11-23.
- Wan, J. M., et al. (1996), Improved glass micromodel methods for studies of flow and transport in fractured porous media, *Water Resources Research*, 32(7), 1955-1964.
- Wan, J. M., and T. K. Tokunaga (1997), Film straining of colloids in unsaturated porous media: Conceptual model and experimental testing, *Environmental Science & Technology*, 31(8), 2413-2420.
- Wan, J. M., and T. K. Tokunaga (2005), Comments on "Pore-scale visualization of colloid transport and retention in partly saturated porous media", *Vadose Zone Journal*, 4(4), 954-956.
- Wang, H. G., et al. (2008), Locally-calibrated light transmission visualization methods to quantify nonaqueous phase liquid mass in porous media, *Journal of Contaminant Hydrology*, 102(1-2), 29-38.
- Weiler, M., and H. Fluhler (2004), Inferring flow types from dye patterns in macroporous soils, *Geoderma*, 120(1-2), 137-153.
- Weisbrod, N., et al. (2002), Imbibition of saline solutions into dry and prewetted porous media, *Advances in Water Resources*, 25(7), 841-855.
- Weisbrod, N., et al. (2003a), Water vapor transport in the vicinity of imbibing saline plumes: Homogeneous and layered unsaturated porous media, *Water Resources Research*, 39(6).

- Weisbrod, N., et al. (2003b), Light transmission technique for the evaluation of colloidal transport and dynamics in porous media, *Environmental Science & Technology*, 37(16), 3694-3700.
- Weisbrod, N., et al. (2004), Migration of saline solutions in variably saturated porous media, *Journal of Contaminant Hydrology*, 72(1-4), 109-133.
- Welker, A. L., et al. (1999), Applied research using a transparent material with hydraulic properties similar to soil, *Geotech. Test. J.*, 22(3), 266-270.
- Wellington, S. L., and H. J. Vinegar (1987), X-ray computerized-tomography, *J. Pet. Technol.*, 39(8), 885-898.
- Werth, C. J., et al. (2010), A review of non-invasive imaging methods and applications in contaminant hydrogeology research, *Journal of Contaminant Hydrology*, 113(1-4), 1-24.
- White, D., et al. (1996), Lux gene technology - A strategy to optimize biological control of soil-borne diseases, *New Phytology*, 133, 173-181.
- Wildenschild, D., et al. (1994), A laboratory analysis of the effect of macropores on solute transport, *Ground Water*, 32(3), 381-389.
- Wildenschild, D., and K. H. Jensen (1999), Laboratory investigations of effective flow behavior in unsaturated heterogeneous sands, *Water Resources Research*, 35(1), 17-27.
- Wildenschild, D., et al. (2002), Using X-ray computed tomography in hydrology: systems, resolutions, and limitations, *Journal of Hydrology*, 267, 285-297.
- Wildenschild, D., et al. (2005), Quantitative analysis of flow processes in a sand using synchrotron-based X-ray microtomography, *Vadose Zone Journal*, 4(1), 112-126.
- Wipfler, E. L., et al. (2004), Infiltration and redistribution of LNAPL into unsaturated layered porous media, *Journal of Contaminant Hydrology*, 71(1-4), 47-66.
- Wong, R. C. K., and R. Wibowo (2000), Tomographic evaluation of air and water flow patterns in soil column, *Geotech. Test. J.*, 23(4), 413-422.
- Wooding, R. A. (1963), Convection in a saturated porous medium at large rayleigh number or pecllet number, *J. Fluid Mech.*, 15, 527-544.
- Yarwood, R. R., et al. (2002), Noninvasive quantitative measurement of bacterial growth in porous media under unsaturated-flow conditions, *Applied and Environmental Microbiology*, 68(7), 3597-3605.
- Yarwood, R. R., et al. (2006), Impact of microbial growth on water flow and solute transport in unsaturated porous media, *Water Resources Research*, 42(10).
- Ye, S. J., et al. (2009), The impact of methanogenesis on flow and transport in coarse sand, *Journal of Contaminant Hydrology*, 103(1-2), 48-57.
- Yoon, J. S., et al. (2006), Visualization of particle behavior within a porous medium: Mechanisms for particle filtration and retardation during downward transport, *Water Resources Research*, 42(6).
- Yu, Z. B., and F. W. Schwartz (1999), Determining concentration fields of tracer plumes for layered porous media in flow-tank experiments, *Hydrogeology Journal*, 7(2), 236-240.
- Zevi, Y., et al. (2005), Distribution of colloid particles onto interfaces in partially saturated sand, *Environmental Science & Technology*, 39(18), 7055-7064.
- Zevi, Y., et al. (2009), Transport and retention of colloidal particles in partially saturated porous media: Effect of ionic strength, *Water Resources Research*, 45.

- Zhang, P. F., and Y. G. Wang (2006), Epi-fluorescence Imaging of colloid transport in porous media at decimeter scales, *Environmental Science & Technology*, 40(19), 6064-6069.
- Zhang, P. F., et al. (2009), Enhanced Mixing and Plume Containment in Porous Media under Time-Dependent Oscillatory Flow, *Environmental Science & Technology*, 43(16), 6283-6288.
- Zhang, Z. F., and J. E. Smith (2001), The velocity of DNAPL fingering in water-saturated porous media: laboratory experiments and a mobile-immobile-zone model, *Journal of Contaminant Hydrology*, 49(3-4), 335-353.
- Zhang, Z. F., and J. Smith (2002), Visualization of DNAPL Fingering Processes and Mechanisms in Water-Saturated Porous Media, *Transport in Porous Media*, 48(1), 41-59.
- Zhong, L. R., et al. (2001), Visualization of surfactant-enhanced nonaqueous phase liquid mobilization and solubilization in a two-dimensional micromodel, *Water Resources Research*, 37(3), 523-537.
- Zhu, W., et al. (2007), Tracer transport in a fractured chalk: X-ray CT characterization and digital-image-based (DIB) simulation, *Transport in Porous Media*, 70(1), 25-42.
- Zinn, B., et al. (2004), Experimental visualization of solute transport and mass transfer processes in two-dimensional conductivity fields with connected regions of high conductivity, *Environmental Science & Technology*, 38(14), 3916-3926.

## APPENDICES

## Appendix A: Spectral Curves of Optical Components

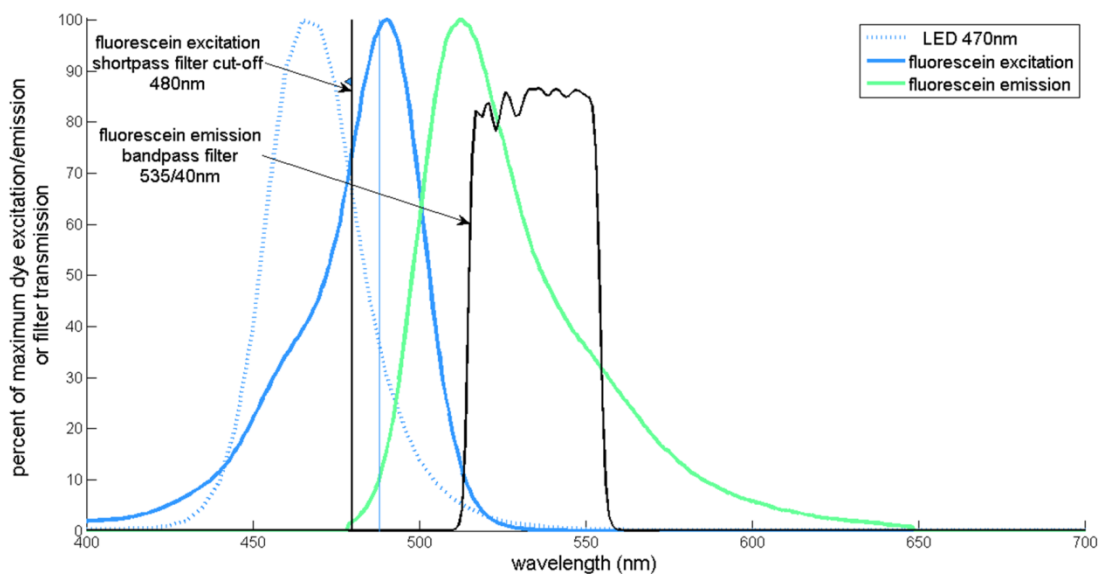


Figure A.1 Excitation and emission curves for fluorescein at pH9 from data provided by Molecular Probes plotted with led spectrum, excitation filter cutoff and emission filter bandpass.

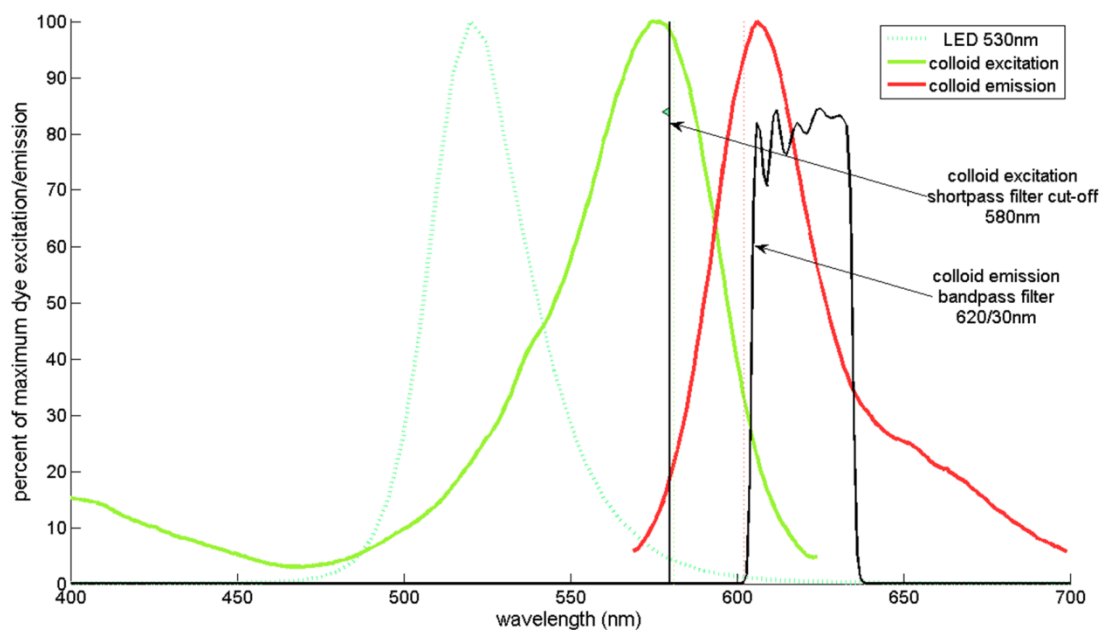


Figure A.2 Fluorescent spectra for red fluorescent microspheres overlain by chosen optical components for microsphere excitation and detection.

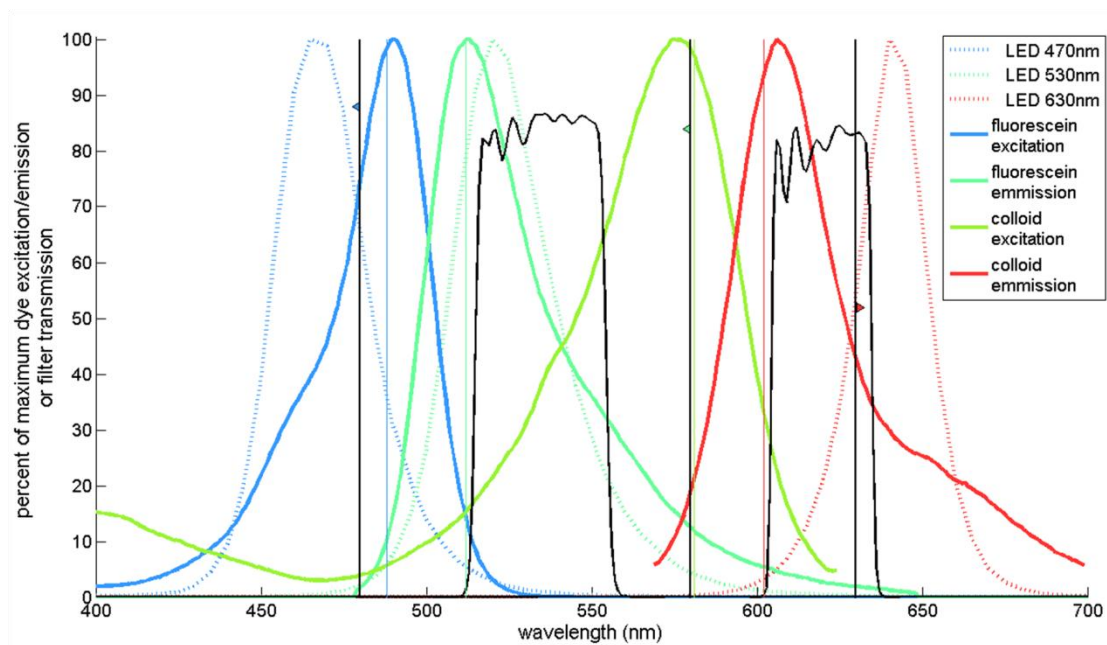


Figure A.3 Excitation and emission curves of FluoSpheres® red fluorescent microspheres/H<sub>2</sub>O and Fluorescein/pH 9.0 generated from data provided by Molecular Probes, Inc. Overlain are the properties of optical components used in the system. Black dotted lines denote the wavelengths used for fluorometer excitation and emission.

## Appendix B: Experimental Protocol

### Chamber assembly, packing, and calculations

- \_\_1. **Clean** all outer chamber parts (light box, chamber frame including bottom block, and bumpers) by sweeping free of sand and wiping down with paper towels.
- \_\_2. **Clean** all inner chamber parts with soap and hot water. (lower manifold, steel mesh, upper manifold) Rinse 4x with tap, 3x with ROW. Then use dilute acid wash (0.1M H<sub>2</sub>SO<sub>4</sub>) and rinse last time with ROW. Allow to air dry. Do not use sulfuric acid on u-shape spacer as it dissolves the silicone between the joints. Instead use remove the o-ring stock from the spacer and rinse well with row, then wipe down with acetone to remove traces of dye. O-ring stock may be washed well with ROW. Make sure all parts are thoroughly air dry before assembly.
- \_\_3. **Clean** the chamber glass first with soap and hot water, then ROW, then ammonia-based glass cleaner and clean paper towel, then acetone and clean paper towel, and lastly with 0.01M sulfuric acid rinse and ROW rinse. Dry by hand with paper towel or allow to air dry and then wipe down once more with acetone.
- \_\_4. **Assemble** the chamber on metal table. First the frame, then the bottom glass, the u-shaped spacer with upper grooves facing up, the manifold and steel mesh, the front glass sheet, the upper corner rubber blocks.
- \_\_5. **Fit** the upper mask into the spacer groove to check that the frame upper spread is correct (18”).
- \_\_6. **Lay** in bottom and side bumper rails and line up with bolts.
- \_\_7. **Clamp** down the chamber allthread bolts against the lined bumper rails using the long-socket ratchet until snug but not forced. Make sure mask still fits loosely and then remove.
- \_\_8. **Check** frontispiece fit.
- \_\_9. **Load** the chamber onto the wooden frame and secure it with the fixed-compression latches.
- \_\_10. **Mark** the sand fill line with a sharpie 0.5cm above the base of the upper mask.
- \_\_11. **Measure** the width height and depth of the assembled pack and record.  
 $C_w = \underline{45.7} \text{ cm}$       $C_h = \underline{62} \text{ cm}$       $C_d = \underline{1} \text{ cm}$
- \_\_12. **Calculate** the sand pack volume.  $V_c = 2833.4 \text{ cm}^3$
- \_\_13. **Plumb** lower I/O tubing.
- \_\_14. **Fill** acid rinsed flask with 3L ROW. Insert, I/O tubing, cover with parafilm and tare on balance.
- \_\_15. **Fill** lower I/O tubing and lower manifold to top of mesh then stop. Record entry volume: **42mL**
- \_\_16. **Retare** balance.
- \_\_17. **Fill** chamber to fill line with ROW. Record pack volume: **2912mL**
- \_\_18. **Leave** pack static 90 minutes to check water holding—see that fill volume is steady.
- \_\_19. **Drain** chamber and assemble drying apparatus. Blow dry until mesh appears dry, and application of CO<sub>2</sub> results in no visible fluid rising.
- \_\_20. **Check** the light array to make sure all sources working correctly. Power supplies should be preset to 21V and 1200mA.
- \_\_21. **Weigh** the clean plastic bucket full of sand of a given grade and record the initial sand mass,  $M_{s,0}$ .  $M_{s,0} = \underline{\hspace{2cm}} \text{ g}$
- \_\_22. **Pack** the chamber by filling the installed, grounded prismatic-filter hopper with the desired sand grade and releasing the stop-plate. Fill to just above the fill line.
- \_\_23. **Tap** down the sand to settle gently using a small hammer on the ends of the allthread bolts.
- \_\_24. **Vacuum** off the sand above the bottom edge of the fill line so that the overburden is collected in the Erlenmeyer flask.
- \_\_25. **Weigh** the sand remaining in the hopper, the flask and in the decanter and record the remaining mass,  $M_{s,r}$ .  
 $M_{s,r} = \underline{\hspace{2cm}} \text{ g}$

- \_\_26. **Calculate** the mass of sand in the chamber as  $M_{s,c} = M_{s,0} - M_u$   $M_{s,c} = 5184 \text{ g}$
- \_\_27. **Calculate** the volume of sand in the chamber as  $V_{s,c} = \frac{M_{s,c}(g)}{2.66g/cm^3}$   $V_{s,c} = 1968 \text{ cm}^3$   
 The volume of the sand pack is  $46w \times 62h \times 1d \text{ cm}^3$
- \_\_28. **Calculate** the porosity of the sand pack as  $\alpha (\%/00) = 1 - \left(\frac{V_{s,c}(cm^3)}{V_c(cm^3)}\right)$   $\alpha = 0.335$
- \_\_29. **Calculate** the mass of one pore volume of water as  
 $pvm(g) = (totvol(cm^3) - sandvol(cm^3))waterdensity(1 \frac{g}{cm^3})$   $pvm = 995 \text{ g}$
- \_\_30. **Calculate** flow rate for one pore volume in ten minutes: flow rate = \_\_\_\_\_ mL/min
- \_\_31. **Cover** the top of the chamber/sand surface to prevent dust from settling.

### Sealing the imaging volume

- \_\_32. **Plumb** system with new PharMed BPT 1/8" ID (6.3mm) as described in tubing schematic protocol. Include overflow line to separate peristaltic pump using same tubing. Include short lengths first through fluorometer, then pH cell, then EC cell.
- \_\_33. **Record** lengths of tubing used.
- \_\_34. **Calibrate** both peristaltic pumps. For dual pump head, calibrate at both positions pump head using a single length of PharMed BPT 1/8" ID (3.2mm) tubing. Enter this tubing as l/s 16 even though l/s 16 is ID 3.1mm. Record the discrepancy between the two lines and calibrate to the mean. For single head overflow pump, calibrate and set to a flow rate of 40 mL/min which is a rate that should never be exceeded in the experimental flow. 4.0 on the dial of the overflow pump is 37 mL/min using 1/8" tubing. Small pump 7/1/09: 5.0 is 44mL/min, 3.0 is 27mL/min.
- \_\_35. **Straighten** and the bend first two turns of steel tubing. The ends of the tubing should be crimped (ideally parallel to the pack width) to prevent sand grain entry on insertion. Tupe three lengths together do that they may be installed as one single unit. Make sure all three and the same length and parallel to eachother.
- \_\_36. **Wipe** steel tubing insertion length with acetone.
- \_\_37. **Install** the steel tubing for plume application into the sand pack to a depth of 9cm below sand surface. This is an elevation from the bottom of the sand pack of 53cm. The horizontal position of the three tubing lengths should be 10cm, 23cm and 36cm from left edge of sand pack.
- \_\_38. **Fasten** steel tubing to to light box with Velcro.
- \_\_39. **Tape** steel to back side of back glass sheet just before the final bend to insure all three lengths remain the same depth.
- \_\_40. **Fit** overflow tubing to the very top of headspace volume. This piece needs improvement!!
- \_\_41. **Tape** upper rubber fillers and I/O tubing to the back of the upper mask with electrical tape so that outlet is **2cm** from lower edge of mask, and so that the rubber edge is 0.5cm below the top of the glass. The sand surface should be 0.5 above the bottom of the mask, and the headspace from sand surface to the top of the glass is 3cm. So tubing at 2cm from edge of mask, tubing outlet should be situated 1.5 cm above sand surface and 1.5 cm below the top of the glass. Make sure that the rubber is pressed between the glass sheets to hole both the I/O and o.f. tubing in place.
- \_\_42. **Install** upper mask with tubing so that mask presses down into top 0.5cm of sand pack.
- \_\_43. **Connect** bottom line to the lower port on the chamber. Use twist tie on connections. Adjust grommet to seal hole in lower support block.
- \_\_44. **Turn** on the camera.

- \_\_45. **Fix** the frontispiece to the chamber using  $\frac{5}{16}$ -inch wing nuts until finger tight. Include upper foam strip between glass and frontispiece.
- \_\_46. **Remove** lens cap from camera.
- \_\_47. **Clean** the camera lens with lens paper and alcohol and then gas duster.
- \_\_48. **Seal** the imaging area by squeezing the dark-room curtain to the chamber's foam cushion using the ratchet strap. Foam blocks inserted at all corners and at ends of upper mask. At bottom corners slack curtain should be rolled snugly in and down.

### Dry images

- \_\_49. **Adjust** room lights for imaging—blue led, pH fluorescent and desk lamp on, overheads off.
- \_\_50. **Turn on** 630nm sources using switch (sk5 on adu218).
- \_\_51. **Collect** one image at every exposure time from 0.02s to 5.17h or oversaturation, whichever comes first, at each filter wheel position. Save as time\_filter\_630nm\_dry
- \_\_52. **Turn off** 630nm (rk5 on adu218) and turn on 470nm (sk0, sk1 on adu200).
- \_\_53. **Collect** one image at every exposure time from 0.02s to 5.17h or oversaturation, whichever comes first, at each filter wheel position. Save as time\_filter\_470nm\_dry
- \_\_54. **Turn off** 470nm (rk0, rk1 on adu200) and turn on 530nm (sk2, sk3 on adu200).
- \_\_55. **Collect** one image at every exposure time from 0.02s to 5.17h or oversaturation, whichever comes first, at each filter wheel position. Save as time\_filter\_530nm\_dry

### Saturating the sand pack and saturated images

- \_\_56. **Rinse** three large flasks with 0.01M H<sub>2</sub>SO<sub>4</sub> and ROW.
- \_\_57. **Fill** 3L flask with ROW and place on balance.
- \_\_58. **Set** second 3L flask on second balance. Insert upper line tubing, cover top with parafilm and tare.
- \_\_59. **Set** third flask(1L) on table. Insert overflow tubing and cover mouth with parafilm.
- \_\_60. **Calibrate** the pH and EC probes.
- \_\_61. **Test** and record pH and EC of source buffer . pH = **7.80** EC =  
**816µS/cm**
- \_\_62. **Insert** lower line tubing to source flask, seal top with parafilm, and tare.
- \_\_63. **Insert** pH and EC probes into flow-through cells.
- \_\_64. **Purge** the sand pack from below with **~35 pore volumes** of CO<sub>2</sub> which is **16cfh** for one to **4 minutes**.
- \_\_65. **Purge** the sand from below at 10mL/min with BUF until the sand is saturated and the purging fluid begins to fill the outlet flask.
- \_\_66. **Stop** flow just as fluid enters outlet flask and then clamp lines.
- \_\_67. Purge lines until BUF appears in image—note volume to visualization: **44mL**
- \_\_68. **Collect** 20 images over saturation at 630nm\_0\_0.02s with 10sec delay. Collect until buffer front is uniformly progressing then switch to longer delay. 0.02 s oversaturates the chip. 30 images at 10s delay at 10mL/min ended before front was uniform, but switched then to 2000s delay 0.01s. Better to have shorter delay to observe start of saturation... Move to 0.01s w/ 10s delay for a few.
- \_\_69. **Collect** 30 images over saturation at 630nm\_0\_0.01s with 200sec delay. Saturation should take ~100min.
- \_\_70. **Install** pH and EC probes to flow-through cells when sand more than half way saturated.
- \_\_71. **Check** fluorometer flowthrough to make lines are connected well and glass is clean.
- \_\_72. **Record** volume applied as fluid reaches the top of the image area: **950mL** (-44mL = 906mL)
- \_\_73. **Pump** until fluid reaches outlet flask. Make sure EC and pH flow though are holding fluid. Stop pump and clamp lines.
- \_\_74. **Allow** chamber to sit saturated for at least one hour or overnight to equilibrate. Record time:

- \_\_75. **Record** the full mass of BUF used for saturation including sand, manifold and lines:  $M_{f,r,2} = \text{g}$
- \_\_76. **Calculate** the fluid mass in the lines and manifold as saturation mass minus calculated pore volume. 1145mL to EC probe—leaking—stop flow before effluent outlet to flask and set overnight  $V_{\text{non-pore}} = \text{mL}$
- \_\_77. **Record** first pH and EC from flow-through cells while static: pH 5.96 EC = 637 $\mu$ S.cm
- \_\_78. **Unclamp** the inlet line.
- \_\_79. **Purge** the sand with an additional two pore volumes of BUF using the peristaltic pump at 92mL/min. Record starting and ending mass and elapsed time of pumping.  
 $t = \text{_____}$   $M_0 = \text{_____g}$   $M_{t2} = \text{_____g}$
- \_\_80. **Test and record** pH and EC of the BUF as it comes off the sand at purged pore-volume intervals.  
 PV1: pH = \_\_\_\_\_ EC = \_\_\_\_\_  
 PV2: pH = \_\_\_\_\_ EC = \_\_\_\_\_  
 PV3: pH = \_\_\_\_\_ EC = \_\_\_\_\_
- \_\_81. **Stop** flow and clamp inlet line, leaving the pack saturated with BUF.
- \_\_82. **Collect** BUF-saturated images.  
 a. Turn on light bank to 470nm, and using emission filter 1 collect a single 49.7 minute image.  
 b. Using no emission filter, collect 0.31 second images every 30 seconds for 49.7minutes.  
 c. Turn off 470nm sources.  
 d. Turn on 530nm sources, and using emission filter 2 collect a single 5.17 hour image.  
 e. Using no emission filter, collect 0.31 second images every five minutes for 5.17 hours.  
 f. Turn off 530nm sources.
- \_\_83. **Save** single images as 049.700m\_1\_470n\_sat and 005.170h\_2\_530nm\_sat, and save image sets each as a single image file stack titled 000.031s\_0\_470nm\_stack\_sat and 000.031s\_0\_530nm\_stack\_sat.

## Solution preparation

- \_\_84. **Calibrate** the pH and EC meter.
- \_\_85. **Separate** out a 4L volume of BUF from the stock jug.
- \_\_86. **Test and record** the pH and electro-conductivity (EC) of a sample of BUF from the 4L flask.  
 pH = \_\_\_\_\_ EC = \_\_\_\_\_
- \_\_87. **Calculate** dilutions for 100mL of ten two-dye solutions stepping down in concentration by single orders of magnitude from 1E3ppm (1ppt) to 1E-4ppm (0.1ppT), where the pure fluorescein powder is 1E6ppm, the colloid stock (2% solids) is 2E4ppm, and 1ppm is equal to 1mg/L.
- \_\_88. **Label** 50mL centrifuge tubes.
- \_\_89. **Sonicate** the colloid stock solution 3 times in 30 second bursts.
- \_\_90. **Mix** 1E3 stock solution by measuring ROW into an Erlenmeyer flask with a stir bar. Add to stirring water fluorescein powder weighed on micro balance and colloids with micropipettor.
- \_\_91. **Mix** serial dilutions by measuring RO water into each centrifuge using a 50mL volumetric flask and removing 5mL with a 1mL micropipettor. To the 1E3ppm tube
- \_\_92. **Read** fluorescence of each dilution at nm and nm.
- \_\_93. **Test and record** the pH and EC, of each dye solution.

- \_\_94. **Place** the so on the shaker table in the incubator at 18°C and 90rpm. Each solution is removed and placed on stir plate for ten minutes prior to use, to ensure sufficient mixing.

### Dye plume application and imaging

- \_\_95. **Weigh** record initial mass of the solution flask on the laboratory balance.
- \_\_96. **Move** lower tubing end to constant head position and secure over clean flask.
- \_\_97. **Apply** 5mL of dye solution to the sand pack through each length of steel tubing starting at the facing-chamber rightmost input (lowest port) and working left (working ports up).
- 5mL pushed into tubing via syringe and left filling tubing for plume imaging.
  - Initial plume volume is 5mL minus the tubing volume specific to each length.
- \_\_98. **Collect** data images **according to the Imaging Protocol**. fluorescein first, then colloids, then fluorescein again
- \_\_99. **Flush** the chamber with BUF from above at 20mL/min until dye removal tails off.
- \_\_100. **Image** the flush at discrete intervals, stopping flow for image every 1 minute.
- \_\_101. **Trace** flush on the spectrofluorometer using appropriate sensitivity.
- \_\_102. **Collect** images of BUF-flushed chamber at all filter combinations to be used as initial condition for next plume images.
- \_\_103. **Start** again at step 94 until all concentrations imaged.
- \_\_104. **Collect** dark images **as described in step 2 of the Imaging Protocol**.

**Appendix C: Fluorometer Calibration**

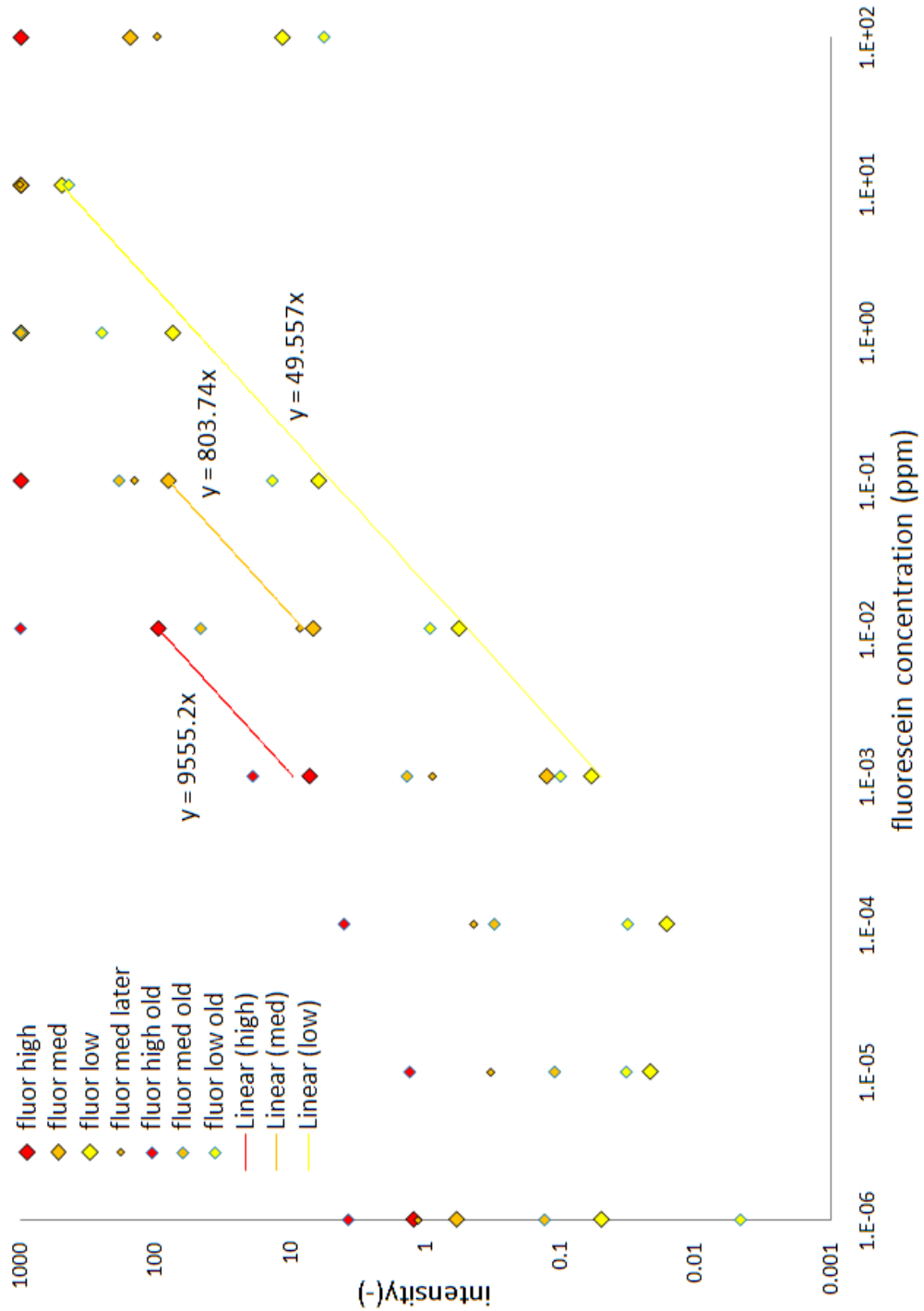


Figure A.4 Fluorometer calibration curves for fluorescein excited at 488nm and emitting at 512nm. Legend notes sensitivity settings, condition of the standards, and linear fits.

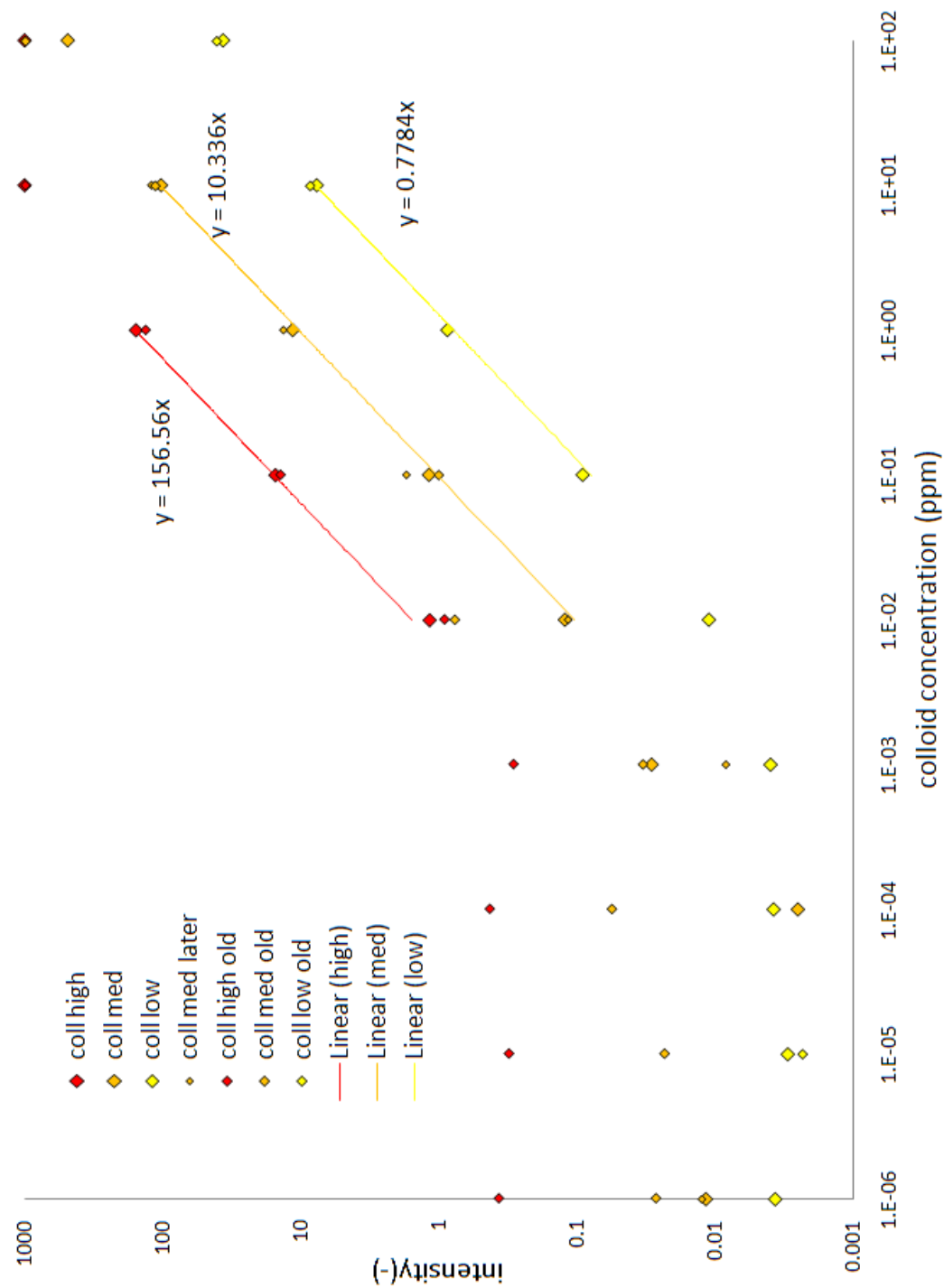


Figure A.5 Fluorometer calibration curves for colloids excited at 577nm and emitting at 601nm. Legend notes sensitivity settings, condition of the standards, and linear fits.

## Appendix D: Imaging Protocol

### Exposure Time Series

Table A.1 Exposure times used in calibration experiments.

exposure time (sec)	exposure time (min)	exposure time (hrs)
0.05		
0.13		
0.31		
0.78		
1.95		
4.88		
12.21		
30.52		
76.29	1.3	
190.73	3.2	
476.84	7.9	
1192.09	19.9	
2980.23	49.7	
7450.58	124.2	2.07
18626.45	310.4	5.17
46566.13	776.1	12.94
116415.32	1940.3	32.34
291038.30	4850.6	80.84
727595.76	12126.6	202.11
1818989.40	30316.5	505.27

### Power Considerations

- Power setting for all wavelengths: 22V 1200mA
- Red is voltage limited, and green and blue are current limited.
- This is reduced power for six in one circuit of red and maximum power for three in two circuits of blue and green.
- Max power setting for a single circuit of three diodes in parallel is:
- 470nm and 530nm: 19.50V and 1200mA (19.5V and 400mA each)
- Max power setting for a single circuit of six diodes as three in parallel of two each in series is:
- 630nm: 26V and 1440mA (13V and 480mA each)

### Imaging

- 1) **Set up folders** in the Dropbox on Glowbug in a main folder for the date of the experiment. For the experiment folder use the convention xx\_xx\_xx for the month, day and year the experiment was performed. Name the folders inside the experimental folder dark, dry, sat and data. Use f-stop 1.4 and default power ratings for all images.
- 2) **Dark Images:** After step 31 of the Experimental Protocol, collect images at exposure times 0.05, 0.13, 0.31, 0.78, 1.95, 4.88, 12.21, 30.52, 76.29, 190.73, 476.84sec; 19.9 and 49.7min; 2.07 and 5.17hrs with lights off and shutter closed, through each emission filter. Save these images to the \dark\ folder using the convention xxsec\_[0,1,2]\_dark where 0, 1, and 2 are the no filter, fluorescein filter and colloid filter respectively. Alternately, these images can be collected at any

other time, particularly for long exposure 2 and 5 hours. Once collected, these images can be used for any experimental data of the same exposure time and excitation filter setting. Dark images do not need to be recollected for each experiment.

- 3) **Dry Images:** After step 31 of the Experimental Protocol, turn on one source at a time and collect images at exposure times 0.05, 0.13, 0.31, 0.78, 1.95, 4.88, 12.21, 30.52, 76.29, 190.73, 476.84sec or until oversaturated, for each source using both no filter (position 0) and the emission filter corresponding to the given source (position 1 for 470nm and position 2 for 530nm). Save these files to the \dry\ folder using the convention `xxsec_[0,1,2]_[470, 530, 630nm]_dry`
- 4) **Sat Images:** After step 44 of the Experimental Protocol, turn on one source at a time and collect images at exposure times 0.05, 0.13, 0.31, 0.78, 1.95, 4.88, 12.21, 30.52, 76.29, 190.73, 476.84sec or until oversaturated, for each source using both no filter (position 0) and the emission filter corresponding to the given source (position 1 for 470nm and position 2 for 530nm). Save these files to the \sat\ folder using the convention `xxsec_[0,1,2]_[470, 530nm]_sat`.
- 5) **Data Images:** After step 51 of the Experimental Protocol, turn on one source at a time and collect images at exposure times to maximize the dynamic range of the camera. Choose from 0.05, 0.13, 0.31, 0.78, 1.95, 4.88, 12.21, 30.52, 76.29, 190.73, 476.84sec; 19.9 and 49.7min; 2.07 and 5.17hrs for each source using its corresponding emission filter. Save these images to the folder \data\ using the file convention `xxsec_[0,1,2]_[470, 530nm]_yyppm` where yy is the concentration in ppm of the solution that saturates the sand during that data set. (If the concentration varies between the two dye types, use both values beginning with the colloid concentration as `_collppm-fluorppm`.)

## ***Appendix E: Image Processing***

### **Protocol**

The goal of data processing is to convert the intensity value at each pixel into an actual concentration value in ppm. In each experiment, four types of images were collected and used to compute concentration—**'dark'**, **'dry'**, **'sat'**, and **'data'**. The conditions under which each of these types were collected, and the way in which they were used to compute actual concentration are described below. In this discussion, data arrays will be noted in bold, while single values will be in regular font.

Images called **'dark'** provide the pixel-by-pixel offset that must be subtracted from all subsequent images to have the image intensity be zero when there is no light. **'dark'** images are collected with the camera's shutter closed, the LED array turned off, and a particular emission filter in place.

Images called **'dry'** are collected before saturation of the sand pack with a given light with excitation filter and emission filter combination. These **'dry'** images are required for computation of water content in variably saturated images.

Images called **'sat'** and **'data'** are collected illuminated by each color of light. With the red LEDs, no emission filter is used. With the blue and green LEDs, the appropriate emission filter is used. Images called **'sat'** are collected after water saturation of the sand pack, and are used to flat-field the data. Images called **'data'** are collected of dye distribution in the system, and contain the target information. These **'data'** images are the basis of the image processing protocol—all operations are performed on these starting arrays.

Image arrays are 512x512 pixels. All images were processed in double precision, and a new variable is saved after each step. The processing protocol and the code employed are provided in Appendix D. The steps used to transform **'data'** into the actual dye concentration referred to as **'actuconc'** are outlined below.

1. Median-filtering of every image. The effect of this is to remove “hot” pixels in the data that are due to defects on the chip. Hot pixels are a normal feature of CCD camera images. They are caused by some of the sensor elements having a higher rate of charge leakage. At long exposure times some pixels may appear brighter due to charge from neighboring elements flooding over and oversaturating the susceptible element. The hot pixels must be removed, and in this work a 3x3 median filter was implemented: of the 9 points in each 3x3 “frame,” the center point was replaced with the median value of pixels within the frame. This process eliminates extreme high and low data without changing their fundamental character. Dye distribution and water content do not tend toward discontinuities that would be represented by these outliers. As this system is built to observe dye distribution and water content, the fundamental, non-extreme character of the data is unaffected by alteration of a data point to fit smoothly into the neighborhood of pixels in which it resides. In this step images called ‘**dark**’ ‘**sat**’ and ‘**data**’ become ‘**mfdark**’ ‘**mfsat**’ and ‘**mfddata**’ respectively.
2. Subtraction of median-filtered dark image ‘**mfdark**’ from each ‘**mfsat**’ and ‘**mfddata**’ image. The ‘**mfdark**’ arrays used in this step employ the same emission filter and exposure time as the image being processed. The resulting dark-subtracted images are referred to as ‘**dssat**’ and ‘**dsdata**’. The reason for this step was the removal of the bias, or offset, of the imaging system. Dark current on the CCD chip was eliminated from the data, as were anomalous physical features such as leakage in the light containment system.
3. Cropping of each dark-subtracted array to remove the chamber frame. Each array is cropped to the same dimensions to match the dimensions of the experimental area. The effect of this step is to remove data that is meaningless with regard to the sand-water-dye system. The resultant images are identified by appending the suffix ‘crop,’ e.g., ‘**dsdata\_crop**’.
4. Calculation of the mean value of the ‘**dssat\_crop**’ array. There is one ‘**sat**’ image for each of the three wavelengths of light. Each of the three ‘**dssat\_crop**’ images results in a single mean value

referred to as 'dssatcrop\_mean'. This is a scaling value used to keep values positive in the following division step.

5. Calculation of relative concentration values for each data array based on the normalization equation:

$$\mathit{relconc} = \left( \frac{\mathit{dsdata\_crop}(\mathit{dssatcrop\_mean})}{\mathit{dssat\_crop}(\mathit{time})} \right) \quad (39)$$

Here, 'time' is a real number representing the exposure time of the original data image (in seconds). The result of this computation is an array which is corrected for inhomogeneity in background illumination (represented by the saturated image) and normalized for time. These relative concentration values are then plotted against the known applied concentration to generate a single calibration function for each dye.

6. Application of the calibration function to the '**relconc**' arrays. This mathematical computation transforms relative concentration data into '**actuconc**' arrays of actual concentration in ppm.

These calibration functions and the process used to acquire them are described in Chapter Four.

A MatLAB script containing the full data processing protocol is provided in Appendix D. Images, histograms, close-up areas, and statistics for a single data array subjected to these image processing steps are presented in Appendix E.

## MatLAB Script

Each processing step requires a significant amount of code, and involves a large amount of data

(~260,000 values per image, up to 28 images per step).

### *Set-up, Input, and Display*

```
%% set-up
clc; clear; close all;
iptsetpref('ImshowBorder','loose');
load 'whitejet';
```

```
%% dark input and display
```

```

dark = dir('dark\*.tif');
darknames = {dark.name}';
darkcount = numel(darknames);
good_darknames = strrep(darknames, '_', '');
darkarray = zeros(512,512,darkcount,'double');
for i = 1:darkcount;
    darkarray(:, :, i) = imread(['dark\',darknames{i}]);
    mfdark(:, :, i) = medfilt2(darkarray(:, :, i));
end
figure('name','dark images');
set(gcf,'Renderer','Zbuffer');
set(gcf,'position',[10 90 1260 865] , 'color',[1,1,1]);
for i = 1:darkcount;
    subplot(3,7,i); imshow(mfdark(:, :, i), 'displayrange', []);
    title({good_darknames{i}; ' mf'});
    caxis auto; colorbar; colormap(whitejet);
end;

%% sat input and display
sat = dir('sat\*_0_*.tif');
satnames = {sat.name}';
satcount = numel(satnames);
good_satnames = strrep(satnames, '_', '');
satarray = zeros(512,512,satcount,'double');
for i = 1:satcount;
    satarray(:, :, i) = imread(['sat\',satnames{i}]);
    mfsat(:, :, i) = medfilt2(satarray(:, :, i));
end
figure('name','sat images'); set(gcf,'Renderer','Zbuffer');
set(gcf,'position',[10 90 1260 865], gcf,'color',[1,1,1]);
for i = 1:satcount;
    subplot(1,2,i); imshow(mfsat(:, :, i), 'displayrange', []);
    title({good_satnames{i}; ' mf'});
    caxis auto; colorbar; colormap(whitejet);
end

%% data 470 input and display
data470 = dir('470conc\*.tif');
data470names = {data470.name}';
data470count = numel(data470names);
good_data470names = strrep(data470names, '_', '');
data470array = zeros(512,512,data470count,'double');
for i = 1:data470count
    data470array(:, :, i) = imread(['470conc\',data470names{i}]);
    mfddata470(:, :, i) = medfilt2(data470array(:, :, i));
end
figure('name','data 470 images');
set(gcf,'Renderer','Zbuffer');
set(gcf,'position',[10 90 1260 865] , 'color',[1,1,1]);
for i = 1:data470count

```

```

subplot(2,4,i); imshow(mfdata470(:, :, i), 'displayrange', []);
title({good_data470names{i}; ' mf'});
caxis auto; colorbar; colormap(whitejet);
end

```

```

%% data 530 input and display
data530 = dir('530conc\*530nm*.tif');
data530names = {data530.name};
data530count = numel(data530names);
good_data530names = strrep(data530names, '_', ' ');
data530array = zeros(512,512,data530count,'double');
figure('name','data 530 images'); set(set(gcf,'Renderer','Zbuffer');
set(gcf,'position',[10 90 1260 865],gcf,'color',[1,1,1]);
for i = 1:data530count
    data530array(:, :, i) = imread(['530conc\'', data530names{i}]);
    mfdata530(:, :, i) = medfilt2(data530array(:, :, i));
end
for i = 1:data530count
    subplot(2,4,i); imshow(mfdata530(:, :, i), 'displayrange', []);
    title({good_data530names{i}; ' mf'});
    caxis auto; colorbar; colormap(whitejet);
end

```

### *Dark Subtraction and Cropping*

```

%% sat dark-subtraction and cropping
rect = [68 8 380 485];
dssatcrop_mean = cell(satcount,1);
satdiv = zeros(512,512,satcount,'double');
sat_stats = cell(satcount,4);
sat_stats = {'file name'; 'ds sat crop mean'; 'satdiv crop mean'};
for i = 1:satcount;
    ds_sat(:, :, i) = mfsat(:, :, i) - mfdark(:, :, 1);
    dssat_crop(:, :, i) = imcrop(ds_sat(:, :, i), rect);
    dssatcrop_mean{i} = mean2(dssat_crop(:, :, i));
end;
for i = 1:satcount;
    satdiv(:, :, i) = dssatcrop_mean{i,1} ./ ds_sat(:, :, i);
    satdiv_crop(:, :, i) = imcrop(satdiv(:, :, i), rect);
    sat_stats{[i+1],1} = satnames{i,1};
    sat_stats{[i+1],2} = dssatcrop_mean{i};
    sat_stats{[i+1],3} = mean2(satdiv_crop(:, :, i));
end
figure('name','ds sat crop'); set(gcf,'position',[10 90 1260 865]); set(gcf,'color',[1,1,1]);
set(gcf,'Renderer','Zbuffer');
for i = 1:satcount;
    subplot(1,2,i); imshow(dssat_crop(:, :, i), 'displayrange', []);
    title({good_satnames{i}; ' ds crop'});
    caxis auto; colorbar; colormap(whitejet);
end

```

```

figure('name', ' ds satdiv crop'); set(set(gcf, 'Renderer', 'Zbuffer');
set(gcf, 'position', [10 90 1260 865], gcf, 'color', [1,1,1]));
for i = 1:satcount;
    subplot(1,2,i); imshow(satdiv_crop(:,:,i), 'displayrange', []);
    title({good_satnames{i}; ' ds satdiv crop'});
    caxis auto; colorbar; colormap(whitejet);
end

%% data 470 dark-subtraction and cropping
dark470 = zeros(512,512,7, 'double');
dark470(:,:,1) = mfdark(:,:,4);
dark470(:,:,2) = mfdark(:,:,4);
dark470(:,:,3) = mfdark(:,:,11);
dark470(:,:,4) = mfdark(:,:,17);
dark470(:,:,5) = mfdark(:,:,18);
dark470(:,:,6) = mfdark(:,:,18);
dark470(:,:,7) = mfdark(:,:,18);
dsdata470crop_mean = cell(data470count,2);
for i = 1:data470count;
    ds_data470(:,:,i) = mfddata470(:,:,i) - dark470(:,:,i);
    dsdata470_crop(:,:,i) = imcrop(ds_data470(:,:,i),rect);
    dsdata470crop_mean{i,1} = good_data470names{i};
    dsdata470crop_mean{i,2} = mean2(dsdata470_crop(:,:,i));
end
figure('name', 'ds data 470'); set(gcf, 'position', [10 90 1260 865]); set(gcf, 'color', [1,1,1]);
set(gcf, 'Renderer', 'Zbuffer');
for i = 1:data470count;
    subplot(2,4,i); imshow(dsdata470_crop(:,:,i), 'displayrange', []);
    title({good_data470names{i}; ' ds crop'});
    caxis auto; colorbar; colormap(whitejet);
end

%% data 530 dark-subtraction and cropping
dark530 = zeros(512,512,7, 'double');
dark530(:,:,1) = mfdark(:,:,8);
dark530(:,:,2) = mfdark(:,:,13);
dark530(:,:,3) = mfdark(:,:,19);
dark530(:,:,4) = mfdark(:,:,15);
dark530(:,:,5) = mfdark(:,:,9);
dark530(:,:,6) = mfdark(:,:,9);
dark530(:,:,7) = mfdark(:,:,9);
dark530(:,:,8) = mfdark(:,:,9);
dsdata530crop_mean = cell(data530count,2);
for i = 1:data530count
    ds_data530(:,:,i) = mfddata530(:,:,i) - dark530(:,:,i);
    dsdata530_crop(:,:,i) = imcrop(ds_data530(:,:,i),rect);
    dsdata530crop_mean{i,1} = good_data530names{i};
    dsdata530crop_mean{i,2} = mean2(dsdata530_crop(:,:,i));
end

```

```

figure('name','ds data 530'); set(gcf,'position',[10 90 1260 865]); set(gcf,'color',[1,1,1]);
set(gcf,'Renderer','Zbuffer');
for i = 1:data530count
    subplot(2,4,i); imshow(dsdata530_crop(:,:,i),'displayrange',[]);
    title({good_data530names{i};' ds crop'});
    caxis auto; colorbar; colormap(whitejet);
end

```

### *Relative Concentration Calculation*

%% 470nm relative concentration

```

time470 = [1.95 1.95 12.21 190.73 476.84 476.84 476.84];
relconc470crop_max = cell(data470count,2);
for i = 1:data470count
    rel_conc_470(:,:,i) = (dsdata470_crop(:,:,i).*dssatcrop_mean{1,1})./(dssat_crop(:,:,1).*time470(i));
    relconc470crop_max{i,1} = good_data470names{i,1};
    relconc470crop_max{i,2} = max(max(rel_conc_470(:,:,i)));
end
figure('name','rel conc 470'); set(gcf,'color', [1,1,1]); set(gcf,'position',[10 90 1260 865]);
set(gcf,'Renderer','Zbuffer');
for i = 1:data470count
    subplot(2,4,i); imshow(rel_conc_470(:,:,i),'displayrange',[]);
    title({good_data470names{i};' rel conc'});
    caxis auto; colorbar; colormap(whitejet);
end

```

%% 530nm relative concentration

```

time530 = [4.88 30.52 476.84 2982 18612 18612 18612 18612];
relconc530crop_max = cell(data530count,2);
for i = 1:data530count
    rel_conc_530(:,:,i) = (dsdata530_crop(:,:,i).*dssatcrop_mean{2,1})./(dssat_crop(:,:,2).*time530(i));
    relconc530crop_max{i,1} = good_data530names{i,1};
    relconc530crop_max{i,2} = max(max(rel_conc_530(:,:,i)));
end
figure('name','rel conc 530'); set(gcf,'color', [1,1,1]); set(gcf,'position',[10 90 1260 865]);
set(gcf,'Renderer','Zbuffer');
for i = 1:data530count
    subplot(2,4,i); imshow(rel_conc_530(:,:,i),'displayrange',[]);
    title({good_data530names{i};' rel conc'});
    caxis auto; colorbar; colormap(whitejet);
end

```

